



TUM School of Engineering and Design

# Parameter Estimation of Lithium-ion Batteries using Distribution of Relaxation Times

Yulong Zhao, M.Sc.

Vollständiger Abdruck der von der School of Engineering and Design der Technischen Universität München zur Erlangung des akademischen Grades eines

**Doktors der Ingenieurwissenschaften (Dr.-Ing.)**

genehmigten Dissertation.

Vorsitz: Prof. Dr. Marcelo Lobo Heldwein  
Prüfer\*innen der Dissertation: 1. Prof. Dr.-Ing. Andreas Jossen  
2. Prof. Dr. Hubert Gasteiger

Die Dissertation wurde am 14.12.2022 bei der Technischen Universität München eingereicht und durch die School of Engineering and Design am 13.03.2023 angenommen.

## Abstract

The increasing integration of the renewable energy sources and growing market share of the electric vehicles (EVs) have led to a rapid development of research and manufacture of Lithium-ion batteries. The physicochemical modeling and simulation of the Lithium-ion batteries have been playing a crucial role in the design and operation of the batteries due to its ability to reflect the internal physicochemical states which are inaccessible by means of conventional measurement methods. The accuracy and thus the power of the physicochemical model of a Lithium-ion battery is to a large extent decided by the parameter set, which is estimated using various methods of different complexity. For the aforementioned reasons, the estimation of the physicochemical parameters has been a highly focused research topic. In this present thesis, first an estimation method for the physicochemical parameters with the distribution of relaxation times (DRT) is proposed, where a theory for the interpretation of the resulting DRT spectra based on a physicochemical impedance model has been developed. The highly dynamic parameters such as the solid-electrolyte-interphase (SEI) and the charge transfer parameters as well as the parameters with a sluggish effect like diffusion are investigated and estimated using the DRT method. Subsequently, different parameter estimation procedures have been investigated and compared to analyze the influence of the external ohmic resistance and estimation method on the parameter identifiability. The experimental results indicate that the state-of-charge (SOC) dependence of the parameters has considerably changed the parameter identifiability and can significantly improve the simulation accuracy, which has highlighted the necessity of the combined application of the time domain and frequency domain methods for the estimation of the physicochemical parameters.

## Kurzfassung

Die zunehmende Verwendung von erneuerbaren Energiequellen und der wachsende Marktanteil von Elektrofahrzeugen (EVs) haben zu einer rapiden Entwicklung bei Forschung und Herstellung von Lithium-Ionen-Batterien geführt. Die physikochemische Modellierung und Simulation von Lithium-Ionen-Batterien hat beim Design und Betrieb der Batterien aufgrund ihrer Fähigkeit, die internen physikochemischen Zustandsvariablen wiederzugeben, welche mittels konventioneller Messmethoden nicht bestimmbar sind, eine wichtige Rolle gespielt. Die Genauigkeit und damit die Stärke des physikochemischen Modells einer Lithium-Ionen-Batterie wird zum großen Teil von dem Parametersatz festgelegt, welcher mittels verschiedener Methoden bestimmt werden kann. Aus den oben genannten Gründen ist die Bestimmung der physikochemischen Parameter ein Forschungsthema von großer Bedeutung geworden. In dieser Arbeit wird zuerst eine Methode zur Bestimmung der physikochemischen Parameter mit der Verteilung der Relaxationszeiten (DRT) entwickelt, wo eine auf einem physikochemischen Impedanzmodell basierende Theorie zur Interpretation der resultierenden DRT Spektren hergeleitet wird. Die hochdynamischen Kenngrößen wie die Parameter von Solid-Electrolyte-Interphase (SEI), Ladungsdurchtritt sowie der Diffusion werden mit der DRT untersucht und bestimmt. Anschließend werden unterschiedliche Parameterbestimmungsverfahren untersucht und miteinander verglichen, um den Einfluss des externen ohmschen Widerstands und des Parameterbestimmungsverfahrens auf die Parameteridentifizierbarkeit zu analysieren. Die experimentellen Ergebnisse zeigen, dass die Abhängigkeit der Parameter vom Ladezustand die Parameteridentifizierbarkeit wesentlich geändert und die Genauigkeit der Simulation verbessert hat, was die Notwendigkeit der kombinierten Anwendung von Methoden im Zeitbereich und Frequenzbereich für die Bestimmung der physikochemischen Parameter hervorgehoben hat.

# Acknowledgment

This PhD thesis is based on my research work at the Chair of Electrical Energy Storage Technology (EES) at the Technical University of Munich (TUM) from August 2017 to November 2022.

First and foremost, I would like to express my sincere gratitude to Prof. Dr.-Ing Andreas Jossen, who has provided me this precious opportunity to conduct my research work and finally to complete the present PhD thesis at EES, without his encouragement, patience and guidance all of this would be impossible. Besides, I would also like to give my deepest appreciation to Prof. Holger Hesse for always being there whenever I needed his support.

Also I would like to thank all colleagues at EES for their constant help. I would like to express my special thanks to Sebastian Ludwig and Simon Kücher for the fruitful scientific discussions and support for the lab experiments. Also I would like to thank Dr. Volkan Kumtepelı at the University of Oxford for the unlimited support and guidance during my 5 years' PhD journey.

Finally, I'm also very grateful to my wife, my parents and other family members and friends. Thank you so much for your firm support, endless love and constant encouragement! Your love and support has always given me the strength and courage to continue and finally to complete my PhD research. This thesis is dedicated to all of you.

# Contents

<b>Abstract</b>	<b>b</b>
<b>Kurzfassung</b>	<b>c</b>
<b>Acknowledgment</b>	<b>d</b>
<b>List of Publications</b>	<b>III</b>
<b>Abbreviations</b>	<b>IV</b>
<b>List of symbols</b>	<b>V</b>
<b>1 Introduction</b>	<b>1</b>
1.1 Parameter Estimation with Electrochemical Impedance Spectroscopy . . . . .	2
1.1.1 Parameter Identification by Model Fitting . . . . .	2
1.1.2 Parameter Identification with the Distribution of Relaxation Times . . . . .	5
1.2 Thesis Outline . . . . .	7
<b>2 Physicochemical Modeling of the Lithium-ion Battery</b>	<b>10</b>
2.1 Structure and Working Principle of the Lithium-ion Battery . . . . .	10
2.2 Physicochemical Modeling of the Lithium-ion Battery in Time Domain . . . . .	11
2.2.1 Material Transport in the Electrolyte . . . . .	13
2.2.2 Charge Balance in the Solid and Liquid Phase . . . . .	14
2.2.3 Electrode Kinetics . . . . .	15
2.2.4 Material Transport in the Solid Phase . . . . .	17
2.2.5 Modeling the Porous Electrode . . . . .	17
2.2.6 Derivation of the p2D Model . . . . .	18
2.3 Parameter Identification in Time Domain with Probability Sampling Method . . . . .	19
2.3.1 Computationally Efficient Simulation with Reduced Order Model (ROM) . . . . .	20
2.3.2 Parameter Sampling with Bayesian Statistics and Markov-Chain-Monte-Carlo . . . . .	20
<b>3 Modeling and Characterization of the Lithium-ion Battery in Frequency Domain</b>	<b>24</b>
3.1 The Working Principle of Electrochemical Impedance Spectroscopy . . . . .	24
3.2 Evaluation of Electrochemical Impedance . . . . .	26
3.3 Physicochemical Modeling of the Lithium-ion Battery in Frequency Domain . . . . .	30
3.3.1 Equations for the Electrode Level . . . . .	31
3.3.2 Equations for the Particle Level . . . . .	32
3.3.3 Derivation of the Analytical Solution . . . . .	33
3.4 Characterization of the Lithium-ion Battery with the Distribution of Relaxation Times . . . . .	35
3.5 DRT-Analyzer: a Toolbox for the Calculation and Evaluation of Distribution of Relaxation Times Spectra . . . . .	38
3.5.1 Data Validation and Calculation . . . . .	39

3.5.2	Peak Analysis . . . . .	39
3.5.3	Results and Data Export . . . . .	40
<b>4</b>	<b>Investigation of the Distribution of Relaxation Times of a Porous Electrode Using a Physics-based Impedance Model</b>	<b>42</b>
<b>5</b>	<b>Investigation of the Diffusion Phenomena in Lithium-ion Batteries with Distribution of Relaxation Times</b>	<b>59</b>
<b>6</b>	<b>Comparative Study of Parameter Identification with Frequency and Time Domain Fitting Using a Physics-Based Battery Model</b>	<b>79</b>
<b>7</b>	<b>Conclusions and Outlooks</b>	<b>106</b>
7.1	Conclusions . . . . .	106
7.2	Outlooks for Future Work . . . . .	109
	<b>References</b>	<b>111</b>
	<b>List of Figures</b>	<b>126</b>

# List of Publications

## Peer-reviewed journal paper contributions (lead author)

- I Zhao, Y.; Kumteveli, V.; Ludwig, S.; Jossen, A.: *Investigation of the distribution of relaxation times of a porous electrode using a physics-based impedance model*, in: *Journal of Power Sources* (530), 2022
- II Zhao, Y.; Kücher, S.; Jossen, A.: *Investigation of the diffusion phenomena in lithium-ion batteries with distribution of relaxation times*, in: *Electrochimica Acta* (432), 2022
- III Zhao, Y.; Jossen, A.: *Comparative Study of Parameter Identification with Frequency and Time Domain Fitting Using a Physics-Based Battery Model*, in: *Batteries* (222), 2022

Self-written sections of peer-reviewed lead author journal paper contributions are partially contained in this doctoral thesis without further reference in the text.

## Peer-reviewed journal paper contributions (co-author)

- I Kosch, S.; Zhao, Y.; Sturm, J.; Schuster, J.; Mulder, G.; Ayerbe, E.; Jossen, A.: *A computationally efficient multi-scale model for lithium-ion cells*, in: *Journal of The Electrochemical Society* (160), 2018
- II Kumteveli, V.; Zhao, Y.; Naumann, M.; Tripathi, A.; Wang, Y.; Jossen, A.; Hesse, H.: *Design and analysis of an aging-aware energy management system for islanded grids using mixed-integer quadratic programming*, in: *International Journal of Energy Research* (43), 2019

## Abbreviations

AM	. . . . .	adaptive Metropolis
APAM	. . . . .	adaptive peak analysis method
BMS	. . . . .	battery management system
CEI	. . . . .	cathode electrolyte interphase
CPE	. . . . .	constant phase element
DFN	. . . . .	Doyle-Fuller-Newman
DRT	. . . . .	distribution of relaxation times
DVA	. . . . .	differential voltage analysis
ECM	. . . . .	equivalent circuit model
EIS	. . . . .	electrochemical impedance spectroscopy
EV	. . . . .	electric vehicle
FEM	. . . . .	finite-element-method
FLW	. . . . .	finite-length Warburg element
FSW	. . . . .	finite-space Warburg element
FT	. . . . .	Fourier transform
GEIS	. . . . .	galvanostatic electrochemical impedance spectroscopy
GITT	. . . . .	galvanostatic intermittent titration technique
KKT	. . . . .	Kramers-Kronig test
LLS	. . . . .	linear least square
MCMC	. . . . .	Markov-Chain-Monte-Carlo
MH	. . . . .	Metropolis-Hastings
OCP	. . . . .	open circuit potential
OLS	. . . . .	ordinary linear square
p2D	. . . . .	pseudo two dimensional
PCM	. . . . .	physicochemical model
PEIS	. . . . .	potentiostatic electrochemical impedance spectroscopy
RMSE	. . . . .	root mean square error
ROM	. . . . .	reduced order model
SEI	. . . . .	solid electrolyte interphase
SOC	. . . . .	state of charge



## List of symbols

$\alpha$	Bruggeman coefficient
$\alpha_a$	Anodic charge transfer coefficient
$\alpha_c$	Cathodic charge transfer coefficient
$\Gamma$	Regularization matrix
$\theta$	Parameter vector
$\epsilon_e$	Measurement noise
$\epsilon_l$	Porosity
$\epsilon_s$	Volume fraction of active materials
$\eta$	Overpotential for the charge transfer in V
$\kappa$	Ionic conductivity in $\text{S m}^{-1}$
$\mu$	Electrochemical potential
$\nu$	Dissociation number
$\omega$	Angular frequency in $\text{rad s}^{-1}$
$\Phi_l(s)$	Potential in liquid phase in frequency domain in V
$\phi_l$	Potential in liquid phase in V
$\Phi_s(s)$	Potential in solid phase in frequency domain in V
$\phi_s$	Potential in solid phase in V
$\psi$	Phase angle
$\sigma$	Electronic conductivity in $\text{S m}^{-1}$
$\sigma_e$	Standard deviation of the measurement noise
$\sigma_W$	Warburg coefficient
$\tau$	Time constant in s, tortuosity of porous media
$\mathbf{A}_C$	System matrix for capacitance
$\mathbf{A}_L$	System matrix for inductance
$\mathbf{A}_{RC}$	System matrix for RC element
$\mathbf{A}_{RL}$	System matrix for RL element

---

$\mathbf{A}_R$	System matrix for resistance
$\mathbf{A}_{\text{sys}}$	System matrix
$\mathbf{b}_m$	Measurement data vector
$\mathbf{K}$	Total regularization matrix
$\mathbf{x}$	Solution vector
$\Delta t$	Step size of time constant in logarithmic scale
$A_{\text{cell}}$	Total area of the electrode layer in $\text{m}^2$
$a_v$	Volumetric interfacial area in $\text{m}^2 \text{m}^{-3}$
$c_0$	Bulk concentration in $\text{mol m}^{-3}$
$C_{\text{dl}}$	Double layer capacitance in $\text{F m}^{-2}$
$c_{1,\text{ref}}$	Reference concentration in liquid phase in $\text{mol m}^{-3}$
$C_1(s)$	Concentration in liquid phase in frequency domain in $\text{mol m}^{-3}$
$c_1$	Concentration in liquid phase in $\text{mol m}^{-3}$
$c_{\text{s,max}}$	Maximum concentration in solid phase in $\text{mol m}^{-3}$
$c_{\text{s,surf}}$	Surface concentration in solid phase in $\text{mol m}^{-3}$
$C_{\text{SEI}}$	SEI capacitance in $\text{F m}^{-2}$
$c_s$	Concentration in solid phase in $\text{mol m}^{-3}$
$D$	Diffusion coefficient in $\text{m}^2 \text{s}^{-1}$
$e^-$	Electron
$F$	Faraday constant, $96\,485.332 \text{ C mol}^{-1}$
$f$	Frequency in Hz
$f_{\pm}$	Activity
$G(\tau)$	DRT function in linear scale
$i_0$	Exchange current density in $\text{A m}^{-2}$
$I_{\text{app}}$	Applied current density in $\text{A m}^{-2}$
$I_{\text{cell}}$	Total current in A
$i_l$	Current density in liquid phase in $\text{A m}^{-2}$
$i_s$	Current density in solid phase in $\text{A m}^{-2}$
$i_v$	Volumetric current density in $\text{A m}^{-3}$
$j$	Imaginary unit
$k$	Kinetic reaction rate constant
$K_{ij}$	Friction coefficient between the species $i$ and $j$
$L$	Inductance in H

---

$l$	Length or thickness in m
$m$	Molality
$n$	Number of the transferred electrons, CPE exponent
$N_f$	Number of frequency points
$N_m$	Total number of measurement points in time domain
$N_1$	Flux density in liquid phase in $\text{mol m}^{-2} \text{s}^{-1}$
$N_\tau$	Number of time constants after discretization
$P(A   B)$	The probability of event $A$ given event $B$
$P(A)$	Probability of event $A$
$P(t)$	DRT function in logarithmic scale
$Q(\tau)$	Distribution function for the RL element
$R$	Gas constant, $8.314 \text{ J mol}^{-1} \text{ K}$
$r$	Length of diffusion path in solid particles in m
$R_{\text{ct}}$	Charge transfer resistance in $\Omega \text{ m}^2$
$R_{\text{diff}}$	Diffusional resistance in $\Omega \text{ m}^2$
$R_1$	Sink or source term of species in the electrolyte $\text{mol m}^{-3} \text{ s}^{-1}$
$R_{\text{ohm}}$	Ohmic resistance in $\Omega$
$R_{\text{SEI}}$	SEI resistivity in $\Omega \text{ m}^2$
$s$	Laplace variable, stoichiometric coefficient
$T$	Temperature in K
$t$	Time in s, time constant in logarithmic scale
$t_+^0$	Transference number of cations
$v$	Velocity in $\text{m s}^{-1}$
$V_m$	Measured voltage in time domain in V
$V_{\text{OC}}$	Open circuit potential in V
$V_{\text{sim}}$	Simulated voltage in time domain in V
$x$	Spatial coordinate
$z$	Valence
$Z_m$	Measured impedance in $\Omega$
$Z_{\text{sim}}$	Simulated impedance in $\Omega$
$Z_W$	Warburg impedance

# 1 Introduction

In the last few decades, electric vehicles (EV) have been attracting more and more attention and gradually become readily available to the public with an affordable price due to the technology development and decreasing cost of the energy storage devices. According to the report of the International Energy Agency, there were more than ten million electric cars on the road in 2020, which have increased for ca. 50% compared to the statistics in 2019[1]. It has also been predicted in the report that the global EV stock will surpass 200 million by the year 2030[1]. Currently, Lithium-ion batteries are used as the mainstream energy sources for EVs. As one of the most costly components in EVs, the Lithium-ion battery has a decisive influence on the driving range and safety[2]. Hence, electrode materials with a higher energy density, longer cycle life, lower cost, and improved safety are being consistently developed. On the other hand, a well designed battery management system (BMS) is indispensable for an efficient and safe operation of EVs. Typical functions of a BMS include: charging/discharging control, estimation of SOX ( $X = \text{charge, power, health, etc.}$ ), and so on. In order to realize the aforementioned functions of the BMS, generally a battery model must be developed and implemented on the microcontroller to estimate the internal states which are inaccessible to the measurement system. Depending on the complexity and the estimated states, equivalent circuit models (ECM), physicochemical models (PCM), data-driven models etc. have been used in BMSs[3].

For any of the aforementioned applications, a precise identification of the cell parameters is crucial, otherwise the internal states cannot be accurately estimated. Among all the cell parameters, transport and kinetic parameters such as reaction rate constant, diffusivity, and conductivity are of particular importance, because unlike the geometric parameters, these parameters can hardly be measured directly using measurement equipment. Compared to other methods, the electrochemical impedance spectroscopy (EIS) is especially suitable for characterizing the dynamic electrochemical processes inside Lithium-ion batteries. Meanwhile, the EIS also provides fruitful analyzable information about the kinetic and transport parameters of the battery cell[4]. Unlike a charging/discharging curve, EIS can effectively separate the contributions from different processes. The present thesis will focus on the parameter identification using the EIS technique.

To identify these parameters indirectly, usually an appropriate battery model needs to be selected and one of multiple external signals must be measured. Then, an optimization program with an appropriate cost function is established and an algorithm must be properly designed to solve the resulting optimization problem. Due to the strongly nonlinear nature of the electrochemical systems, the resulting problems are mostly strongly nonlinear and are inevitably subjected to a high computation effort and identifiability issues. Although sometimes ECMs may be selected for the reason of simplicity, a direct correlation of the identification results with the fundamental electrochemical processes is unclear or even missing.

In the present thesis, a comprehensive theory will be proposed to estimate the transport and kinetic parameters with the distribution of relaxation times (DRT) method, where only a linear least squares (LLS) problem needs to be solved, instead of nonlinear optimization problems. Furthermore, an analytical expression for the DRT spectra is derived based on a physicochemical impedance model instead

of ECMs. Finally, the parameter identification results will be validated using highly dynamic load profiles. A literature overview on the parameter estimation of Lithium-ion batteries using electrochemical impedance spectroscopy will be given in the next section.

## 1.1 Parameter Estimation with Electrochemical Impedance Spectroscopy

The working principle of the EIS technique is to stimulate the Lithium-ion battery being in an equilibrium state with a current/potential signal of a small amplitude and varying frequency so that the electrochemical system is pseudo-linear. Under the pseudo-linear condition, if the excitation signal is sinusoidal, the response is also sinusoidal at the same frequency and possibly with a different phase angle. The impedance data in different frequency range contains the information about the corresponding electrochemical processes, such as the solid-electrolyte-interphase (SEI) process, the charge transfer process, the diffusion in the solid and liquid phases, etc.. The commonly used representation of an impedance includes the Nyquist plot and the Bode plot. A typical Nyquist plot of the impedance of a Lithium-ion battery is shown in Fig. 1.1b, where different parts have been marked with numbers. In the shown Nyquist plot, the real part of the impedance is represented by  $Z'$  and the imaginary part is represented by  $Z''$ . The impedance curve starts from the left-lower part with the highest frequency to the right-upper part with the lowest frequency. According to the characteristic frequency, the impedance can be generally divided into four regions: region I has a zero imaginary part and represents the ohmic resistance of the electrode, which is generally attributed to the ohmic conduction phenomena in the solid and liquid phase. This process is usually modeled with a resistance element; region II is mostly attributed to the electrode/current collector contact and is generally described using a RC or RQ element; region III often gains the most attention and is attributable to the SEI and charge transfer reactions in the anode and cathode. Both can be modeled using a RC or RQ element; the impedance in region IV has a remarkable feature that a close to  $45^\circ$  slope can be observed, which can be explained by the diffusion in the solid particles and electrolyte. The diffusion processes are usually modeled using the Warburg element of different kinds. Besides the processes depicted in Fig. 1.1, an inductive behavior may be observed in the impedance of a cylindrical cell due to its spiral structure. Generally, the inductive part can be observed in the high frequency range and is represented by a positive imaginary part below the real axis.

The measured impedance can provide fruitful information about the dynamic processes occurring in the battery, thus enabling the estimation of the electrochemical parameters. To identify the corresponding kinetic and transport parameters, various methods have been proposed and investigated. Based on the mathematical methods used, the parameter identification with EIS can be classified in two large groups. In the following sections, each group will be briefly introduced and a summary will be given at the end.

### 1.1.1 Parameter Identification by Model Fitting

In the first group, first an impedance model must be selected to compute the frequency response of the battery:

$$Z_{\text{sim}} = \mathcal{Z}(j\omega|\theta) \quad (1.1)$$

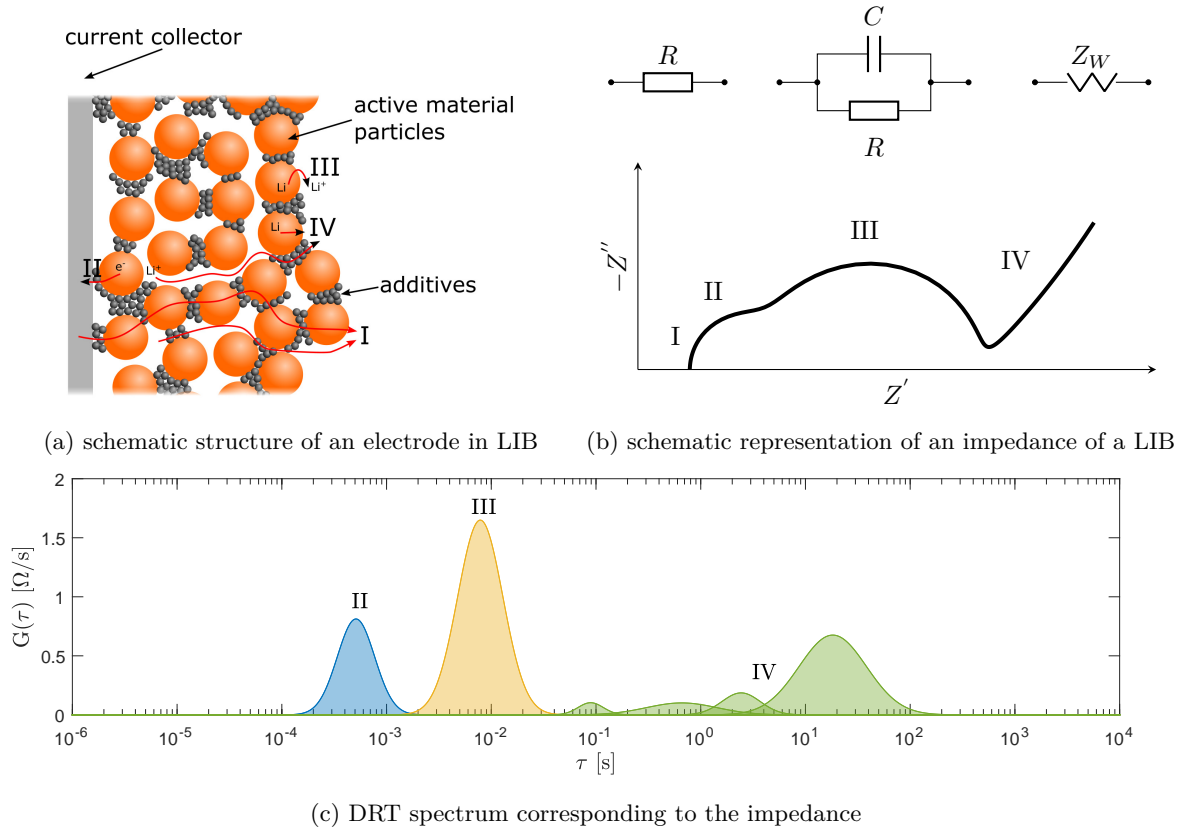


Figure 1.1: A schematic representation of (a): the structure of an electrode and (b): the corresponding impedance part in each frequency range and (c): the DRT spectrum corresponding to the shown impedance

where  $Z_{\text{sim}}$  is the simulated impedance,  $\mathcal{Z}$  is the defined impedance model,  $\omega$  is the angular frequency and  $\omega = 2\pi f$ ,  $f$  is the frequency in Hz,  $\theta$  is the parameter set of the selected impedance model. Depending on the model complexity and comprehensiveness, different impedance model classes have been used. The most widely used model class is the ECM, where the physicochemical processes are represented by a series of circuit elements such as resistance, capacitance, and RC elements. An example of an ECM is shown in Fig. 1.2, which consists of an inductance, an ohmic resistance, three RC elements representing the interface processes, and two Warburg elements modeling the diffusion phenomena in the active material particles.

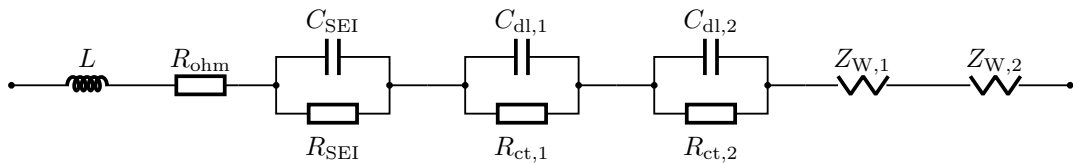


Figure 1.2: Typical equivalent circuit impedance model of a Lithium-ion battery

After the impedance model has been defined, a cost function is selected and subsequently minimized using an appropriate optimization algorithm. In practical applications, generally the least square

function is used so that the measurement data can be best fitted by the selected model:

$$F(\theta) = \sum_{i=1}^{N_f} \{[\Re(Z_{\text{sim},i}(j\omega|\theta) - Z_{\text{m},i})]^2 + [\Im(Z_{\text{sim},i}(j\omega|\theta) - Z_{\text{m},i})]^2\} \quad (1.2)$$

where  $N_f$  is the total number of frequency points,  $Z_{\text{m},i}$  is the measured impedance at the frequency point  $f_i$ .

Kalogiannis et al.[5] used an equivalent circuit similar to that shown in Fig. 1.2 to extract the cell parameters with EIS. The proposed circuit was considered to be appropriate because the fitting has achieved a low fitting residue. Beyond that, no clear proof or further information has been provided regarding the selection of the circuit elements and structure. In addition, the identified circuit parameters were directly used to describe the corresponding physicochemical processes without further explanation. Vyroubal et al.[6] used an equivalent circuit consisting of two RC elements to model the impedance of of a Lithium-ion battery. The proposed circuit model was fitted to a set of impedance data at various state of charge (SOC) to extract the parameters. The impedance model was based on a strong simplification of the electrochemical processes in the electrode so that the porous structure and the transport processes in the porous structure were not considered in the model. Then, the extracted parameters were used for a validation purpose and an obvious discrepancy could be observed between the simulated and the measured voltage profile.

Other than the charge transfer kinetics, the diffusion parameters have also been estimated by fitting the corresponding diffusion impedance elements to the impedance data. Charbonneau et al.[7] built an ECM with a Warburg element for the solid diffusion in the spherical solid particles to extract the diffusion coefficients. Similar to the cases analyzed before, the circuit model is rather based on a strong simplification. Gabano et al.[8] made a detailed analysis on the single diffusion impedance elements and estimated the diffusion parameters while considering the parameter sensitivity. Again, the proposed impedance model is a simplified circuit model with two RC elements and a diffusion impedance element, the porous electrode structure and the transport processes in the electrolyte were not considered. To summarize the literature analyzed above, it can be concluded that the parameter identification with the ECMs and impedance data has two inherent deficiencies: first, the structure of the ECM used is selected rather in an intuitive manner and no clear explanation and proof has been given for the selection, i.e., the impedance model is not based on a well formulated physicochemical model which is able to describe the dynamics in the Lithium-ion battery using the first principle equations; second, because the impedance models used are strongly simplified and not based on the first principle equations, a correlation of the estimation results with the physicochemical parameters of the Lithium-ion battery cannot be obtained, therefore a direct application of the estimated parameters to a physics-based battery model will most likely be problematic.

Besides the ECMs, a few studies have used the physicochemical impedance model to identify the cell parameters. Sikha et al.[9; 10] were the first to derive a physicochemical impedance model based on the well-known pseudo-two-dimensional (p2D) battery model. Furthermore, an analytical solution was derived and an attempt has been made to estimate the diffusion coefficients in the solid particles with a simplified version of the proposed model. However, neither an identification of other cell parameters was given nor any identifiability analysis was carried out. Murbach et al.[11] used an impedance model based on the p2D model to extract the physicochemical parameters with a local optimization method. The authors have also concluded in this work that the parameter identifiability when fitting the impedance data to a physicochemical impedance model could be a potential issue. Huang et al.[12]

had also attempted to identify the cell kinetic and transport parameters using a physicochemical impedance model. The impedance model was fitted to the impedance data using the global-search algorithm and the fitting program was run 50 times for each SOC to improve the probability of finding the global optimum. All in all, compared to the ECM, the physicochemical impedance model has established a direct connection between the estimated parameters and the underlying electrochemical phenomena. Nevertheless, it can be readily seen that the fitting process is subjected to the parameter identifiability issue due to the strongly nonlinear nature of the electrochemical systems. Besides, the higher computational effort of the physicochemical impedance model must be taken into account as well, if an analytical solution cannot be derived.

### 1.1.2 Parameter Identification with the Distribution of Relaxation Times

Compared to the model fitting introduced before, the second method group is based on the integral transform. With the integral transform, the data in frequency domain (impedance) can be transformed into time constant domain to obtain the distribution spectrum of the relaxation times, also known as the DRT. The DRT was first used to describe the dielectric relaxation process where the relaxation process could not be well described by a single Debye-relaxation[13]. Later the concept of DRT was introduced to describe the interfacial polarization process in materials[14], the solid electrolytes[15], and the processes in the electrochemical systems[16]. The DRT method can effectively resolve the issue that the circuit selected to fit the impedance data may be arbitrarily chosen and the impedance data may be well fitted with circuits of different structures[4]. For the aforementioned reasons, the DRT method is usually defined as a model-free representation of the impedance data, because no concrete model has been defined for the investigated devices. In this sense, the physical meaning of the DRT spectrum does not seem to be fully clear and there still exists a gap between the DRT spectrum and the physicochemical parameters. A typical DRT spectrum corresponding to the impedance data shown in Fig. 1.1b is shown in Fig. 1.1c, with time constants as the abscissa and the DRT function as the ordinate. Three groups of peaks can be observed in the DRT spectrum, which correspond to different electrochemical processes in the electrode. Peak II has the lowest time constant and represents the contact impedance between the current collector and the active materials. Peak III corresponds to the interfacial processes between the active materials and the electrolyte such as the charge transfer and the SEI process. The peak group IV consists of multiple peaks and is usually attributed to the diffusion in the solid and liquid phases and has the highest time constants due to the sluggish diffusion phenomena. Point I in Fig. 1.1b has a zero imaginary part and is usually defined as the ohmic resistance of the electrode. It is worth mentioning here that the peak attribution stated above is merely in a qualitative or even an intuitive manner and does not have any physicochemical explanation behind.

Regarding the DRT, most of the research works have been focusing on two topics: calculation of the DRT and interpretation of the DRT. In the following sections, a brief introduction to the two topics mentioned above will be given and the unsolved research questions will be discussed.

#### 1.1.2.1 Calculation of the Distribution of Relaxation Spectrum

The original DRT function is usually defined using the following equation:

$$Z_m(j\omega) = R_{\text{ohm}} + \int_0^{\infty} \frac{G(\tau)}{1 + j\omega\tau} d\tau \quad (1.3)$$



where  $\tau$  is the time constant and  $G(\tau)$  is the DRT function searched for,  $R_{\text{ohm}}$  is the ohmic resistance. It is often expected that the time constants will span over several orders of magnitude, thus it is more convenient to apply the logarithmic scale to the equation defined above. By defining  $t = \log_{10}(\tau)$  and substituting the defined relation into Eq. 1.3, the following equation can be obtained:

$$Z_m(j\omega) = R_{\text{ohm}} + \int_{-\infty}^{\infty} \frac{P(t)}{1 + j\omega\tau} dt \quad (1.4)$$

where the DRT function in logarithmic scale  $P(t)$  is related to that in linear scale in the following way:

$$P(t) = \ln(10)\tau G(\tau) \quad (1.5)$$

To solve for the  $G(\tau)$  or  $P(t)$  function with the given impedance data, the defined integral equation must be inverted with a properly chosen method. One of the most widely used inversion methods is the Fourier transform method (FT)[17–21]. Though with the FT method the DRT spectrum can be conveniently calculated with an analytical solution, the inversion may encounter problems at the upper and lower frequency limit of the impedance[20].

Another widely used inversion method is a numerical method based on the regularization technique. To solve Eq. 1.4 numerically, the integral equation must first be discretized and the following linear least squares problem can be obtained:

$$\hat{\mathbf{x}} = \min \{ \|\mathbf{A}\mathbf{x} - \mathbf{b}\|_2^2 \} \quad (1.6)$$

where  $\mathbf{x}$  is the DRT function being sought,  $\mathbf{b}$  is the measurement data vector and  $\mathbf{b} = [\Re(Z_m), \Im(Z_m)]^\top$ ,  $\mathbf{A}$  is the system matrix after the discretization:

$$\mathbf{A} = \left[ \begin{array}{c} \Re \left\{ \frac{1}{1 + j\omega_i \tau_j} \right\} \\ \Im \left\{ \frac{1}{1 + j\omega_i \tau_j} \right\} \end{array} \right]_{i=1, \dots, N_f; j=1, \dots, N_\tau} \quad (1.7)$$

where  $N_f$  and  $N_\tau$  are the number of frequencies and time constants respectively. Generally such an ordinary linear least squares problem (OLS) can be easily solved using the estimator:

$$\hat{\mathbf{x}} = (\mathbf{A}^\top \mathbf{A})^{-1} \mathbf{A}^\top \mathbf{b} \quad (1.8)$$

However, due to the fact that the columns of  $\mathbf{A}$  are highly colinear and thus the resulting OLS problem is highly ill-posed. A direct application of Eq. 1.8 to the OLS problem will lead to meaningless results. Therefore, the regularization technique is used and a penalty term is added to Eq. 1.6 to resolve the ill-posedness of the OLS problem:

$$\hat{\mathbf{x}} = \min \{ \|\mathbf{A}\mathbf{x} - \mathbf{b}\|_2^2 + \|\lambda \mathbf{\Gamma} \mathbf{x}\|_2^2 \} \quad (1.9)$$

where  $\mathbf{\Gamma}$  is the so-called regularization matrix or the Tikhonov matrix[22], which can be chosen according to the desired effect. For example, the identity matrix is selected to achieve a solution with a smaller norm, other possible candidates include the first-order and second-order derivative matrix.  $\lambda$  is

a hyperparameter which is used to tune the effect of the regularization, when  $\lambda = 0$ , the regularization effect disappears and the regularization problem reduces to an OLS problem. To solve the Tikhonov regularization problem, the following estimator is given:

$$\hat{\mathbf{x}}_{\text{reg}} = (\mathbf{A}^T + \lambda \Gamma \mathbf{A})^{-1} \mathbf{A}^T \mathbf{b} \quad (1.10)$$

Wan et al.[23] and Liu et al.[24] used the regularization method to deconvolute the impedance data and released the widely used open-source MATLAB<sup>®</sup> toolbox DRTtools. Nevertheless, this toolbox has only modeled the effect of RC elements, while the impedance data of a Lithium-ion battery may contain inductive and capacitive components. Therefore, the impedance data must be preprocessed to remove the inductive and capacitive components so that the solution of Eq. 1.4 can converge. Danzer [25] proposed an improved version of the regularization problem which has taken into account the inductive, resistive-inductive, and capacitive components as well.

### 1.1.2.2 Interpretation of the Distribution of Relaxation Times Spectrum

While most of the research works are devoted to the calculation of the DRT spectrum using different algorithms, nearly no attention has been paid to the evaluation and interpretation of the calculated DRT spectrum. Though the time constant and the polarization resistance of each process can be calculated from the DRT spectrum with low effort, the correlation of the DRT spectrum to the underlying physicochemical processes are still unclear. Boukamp analyzed the DRT spectrum of a few common impedance elements including the finite-length Warburg element[26], Havriliak-Negami element, and Gerischer element[18] and derived the analytical expression for the DRT spectra. Because the Havriliak-Negami element and Gerischer element are rather empirical elements, the finite-length Warburg element is the only element investigated with a clear physical meaning behind.

In summary, while much progress has been made in the calculation of the DRT spectrum, yet a clear physical meaning has not been assigned to the calculation results and the underlying physicochemical phenomena cannot be well characterized and explained satisfactorily with the DRT spectrum.

## 1.2 Thesis Outline

From the literature review made above, the following facts can be summarized about the parameter identification for the Lithium-ion battery with the impedance data: 1. circuit fitting with ECMs may lead to ambiguous results regarding the meaning of the fitting results; 2. fitting with PCMs will cause a higher computational effort compared to that with ECMs and the fitting process will very likely suffer from identifiability and parameter sensitivity issues, the reliability of the fitting results cannot be guaranteed; 3. the DRT method can resolve the computation and parameter identifiability issues by transforming the nonlinear optimization problem into a regularization problem where a unique analytical solution exists; 4. while the DRT method possesses the advantages of fast calculation speed and a unique solution, the physical meaning behind the results are still unclear and the results can be hardly applied to the physicochemical model.

Based on the analysis made above, the motivation of the present thesis can be raised: a theory should be developed to explain and interpret the DRT spectrum within the context of the physicochemical model of a Lithium-ion battery, i.e., to enable an estimation of the physicochemical parameters with

the DRT spectrum while the underlying physicochemical phenomena inside the battery should be considered as much as possible.

The structure of the present thesis is visualized in Fig. 1.3 and the remainder of the thesis will be organized as follows: in chapter 2 and 3, the physicochemical modeling of a Lithium-ion battery in time domain and frequency domain will be introduced respectively, which is used in the rest of the thesis for the theory development.

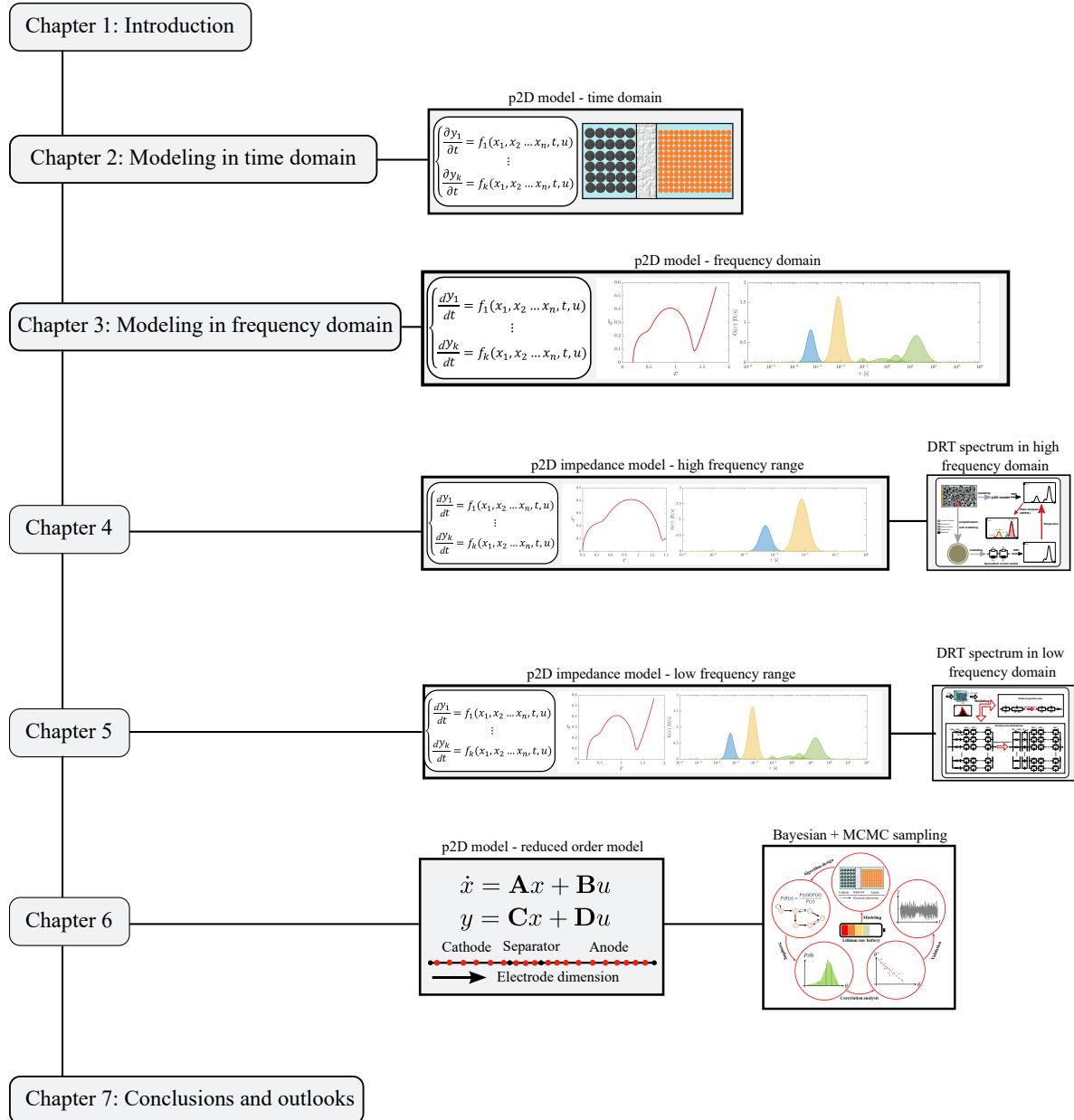


Figure 1.3: Outline of the thesis

In chapter 4, the theory to explain and interpret the kinetic parameters in the mid-high frequency range will be developed. Specifically, a closed-form analytical expression for the DRT spectrum in the mid-high frequency range will be derived with the p2D model. Consequently, the developed theory is applied to a commercially available Lithium-ion battery cell, the estimated parameters include the area-

specific SEI capacitance, resistance, the kinetic reaction rate constant, the double layer capacitance, and the contact impedance between the electrode and the current collector. Besides, the temperature and SOC dependence of the parameters will be investigated as well.

In chapter 5, based on the theory and conclusions in chapter 4, a new theory to investigate the DRT spectrum in mid-low frequency range is developed and correspondingly an analytical expression of the DRT spectrum in the mid-low frequency range is derived. With the developed theory, the diffusion coefficients in the solid and liquid phases can be estimated with regard to a physicochemical model, especially when the ionic conduction and diffusion in the electrolyte are taken into account. Apart from the model with a uniform particle size, the theory which takes the particle size distribution into account is also developed, the influence of the nonuniform particle size distribution is analyzed, and the estimation of the diffusion coefficients in such case is investigated. Then a commercially available Lithium-ion battery cell is used in the lab experiment and the diffusion coefficients are estimated. Furthermore, a measurement using the galvanostatic intermittent titration technique (GITT) has been conducted on the same cells, the results are compared and the merits of the DRT method are demonstrated.

In chapter 6, a comparative parameter identification study is conducted to investigate the impact of the parameter identification method on the parameter identifiability and the model accuracy. In this present study, the parameter identification performance of the time domain fitting and the combined method using both time domain and frequency domain fitting will be investigated and compared in detail. Chapter 7 concludes the thesis and a few suggestions are made regarding the possible research direction in the future work.

## 2 Physicochemical Modeling of the Lithium-ion Battery

In this chapter, the basic working principles and the fundamentals of the physicochemical modeling of the Lithium-ion battery will be introduced. In section 2.1, the general structure and basic working principle of a Lithium-ion battery will be briefly explained. In section 2.2, the physicochemical modeling of a Lithium-ion battery with the well-known Doyle-Fuller-Newman (DFN) model will be explained and the corresponding equations describing the electrochemical processes in the Lithium-ion battery, such as the material transport, the charge transfer kinetics, and the conduction phenomena are derived. Then, a widely spread simplified version of the DFN model, namely the p2D model will be derived and explained in detail. In section 2.3, first the reduced-order-model (ROM) used for the computationally efficient simulation of a Lithium-ion battery will be introduced; then the sampling method for the parameter identification study will be presented and briefly explained.

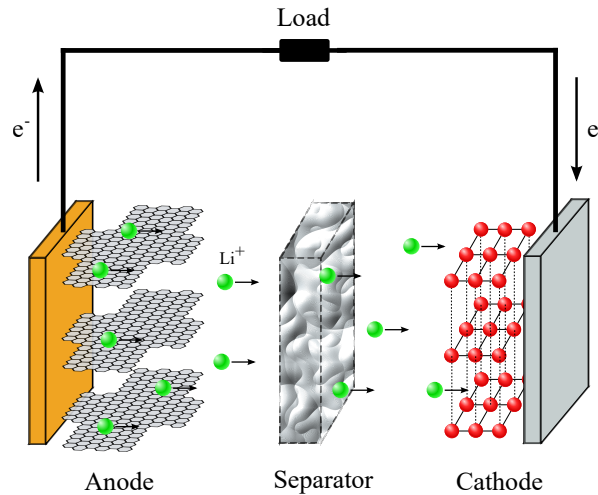


Figure 2.1: Schematic structure of a Lithium-ion battery. The battery is discharged and the lithium ions move from the anode toward the cathode

### 2.1 Structure and Working Principle of the Lithium-ion Battery

Since its invention, the Lithium-ion battery has been widely applied in diverse scenarios like electric vehicles, grid-connected energy storage system and consumer electronics due to its high specific power and energy density. The major improvement of the rechargeable Lithium-ion battery compared to the traditional throwaway lithium battery is that an intercalation material is used to host the lithium during charging, so that no spongy lithium metal will be deposited and further lithium loss can be avoided[27]. In principle, a lithium-ion battery consists of an anode, a separator and a cathode, as depicted in Fig. 2.1, where the Lithium-ion battery is being discharged and the lithium ions deintercalate from the anode, pass through the separator and move to the cathode. Besides, one current collector must be added to each electrode to serve as the electrical contact to the external circuit as well as the support

for the coating materials[28]. During charging, the lithium deintercalates from the cathode material, passes through the separator and moves to the anode. There the lithium will intercalate into the anode, and vice versa during discharging. The anode and cathode are separated by the separator to avoid a direct contact so that a short circuit can be prevented. Currently, the anode is mostly made of carbon-based materials due to their high specific charge capacity and low redox potential[29]. Among the carbons used as the anode material, graphitic carbon material is the most widely used. The intercalation/deintercalation reaction in the anode can be described by the following equation:



For the cathode, the most widely used materials are the inorganic transition-metal oxides, which have gained more attention than other materials such as the organic molecules and polymers[29]. The metal oxides materials can be classified into different groups according to their crystal structure. Typical structure of the metal oxides cathode material includes the layered structure (NMC, LCO), disordered rock-salt structure ( $\alpha$ -FeO<sub>2</sub>), spinel structure (LMN, LMO), and polyanion (LFP)[30]. Similar to the anode, the chemical reaction in the cathode during the charging and discharging can be represented by the following equation:



where MO<sub>2</sub> is the metal oxide. The separator of the Lithium-ion battery has a microporous structure and is generally made of polyolefin materials such as polyethylene, polypropylene, or a mixture of the both[31].

While the basic working principle of a Lithium-ion battery can be well explained by the schematic structure depicted in Fig. 2.1, such a battery with a single layer coating is unsuitable for practical applications. Various cell formats and packaging types have been developed for the industrialized production and practical application. At present, there are three packaging types for the commercially available Lithium-ion battery: cylindrical, flat jelly roll, and stacking[32], which are depicted in Fig. 2.2. Both the cylindrical and the flat jelly roll structure utilize the similar packaging concept: the double coated electrode layers (anode, cathode) and the separator are stacked together and then rolled up to form a jelly roll structure. The stacking structure is formed by stacking the electrode layers together without rolling-up. Consequently, the formed electrode rolls can be packaged into a cylindrical metal casing to produce a cylindrical round cell, or a rectangular metal can to produce a prismatic cell; the stacks can also be packaged into a bag made of aluminium to produce a pouch bag cell[32].

## 2.2 Physicochemical Modeling of the Lithium-ion Battery in Time Domain

Since proposed, the DFN model[33–35] has been widely applied in various application scenarios, such as simulation[36; 37], design optimization[38; 39], and parameter identification[40–42] of the Lithium-ion battery. The DFN model is based on the theory of porous electrodes and concentrated solutions and describes the physicochemical processes using a group of coupled partial differential equations. The

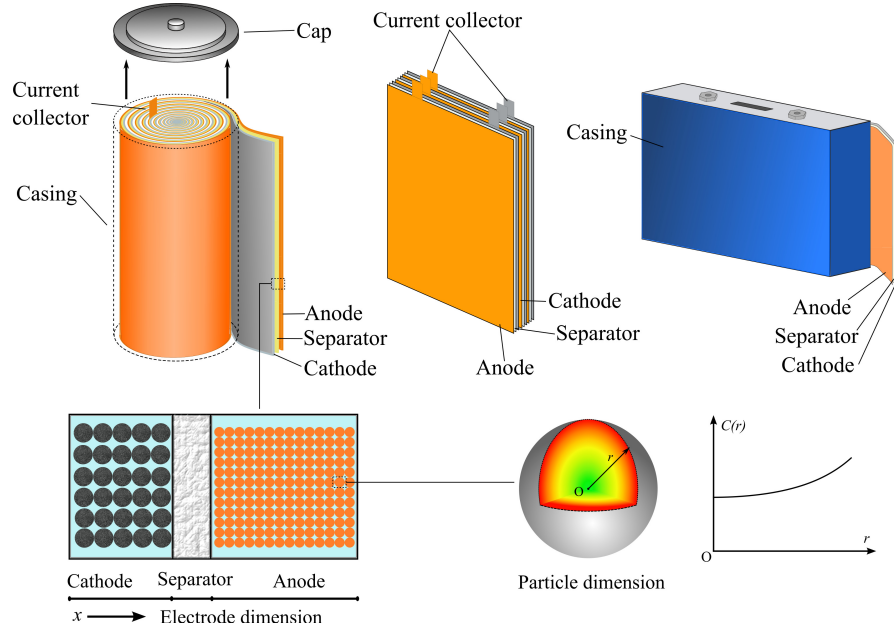


Figure 2.2: Different packaging types and the p2D modeling concept for the Lithium-ion battery

DFN model is generally applicable to any 3D geometry, where appropriate numerical methods like the finite-element-method (FEM) must be applied to solve the model. In most practical applications, the DFN model has been simplified with reasonable assumptions and the p2D model is derived. The p2D model assumes that the lithium-ions only move in the direction perpendicular to the electrode layer, while the concentration and potential difference along the electrode layer can be neglected. Besides, the electrode is assumed to be homogenized, i.e., at each location the electrode is assumed to be made of a mixture of the solid and liquid phases. At each location in the electrode, the intercalation/deintercalation in the solid active material particles occurs and the dimension inside the active material particles is defined as the second dimension (see. Fig. 2.2). To simplify the calculation, usually a planar, cylindrical or spherical geometry is assumed for the active material particles so that only one dimension is necessary to describe the material transport inside the particles. Because the second dimension is only defined in the solid particles and not in the electrode, the model is thus defined as p2D. The physicochemical model used in this thesis is based on the p2D model.

According to the definition of the p2D model introduced above, four state variables are solved for in the p2D model:

1. concentration in the electrolyte:  $c_1(x, t)$  in  $\text{mol m}^{-3}$
2. potential in the electrolyte:  $\phi_1(x, t)$  in V
3. concentration in the solid particles:  $c_s(x, r, t)$  in  $\text{mol m}^{-3}$
4. potential in the solid phase:  $\phi_s(x, t)$  in V

In the following sections, the equations describing the physicochemical processes in the p2D model will be derived, the equations are based on the DFN model proposed by Doyle et al.[33–35] and the work of Newman[43].

### 2.2.1 Material Transport in the Electrolyte

The transport and interaction of different species in the electrolyte are driven by the electrochemical potential gradient. As a result, the electrochemical potential will first be investigated. According to the theory of the concentrated solutions, the electrochemical potential gradient can be described by the following equation:

$$c_i \nabla \mu_i = \sum_j K_{ij} (v_j - v_i) = RT \sum_j \frac{c_i c_j}{c_T D_{ij}} (v_j - v_i) \quad (2.3)$$

where  $K_{ij}$  is the friction or the interaction coefficient between the species  $i$  and  $j$  and it is assumed that  $K_{ij} = K_{ji}$ .  $v_i$  and  $v_j$  are the velocity of the species  $i$  and  $j$  respectively.  $R$  is the gas constant and  $T$  is the temperature in K.  $D_{ij}$  is the diffusion coefficient and represents the interaction between the species. The total concentration of the species in the electrolyte is given as:

$$c_T = \sum_i c_i \quad (2.4)$$

For a binary electrolyte which contains one cation and one anion, Eq. 2.3 can be simplified to obtain the following equations:

$$c_+ \nabla \mu_+ = K_{0+} (v_0 - v_+) + K_{+-} (v_- - v_+) \quad (2.5)$$

for the cation and:

$$c_- \nabla \mu_- = K_{0-} (v_0 - v_-) + K_{+-} (v_+ - v_-) \quad (2.6)$$

for the anion. The current flow in the electrolyte is attributed to the transport of the charged species. As a result, the current density in the electrolyte  $i_1$  is given by the following equation:

$$i_1 = F \sum_i z_i N_i \quad (2.7)$$

where  $F$  is the Faraday constant,  $z_i$  is the valence of the species,  $N_i$  is the flux density. If  $c_+ v_+$  and  $c_- v_-$  are solved for using Eq. 2.5 and 2.6 and then substituted into Eq. 2.3, the following equations can be obtained:

$$N_+ = c_+ v_+ = -\frac{\nu_+ \mathcal{D}}{\nu RT} \frac{c_T}{c_0} c \nabla \mu_e + \frac{i_1 t_+^0}{z_+ F} + c_+ v_0 \quad (2.8)$$

$$N_- = c_- v_- = -\frac{\nu_- \mathcal{D}}{\nu RT} \frac{c_T}{c_0} c \nabla \mu_e + \frac{i_1 t_-^0}{z_- F} + c_- v_0 \quad (2.9)$$

where  $t_i^0$  is the transference number of the species  $i$ .  $\nu = \nu_+ + \nu_-$ , where  $\nu_+$  and  $\nu_-$  is the number of the produced cations and anions when one solvent molecule is dissociated.  $c$  is the electrolyte



concentration and is defined as follows:

$$c = \frac{c_+}{\nu_+} = \frac{c_-}{\nu_-} \quad (2.10)$$

For the electrochemical potential of the ions, the following equation holds:

$$\mu_e = \nu_+ \mu_+ + \nu_- \mu_- \quad (2.11)$$

The diffusion coefficient  $\mathcal{D}$  is defined as follows:

$$\mathcal{D} = \frac{D_{0+} D_{0-} (z_+ - z_-)}{z_+ D_{0+} - z_- D_{0-}} \quad (2.12)$$

Here  $\mathcal{D}$  is a quantity describing the relative diffusion of the ions. The normally measured diffusion coefficient in the electrolyte is related to  $\mathcal{D}$  by:

$$D = \mathcal{D} \frac{c_T}{c_0} \left( 1 + \frac{d \ln \gamma_{+-}}{d \ln m} \right) \quad (2.13)$$

where  $\gamma_{+-}$  is the mean molal activity coefficient and  $m$  is the molality. Finally, the concentration gradient can be represented using the electrochemical potential gradient:

$$\frac{\mathcal{D}}{\nu RT} \frac{c_T}{c_0} e \nabla \mu_e = D \left( 1 - \frac{d \ln c_0}{d \ln c} \right) \nabla c \quad (2.14)$$

On the other hand, the concentration of a species can be described using the continuity equation:

$$\frac{\partial c_1}{\partial t} = -\nabla N_1 + R_1 \quad (2.15)$$

where  $R_1$  is the source or sink of the species. If Eq. 2.14 is substituted into Eq. 2.8 and the resulting equation is further substituted into Eq. 2.15, the following equation can be obtained:

$$\frac{\partial c_1}{\partial t} + \nabla(c_1 v_0) = \nabla \left[ D \left( 1 - \frac{d \ln c_0}{d \ln c_1} \right) \nabla c_1 - \frac{i_1 t_+^0}{z_+ \nu_+ F} \right] + R_1 \quad (2.16)$$

Generally the convection inside a Lithium-ion battery can be neglected so that  $\nabla(c_1 v_0) = 0$ ; besides, it is assumed that the solvent concentration is independent of the electrolyte concentration[43]. As a result, Eq. 2.16 can be simplified to:

$$\frac{\partial c_1}{\partial t} = \nabla(D \nabla c_1) - \frac{i_1 \nabla t_+^0}{z_+ \nu_+ F} - \frac{t_+^0 \nabla i_1}{z_+ \nu_+ F} + R_1 \quad (2.17)$$

### 2.2.2 Charge Balance in the Solid and Liquid Phase

Considering that the electrolyte is electroneutral, the following equation holds:

$$\sum_i c_i z_i = 0 \quad (2.18)$$

Besides the concentration gradient, another driving force for the transport of ions in the electrolyte is the electric potential. To derive the equation for the electric potential in the electrolyte, the following general chemical reaction can be defined:



Here  $M_+$  is the cation,  $M_-$  is the anion and  $M_0$  is the neutral molecules in the electrolyte,  $e^-$  is the electron.  $s_i$  is the stoichiometric coefficient and  $n$  is the number of the transferred electrons. By using the thermodynamic principle, the equation derived above can be written as[43]:

$$s_- \nabla \mu_- + s_+ \nabla \mu_+ + s_0 \nabla \mu_0 = -nF \nabla \phi_1 \quad (2.20)$$

The ionic current density in the electrolyte can be represented in terms of the electrochemical potential[43]:

$$i_1 = -\kappa \nabla \phi_1 - \frac{\kappa}{F} \left( \frac{s_+}{n_+} + \frac{t_+^0}{z_+ \nu_+} - \frac{s_0 c}{n c_0} \right) \nabla \mu_e \quad (2.21)$$

where  $\kappa$  is the conductivity in the electrolyte. For a binary electrolyte, the following values can be assumed:  $s_+ = -1$ ,  $n = 1$ ,  $\nu_+ = 1$ ,  $z_+ = 1$  and  $s_0 = 0$ . Following the same principle, the electrochemical potential gradient is eliminated by substituting Eq. 2.14 into the equation above, and it is again assumed that the solvent concentration is independent of the ionic concentration. As a result, the following equation is obtained:

$$i_1 = -\kappa \nabla \phi_1 + \frac{2\kappa RT(1 - t_+^0)}{F} \left( 1 + \frac{d \ln f_{\pm}}{d \ln c} \right) \nabla \ln c_1 \quad (2.22)$$

where  $f_{\pm}$  is the activity.

The electric potential in the solid phase is caused by the flux of electrons and the potential distribution can be described using the Ohm's law:

$$i_s = -\sigma \nabla \phi_s \quad (2.23)$$

where  $i_s$  is the current density in the solid phase and  $\sigma$  is the solid phase conductivity.

### 2.2.3 Electrode Kinetics

The electrochemical reactions, i.e., the charge transfer reactions occur at the surface of the active material particles. Here the Butler-Volmer equation is used to calculate the reaction current density[43]:

$$i_n = i_0 \left[ \exp \left( \frac{\alpha_a F}{RT} \eta \right) - \exp \left( -\frac{\alpha_c F}{RT} \eta \right) \right] \quad (2.24)$$

where  $i_n$  is the reaction current density in  $\text{A m}^{-2}$ ,  $i_0$  is the exchange current density in  $\text{A m}^{-2}$ .  $\alpha_a$  and  $\alpha_c$  are the anodic and cathodic charge transfer coefficient respectively and both are assumed to

be equal to 0.5 in this thesis.  $\eta$  is the overpotential over the interface and is defined as follows:

$$\eta = \phi_s - \phi_l - U_{\text{OCP}} \quad (2.25)$$

where  $U_{\text{OCP}}$  is the open circuit potential (OCP) of the electrode. The exchange current density is defined by the following equation:

$$i_0 = F k_c^{\alpha_a} k_a^{\alpha_c} (c_{s,\text{max}} - c_{s,\text{surf}})^{\alpha_a} c_{s,\text{surf}}^{\alpha_c} \left( \frac{c_l}{c_{l,\text{ref}}} \right)^{\alpha_a} \quad (2.26)$$

where  $k_i$  is the reaction rate constant in  $\text{m s}^{-1}$ ,  $c_{s,\text{max}}$  is the maximum possible concentration in the solid phase in  $\text{mol m}^{-3}$ ,  $c_{s,\text{surf}}$  is the concentration at the surface of the solid phase in  $\text{mol m}^{-3}$ ,  $c_{l,\text{ref}}$  is the reference concentration in the electrolyte and is assumed to be  $1 \text{ mol m}^{-3}$ .

After the electrochemical reaction current density has been defined with the Butler-Volmer equation, the sink/source term coupling the solid and liquid phases can be calculated by the following equation:

$$i_v = \nabla i_l \quad (2.27)$$

$$R_l = \frac{i_v}{F} \quad (2.28)$$

$i_v$  is the volumetric reaction current density in  $\text{A m}^{-3}$ . In most practical applications, it is usually assumed that all particles in the solid phase have the same particle size. If the particles are assumed to be spherical, then the total interfacial area inside the unit volume can be calculated as follows:

$$a_v = \frac{4\pi r^2}{\frac{4}{3\epsilon_s}\pi r^3} = \frac{3\epsilon_s}{r} \quad (2.29)$$

where  $r$  is the particle radius,  $\epsilon_s$  is the volume fraction of the active materials,  $a_v$  is the volumetric interfacial area in  $\text{m}^2 \text{ m}^{-3}$  and describes the average interfacial area between the solid and liquid phases. With the volumetric interfacial area, the volumetric reaction current density can be represented with regard to the areal reaction current density by the following equation:

$$i_v = a_v i_n \quad (2.30)$$

According to the charge balance in the solid and liquid phases, the total current density in the electrode must be constant:

$$\nabla(i_s + i_l) = 0 \quad (2.31)$$

As a result, the following equation can be obtained:

$$\nabla i_s = -a_v i_n \quad (2.32)$$

### 2.2.4 Material Transport in the Solid Phase

The transport of lithium in the solid phase is described using Fick's law of diffusion:

$$\frac{\partial c_s}{\partial t} = \nabla(D_s \nabla c_s) \quad (2.33)$$

where  $D_s$  is the diffusion coefficient in the solid phase. If the particles are assumed to be spherical and the solid phase diffusion coefficient is assumed to be independent of the concentration, the diffusion equation can be reformulated using spherical coordinate:

$$\frac{\partial c_s}{\partial t} = D_s \left( \frac{\partial^2 c_s}{\partial r^2} + \frac{2}{r} \frac{\partial c_s}{\partial r} \right) \quad (2.34)$$

### 2.2.5 Modeling the Porous Electrode

The electrode of a Lithium-ion battery consists of a large number of small active material particles, inactive materials, binder, and the remaining pore is filled with electrolyte. Such an electrode has a porous structure which has a significant influence on the material transport and electrical conduction. In the bulk electrolyte, the lithium ions can move without any barrier. However, in the porous media, the diffusion path of the lithium ions will be hindered by the porous structure and the material transport will be slowed down. As a result, the bulk values of the transport parameters must be corrected to account for this slow-down effect.

To describe the slow-down effect caused by the porous structure, the tortuosity has been introduced[44]:

$$\tau = \frac{l_{\text{eff}}}{l} \quad (2.35)$$

where  $\tau$  is the tortuosity,  $l_{\text{eff}}$  is the effective path in the porous structure,  $l$  is the direct path when no porous structure exists. According to Doyle et al.[35] the effective transport parameters can be represented in terms of the bulk value and tortuosity using the following equations:

$$\kappa = \frac{\epsilon_1}{\tau} \kappa_0 \quad (2.36)$$

$$\sigma = \frac{\epsilon_s}{\tau} \sigma_0 \quad (2.37)$$

$$D_1 = \frac{\epsilon_1}{\tau} D_{1,0} \quad (2.38)$$

where  $\epsilon_1$  is the porosity,  $\kappa_0$ ,  $\sigma_0$  and  $D_{1,0}$  are the bulk values. On the other hand, the tortuosity can be defined by the following equation[35]:

$$\tau = \epsilon^{1-\alpha} \quad (2.39)$$

where  $\alpha$  is the Bruggeman coefficient and is usually assumed to be 1.5 based on the following assumptions: all particles are densely packed, have a spherical geometry, and have the same size[45].

### 2.2.6 Derivation of the p2D Model

If we combine Eq. 2.17, 2.22, 2.23, 2.27, 2.28, 2.30, 2.32, and 3.36 and further assume: 1.  $t_+^0$  is a constant; 2. the electrode variables vary only in the direction perpendicular to the electrode layer (p2D assumption) and consider that the electrode is regarded as superimposed continua, the complete model equations can be derived and summarized in the follows.

Material balance in the electrolyte:

$$\epsilon_1 \frac{\partial c_1}{\partial t} = \frac{\partial}{\partial x} \left( D_1 \frac{\partial c_1}{\partial x} \right) + \frac{a_v(1-t_+^0)}{F} i_n \quad (2.40)$$

Charge balance in the electrolyte:

$$\frac{\partial}{\partial x} \left( -\kappa \frac{\partial \phi_1}{\partial x} \right) + \frac{2RT(1-t_+^0)}{F} \frac{\partial}{\partial x} \left[ \kappa \left( 1 + \frac{d \ln f_{\pm}}{d \ln c_1} \right) \nabla \ln c_1 \right] = a_v i_n \quad (2.41)$$

Material balance in the solid phase:

$$\frac{\partial c_s}{\partial t} = D_s \left( \frac{\partial^2 c_s}{\partial r^2} + \frac{2}{r} \frac{\partial c_s}{\partial r} \right) \quad (2.42)$$

Charge balance in the solid phase:

$$\frac{\partial}{\partial x} \left( \sigma \frac{\partial \phi_s}{\partial x} \right) = a_v i_n \quad (2.43)$$

Electrode kinetics:

$$i_n = i_0 \left[ \exp \left( \frac{\alpha_a F}{RT} \eta \right) - \exp \left( -\frac{\alpha_c F}{RT} \eta \right) \right] \quad (2.44)$$

$$i_0 = F k_c^{\alpha_a} k_a^{\alpha_c} (c_{s,\max} - c_{s,\text{surf}})^{\alpha_a} c_{s,\text{surf}}^{\alpha_c} \left( \frac{c_1}{c_{1,\text{ref}}} \right)^{\alpha_a} \quad (2.45)$$

Because there is no active material and thus no charge transfer reaction in the separator, only the concentration and potential in the electrolyte will be solved in the separator. Therefore, the model equations for the separator are given as follows:

$$\epsilon_1 \frac{\partial c_1}{\partial t} = \frac{\partial}{\partial x} \left( D_1 \frac{\partial c_1}{\partial x} \right) \quad (2.46)$$

Charge balance in the electrolyte:

$$\frac{\partial}{\partial x} \left( -\kappa \frac{\partial \phi_1}{\partial x} \right) + \frac{2RT(1-t_+^0)}{F} \frac{\partial}{\partial x} \left[ \kappa \left( 1 + \frac{d \ln f_{\pm}}{d \ln c_1} \right) \nabla \ln c_1 \right] = 0 \quad (2.47)$$

To solve the derived partial differential equation system, proper boundary conditions must be defined. At the current collector/anode interface, the potential reference point is defined and the following boundary condition is defined:

$$\phi_s|_{x=0} = 0 \quad (2.48)$$

The ionic flux cannot penetrate through both current collectors, thus the following boundary conditions are valid:

$$\left. \frac{\partial c_l}{\partial x} \right|_{x=0, l_{\text{cell}}} = 0 \quad (2.49)$$

$$\left. \frac{\partial \phi_l}{\partial x} \right|_{x=0, l_{\text{cell}}} = 0 \quad (2.50)$$

where  $l_{\text{cell}}$  is the total thickness of the electrode layers and  $l_{\text{cell}} = l_{\text{neg}} + l_{\text{sep}} + l_{\text{pos}}$ . Besides, the total current density applied to the battery can be defined:

$$-\sigma \left. \frac{\partial \phi_s}{\partial x} \right|_{x=0, l_{\text{cell}}} = i_{\text{app}} \quad (2.51)$$

where  $i_{\text{app}}$  is the total current density applied to the battery in  $\text{A m}^{-2}$  and is defined as:

$$i_{\text{app}} = \frac{I_{\text{cell}}}{A_{\text{cell}}} \quad (2.52)$$

where  $I_{\text{cell}}$  is the total current applied to the battery in A and  $A_{\text{cell}}$  is the total area of each electrode layer. At the solid/liquid phase interface, the following boundary condition is defined:

$$-D_s \left. \frac{\partial c_s}{\partial r} \right|_{r=r_p} = \frac{i_n}{F} \quad (2.53)$$

where  $r_p$  is the particle radius. Due to symmetry, at the particle center there is no flux:

$$\left. \frac{\partial c_s}{\partial r} \right|_{r=0} = 0 \quad (2.54)$$

At the anode/separator and separator/cathode interface, the electrolyte concentration, electrolyte potential, and ionic flux are all continuous and thus the continuity boundary conditions apply.

## 2.3 Parameter Identification in Time Domain with Probability Sampling Method

With the physicochemical model introduced in previous sections, the operation performance of a Lithium-ion battery can be simulated using a group of model parameters and a selected numerical

method. In practical applications, while the voltage of the Lithium-ion battery under a given current profile can be easily measured, the internal states and parameters of the tested Lithium-ion battery often cannot be determined straightforwardly. To determine some of the parameters, the investigated battery cell can be disassembled and some parameters can be determined or measured using specific measurement equipment[37; 46]. Alternatively, an externally measured signal, such as the voltage or temperature, can be fed into a preselected model and a proper cost function can be defined to form an optimization problem. The resulting optimization problem can be solved to estimate the unknown parameters. Generally, a nonlinear least square problem can be defined as follows to identify the model parameters:

$$\hat{\theta} = \operatorname{argmin} \left\{ \sum_{i=1}^{N_m} [V_{\text{sim}}(t_i|\theta) - V_m(t_i)]^2 \right\} \quad (2.55)$$

where  $\theta$  is the model parameter vector,  $t_i$  is the  $i$ -th measurement time point,  $N_m$  is the total number of measurement points. Due to the strongly nonlinear nature of the electrochemical systems, the resulting optimization problem must be solved using a proper algorithm. The optimization algorithms used to solve the nonlinear optimization problem include the gradient-based methods[47–49], heuristic methods[41; 50; 51] and probability-based methods[40; 52]. By using any method mentioned above, the physicochemical model must be evaluated iteratively for a large number of times, which will lead to a high computational effort. Therefore, in this thesis a ROM based on the orthogonal collocation method will be used to reduce the computational burden of the physicochemical model and accelerate the simulation.

### 2.3.1 Computationally Efficient Simulation with Reduced Order Model (ROM)

The p2D model of a Lithium-ion battery consists of a series of coupled partial differential equations and thus demands a high computational effort. In this thesis, the ROM developed by Kosch et al.[53] based on the Chebyshev polynomials will be used to simulate the Lithium-ion battery.

In order to apply the ROM to the parameter identification, the mathematical model was first reformulated and then implemented in the simulation environment Simscape<sup>TM</sup>. To implement the model, the original model equations were first reformulated to meet the semantic requirements of the *ssc* language. Then the corresponding initial values and variable definitions were added to the script. Subsequently, all equations and definitions were combined to form a *.ssc* script which is compilable. Finally, the *.ssc* script was compiled to generate a model block in Simulink. The generated model block can be used with any algorithm implemented in MATLAB<sup>®</sup> or Simulink.

### 2.3.2 Parameter Sampling with Bayesian Statistics and Markov-Chain-Monte-Carlo

In the framework of the parameter identification, Bayesian statistics is a method which can express and interpret the fitting quality of the selected model parameters from the viewpoint of probability. Bayesian statistical methods are based on the Bayes' theorem, which is stated as follows:

$$P(A|B) = \frac{P(B|A)P(A)}{P(B)} \quad (2.56)$$

where  $A$  and  $B$  are events and  $P(B) \neq 0$  and:

- $P(A|B)$  is the conditional probability of event  $A$  given that event  $B$  is true
- $P(B|A)$  is the conditional probability of event  $B$  given that event  $A$  is true
- $P(A)$  and  $P(B)$  are the probabilities of event  $A$  and  $B$  respectively

For a set of measurement data, e.g. a voltage profile measured with a measurement equipment, the data will be subjected to noise inevitably. Generally, the measurement noise is normally distributed and the measured value can be represented as follows:

$$V_m = \widehat{V} + \epsilon_e \quad (2.57)$$

where  $\widehat{V}$  is the cell voltage without noise,  $V_m$  is the measured voltage subjected to noise,  $\epsilon_e$  is the noise and is normally distributed:

$$\epsilon_e \sim \mathcal{N}(0, \sigma_e^2) \quad (2.58)$$

where the distribution is assumed to have a zero mean and  $\sigma_e$  is the standard deviation of the distribution. If we assume that the voltage value without noise can be represented by the simulated value, then  $(V_m - V_{\text{sim}}) \sim \mathcal{N}(0, \sigma_e)$ . The following equation can be obtained by applying the Bayes' theorem:

$$P(\epsilon_e|\boldsymbol{\theta}) = \frac{P(\boldsymbol{\theta}|\epsilon_e)P(\epsilon_e)}{P(\boldsymbol{\theta})} \quad (2.59)$$

where  $\boldsymbol{\theta}$  represents the collection of all model parameters that should be investigated. The equation derived above can be reformulated to obtain the following equation:

$$P(\boldsymbol{\theta}|\epsilon_e) = \frac{P(\epsilon_e|\boldsymbol{\theta})P(\boldsymbol{\theta})}{P(\epsilon_e)} \quad (2.60)$$

Because the distribution of  $\epsilon_e$  is decided by the measurement equipment and is independent of the model parameters, the equation derived above can be further simplified to:

$$P(\boldsymbol{\theta}|\epsilon_e) \propto P(\boldsymbol{\theta})P(\epsilon_e|\boldsymbol{\theta}) = P(\boldsymbol{\theta}) \prod_{i=1}^{N_m} \frac{1}{\sigma_e \sqrt{2\pi}} \exp \left( -\frac{1}{2} \left( \frac{V_m^i - \widehat{V}_{\text{sim}}^i(\boldsymbol{\theta})}{\sigma_e} \right)^2 \right) \quad (2.61)$$

$P(\boldsymbol{\theta})$  is the prior probability distribution of the parameters and is generally based on the available information and knowledge about the estimated parameters. As an informative prior distribution, the beta-distribution is frequently used. In some cases where there is no information about the parameter or the information available cannot specify a distribution function, then a uniform distribution can be used. In this thesis, an informative prior distribution cannot be specified with the available information, thus a uniform distribution will be used. The lower and upper bound of the estimated parameters will be set according to the values found in the literature.

Theoretically, with Eq. 2.60 and 2.61 the probability density can be calculated. However, the normalization factor  $P(\epsilon_e)$  is difficult to calculate especially in higher dimensions. Therefore, a sampling algorithm is applied to sample the parameter space. With the original Markov-Chain-Monte-Carlo



(MCMC) algorithm, first a parameter sample is chosen arbitrarily in the parameter space and the probability is calculated using Bayes' theorem. Then a candidate sample is generated based on the current sample using a proposal distribution and the probability is calculated. A commonly used proposal distribution is the multidimensional normal distribution. The calculated probabilities of the current and the candidate sample are compared according to a defined criterion. If the criterion is fulfilled, then the candidate sample will be selected as the next sample and saved in the chain. The procedures described above will be repeated until a predefined number of samples have been reached. Various algorithms have been proposed to generate the Markov chain, where one of the most widely used algorithms is the Metropolis-Hastings (MH) algorithm and its variants[54; 55]. The general MH algorithm can be briefly summarized using the following pseudo code.

---

**Algorithm 1:** Metropolis-Hastings algorithm for parameter sampling

---

**Input** : Parameter dimension  $N_d$ , Sample size  $N_s$ , proposal distribution  $q(\mathbf{x}_k)$ , posterior probability  $p(\mathbf{x})$

**Output:** Parameter sample chain  $\mathbf{x}_k$

```

1 Initialization:  $k \leftarrow 0$ ;
2 Select the initial sample  $\mathbf{x}_k \in \mathbb{R}^{N_d}$ ;
3 while  $k < N_s$  do
4    $\mathbf{x}_{k+1} = q(\mathbf{x}_k)$ ;
5    $\pi(\mathbf{x}_k) = p(\mathbf{x}_k)$ ;
6    $\pi(\mathbf{x}_{k+1}) = p(\mathbf{x}_{k+1})$ ;
7    $\alpha = \min\left(1, \frac{\pi(\mathbf{x}_{k+1})}{\pi(\mathbf{x}_k)}\right)$ ;
8   accept  $\mathbf{x}_{k+1}$  with the probability  $\alpha$ ;
9 end
    
```

---

The original MCMC algorithm uses constant parameters for the proposal distribution, which will lead to a slow convergence in some cases. To improve the convergence performance, the adaptive Metropolis (AM) algorithm has been proposed. The AM algorithm uses a varying covariance matrix and the covariance matrix will be constantly adapted based on the history of the chain. The covariance is calculated as follows:

$$\text{Cov}(\mathbf{x}_0, \mathbf{x}_1, \mathbf{x}_2, \dots, \mathbf{x}_k) = \frac{1}{k} \left( \sum_{i=0}^k \mathbf{x}_i \mathbf{x}_i^\top - (k+1) \bar{\mathbf{x}}_k \bar{\mathbf{x}}_k^\top \right) \quad (2.62)$$

where

$$\bar{\mathbf{x}}_k = \frac{1}{k+1} \sum_{i=0}^k \mathbf{x}_k \quad (2.63)$$

As a result, the AM algorithm is given with the following pseudo code. In this thesis, the AM algorithm developed by Kumbhare et al.[56] will be used to generate the parameter samples. The adaption step size is set to  $t = 4N_d$  and  $N_d$  is the dimension of the parameter space. The initial covariance matrix is set to the identity matrix, the number of collected parameter samples is 50000.

---

**Algorithm 2:** Adaptive Metropolis algorithm for parameter sampling

---

**Input** : Parameter dimension  $N_d$ , Sample size  $N_s$ , proposal distribution  $q(\mathbf{x}_k, \text{Cov})$ , posterior probability  $p(\mathbf{x})$ , adaption step size  $t$ **Output:** Parameter sample chain  $\mathbf{x}_k$ 

```
1 Initialization:  $k \leftarrow 0$ ;  
2 Select the initial sample  $x_k \in \mathbb{R}^{N_d}$ ;  
3 while  $k < N_s$  do  
4   For every  $t$  steps, calculate and update Cov;  
5    $\mathbf{x}_{k+1} = q(\mathbf{x}_k, \text{Cov})$ ;  
6    $\pi(\mathbf{x}_k) = p(\mathbf{x}_k)$ ;  
7    $\pi(\mathbf{x}_{k+1}) = p(\mathbf{x}_{k+1})$ ;  
8    $\alpha = \min\left(1, \frac{\pi(\mathbf{x}_{k+1})}{\pi(\mathbf{x}_k)}\right)$ ;  
9   accept  $\mathbf{x}_{k+1}$  with the probability  $\alpha$ ;  
10 end
```

---

### 3 Modeling and Characterization of the Lithium-ion Battery in Frequency Domain

In this chapter, the characterization of the Lithium-ion battery in frequency domain will be introduced. First, the general working principle of the EIS will be explained. Then the circuit elements commonly used to model and interpret the impedance will be presented and explained. Next, a physics-based impedance model based on the p2D model will be derived to model the physicochemical processes in frequency domain. Finally, the DRT, as a powerful mathematical tool to deconvolute and evaluate the impedance data, will be introduced.

#### 3.1 The Working Principle of Electrochemical Impedance Spectroscopy

The EIS, as a frequently used electrochemical characterization method, is powerful at characterizing materials and their interface properties[57]. Furthermore, the EIS is a nondestructive method and can be conveniently applied to the tested battery throughout the whole life cycle. The EIS is conducted by applying a small current/potential signal to the sample and the potential/current response is measured to calculate the impedance. The measurement technique is usually called galvanostatic electrochemical impedance spectroscopy (GEIS) in the former case and potentiostatic electrochemical impedance spectroscopy (PEIS) in the latter case. In the following section, the working principle of the EIS will be explained at the example of GEIS.

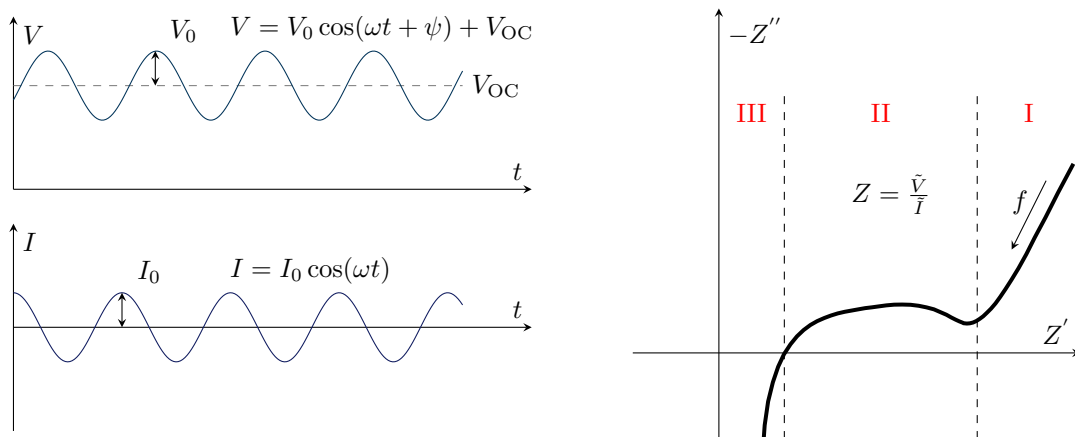


Figure 3.1: The working principle of the EIS (left) and a typical EIS of a Lithium-ion battery (right). The shown impedance is separated into three parts which are marked with I, II, and III.

Generally, the EIS of a Lithium-ion battery is measured in equilibrium state with a small excitation signal so that the whole system can be regarded as pseudo-linear or linear and the measured impedance should be ideally nonindependent of the magnitude of the applied current. It is assumed that the

measured system is in equilibrium state and has an open circuit voltage  $V_{OC}$ . Then a small AC current signal is applied to the system (see Fig. 3.1):

$$I = I_0 \cos(\omega t) \quad (3.1)$$

where  $I_0$  is the current amplitude,  $\omega$  is angular frequency and  $\omega = 2\pi f$ ,  $f$  is the frequency in Hz. According to the linearity of the system, an AC voltage signal of the same frequency will be superimposed on the open circuit voltage of the system (see Fig. 3.1). As a result, the measured voltage signal can be represented as follows:

$$V = V_0 \cos(\omega t + \psi) + V_{OC} \quad (3.2)$$

where  $\psi$  is the phase angle of the voltage signal. According to the working principle of EIS, only the AC perturbation is used to calculate the impedance. On the other hand, the sinusoidal signal can be represented using the phasor. As a result, the current and voltage perturbation can be represented as:

$$\tilde{I} = I_0 e^{j\omega t} \quad (3.3)$$

$$\tilde{V} = V_0 e^{j(\omega t + \psi)} \quad (3.4)$$

The impedance is then defined as:

$$Z = \frac{\tilde{V}}{\tilde{I}} = \frac{V_0 e^{j(\omega t + \psi)}}{I_0 e^{j\omega t}} = |Z| e^{j\psi} = |Z| \cos(j\psi) + j|Z| \sin(j\psi) \quad (3.5)$$

Eq. 3.5 indicates that the measured impedance can be represented using a complex number with the corresponding real and imaginary part (see Fig. 3.1). The imaginary part of an impedance is usually plotted against the real part to obtain the Nyquist plot. In battery engineering, the Nyquist plot is usually inverted with the positive imaginary axis below the real axis, because the impedance is generally capacitive in the frequency range of interest. A disadvantage of the Nyquist plot is that it does not contain any information about the frequency. An example of the impedance of a Lithium-ion battery is shown in Fig. 3.1. The impedance curve can be roughly separated into three parts which are marked with I, II, and III. Part I manifests itself as a slope with a ca.  $45^\circ$  angle, which generally characterizes the diffusion in the solid and liquid phases. Part II consists of one or multiple half circles, which generally characterize the interfacial processes occurring in the electrode. Part III has a positive imaginary part and is usually attributed to the inductance of the battery or the measurement cables.

Before the measurement data is subjected to the further evaluation and application, the Kramers-Kronig test (KKT) is frequently applied to validate the data. To pass the KKT, the tested system must satisfy the following four criteria[4]: linearity, causality, stability, and finiteness. Assuming that the aforementioned criteria are satisfied, the imaginary part of the impedance can be calculated using the following relation, given the real part of the impedance:

$$Z''(\omega) = - \left( \frac{2\omega}{\pi} \right) \int_0^\infty \frac{Z'(x) - Z'(\omega)}{x^2 - \omega^2} dx \quad (3.6)$$

Similarly, the imaginary part can be calculated using the real part:

$$Z'(\omega) = Z'(\infty) + \frac{2}{\pi} \int_0^{\infty} \frac{xZ''(x) - \omega Z''(\omega)}{x^2 - \omega^2} dx \quad (3.7)$$

It can be seen from the equations shown above that the KKT requires the integration over an infinite frequency range, which is practically impossible to carry out. To apply the KKT to the measurement data, various approximation methods have been proposed as a workaround. For example, the real and imaginary part of the impedance can be approximated using polynomials of  $\omega$  and the integration can be conducted[58–60]. Agarwal et al.[61; 62] proposed to use the Voigt circuit due to the fact that if a system can be well fitted by a linear circuit, then it must be KKT-compliant. Besides, Boukamp et al.[63] proposed to apply the distribution of relaxation times to the validation with the KKT. Generally, the reconstructed impedance data cannot fully coincide with the original measurement data and no specific quantitative criteria can be defined for the KKT. Usually, the validity of the impedance data can be tested by comparing the measurement data with the reconstructed data, the measurement data can be regarded as valid as long as no systematic error pattern has been observed[4].

## 3.2 Evaluation of Electrochemical Impedance

Although the measured impedance may be evaluated qualitatively with a certain background knowledge, more information can only be extracted with a quantitative evaluation method. To enable a quantitative evaluation of the impedance, different ideal circuit elements have been used to model the physical and chemical processes in the Lithium-ion battery. However, the complicated physical and chemical processes in the Lithium-ion battery can be hardly described satisfactorily using merely a few ideal circuit elements. A comprehensive connection between the physics-based battery model and the EIS has not been fully established yet. In this section, the commonly used ideal circuit elements will be introduced and their properties in the frequency domain will be shown and explained. In the next section, a physics-based impedance model will be derived and the deep connection of the simple circuit elements with the physics-based battery model will be established.

The ohmic resistance element is used to describe the processes where the current and voltage have a simple proportional relationship. The defined proportion factor must be positive, real, and independent of the frequency. Such processes include the electronic and ionic conduction. The charge transfer process can be approximated with an ohmic resistance when the excitation current is small enough so that the current and voltage have a quasi linear relationship. The impedance of an ohmic resistance is given as:

$$Z_R = R \quad (3.8)$$

An ohmic resistance can be represented by a single point on the real axis in the Nyquist plot (see Fig. 3.2a).

The inductance is used to model the inductive behavior occurring in the EIS. The impedance of an inductance always has a phase angle of  $90^\circ$  and lies on the positive imaginary axis (see Fig. 3.2b). Unlike the ohmic resistance, the impedance of inductance is dependent of the excitation frequency and will become more and more relevant with increasing frequency. The impedance of an inductance is

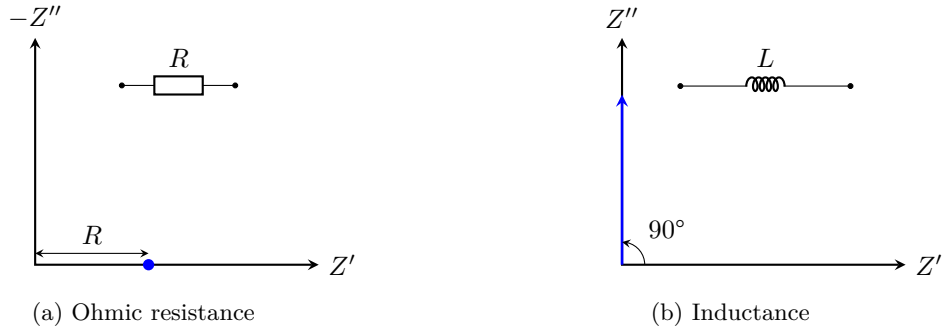


Figure 3.2: Nyquist plot for (a): ohmic resistance and (b): inductance

given as follows:

$$Z_L = j\omega L \quad (3.9)$$

The capacitance is used to model the capacitive behavior of the battery cell. For example, the double layer capacitance at the solid/liquid phase interface can be modeled using a capacitance. At extremely low excitation frequency when other dynamic processes such as the charge transfer and diffusion can be regarded as a resistance, the impedance of the Lithium-ion battery can be approximated using a capacitance and an ohmic resistance connected in series. The impedance of a capacitance always has a phase angle of  $-90^\circ$  and lies on the negative imaginary axis (see Fig. 3.3a). The impedance of a capacitance is given as follows:

$$Z_C = \frac{1}{j\omega C} \quad (3.10)$$

In some practical applications, an impedance with a constant phase angle  $|\psi| < 90^\circ$  can be observed instead of an ideal capacitance, which shows a nonideal capacitive behavior. Such a nonideal capacitive behavior has been attributed to surface adsorption, impurities, or atomic scale heterogeneity in polycrystalline solid electrodes[64–66]. As a result, a special circuit element has been defined to describe this nonideal capacitive behavior, which is called the constant phase element (CPE). The impedance of a CPE is given as follows:

$$Z_{CPE} = \frac{1}{(j\omega C)^n} \quad (3.11)$$

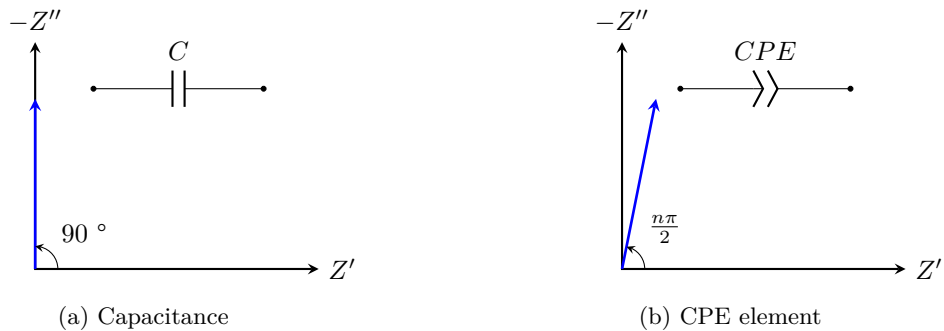


Figure 3.3: Nyquist plot for (a): capacitance and (b): CPE element

where  $n$  is a parameter and usually  $0 < n < 1$ . According to the definition of the CPE, the impedance lies always on a straight line passing through the origin (see Fig. 3.3b).

Besides single circuit elements, sometimes a group of circuit elements can be connected to model the processes which cannot be described by a single circuit element. The parallel RC element can be used to model the interfacial process at the electrode/electrolyte interface, where the charge transfer is modeled by a resistance and the double layer capacitance is represented by a capacitance. The impedance of the RC element is given as follows:

$$Z_{RC} = \frac{R}{1 + j\omega RC} = \frac{R}{1 + j\omega\tau} \quad (3.12)$$

where  $\tau = RC$  is the time constant of the RC element. By eliminating the frequency in Eq. 3.12, it can be shown that the impedance of a RC element is an ideal half circle in the Nyquist plot passing through the origin and with its center on the positive real axis (see Fig. 3.4a). When the frequency approaches infinity, the RC element can be regarded as short-circuited due to the capacitance:

$$\lim_{\omega \rightarrow \infty} Z_{RC}(j\omega) = 0 \quad (3.13)$$

When the frequency approaches zero, the RC element can be regarded as an ohmic resistance:

$$\lim_{\omega \rightarrow 0} Z_{RC}(j\omega) = R \quad (3.14)$$

For generality, the ideal capacitance in the RC element can be replaced by the CPE to form a new circuit element, which is usually called the RQ or ZARC element. The impedance of an RQ element is given as:

$$Z_{RQ} = \frac{R}{1 + (j\omega C)^n R} \quad (3.15)$$

Similarly, it can be shown that the Nyquist plot of a ZARC element is a part of a circle passing through the origin and with its center located in the fourth quadrant (see Fig. 3.4b).

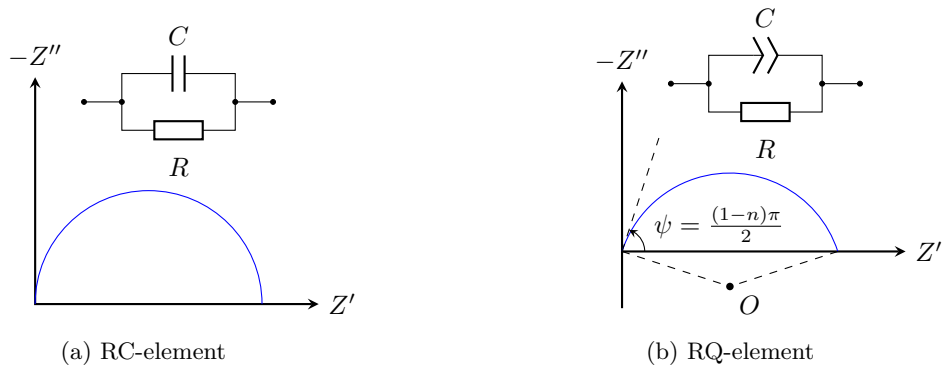


Figure 3.4: Nyquist plot for (a): RC-element and (b): RQ-element

Another group of special circuit elements that has been frequently used to model the physicochemical processes in the Lithium-ion battery is the Warburg impedance element. The Warburg impedance is usually applied to describe the diffusion phenomena in the battery. The original Warburg impedance

assumes a semi-infinite diffusion in a planar geometry and takes the form of a CPE[67; 68]. The original Warburg impedance is given by the following equation:

$$Z_W = \frac{\sigma_W}{\sqrt{\omega}} - j \frac{\sigma_W}{\sqrt{\omega}} \quad (3.16)$$

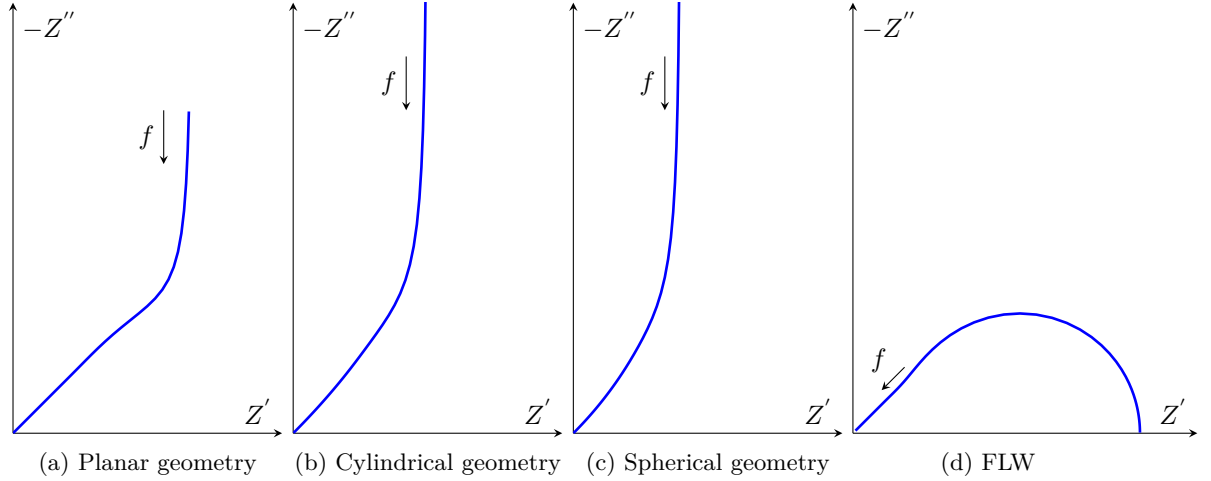


Figure 3.5: The Nyquist plot of the Warburg impedance element in the frequency range 1 mHz  $\sim$  1 kHz with (a): planar geometry, (b): cylindrical geometry, (c): spherical geometry, and (d) with transmissive boundary conditions and planar geometry

where  $\sigma_W$  is the Warburg coefficient. The original Warburg impedance is less often applied to the impedance of the Lithium-ion battery due to its obvious limitation that the semi-infinite diffusion with a planar geometry rarely appears in practical applications. To better model the diffusion phenomena in the Lithium-ion battery, the finite-space Warburg element (FSW) has been derived to describe the diffusion in the active material particles with a finite size. The FSW impedance for a solid particle with planar, cylindrical, and spherical geometry is given as follows[69; 70]:

$$Z_{W,\text{planar}} = R_{\text{diff}} \frac{\coth(\sqrt{j\omega\tau_0})}{\sqrt{j\omega\tau_0}} \quad (3.17)$$

$$Z_{W,\text{cylindrical}} = R_{\text{diff}} \frac{I_0(\sqrt{j\omega\tau_0})}{\sqrt{j\omega\tau_0} I_1(\sqrt{j\omega\tau_0})} \quad (3.18)$$

$$Z_{W,\text{spherical}} = R_{\text{diff}} \frac{\tanh(\sqrt{j\omega\tau_0})}{\sqrt{j\omega\tau_0} - \tanh \sqrt{j\omega\tau_0}} \quad (3.19)$$

where  $I_k$  is the  $k$ -order modified Bessel function of first kind.  $\tau_0$  is the characteristic diffusion time constant and is given as follows:

$$\tau_0 = \frac{r^2}{D_s} \quad (3.20)$$

where  $r$  is the length of the diffusion path and corresponds to the half thickness for the planar geometry, the radius of the cylinder for the cylindrical geometry, and the radius of the sphere for the spherical



geometry.  $D_s$  is the solid diffusion coefficient.  $R_{\text{diff}}$  is the diffusional resistance and is defined by the following equation:

$$R_{\text{diff}} = \left( -\frac{\partial U_{\text{OCP}}}{\partial c_s} \right) \frac{r}{FD_s} \quad (3.21)$$

While the Warburg impedance with reflective boundary conditions can be generally used to describe the solid phase diffusion phenomena, the diffusion in electrolyte is usually related to transmissive boundary conditions[4; 67; 71; 72]. The Warburg impedance with transmissive boundary conditions is usually called the finite-length Warburg element (FLW) and is given by the following equation[4; 71; 72]:

$$Z_{\text{FLW}} = R_{\text{diff}} \frac{\tanh(\sqrt{j\omega\tau_0})}{\sqrt{j\omega\tau_0}} \quad (3.22)$$

where  $\tau_0$  is the diffusion time constant and  $R_{\text{diff}}$  is the diffusional resistance, which is to be defined in specific applications. The Nyquist plot of the FLW is shown in Fig. 3.5d. It can be seen that in high frequency range the FLW shows a CPE behavior, which can be observed in the solid diffusion as well (see Fig. 3.5a-c). However, unlike the solid diffusion impedance, no capacitive behavior can be observed for the FLW in low frequency range. Instead, the FLW shows a resistive behavior when the frequency approaches zero:

$$\lim_{\omega \rightarrow 0} Z_{\text{FLW}}(j\omega) = R_{\text{diff}} \quad (3.23)$$

The unique feature of the FLW that it shows no capacitive behavior in low frequency range has led to the following fact: the bumped half circle in the Warburg region of the impedance can be used as an effective indicator for a non-negligible contribution from the liquid diffusion[67; 73]. Furthermore, this fact has a profound impact on the determination of the solid diffusion coefficient using methods such as GITT, when the liquid diffusion is no more negligible. A detailed analysis and comparison of the GITT and DRT regarding the determination of the solid diffusion coefficient will be conducted in chapter 5.

In summary, the equivalent circuit elements introduced in this section can be used in frequency domain to model some common physical and chemical phenomena in the Lithium-ion battery. However, the circuit elements are mostly based on local phenomena, i.e., at a micro-scale level. To describe the impedance of a Lithium-ion battery with a complicated electrode structure, a more comprehensive physics-based impedance model must be derived.

### 3.3 Physicochemical Modeling of the Lithium-ion Battery in Frequency Domain

In this section, the impedance model of a Lithium-ion battery based on the p2D model will be introduced and an analytical solution for this model will be derived. Unlike the ECM which is phenomenological and is not directly based on any fundamental theory, the physicochemical impedance model consists of a series of first principle equations describing the material transport and potential distribution in the porous electrode. In the following sections, first the physics-based impedance model

based on the well-known p2D model will be introduced, then an analytical solution to the introduced impedance model will be derived.

### 3.3.1 Equations for the Electrode Level

According to the measurement principle of the EIS introduced in section 3.1, Eq. 2.40, 2.41 and 2.43 can be reformulated as follows when the Lithium-ion battery is perturbed by a small current/potential signal:

$$\epsilon_1 \frac{\partial(\bar{c}_1 + \tilde{c}_1)}{\partial t} = \frac{\partial}{\partial x} \left[ D_1 \frac{\partial(\bar{c}_1 + \tilde{c}_1)}{\partial x} \right] + \frac{a_v(1-t_+^0)}{F} \tilde{i}_n \quad (3.24)$$

$$\frac{\partial}{\partial x} \left[ -\kappa \frac{\partial(\bar{\phi}_1 + \tilde{\phi}_1)}{\partial x} \right] + \frac{2RT(1-t_+^0)}{F} \frac{\partial}{\partial x} \left[ \kappa \left( 1 + \frac{d \ln f_{\pm}}{d \ln c_1} \right) \frac{\partial \ln(\bar{c}_1 + \tilde{c}_1)}{\partial x} \right] = a_v \tilde{i}_n \quad (3.25)$$

$$\frac{\partial}{\partial x} \left[ \sigma \frac{\partial(\bar{\phi}_s + \tilde{\phi}_s)}{\partial x} \right] = a_v \tilde{i}_n \quad (3.26)$$

where  $\bar{p}$  is the variable when there is no perturbation and can be regarded as a constant given the equilibrium state condition.  $\tilde{p}$  is the perturbation variable which is assumed to be sinusoidal and has the same frequency as the excitation signal. Furthermore, it is assumed that: 1. the transport, electrical, and thermodynamic properties are constant along the electrode thickness and are equal to the values in equilibrium state, because the parameter variation along the electrode thickness caused by the perturbation is negligible; 2. the concentration perturbation in the electrolyte is negligible compared to the equilibrium state so that the following equation holds:

$$\frac{\partial \ln(\bar{c}_1 + \tilde{c}_1)}{\partial x} \approx \frac{1}{\bar{c}_1} \frac{\partial \tilde{c}_1}{\partial x} \quad (3.27)$$

As a result, the following equations can be obtained:

$$\epsilon_1 \frac{\partial \tilde{c}_1}{\partial t} = D_1 \frac{\partial^2 \tilde{c}_1}{\partial x^2} + \frac{a_v(1-t_+^0)}{F} \tilde{i}_n \quad (3.28)$$

$$-\kappa \frac{\partial^2 \tilde{\phi}_1}{\partial x^2} + f_1 \frac{\partial^2 \tilde{c}_1}{\partial x^2} = a_v \tilde{i}_n \quad (3.29)$$

$$\sigma \frac{\partial^2 \tilde{\phi}_s}{\partial x^2} = a_v \tilde{i}_n \quad (3.30)$$

where the coefficient  $f_1$  is given as follows:

$$f_1 = \frac{2RT(1-t_+^0)\kappa}{F\bar{c}_1} \left( 1 + \frac{d \ln f_{\pm}}{d \ln c} \right) \Big|_{c=\bar{c}_1} \quad (3.31)$$

Subsequently, the equations derived above are transformed into frequency domain using the Laplace transform:

$$s\epsilon_1 C_1(s) = D_1 \frac{d^2 C_1(s)}{dx^2} + \frac{a_v(1-t_+^0)}{F} I_n(s) \quad (3.32)$$

$$-\kappa \frac{d^2 \Phi_1(s)}{dx^2} + f_1 \frac{d^2 C_1(s)}{dx^2} = a_v I_n(s) \quad (3.33)$$

$$\sigma \frac{d^2 \Phi_s(s)}{dx^2} = a_v I_n(s) \quad (3.34)$$

Similarly, the equations for the separator are given as follows:

$$s\epsilon_1 C_1(s) = D_1 \frac{d^2 C_1(s)}{dx^2} \quad (3.35)$$

$$-\kappa \frac{d^2 \Phi_1(s)}{dx^2} + f_1 \frac{d^2 C_1(s)}{dx^2} = 0 \quad (3.36)$$

where  $s = j\omega$  is the Laplace variable.  $C_1(s)$ ,  $\Phi_1(s)$ ,  $\Phi_s(s)$  and  $I_n(s)$  are the corresponding variables in the  $s$  domain.

### 3.3.2 Equations for the Particle Level

On the particle level, the charge transfer reaction will occur due to the electrochemical reactions at the electrode/electrolyte interface. Besides, the double layer capacitance will be constantly charged/discharged by the AC excitation current. The charge transfer reaction will further cause a perturbation for the solid concentration inside the particle, which is modeled by a FSW element. Outside the active material particle, a so-called solid-electrolyte-interphase SEI or cathode-electrolyte-interphase (CEI) is usually formed in the anode and cathode respectively. This outer layer is permeable for the lithium ions and has a certain capacitance, thus it is modeled using a RC element. The total structure of the active material surface and the corresponding circuit is shown in Fig. 3.6. In this thesis, the active material particles are assumed to be spherical and have the same size.

According to the p2D assumption, the reaction current density and thus the impedance at the particle surface are assumed to be homogeneous. Therefore, the area-specific impedance for the particle can

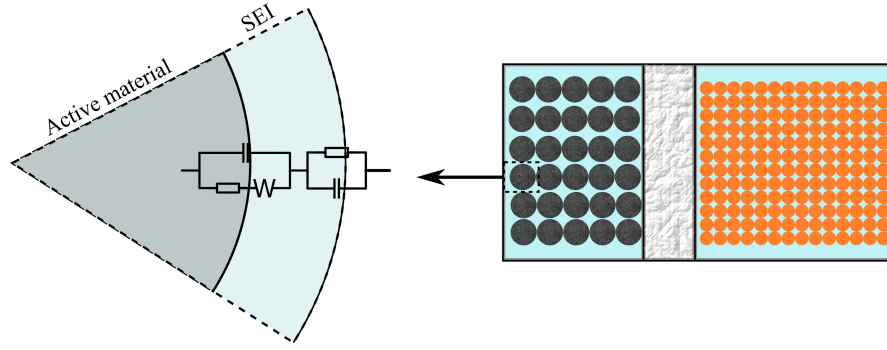


Figure 3.6: The surface structure of an active material particle in a Lithium-ion battery and its equivalent circuit model. The active material particles are assumed to have a spherical geometry and the same size

be represented by the following equation:

$$Z_p = \frac{R_f}{1 + sR_fC_f} + \frac{R_{ct} + Z_W}{1 + sC_{dl}(R_{ct} + Z_W)} \quad (3.37)$$

where  $R_f$  is the area-specific film resistance in  $\Omega \text{ m}^2$ ,  $C_f$  is the area-specific capacitance in  $\text{F m}^{-2}$ .  $R_{ct}$  is the area-specific charge transfer resistance in  $\Omega \text{ m}^2$  and  $C_{dl}$  is the area-specific double layer capacitance in  $\text{F m}^{-2}$ . To derive the expression for the charge transfer resistance given a small excitation current signal, the Butler-Volmer equation must be linearized. Considering that  $e^x \approx (1 + x)$  is valid for small  $x$  and  $\alpha_a = \alpha_c = 0.5$ , Eq. 2.44 can be reformulated as:

$$i_{n,ct} = i_0 \left[ 1 + \frac{\alpha_a F}{RT} \eta - \left( 1 - \frac{\alpha_c F}{RT} \eta \right) \right] = \frac{i_0 F}{RT} \eta \quad (3.38)$$

where  $i_{n,ct}$  is the current density for the charge transfer reaction. As a result, the area-specific charge transfer resistance is defined as:

$$R_{ct} = \frac{\eta}{i_{n,ct}} = \frac{RT}{i_0 F} \quad (3.39)$$

The total current density at the interface can be represented with regard to the particle impedance and the potential difference as follows:

$$I_n(s) = \frac{\Phi_s(s) - \Phi_l(s)}{Z_p} \quad (3.40)$$

It can be seen that with Eq. 3.32-3.34 and Eq. 3.40 the micro-scale (particle level) can be coupled with the macro-scale (electrode level) through the reaction current density  $I_n(s)$ .

### 3.3.3 Derivation of the Analytical Solution

To derive the analytical solution for the impedance model, first Eq. 3.40 is substituted into Eq. 3.32-3.34 to eliminate the local reaction current density  $I_n(s)$ . The resulting equations are rearranged and combined to form the following second-order linear ordinary differential equation system, which

is formulated in the matrix form to ease the solution derivation:

$$\frac{d^2}{dx^2} \begin{bmatrix} C_1(s) \\ \Phi_1(s) \\ \Phi_s(s) \end{bmatrix} = \begin{bmatrix} \frac{\epsilon_1 s}{D_1} & \frac{a_v(1-t_+^0)}{D_1 F Z_p} & -\frac{a_v(1-t_+^0)}{D_1 F Z_p} \\ \frac{\epsilon_1 f_1 s}{D_1 \kappa} & \frac{a_v f_1(1-t_+^0) + D_1 F a_v}{D_1 F Z_p \kappa} & -\frac{a_v f_1(1-t_+^0) + D_1 F a_v}{D_1 F Z_p \kappa} \\ 0 & -\frac{a_v}{Z_p \sigma} & \frac{a_v}{Z_p \sigma} \end{bmatrix} \begin{bmatrix} C_1(s) \\ \Phi_1(s) \\ \Phi_s(s) \end{bmatrix} \quad (3.41)$$

which is further rewritten in the following form:

$$\mathbf{u}'' = \mathbf{A}\mathbf{u} \quad (3.42)$$

where  $\mathbf{u}$  is the solution vector and  $\mathbf{A}$  is the system matrix as shown in Eq. 3.41. To solve the second-order system, the original system can be transformed into the following equation system to reduce the order of the system:

$$\mathbf{v}' = \mathbf{B}\mathbf{v} \quad (3.43)$$

where  $\mathbf{v}$  is a new solution vector defined as:

$$\mathbf{v} = [\mathbf{u}, \mathbf{u}']^\top \quad (3.44)$$

and the matrix  $\mathbf{B}$  has the following form:

$$\mathbf{B} = \left[ \begin{array}{c|c} \mathbf{0} & \mathbf{I} \\ \hline \mathbf{A} & \mathbf{0} \end{array} \right] \quad (3.45)$$

The resulting first-order system can be easily solved to obtain the solution vector  $\mathbf{v}$ . Then it can be shown that the solution vector  $\mathbf{u}$  has the following form:

$$\mathbf{u} = k_1 \mathbf{V}_1 + k_2 \mathbf{V}_1 x + k_3 \mathbf{V}_2 e^{\lambda_2 x} + k_4 \mathbf{V}_3 e^{\lambda_3 x} + k_5 \mathbf{V}_4 e^{\lambda_4 x} + k_6 \mathbf{V}_5 e^{\lambda_5 x} \quad (3.46)$$

where  $\lambda_i$  is the  $i$ -th eigenvalue and  $\mathbf{V}_i$  is the corresponding eigenvector of the system matrix  $\mathbf{B}$  with the first three rows. Specifically, it can be shown that  $\lambda_1 = 0$  and  $\mathbf{V}_1 = [0, 1, 1]^\top$ .  $k_i$  is the unknown coefficient. With the same procedure, the solution for the variables in the separator can be obtained:

$$\mathbf{u} = k_1 \mathbf{V}_1 + k_2 \mathbf{V}_1 x + k_3 \mathbf{V}_2 e^{\lambda_2 x} + k_4 \mathbf{V}_3 e^{\lambda_3 x} \quad (3.47)$$

The unknown coefficient  $k_i$  can be determined by substituting the boundary conditions Eq. 2.48-2.51 together with the continuity boundary conditions into the solution derived above. The resulting linear equation system with the unknown coefficients can be solved with two different procedures:

1. The resulting symbolic linear equation system can be solved using the Symbolic Math Toolbox in MATLAB<sup>®</sup>. Special attention must be paid to the exponential function in the derived analytical solution. At high frequency values, the exponential functions may suffer from overflow problems and give an Inf value. To resolve this issue, the exponential functions can be transformed to the hyperbolic tangent functions to avoid the overflow problems. Another possible issue is that the the symbolic analytical solutions may contain lengthy expressions and cannot be evaluated or

displayed properly.

2. In the calculation of the impedance, the known parameters can be substituted into the linear equation system so that a numerical linear equation system will be solved instead of a symbolic equation system. The overflow issue caused by the exponential functions may occur again and can be resolved by transforming the exponential functions to the hyperbolic tangent functions.

The total impedance of a Lithium-ion battery with an anode, a cathode, and a separator based on the p2D model can be obtained:

$$Z_{\text{PCM}} = \left. \frac{\Phi_s(s)}{i_{\text{app}}(s)} \right|_{x=l_{\text{cell}}} \quad (3.48)$$

### 3.4 Characterization of the Lithium-ion Battery with the Distribution of Relaxation Times

Since proposed, the DRT has been applied in various scenarios and to different devices. The original representation of the DRT only considered the ohmic resistance and the distribution function of the RC elements[16; 18–20; 74; 75]:

$$Z_e(j\omega) = R_{\text{ohm}} + \int_0^{\infty} \frac{G(\tau)}{1 + j\omega\tau} d\tau \quad (3.49)$$

In the impedance of the Lithium-ion battery, an inductive part can be observed in certain cases due to the spiral structure of the cylindrical cells or the measurement cables. In such a case, an inductance has been added to the mathematical model of the DRT problem[24]:

$$Z_e(j\omega) = R_{\text{ohm}} + j\omega L + \int_0^{\infty} \frac{G(\tau)}{1 + j\omega\tau} d\tau \quad (3.50)$$

In the low frequency range, the impedance of a Lithium-ion battery is dominated by the diffusion in the solid and liquid phases and the capacitive effect. According to the original definition of the DRT in Eq. 3.49-3.50, the integral equation becomes divergent when handling the low frequency part. In such a case, the low frequency part must be removed manually so that the DRT can be applied to evaluate the impedance in the mid-high frequency range. As a result, the diffusion impedance cannot be evaluated by the DRT and the corresponding information cannot be extracted. To resolve the issue caused by the low frequency impedance and consider the effect of the RL element, Danzer[25] proposed a generalized formulation for the DRT problem by adding a capacitance and an integral for the distribution function of the RL element. The new formulation is defined by the following equation:

$$Z_e(j\omega) = R_{\text{ohm}} + j\omega L + \frac{1}{j\omega C} + \int_0^{\infty} \frac{j\omega\tau H(\tau)}{1 + j\omega\tau} d\tau + \int_0^{\infty} \frac{G(\tau)}{1 + j\omega\tau} d\tau \quad (3.51)$$

With the extended DRT problem defined above, no preprocessing for the impedance data is necessary and a direct application of the DRT to the raw measurement data is possible. However, in most practical applications, an ideal capacitive behavior can be seldom seen. Instead, the capacitive part of the impedance has a form of a CPE element and an application of the DRT with the formulation shown above will lead to erroneous results (see Fig. 3.7). Therefore, in this thesis an improved formulation

for the DRT problem by considering the CPE element is proposed:

$$Z_e(j\omega) = R_{\text{ohm}} + j\omega L + \frac{1}{(j\omega C)^n} + \int_0^{\infty} \frac{j\omega\tau H(\tau)}{1 + j\omega\tau} d\tau + \int_0^{\infty} \frac{G(\tau)}{1 + j\omega\tau} d\tau \quad (3.52)$$

where  $n$  is the CPE exponent and  $0 < n \leq 1$  is usually valid for the capacitive region of the impedance of a Lithium-ion battery. The CPE exponent can be determined by conducting a curve-fitting on the capacitive part of the impedance.

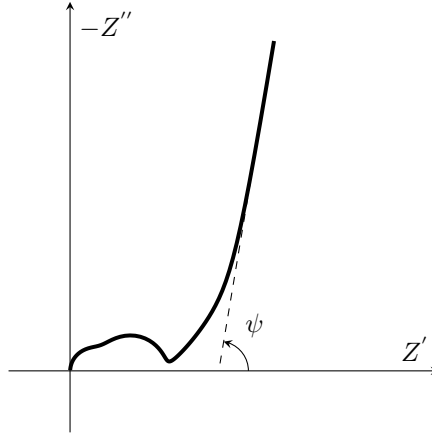


Figure 3.7: Schematic illustration of an impedance, where the capacitive region is represented by a CPE element

If the angle of the fitting line is  $\psi$  as depicted in Fig. 3.7, then the CPE exponent can be determined using the following equation:

$$n = \frac{\psi}{\frac{\pi}{2}} \quad (3.53)$$

After the CPE exponent has been determined, the integral equation can be solved without the convergence issue. Due to the fact that the time constant can span over a few orders of magnitude, the logarithmic scale is used instead of the linear scale:

$$t = \log_{10}(\tau) \quad (3.54)$$

By substituting the equation above into Eq. 3.52, the original integral equation can be transformed into the following form:

$$Z_e = R_{\text{ohm}} + j\omega L + \frac{1}{(j\omega C)^n} + \int_{-\infty}^{+\infty} \frac{j\omega\tau Q(t)}{1 + j\omega\tau} dt + \int_{-\infty}^{+\infty} \frac{P(t)}{1 + j\omega\tau} dt \quad (3.55)$$

where  $Q(t)$  and  $P(t)$  are the distribution functions in logarithmic scale and  $Q(t) = \ln(10)\tau H(\tau)$  and  $P(t) = \ln(10)\tau G(\tau)$ . To solve Eq. 3.55 numerically, the integral equation must first be discretized

$$t_i = t_{\min} + (i - 1)\Delta t \quad (i = 1, 2, 3 \dots) \quad (3.56)$$

where  $t_{\min}$  is the minimum time constant in logarithmic scale,  $\Delta t$  is the step size for the time constant

and is defined as:

$$\Delta t = \frac{t_{\max} - t_{\min}}{N_t} \quad (3.57)$$

where  $t_{\max}$  is the maximum time constant in logarithmic scale and  $N_t$  is the number of time constant after discretization. In the present thesis, we choose to define the following relation:

$$N_t = 5N_f \quad (3.58)$$

where  $N_f$  is the number of the frequency points. The maximum and minimum values of the time constant is defined as:

$$t_{\min} = \log_{10} \left( \frac{1}{1000f_{\max}} \right) \quad (3.59)$$

$$t_{\max} = \log_{10} \left( \frac{1000}{f_{\min}} \right) \quad (3.60)$$

To solve the integral equation, both the real and imaginary parts of the impedance are used and the following measurement data vector is defined:

$$\mathbf{b}_m = \left[ Z'_e(j\omega_1) \quad Z'_e(j\omega_2) \quad \dots \quad Z'_e(j\omega_{N_f}) \quad Z''_e(j\omega_1) \quad Z''_e(j\omega_2) \quad \dots \quad Z''_e(j\omega_{N_f}) \right]^T \quad (3.61)$$

The system matrix for the RC elements is generated by discretizing the RC elements:

$$(\mathbf{A}_{\mathbf{RC}})_{i,j} = \frac{1}{1 + j\omega_i\tau_j} \quad (i = 1, 2, \dots, N_f; j = 1, 2, \dots, N_t) \quad (3.62)$$

Similarly, the system matrix for the RL elements is generated as follows:

$$(\mathbf{A}_{\mathbf{RL}})_{i,j} = \frac{j\omega_i\tau_j}{1 + j\omega_i\tau_j} \quad (i = 1, 2, \dots, N_f; j = 1, 2, \dots, N_t) \quad (3.63)$$

The ohmic resistance, inductance, and CPE element have no distribution functions, therefore their system matrices are defined as follows:

$$\mathbf{A}_{\mathbf{R}} = \left[ 1 \quad 1 \quad \dots \quad 1 \right]_{(N_f \times 1)}^T \quad (3.64)$$

$$\mathbf{A}_{\mathbf{L}} = \left[ j\omega_1 \quad j\omega_2 \quad \dots \quad j\omega_{N_f} \right]_{(N_f \times 1)}^T \quad (3.65)$$

$$\mathbf{A}_{\mathbf{CPE}} = \left[ \frac{1}{(j\omega_1)^n} \quad \frac{1}{(j\omega_2)^n} \quad \dots \quad \frac{1}{(j\omega_{N_f})^n} \right]_{(N_f \times 1)}^T \quad (3.66)$$



Then, the complete system matrix can be built by combing the system matrix of each component:

$$\mathbf{A}_{\text{sys}} = \begin{bmatrix} \mathbf{A}_{\text{RC}} & \mathbf{A}_{\text{RL}} & \mathbf{A}_{\text{R}} & \mathbf{A}_{\text{L}} & \mathbf{A}_{\text{CPE}} \end{bmatrix}^{\text{T}} \quad (3.67)$$

Considering that both the real and imaginary parts are used for the DRT deconvolution, the final system matrix is defined as:

$$\mathbf{A}_{\text{Re,Im}} = \begin{bmatrix} \Re(\mathbf{A}_{\text{sys}}) \\ \Im(\mathbf{A}_{\text{sys}}) \end{bmatrix} \quad (3.68)$$

Finally, the following optimization problem can be defined to solve for the unknowns:

$$\begin{bmatrix} P(t) & Q(t) & R & L & C \end{bmatrix}^{\text{T}} = \underset{\mathbf{x}}{\text{argmin}} \left\{ \|\mathbf{A}_{\text{Re,Im}}\mathbf{x} - \mathbf{b}_{\text{m}}\|_2^2 \right\} \quad (3.69)$$

The optimization problem defined above has the following analytical solution:

$$\hat{\mathbf{x}} = \left( \mathbf{A}_{\text{Re,Im}}^{\text{T}} \mathbf{A}_{\text{Re,Im}} \right)^{-1} \mathbf{A}_{\text{Re,Im}}^{\text{T}} \mathbf{b}_{\text{m}} \quad (3.70)$$

In the case of the DRT deconvolution, it can be seen from Eq. 3.62-3.63 that the columns of the system matrix are strongly linearly correlated so that the resulting problem is ill-posed. To resolve the ill-posedness caused by the collinearity, the Tikhonov regularization is applied to the original problem and the following reformulated problem can be defined:

$$\begin{bmatrix} P(t) & Q(t) & R & L & C \end{bmatrix}^{\text{T}} = \underset{\mathbf{x}}{\text{argmin}} \left\{ \|\mathbf{A}_{\text{Re,Im}}\mathbf{x} - \mathbf{b}_{\text{m}}\|_2^2 + \lambda^2 \|\mathbf{K}\mathbf{x}\|_2^2 \right\} \quad (3.71)$$

where  $\lambda$  is the regularization parameter and  $\mathbf{K}$  is the regularization matrix. Because only the two distribution functions should be regularized, the  $\mathbf{K}$  matrix is then defined as follows:

$$\mathbf{K} = \begin{bmatrix} \mathbf{I}_{N_t \times N_t} \\ \mathbf{I}_{N_t \times N_t} \\ \mathbf{0} \\ \mathbf{0} \\ \mathbf{0} \end{bmatrix} \quad (3.72)$$

Considering further that the distribution functions and the values of the resistance, inductance, and capacitance should be nonnegative, in this thesis the resulting problem is solved using the function *lsqnonneg* in MATLAB®.

### 3.5 DRT-Analyzer: a Toolbox for the Calculation and Evaluation of Distribution of Relaxation Times Spectra

To conduct the DRT analysis and ease the data processing, the toolbox "DRT-Analyzer" has been developed in this thesis. The toolbox is based on the algorithm in Eq. 3.71 and consists of three sections, each with the corresponding function: **Data validation & DRT calculation**, **Peak analysis**, and

**Results and data export** (see Fig. 3.8). In this section the three sections will be introduced and explained in detail.

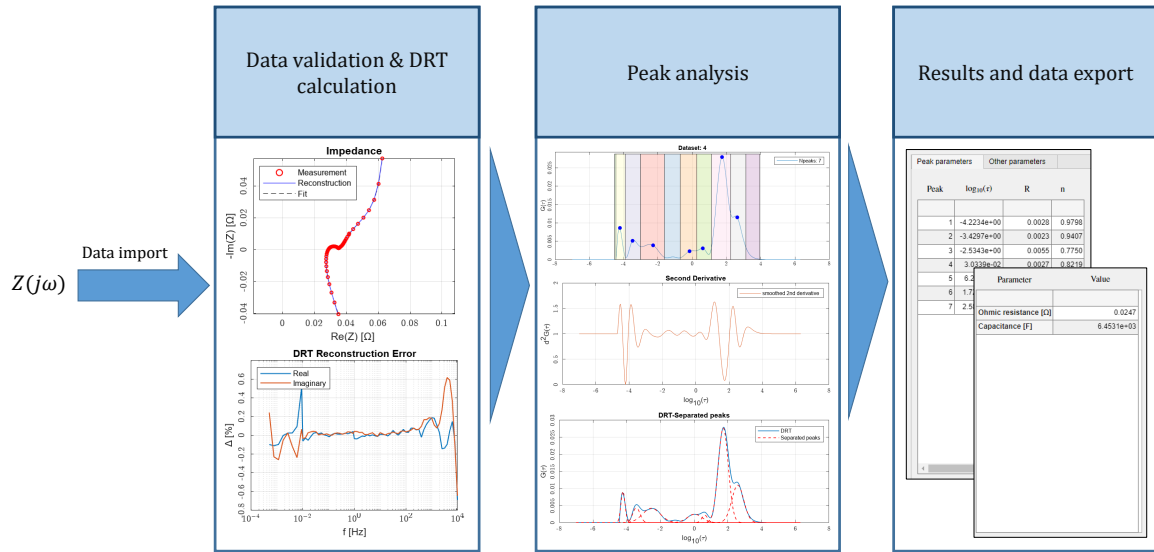


Figure 3.8: Flow chart of the toolbox DRT-Analyzer. The toolbox consists of three principal sections: data validation and DRT calculation, peak analysis and results and data export.

### 3.5.1 Data Validation and Calculation

To conduct the DRT analysis, first the impedance data of a specific format must be loaded into the toolbox. Currently, the *.txt* file exported by the Biologic electrochemical workstation can be accepted. Alternatively, for non-Biologic users, the impedance data can be saved in *.mat* files, which can be also loaded by the toolbox. In this toolbox, multiple impedance data can be loaded and evaluated at the same time so that a batch processing is possible. Then the process parameters necessary for the calculation of the DRT spectrum must be defined. First, the regularization parameter  $\lambda$  can be input into the toolbox to tune the regularization effect, the default value defined in the toolbox is 0.2. Then, in certain cases the capacitive part of the impedance shows a CPE behavior, thus the CPE exponent  $\phi$  must be defined. In this toolbox, the data points used for the calculation of the CPE exponent can be selected by the user. Based on the selected data points, the curve fitting will be conducted and the CPE exponent can be calculated (see Fig. 3.9).

As the next step, the DRT calculation can be conducted and the reconstruction error is provided for the validation purpose. Generally the reconstruction error should be randomly distributed around the  $x$  axis, otherwise the measurement data may be invalid.

### 3.5.2 Peak Analysis

After the impedance data has been validated and the DRT spectrum has been calculated, the peak analysis can be conducted to separate the contribution of the overlapping peaks and obtain the time constants. To conduct the peak analysis, the displayed DRT spectrum must be first switched to the "peak view" so that the peak location (marked with blue dot, see Fig. 3.10) and boundary (marked with different colors, see Fig. 3.10) can be automatically recognized by an embedded algorithm and

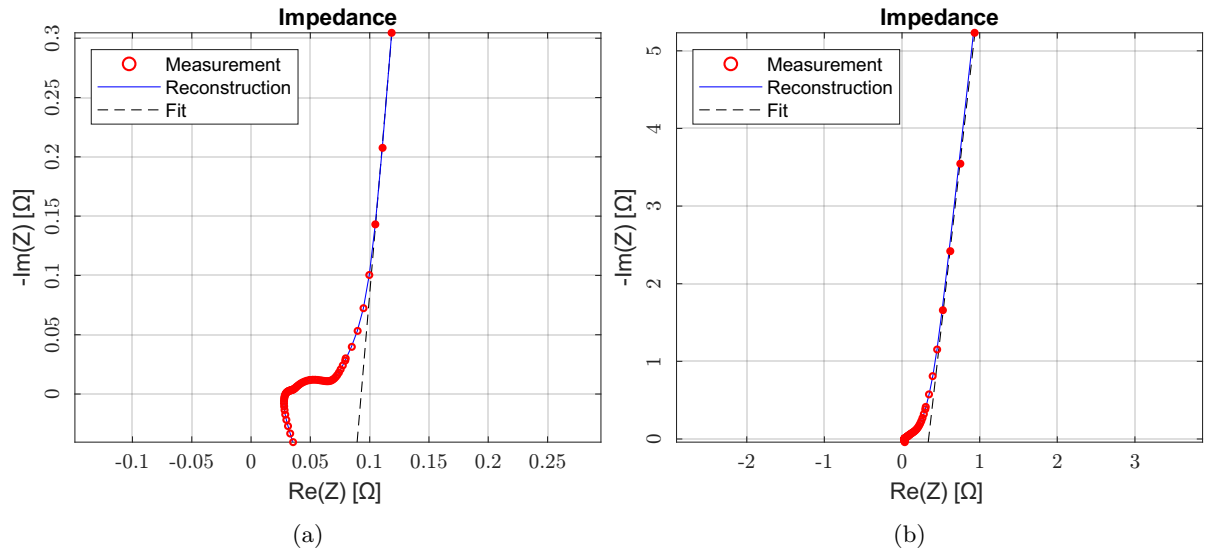


Figure 3.9: Calculation of the CPE exponent by curve fitting in different cases. In case b the capacitive part is much larger and a linear relationship can be clearly observed in the capacitive region. As a result, case b is more suitable for calculating the CPE exponent

set as the initial values for the peak analysis. Occasionally, not all the peaks can be recognized by the algorithm, the operator has the option to define additional peaks manually. All defined peaks and boundaries can be edited by the operator if necessary.

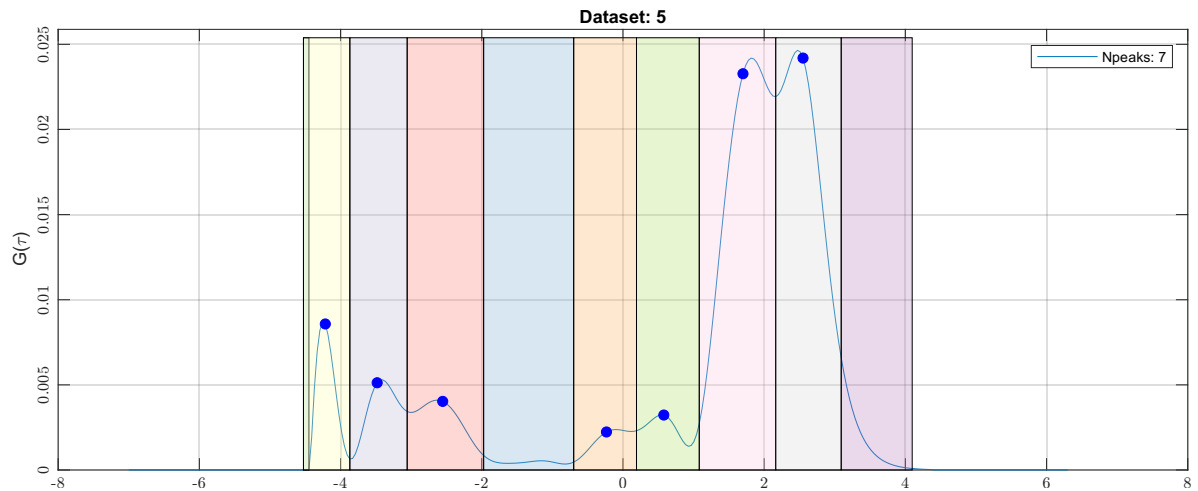


Figure 3.10: Peak view of the calculated DRT spectrum with the defined peak locations and boundaries.

Next, for each defined peak, one or multiple candidate fitting functions must be selected to conduct the peak analysis. The detailed information on the candidate functions and optimization algorithms can be found in chapter 4.

### 3.5.3 Results and Data Export

After the peak analysis has been finished, the DRT spectrum will be separated with the contribution of each process observable (see Fig. 3.11). Furthermore, the calculated parameters for each peak will be displayed in a table (see Fig. 3.11). The polarization resistance, time constant, and CPE exponent

of each peak will be displayed in the table. Besides, the total ohmic resistance and capacitance of the evaluated impedance will also be calculated and displayed. Each separated peak as well as the parameters displayed in the table can be exported to the workspace of MATLAB®.

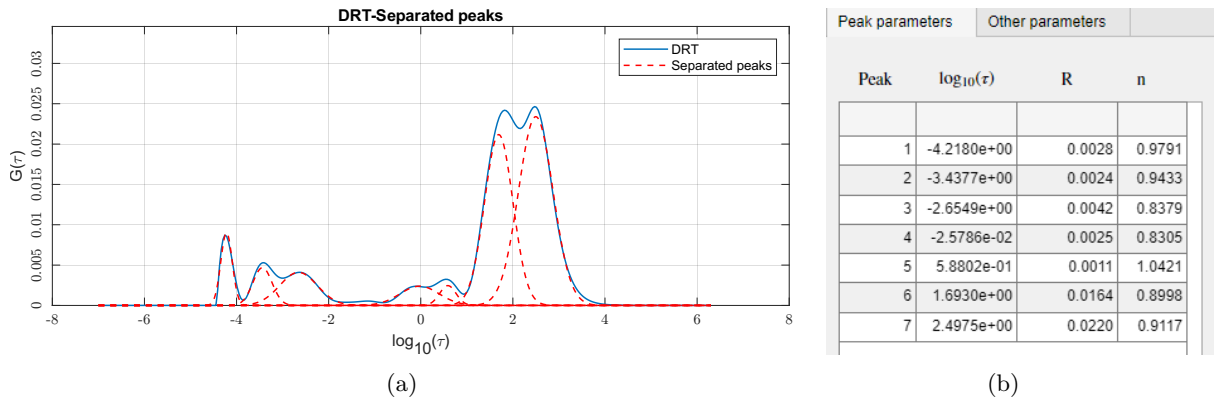


Figure 3.11: Results for the peak analysis with (a): the separated peaks showing the contribution of each process and (b): the calculated parameters of each separated peak, where the time constant  $\tau$  is in s and the resistance is in  $\Omega$

## 4 Investigation of the Distribution of Relaxation Times of a Porous Electrode Using a Physics-based Impedance Model

The EIS technique has been applied to the Lithium-ion battery due to its capability of characterizing the physical and chemical processes with different characteristic frequencies in the battery. The evaluation of the impedance data requires an properly selected impedance model which includes the processes of interest. Commonly used impedance models include the ECM and the PCM. While the ECM has the merits of simple structure and fast computation speed, it is not based on any fundamental theory and thus lacking a direct connection with the physicochemical parameters of the Lithium-ion battery. The physicochemical impedance model can compensate for the shortcomings of the ECM but requires a significantly higher computation effort and has a complicated structure. Therefore, both an intuitive and a quantitative interpretation of the impedance data with a physicochemical impedance model remain a challenging task.

To estimate the battery parameters of interest with the selected impedance model and measurement data, an optimization problem will be established and an appropriate algorithm must be implemented to solve the problem. Due to the strongly nonlinear nature of the electrochemical systems, the defined optimization problem will be subjected to identifiability issues inevitably, irrespective whether an ECM or a physicochemical impedance model is used.

The DRT, since proposed, has been widely applied to the impedance data of various devices. The DRT can transform the defined nonlinear optimization problems to a linear least square problem and therefore resolve the identifiability issues. However, when the DRT is applied to estimate the battery parameters combined with a physicochemical impedance model, a comprehensive theoretical model must be proposed to interpret the results with regard to the physicochemical impedance model.

For the aforementioned reasons, in this chapter a comprehensive theory has been developed to interpret the DRT spectrum of a Lithium-ion battery in mid-high frequency range with regard to a physicochemical impedance model. An analytical expression for the DRT spectrum has been derived and explained using a synthetic impedance data. Furthermore, the developed theory has been applied to the impedance data of a commercially available Lithium-ion battery cell. The kinetic reaction rate constant of the anode and cathode as well as the SEI resistivity have been estimated the temperature dependence of the estimated parameters have been investigated.

### **Author contribution**

Yulong Zhao was the principal author tasked with coordinating and writing the paper, developing the theory and model, conducting the lab experiment with the coin cells, and evaluating the measurement data. Volkan Kumtepelı assisted with developing the APAM algorithm. Sebastian Ludwig conducted the impedance measurement with the full cells. Andreas Jossen contributed via fruitful scientific discussions and reviewed the manuscript.

## **Investigation of the distribution of relaxation times of a porous electrode using a physics-based impedance model**

Yulong Zhao, Volkan Kumtepe, Sebastian Ludwig, and Andreas Jossen

Journal of Power Sources 530 (2022) 231250

Permanent weblink:

<https://doi.org/10.1016/j.jpowsour.2022.231250>

Reproduced by permission of Elsevier.



Contents lists available at ScienceDirect

Journal of Power Sources

journal homepage: [www.elsevier.com/locate/jpowsour](http://www.elsevier.com/locate/jpowsour)



## Investigation of the distribution of relaxation times of a porous electrode using a physics-based impedance model

Yulong Zhao<sup>a,\*</sup>, Volkan Kumtepe<sup>b</sup>, Sebastian Ludwig<sup>a</sup>, Andreas Jossen<sup>a</sup>

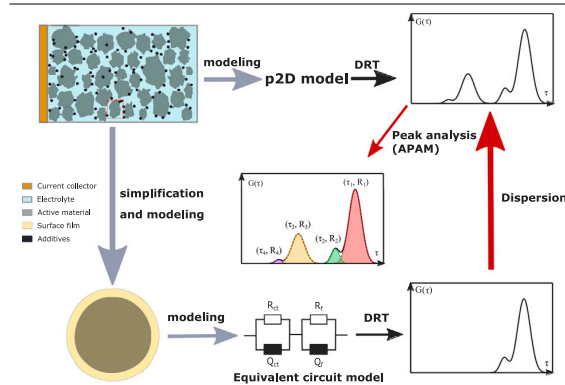
<sup>a</sup> Institute for Electrical Energy Storage Technology (EES, Technical University of Munich (TUM)), Arcisstrasse 21, Munich, 80333, Bavaria, Germany

<sup>b</sup> Department of Engineering Science, University of Oxford, OX1 3PJ, Oxford, United Kingdom

### HIGHLIGHTS

- Cell characterization by deep understanding of physics-based impedance model and DRT.
- Derivation of analytical expressions for the DRT spectrum of full cell.
- Development of an improved peak analysis for separating fully overlapping peaks.
- Quantitative relation of microscopic parameters to the DRT spectrum of electrode.
- Characterization of cell parameters and their temperature/SOC dependence.

### GRAPHICAL ABSTRACT



### ARTICLE INFO

**Keywords:**  
Electrochemical impedance spectroscopy  
Physics-based model  
Distribution of relaxation times  
Dispersion

### ABSTRACT

Recently, the analysis of the distribution of relaxation times (DRT) has drawn wide attention in battery engineering due to its nondestructive nature and the ability to separate the electrochemical processes with different time constants. Since proposed, the DRT is only interpreted using the equivalent circuit model (ECM), and an interpretation based on physicochemical model is still missing. To characterize the cell parameters and extract the valuable information more effectively, a new theory is developed based on the deep understanding of the physics-based impedance model and the DRT method. Particularly, a closed-form analytical expression for the DRT spectrum is derived, therefore the DRT spectrum can be explained and interpreted with a clear physical meaning. In addition, it is found that the relaxation time dispersion of EIS may have multiple origins: the porous structure of the electrode, the regularization technique used to calculate the DRT and the constant phase element type behavior of the active material particles. Based on the theory developed in this work, an optimized data analysis framework is created to better interpret the DRT spectrum. Finally, the developed DRT analysis framework is applied to the impedance data of a commercial LIB to demonstrate its advantages and effectiveness.

### 1. Introduction

In recent years, thanks to their rapid development, LIBs are being deployed in a range of sectors including electric vehicles and stationary

energy storage systems. For improved production, modeling and diagnostics of LIBs, accurate and fast parameter estimation is indispensable. To estimate the physicochemical parameters of a battery cell, a set of external measurement data is fed into an optimization program with

\* Corresponding author.  
E-mail address: [yulong.zhao@tum.de](mailto:yulong.zhao@tum.de) (Y. Zhao).

<https://doi.org/10.1016/j.jpowsour.2022.231250>

Received 23 December 2021; Received in revised form 24 February 2022; Accepted 1 March 2022

Available online 16 March 2022

0378-7753/© 2022 Elsevier B.V. All rights reserved.

Nomenclature	
<b>Greek letters</b>	
$\alpha$	Variable related to local particle impedance; charge transfer coefficient, –
$\beta$	Damping factor of dispersion, –
$\delta$	Dirac delta function
$\gamma$	coefficients of terms in cost function
$\kappa$	Liquid phase conductivity, S m <sup>-1</sup>
$\mu$	Peak location of peak fitting
$\nu/f$	Frequency, Hz
$\omega$	angular frequency, rad s <sup>-1</sup>
$\phi$	Exponent for CPE element
$\sigma$	Solid phase conductivity, S m <sup>-1</sup>
$\tau$	Time constant, s
$\theta$	Variable related to local particle impedance
<b>Subscripts</b>	
CPE	Variables related to CPE element
ct	Variables related to charge transfer
e	Variables related to electrode
f	Variables related to film
loc	Variables related to active material particles
ohm	Variables related to ohmic resistance
p	Variables related to positive electrode
RC	Variables related to an RC element
sep	Variables related to the separator
ZARC	Variables related to a ZARC element
$k$	Universal subscript for electrode, $k = n, sep, p$
$n$	Variables related to the negative electrode; variables related to the $n$ th order dispersion
<b>Symbols</b>	
$\mathbb{Z}$	Set of integers
$F$	Faraday constant
$A$	Peak magnitude of peak fitting
$a$	Pole for meromorphic function expansion
$a_v$	Specific volumetric area, m <sup>-1</sup>
$b$	Coefficient for meromorphic function expansion
$C$	Capacitance, F
$c$	Magnitude of dispersion peak
$G$	DRT spectrum function of electrode
$g$	DRT spectrum function of RC/ZARC element
$h$	Peak height of peak fitting
$j$	Imaginary unit
$J$	Cost function of peak fitting
$L$	Inductance, H
$l$	Electrode thickness, m

$R$	With subscript - resistance, $\Omega$ ; without subscript - gas constant, J K <sup>-1</sup> mol <sup>-1</sup>
$s$	Laplace variable, $j\omega$
$y$	Data for peak fitting
$Z$	Impedance, $\Omega$

domain, the EIS data of the LIB at several state of charge (SOC) points is used to fit a preselected battery impedance model. Depending on the model complexity and comprehensiveness, the equivalent circuit model (ECM) [10–15] and physicochemical model (PCM) [16–20] have been selected to interpret the EIS data. Due to the strongly nonlinear nature of the physicochemical impedance model, generally a comprehensive parameter identifiability analysis must be conducted to pick out the identifiable parameters [21] and a nonlinear optimization program must be established to identify the parameters of interest. The methods based on nonlinear optimization usually require a complicated algorithm design and large computational effort. Furthermore, they also suffer from under-fitting or over-fitting problems if the model used and the estimated parameters are not properly chosen. In recent years, the DRT analysis has been frequently used for fast parameter estimation of LIBs due to the fact that it is a linear optimization-based and nondestructive method. Via DRT analysis, the time constants and polarization resistance of kinetic processes inside the LIBs can be determined. Among the investigated publications related to DRT analysis, some emphasized on the optimization and further development of the numerical algorithm used to solve the inversion problem [22–26], some focused on the characterization and interpretation of the DRT spectrum for electrochemical processes inside the LIBs [27–32], and some derived and investigated the analytical DRT expressions of different circuit elements such as RC, constant phase element (CPE), finite length Warburg element etc. to better understand and interpret the DRT spectrum [33–36]. A missing yet quite essential piece in the large puzzle of DRT analysis is: how the DRT spectrum is related to the fundamental physicochemical processes and fundamental parameters of LIBs, what mathematical relation exists between them, and how this could contribute to a better interpretation of DRT results? In this present work, the questions raised above will be answered and a theory for characterizing the cell parameters and extracting more valuable information by the deep understanding of the physics-based impedance model and the DRT method will be developed. A comparison of the published works so far regarding the battery model and evaluation method for the interpretation of the DRT spectra is shown in Table 1.

The remaining part of the work is organized as follows: the detailed development and analysis of the proposed model is presented in Section 2; Section 3 applies the developed framework to the impedance data of a commercial LIB; Section 4 concludes this work and covers the outlook for future work.

## 2. Theory

### 2.1. Impedance deconvolution with DRT

The DRT analysis is a popular method used to deconvolve the impedance data, which can effectively resolve the under- or overfitting problem when trying to fit the impedance data with an ECM. Furthermore, this nonlinear fitting problem can be transformed into a linear optimization problem; therefore, repeated setting up of optimization problem and large computation burden can be avoided. In this work, Eq. (1) is used to model the effects of the RC elements, RL elements, capacitance and ohmic resistance respectively:

$$Z_c = R_{ohm} + \frac{1}{j\omega C} + j\omega L + \int_0^\infty \frac{j\omega\tau H(\tau)}{1 + j\omega\tau} d\tau + \int_0^\infty \frac{G(\tau)}{1 + j\omega\tau} d\tau \quad (1)$$

a predefined objective function and constraints, which is then solved using appropriate methods. LIB parameter extraction can be done using either time domain or frequency domain data. In time domain, the measured battery current, voltage and temperature data under several C-rates are used as the input for the optimization [1–9]. In frequency



**Table 1**  
Comparison of the published works regarding the battery model and methods for the evaluation of DRT spectra.

Battery model	Evaluation		
	No evaluation	Qualitative	Quantitative
Not considered	[40–42]	[43–45]	[46,47]
Equivalent circuit model	[48]	[49]	[35,50–53]
Physicochemical model			present work

where  $\omega$  is the angular frequency,  $Z_c$  is the measured impedance,  $R_{ohm}$  is the total ohmic resistance,  $H(\tau)$  is the distribution function for the RL elements,  $G(\tau)$  is the distribution function for the RC elements,  $C$  is the total capacitance and  $L$  is the total inductance. To solve the integral equation numerically, the equation above is discretized and transformed into a linear equation system. The resulting system is an ill-posed problem by its nature and cannot be inverted directly, as a result regularization technique is applied to invert the equation. Finally the following linear optimization problem is obtained:

$$[R_{ohm}, L, C, H(\tau), G(\tau)] = \underset{x>0}{\operatorname{argmin}} \left\{ \|Ax - b\|_2^2 + \lambda^2 \|x_\tau\|_2^2 \right\} \quad (2)$$

where  $A$  is the system matrix after the integral discretization,  $x$  is the total solution vector,  $b$  represents the measurement data,  $x_\tau$  is the component of  $x$  corresponding to the two distribution functions  $G(\tau)$  and  $H(\tau)$ .

## 2.2. Impedance model

Since proposed, the Pseudo-two-Dimensional (p2D) model developed by Newman, Doyle et al. [37–39] has been widely applied to LIBs for different purposes. The p2D model describes the physicochemical processes inside the LIBs with coupled partial differential and algebraic equations, which include the fundamental electrochemical parameters and have a physical meaning behind them. Therefore, the physics-based impedance model used in this work is derived based on the p2D model.

To derive the impedance model used for LIBs, the p2D model is transformed from the time domain to the frequency domain using the Fourier or Laplace transform. With appropriate assumptions, an analytical solution can be obtained — the detailed model derivation can be found in Appendix. In this work, we aim to investigate the kinetic processes occurring mainly in the mid- to high frequency range (usually from a few Hz to a few kHz), in which the charge transfer and SEI processes are dominating; the impedance contributions of diffusion in liquid and solid phases are therefore neglected. Under these assumptions, the anode, cathode and separator of the LIB can be regarded as being coupled solely by electrical conduction in the liquid phase because the diffusion and the concentration gradients in the liquid phase are neglected. Therefore, the impedance expression for both the anode and cathode has the same structure and the impedance of the separator is reduced to an ohmic resistance that represents the ionic conduction in the liquid phase. Because the p2D model takes the current density perpendicular to the current collector as model input, the derived impedance represents an area-specific impedance. The impedance for each layer is expressed using the following equation:

$$Z_{c,k} = \begin{cases} \frac{l_{sep}}{\kappa_{sep}}, & \text{for } k = \text{sep} \\ \frac{l_k}{\kappa_k + \sigma_k} + \frac{(\kappa_k^2 + \sigma_k^2) \coth(\sqrt{\theta_k} l_k)}{\kappa_k \sigma_k (\kappa_k + \sigma_k) \sqrt{\theta_k}} + \frac{1}{(\kappa_k + \sigma_k) \sqrt{\theta_k} \sinh(\sqrt{\theta_k} l_k)}, & \text{for } k \in \{n, p\} \end{cases} \quad (3)$$

where  $Z_{c,k}$  and  $l_k$  are impedance and thickness of the layer  $k$ . Here,  $k \in \{n, p, \text{sep}\}$  denotes the negative electrode, positive electrode and

the separator respectively.  $\kappa$  and  $\sigma$  are the conductivities in the liquid and solid phases respectively, and  $\theta$  is the variable related to the local particle impedance:

$$\theta_k = \left( \frac{1}{\sigma_k} + \frac{1}{\kappa_k} \right) \frac{a_{v,k}}{Z_{k,loc}(s)} \quad (4)$$

where  $s$  is the Laplace variable and  $s = j\omega$ ,  $Z_{k,loc}(s)$  represents the area-specific particle impedance and  $a_{v,k}$  is the volumetric interfacial area. If the charge transfer and film process are modeled with ideal RC elements, the local particle impedance can be expressed using the following equation:

$$Z_{k,loc}(s) = \frac{R_{k,ct}}{1 + s\tau_{k,ct}} + \frac{R_{k,f}}{1 + s\tau_{k,f}} \quad (5)$$

where  $R_{k,ct}$  and  $R_{k,f}$  represent the area-specific charge transfer and film resistance respectively,  $\tau_{k,ct}$  and  $\tau_{k,f}$  represent the characteristic time constants for the charge transfer and film process at the solid/liquid interface. If the imperfection of the active material is taken into consideration, the particle impedance will show a frequency dispersion behavior, where the double-layer capacitance or film capacitance is described using a constant phase element (CPE) instead of an ideal capacitance. Martin and Pajkossy believed that the CPE behavior is more attributable to the specific adsorption caused by impurities in the electrolyte [54,55]; Kerner claimed that the atomic scale heterogeneity in polycrystalline solid electrodes, which is often the case when the extent of macroscopic surface roughness is large, is responsible for the CPE behavior [56]. When the CPE element is connected to a resistance in parallel, the resulting impedance curve appears as a circle with its center below the real axis; therefore, this element is commonly referred to as a ZARC element. To ensure general applicability, we choose to derive the theory with both an RC-element and a ZARC element for particle impedance. The particle impedance with a ZARC element is expressed as follows:

$$Z_{k,loc}(s) = \frac{R_{k,ct}}{1 + (s\tau_{k,ct,CPE})^{\phi_1}} + \frac{R_{k,f}}{1 + (s\tau_{k,f,CPE})^{\phi_2}} \quad (6)$$

where  $\phi_1$  and  $\phi_2$  are the CPE exponents for the active material/film and film/electrolyte interface respectively, and  $\tau_{k,ct,CPE}$  and  $\tau_{k,f,CPE}$  are the corresponding characteristic time constants. As explained, the impedance expressions for anode, separator and cathode are decoupled and thus have the same structure. Hence, the derivation will be conducted with one electrode and the subscript  $k$  will be omitted for simplicity.

## 2.3. Theory development

### 2.3.1. Particle impedance with RC-element

The impedance of the electrode  $Z_c$  is related to the DRT function via the following integral equation:

$$Z_c(s) - Z_c(\infty) = Z_{c,RC} = \int_0^\infty \frac{G(\tau)}{1 + s\tau} d\tau \quad (7)$$

where  $G(\tau)$  is the searched for DRT spectrum function,  $Z_c(\infty)$  is the impedance when the frequency approaches infinity, i.e. the ohmic resistance of the electrode, and  $Z_{c,RC}$  is the electrode impedance without the ohmic component. To solve for the  $G(\tau)$  function analytically, the integral equation must be solved. Considering the complicated form of the electrode impedance expression, a direct inversion using an inverse transform table or the formula given by Titchmarsh [57] is rather impractical. As a result, we choose to derive the inverse transform with the help of complex function expansion. If we substitute Eq. (5) into Eq. (3) and (4), a meromorphic function of the Laplace variable  $s$  is obtained. It can be seen that the resulting meromorphic function has an infinite number of isolated poles and can thus be expanded. By applying the Mittag-Leffler expansion theorem to the impedance expression [58], the following equation is obtained:

$$Z_{c,RC}(s) = Z_{c,RC}(0) + \sum_{n=0}^{\infty} \left( \frac{b_n}{s - a_n} + \frac{b_n}{a_n} \right) \quad (8)$$

where  $a_n$  and  $b_n$  are poles and corresponding expansion coefficients. Further, if we let  $s$  approach infinity and note that  $Z_{e,RC}(\infty) = 0$ , the following equation is derived:

$$Z_{e,RC}(0) + \sum_{n=0}^{\infty} \frac{b_n}{a_n} = 0 \quad (9)$$

As a result, Eq. (8) can be further reduced to the following form:

$$Z_{e,RC}(s) = \sum_{n=0}^{\infty} \frac{b_n}{s - a_n} \quad (10)$$

Subsequently the inversion can be conducted on Eq. (10) by noting that equation:

$$\frac{b_n}{s - a_n} = \int_0^{\infty} \frac{g(\tau)}{1 + s\tau} d\tau \quad (11)$$

can be easily solved to obtain the solution:

$$g(\tau) = -\frac{b_n}{a_n} \delta\left(\tau + \frac{1}{a_n}\right) \quad (12)$$

where  $\delta(\tau)$  represents the Dirac delta function. By combining Eq. (10), (11) and (12),  $G(\tau)$  can be expressed by the following equation:

$$G(\tau) = \sum_{n=0}^{\infty} \left[ c_n \delta\left(\tau + \frac{1}{a_n}\right) \right] \quad (13)$$

which produces an infinite sum of Dirac delta functions with the time constants  $(-1/a_n)$  and the magnitude of  $c_n = -b_n/a_n$ , indicating a certain dispersion behavior in the DRT spectrum. We further note that  $(-a_n)$  has units of Hertz and is thus interpreted as the dispersion frequency  $\nu_n$ ,  $(-1/a_n)$  has units of second and thus represents the dispersion time constant  $\tau_n$ . As a result, Eq. (13) indicates that the DRT spectrum of the porous electrode consists of an infinite sum of Dirac delta peaks with the time constants  $\tau_n$  or the frequency  $\nu_n$ , showing a certain pattern of frequency dispersion. To investigate the dispersion pattern quantitatively, first the dispersion time constants of the DRT spectrum must be obtained by solving for the singularities of the impedance expression using the following equations:

$$\theta = 0 \quad (14)$$

and

$$\sinh(\sqrt{\theta}l) = 0 \Rightarrow \sqrt{\theta}l = in\pi \quad n \in \mathbb{Z} - \{0\} \quad (15)$$

It is readily observed that Eq. (14) has two solutions which correspond to the characteristic time constants of the charge transfer and film process:

$$\tau_{ct} = -\frac{1}{a_{ct,0}} \quad (16)$$

$$\tau_f = -\frac{1}{a_{f,0}} \quad (17)$$

We refer to time constants (or frequencies) derived above as zero order time constants (or frequencies), as they are only decided by the time constants of the local processes. Similarly, Eq. (15) has an infinite number of solutions corresponding to the charge transfer and film processes; upon solving the hyperbolic equation we can obtain:

$$\tau_{ct,n} = -\frac{1}{a_{ct,n}} = \frac{2\alpha\tau_f\tau_{ct}}{f_1 - f_2} \quad (18)$$

$$\tau_{f,n} = -\frac{1}{a_{f,n}} = \frac{2\alpha\tau_f\tau_f}{f_1 + f_2} \quad (19)$$

where  $f_1$  and  $f_2$  are defined as follows:

$$f_1 = \alpha(\tau_f + \tau_{ct}) + n^2\pi^2(R_{ct}\tau_f + R_f\tau_{ct}) \quad (20)$$

$$f_2 = \sqrt{[n^2\pi^2(R_{ct}\tau_f - R_f\tau_{ct}) + \alpha(\tau_f - \tau_{ct})]^2 + 4n^4\pi^4R_{ct}R_f\tau_{ct}\tau_f} \quad (21)$$

where  $\alpha = a_v l^2 (1/\kappa + 1/\sigma)$ , and we refer to the higher order terms ( $n \geq 1$ ) as harmonics compared to the fundamental terms. For clarity, Eq. (13) can be rewritten with regard to the two processes:

$$G(\tau) = \sum_0^{\infty} [c_{ct,n}\delta(\tau - \tau_{ct,n}) + c_{f,n}\delta(\tau - \tau_{f,n})] \quad (22)$$

While the time constants at which the dispersion occurs have been determined, the magnitude of the dispersion still remains to be calculated. The coefficients  $b_n$  can be determined using the residue method:

$$b_n = \lim_{s \rightarrow a_n} (s - a_n) Z_{e,RC}(s) \quad (23)$$

Upon substituting the expression for  $Z_{e,RC}$ , Eq. (5), (16) and (17) into the equation above, we can obtain the coefficients for the fundamental order term:

$$b_{ct,0} = \frac{R_{ct}}{a_v l \tau_{ct}} \quad (24)$$

$$b_{f,0} = \frac{R_f}{a_v l \tau_f} \quad (25)$$

Similarly, the coefficients for the higher order harmonics are given by:

$$b_{ct,n} = \frac{2\alpha l (a_{ct,n} \tau_f + 1)^2 (a_{ct,n} \tau_{ct} + 1)^2 [\kappa^2 + 2\kappa\sigma(-1)^n + \sigma^2]}{n^4 \pi^4 \kappa \sigma (\sigma + \kappa) [R_{ct} \tau_{ct} (a_{ct,n} \tau_f + 1)^2 + R_f \tau_f (a_{ct,n} \tau_{ct} + 1)^2]} \quad (26)$$

$$b_{f,n} = \frac{2\alpha l (a_{f,n} \tau_f + 1)^2 (a_{f,n} \tau_{ct} + 1)^2 [\kappa^2 + 2\kappa\sigma(-1)^n + \sigma^2]}{n^4 \pi^4 \kappa \sigma (\sigma + \kappa) [R_{ct} \tau_{ct} (a_{f,n} \tau_f + 1)^2 + R_f \tau_f (a_{f,n} \tau_{ct} + 1)^2]} \quad (27)$$

From Eq. (26) and (27), we can observe that the magnitudes of higher order harmonics decay rapidly with  $n$ , which means that in practice the harmonics can only appear in the DRT spectrum under certain conditions — we will investigate this aspect in detail later. In the next section, we will derive the analytical DRT expression with ZARC elements as the local particle impedance.

### 2.3.2. Particle impedance with ZARC elements

Based on the DRT expression derived above with RC-elements, the DRT for particle impedance with ZARC elements instead of ideal capacitance can be derived by replacing  $s^{\phi_1}$  and  $s^{\phi_2}$  in Eq. (6) with  $s$  and assuming  $\tau_{ct} = (\tau_{ct,CPE})^{\phi_1}$  and  $\tau_f = (\tau_{f,CPE})^{\phi_2}$ . On the one hand, with the same routine as shown in Section 2.3.1, the impedance expression can be expanded as:

$$Z_{e,ZARC}(s) = \sum_{n=0}^{\infty} \frac{b_{ct,n}}{s^{\phi_1} - a_{ct,n}} + \sum_{n=0}^{\infty} \frac{b_{f,n}}{s^{\phi_2} - a_{f,n}} \quad (28)$$

On the other hand, we notice that the normalized DRT of the ZARC element is described as follows [34]:

$$\frac{1}{1 + (s\tau_0)^{\phi}} = \int_0^{\infty} \frac{g_{ZARC}(\tau)}{1 + s\tau} d\tau \quad (29)$$

$$g_{ZARC}(\tau) = \frac{1}{2\pi\tau} \frac{\sin(\phi\pi)}{\cosh[\phi \ln(\tau/\tau_0)] + \cos(\phi\pi)} \quad (30)$$

where  $\tau_0$  is the characteristic time constant of the ZARC element. Combining the Eq. (28), (29) and (30), the total DRT expression can be written as:

$$G(\tau) = \sum_{n=0}^{\infty} \left( -\frac{b_{ct,n}}{a_{ct,n}} \right) \frac{1}{2\pi\tau} \frac{\sin(\phi_1\pi)}{\cosh[\phi_1 \ln(\tau/\tau_{ct,CPE,n})] + \cos(\phi_1\pi)} + \sum_{n=0}^{\infty} \left( -\frac{b_{f,n}}{a_{f,n}} \right) \frac{1}{2\pi\tau} \frac{\sin(\phi_2\pi)}{\cosh[\phi_2 \ln(\tau/\tau_{f,CPE,n})] + \cos(\phi_2\pi)} \quad (31)$$

The equation derived above reveals that when RC elements of the local particle impedance are replaced by ZARC elements, the conclusions about the frequency dispersion still remain true, except that at each characteristic time constant the Dirac delta peak becomes a peak defined by Eq. (30). In contrast to the Dirac delta peak with infinite height and zero width, a peak defined by Eq. (30) has a certain width and thus shows a dispersion behavior, which is caused by the CPE element.

2.4. Theory analysis

In this section, the derived model will be analyzed, especially the distribution of dispersion time constants and the magnitude of dispersion peaks. Subsequently, we will analyze how the conclusions made can help to better interpret the DRT spectrum.

2.4.1. Dispersion frequency and magnitude

First, the dispersion patterns of time constants are investigated. Considering Eq. (18) and (19), when  $n$  is relatively small, they can be approximated as:

$$\tau_{ct,n} \approx \frac{\tau_{ct}}{\left(1 + \frac{n^2 \pi^2 R_{ct}}{\alpha}\right)} \quad (32)$$

$$\tau_{f,n} \approx \frac{\tau_f}{\left(1 + \frac{n^2 \pi^2 R_f}{\alpha}\right)} \quad (33)$$

It is clear that the time constants of the dispersion peaks decrease with increasing order  $n$ . If the constant terms in the denominator of Eq. (32) and (33) are neglected, we can further conclude that the dispersion time constants decrease approximately with  $1/n^2$ . If  $n$  tends to infinity, we have:

$$\tau_{ct,\infty} = \lim_{n \rightarrow \infty} (\tau_{ct,n}) = \frac{R_{ct} \tau_f + R_f \tau_{ct}}{R_{ct} + R_f} \quad (34)$$

$$\tau_{f,\infty} = \lim_{n \rightarrow \infty} (\tau_{f,n}) = 0 \quad (35)$$

From the analysis above, we can conclude that the dispersion only occurs in the direction of decreasing time constants and the largest time constant is the fundamental order time constant. For the charge transfer process, there exists a cut-off time constant, while for the film process, the dispersion can approach 0. In addition, the dispersion has a well-defined pattern with respect to the two processes occurring in the particle.

For impedance, where the local particle is modeled using RC or ZARC elements, the highest time constant is always equal to the characteristic time constant of the RC or ZARC elements and will not be interfered with by the geometric/transport parameters of the porous electrode, as indicated by Eq. (16) and (17). The polarization resistance of each process or the magnitude of each fundamental order peak is the area under each peak, which is calculated by:

$$c_{ct,0} = -\frac{b_{ct,0}}{a_{ct,0}} = \frac{R_{ct}}{a_v l} \quad (36)$$

$$c_{f,0} = -\frac{b_{f,0}}{a_{f,0}} = \frac{R_f}{a_v l} \quad (37)$$

These two equations lead to another essential conclusion: even if the DRT spectrum of the porous electrode shows a certain complicated dispersion pattern, the main and also the most prominent peak which can be detected in the DRT spectrum will only be decided by the specific resistance of the particle and the total interfacial area between liquid and solid phase and will not be influenced by the electrode transport parameters. This is exactly the same as the case for the single particle model (SPM), where the total electrode impedance is calculated by scaling the local particle impedance using the interfacial area and electrode thickness:

$$Z_{c,SPM} = \frac{Z_{loc}}{a_v l} \quad (38)$$

By combining Eq. (18), (19), (26) and (27), it can be observed that the magnitudes of dispersion peaks decrease with increasing order  $n$ . For the electrodes of LIBs,  $\sigma > \kappa$  is generally valid, especially for the anodes,  $\sigma \gg \kappa$  generally holds, hence, Eq. (26) and (27) can be approximated as:

$$b_{ct,n} \approx \frac{2\alpha(a_{ct} \tau_f + 1)^2 (a_{ct} \tau_{ct} + 1)^2}{n^4 \pi^4 \kappa [R_{ct} \tau_{ct} (a_{ct,n} \tau_f + 1)^2 + R_f \tau_f (a_{ct,n} \tau_{ct} + 1)^2]} \quad (39)$$

$$b_{f,n} \approx \frac{2\alpha(a_{f,n} \tau_f + 1)^2 (a_{f,n} \tau_{ct} + 1)^2}{n^4 \pi^4 \kappa [R_{ct} \tau_{ct} (a_{f,n} \tau_f + 1)^2 + R_f \tau_f (a_{f,n} \tau_{ct} + 1)^2]} \quad (40)$$

Recalling that according to Eq. (32) and (33), the characteristic dispersion time constants decrease with increasing order, the magnitudes of dispersion peaks drop even more drastically with increasing order. When  $\kappa \approx \sigma$ , Eq. (26) and (27) can be approximated as:

$$b_{ct,n} \approx \begin{cases} 0 & \text{for odd } n \\ \frac{2\alpha(a_{ct} \tau_f + 1)^2 (a_{ct} \tau_{ct} + 1)^2}{n^4 \pi^4 \kappa \sigma [R_{ct} \tau_{ct} (a_{ct,n} \tau_f + 1)^2 + R_f \tau_f (a_{ct,n} \tau_{ct} + 1)^2]} & \text{for even } n \end{cases} \quad (41)$$

$$b_{f,n} \approx \begin{cases} 0 & \text{for odd } n \\ \frac{2\alpha(a_{f,n} \tau_f + 1)^2 (a_{f,n} \tau_{ct} + 1)^2}{n^4 \pi^4 \kappa \sigma [R_{ct} \tau_{ct} (a_{f,n} \tau_f + 1)^2 + R_f \tau_f (a_{f,n} \tau_{ct} + 1)^2]} & \text{for even } n \end{cases} \quad (42)$$

Eq. (41) and (42) imply that when the conductivities in solid and liquid phases are close to each other, the odd order of dispersion peaks will tend to disappear, the next observable dispersion peak is the 2nd order instead of the 1st order. In reality, if there is no observable dispersion, it can either be caused by high conductivity in both solid and liquid phases, or by the condition  $\kappa \approx \sigma$ . Since in most cases the 1st order dispersion peak can be detected more easily, we further define the ratio of the magnitude of the 1st order dispersion peak to the magnitude of fundamental order peak as the damping factor:

$$\beta = \frac{c_1}{c_0} \quad (43)$$

which is an important parameter characterizing the dispersion behavior. According to Eq. (39)–(42),  $\beta$  decreases with increasing  $\kappa$  and  $\sigma$ , indicating that the dispersion decays as the conductivity increases. If the conductivities in both liquid and solid phases are high enough or have close values, the magnitude of the dispersion peaks will be negligible and in practice there will be no observable dispersion. Thus they coincide with the SPM assumption, where both  $\kappa$  and  $\sigma$  are large enough to ensure that the distributed features in the electrode caused by the transport process can be neglected. The model analysis above also applies to the case with a ZARC element, since both models have a similar derivation process and model structure.

Regarding the model analysis on the ZARC element, another essential conclusion can be made: when the active material particle shows a CPE-type dispersion for a particular reason such as impurities in the electrolyte or particle surface inhomogeneity, the CPE behavior will be directly reflected by the most prominent peak or the fundamental order peak in the DRT spectrum, and will not be interfered with by the distributed features of the porous electrode. This conclusion implies on the one hand that it is possible to evaluate the polarization resistance and relaxation times of the electrochemical processes on the microscopic level based on measured cell EIS and on the other hand that by investigating the DRT spectrum we can determine whether CPE-type behavior exists in the solid phase particles. In the next section, an optimized DRT data analysis framework based on the conclusions made above will be proposed to better interpret the DRT spectrum.

2.5. Adaptive peak analysis method (APAM)

As discussed in the last section, the fundamental order peak, i.e., the peak with the largest magnitude, will provide us with the necessary information about the local microscopic process, which can be either described using RC or ZARC elements. In practical applications, the calculated DRT spectrum often consist of a series of overlapping peaks, thus the peak parameters cannot be simply read or calculated. As a result, a proper peak separation must be conducted by assuming an

appropriate fitting function for each possible peak and then a nonlinear curve fitting must be performed. Common candidate functions for peak analysis with a relatively clear physical meaning include Gaussian functions and skewed Gaussian functions [59]. In Section 2.2 and Section 2.3 we have also shown that application of the DRT function of a ZARC element to peak fitting has a clear physical meaning. It has been shown that  $L_2$  regularization can be understood as imposing a Gaussian prior on the solution, a skewed Gaussian function is used when the impedance data is limited and the spectrum peak has a certain skewness, which usually occurs when it comes close to the frequency limit [30]. As for circuit elements like fractal-elements, Gerischer-elements etc. which thus far have not been assigned a clear physical meaning, we exclude them from the library of peak fitting candidate functions. Based on the reasons and assumptions given above, we have chosen to include Gaussian functions, skewed Gaussian functions and DRT functions of a ZARC element in the function library.

After deciding candidates, the steps followed to find optimal decomposition to individual functions are given below:

- The input DRT spectrum is normalized to set the highest data point to 1.
- Possible peak locations in the DRT spectrum are detected using a 2nd derivative by Savitzky-Golay filter and a non-optimization based algorithm (MATLAB's *findpeaks* function).
- Then, the operator visually inspects the output of the previous step to see if any peaks are missed or wrongly located.
- After the peak locations have been selected, the candidate functions to be fitted for each peak are selected. In our case, we select skewed Gaussian for first and last peaks, and both Gaussian and DRT function of ZARC element for the peaks in between.
- Then the data, unknown parameters and a warm-start for these unknown parameters are passed with an appropriate objective function (Eq. (44)) to a global solver (here, MATLAB's *GlobalSearch* function), which perturbs the warm-start points to avoid local optima.
- The output of the global solver is then passed to a local solver (here, MATLAB's *fmincon*) which tries to find a local optimum according to the same objective function (Eq. (44)).
- It should be noted that only the nonlinear parameters (e.g.,  $\phi$ ,  $\mu$ , skewness etc.) are the decision variables for local and global solvers. After deciding these parameters, heights can be found using the linear least squares algorithm (here, MATLAB's *lsqnonneg* function). Also, since we need to select only one peak per candidate function, all candidate functions belonging to the same peak share the same peak location ( $\mu$ ) parameter.
- Then, only the candidate with the maximum height for each peak is selected while the other candidates are discarded. The fitness of the estimated data points is evaluated using a cost function and the cost is fed to the local solver. Lastly, the final decision of the local solver and its cost value is fed to the global solver to decide the next set of initial values.

The cost function is given by the following equation:

$$J = \gamma_1 \|y - \hat{y}\|_2^2 + \gamma_2 \|h_{\min}\|_1 + \gamma_3 \|h_{\min}\|_2^2 + \gamma_4 \|A\|_2^2 \quad (44)$$

where  $y$  is the set of actual (normalized) data points,  $\hat{y}$  is the set of estimated data points,  $h_{\min}$  are height values for candidates except the candidate with maximum height and  $A$  denotes the area under each peak candidate (only for candidates with maximum height for each peak). Lastly,  $\gamma_i$  values are the weight factors in the cost function that are found by trial and error.

### 3. Results and discussion

In this section, the developed model and theory will be applied to synthetic impedance data generated using assumed parameters;

then the impedance data of a commercial LIB will be analyzed to derive some fundamental parameters describing the microscopic electrochemical processes. The data processing steps are summarized as follows:

1. DRT analysis: the DRT analysis is conducted to remove the inductive part in order to obtain the ohmic resistance and the DRT spectrum of the LIB.
2. Peak analysis: the developed APAM is applied to find the location, magnitude and functional form of each separated peak.
3. Electrochemical parameters are calculated based on the peak parameters, peaks are attributed to the corresponding electrode as well as processes.

#### 3.1. Validation with synthetic impedance data

In this section, simulations with synthetic impedance data will be conducted to validate the proposed model. Two sets of synthetic impedance data are generated that correspond to two cases: (1) low  $\sigma$  and  $\kappa$ ,  $\sigma \gg \kappa$ ; (2) high  $\kappa$  and  $\sigma$ ,  $\sigma \gg \kappa$ . Case 1 generally represents the electrodes with a limited electronic conductivity, for example, the LFP electrode, or degraded electrodes with a reduced electrical and electronic conductivity; case 2 generally represents the electrodes with a high electronic conductivity, like the graphite anode. To ensure general applicability, instead of RC elements, ZARC elements are used for particle impedance, and a measurement noise is added to the generated synthetic impedance:

$$Z_e^{\text{measured}} = Z_e^{\text{synthetic}} + \varepsilon X Z_e^{\text{synthetic}} \quad (45)$$

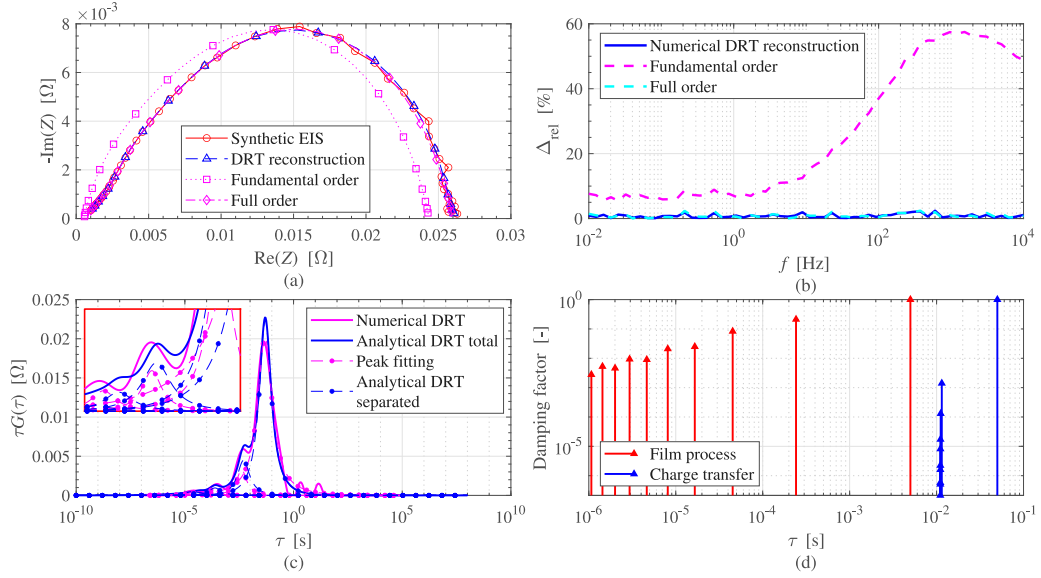
where  $\varepsilon$  is the noise level and is set to be 1% according to the measurement accuracy of the test equipment used later to measure the cell impedance.  $X$  is a normally distributed random variable, i.e.,  $X \sim \mathcal{N}(0,1)$ . In addition, to demonstrate the advantages and effectiveness of the DRT for parameter estimation, an ECM with two serially connected ZARC elements (see Eq. (6)) is created with MATLAB to fit the impedance data and to extract the cell parameters, then the extracted parameters will be compared with the results from the DRT and APAM. For the ECM fitting, the possible numbers and locations of peaks are first estimated from the DRT spectrum and set as the initial values for the fitting program, then the optimization program using the embedded toolbox *Multistart* in MATLAB is run once to estimate the parameters. To increase the possibility of finding the optimal solution, the number of starting points is set to 100. The electrode parameters used in synthetic simulation experiments are listed in Table 2.

The frequency range for generating the impedance is 10 mHz~100 kHz with 10 points per decade. For reconstruction of the impedance with the derived analytical DRT spectrum, we choose to use the fundamental order peaks (P0) and the fundamental order peaks plus the first 1000 order harmonics (P1000). Practically, as the coefficients of harmonics generally decay to 0 after the 10th order, (P0 + P1000) can essentially be regarded as the exact spectrum.

The results for case 1 are shown in Fig. 1. In Fig. 1, the generated synthetic impedance is compared with the reconstructed impedance using different methods. For impedance reconstruction with only fundamental order peaks, a clear deviation from the reference impedance can be observed that occurs mainly in the high frequency range. This observation coincides with the proposed theory that the dispersion occurs in the direction of smaller time constants or higher frequencies. Compared to fundamental order reconstruction, both analytical DRT and numerical DRT can precisely reconstruct the reference impedance with a relative error less than 2% across the whole frequency range (see Fig. 1b). The reconstruction error is believed to be mainly caused by the measurement noise, without noise the error should be much lower. In Fig. 1c the numerically deconvolved DRT spectrum is shown together with the analytical DRT, where a minor deviation can be seen, which is probably caused by the biased nature of the regularization

**Table 2**  
Electrode parameters for synthetic simulation experiments.

Parameter	$R_{ct}$ [ $\Omega$ m <sup>2</sup> ]	$R_f$ [ $\Omega$ m <sup>2</sup> ]	$\tau_{ct}$ [s]	$\tau_f$ [s]	$\phi_1$	$\phi_2$	$l$ [ $\mu$ m]	$\sigma$ [S/m]	$\kappa$ [S/m]	$a_v$ [1/m]
Case 1:	0.5	0.1	$5 \times 10^{-2}$	$5 \times 10^{-3}$	0.8	0.8	60	0.1	0.01	$4.2 \times 10^5$
Case 2:	0.5	0.1	$5 \times 10^{-2}$	$5 \times 10^{-3}$	0.8	0.8	60	100	1	$4.2 \times 10^5$



**Fig. 1.** Simulation and analysis results for case 1. (a): generated and reconstructed impedance, (b): relative impedance reconstruction error, (c): analytic DRT spectrum compared with the numerical calculated DRT spectrum, together with the separated peaks using APAM, (d): damping factors for charge transfer and SEI process.

**Table 3**  
Comparison of estimated parameters with reference parameters for case 1.

Parameter	$R_{ct}$ [ $\Omega$ m <sup>2</sup> ]	$R_f$ [ $\Omega$ m <sup>2</sup> ]	$\tau_{ct}$ [s]	$\tau_f$ [s]	$\phi_1$	$\phi_2$
Reference:	0.5	0.1	$5 \times 10^{-2}$	$5 \times 10^{-3}$	0.8	0.8
Estimated:	0.58	0.066	$4.83 \times 10^{-2}$	$4.1 \times 10^{-3}$	0.74	0.81

method and the measurement noise. Two main peaks with the time constants  $4.83 \times 10^{-2}$  s and  $4.1 \times 10^{-3}$  s can be observed, which represent the charge transfer and SEI processes respectively. Apart from the two dominant peaks representing the two corresponding processes, two smaller peaks with time constant  $2.34 \times 10^{-4}$  s and  $3.16 \times 10^{-5}$  s can be observed. By comparing the peak location and magnitude as well as the damping factor as shown in Fig. 1d, we can conclude that these peaks represent the 1st and 2nd order harmonics of the film process. According to Fig. 1d, the magnitudes of the 1st and 2nd order harmonic are approximately 0.28 and 0.1 times that of the main peak so that they remain observable. Further higher order harmonics cannot be clearly resolved because of the regularization algorithm used and the measurement noise. Furthermore, the existence and observability of higher order harmonics in the deconvolved DRT spectrum implies that the electrode may suffer from aging effects which lead to degraded transport parameters in both solid and liquid phases. In addition, a few small peaks with the time constant greater than 1 s are observed, we believe that these peaks are rather attributable to the wider DRT spectrum of ZARC elements than to the noise. The original peak is splitted into a dominant peak and a few smaller peaks, which may be caused by nonoptimal regularization parameters and inversion algorithms, thus justifying the importance of more advanced inversion techniques.

The model parameters calculated for case 1 using the APAM are listed in Table 3. It can be readily seen that most parameters are estimated with a minor error except the SEI resistance, we assume

that the slightly higher error is probably caused by the smaller value of SEI resistance and the regularization process. The parameters calculated using ECM are not listed here because after repeated trials no satisfactory solutions have been found; we have also found that only when the initial values are set to be very close to the optimal solutions, the optimization algorithm can possibly converge to the reference solution. However, on the one hand, in practical applications many peaks can overlap, which makes it extremely difficult to obtain a reasonable initial guess for resistance value and time constant; on the other hand, the measurement data is usually exposed to noise, which will further deteriorate the fitting quality of ECM and highlight the existing under/over-fitting and parameter sensitivity problems.

The results for case 2 are shown in Fig. 2a in which no significant impedance deviation can be observed for fundamental order reconstruction, because in this case dispersion is almost negligible. Although the relative error of impedance reconstruction using a fundamental order peak approaches 30% towards the higher frequency limit, the absolute error is scarcely observable. Instead of many peaks, there are only two observable dominant peaks in the deconvolved DRT spectrum (see Fig. 2c), which fulfills the theoretical prediction that the magnitude of the 1st order harmonic is already smaller than 0.3% of the main peak (see Fig. 2d). Again the smaller peaks with the time constant greater than 1 s are assumed to be attributed to the ZARC element. The calculated model parameters are listed in Table 4, all parameters show a minor deviation from the reference values except the SEI resistance, the deviation may be caused by both the regularization and the noise.

To analyze the dispersion phenomenon in a more straightforward way and relate it to the electrode transport parameters, the logarithmic damping factor  $\log_{10}(\beta)$  (see Eq. (43)) for charge transfer and film process are calculated and plotted in Fig. 3a and b respectively against the solid phase conductivity  $\sigma$  and the ratio  $\kappa/\sigma$ . For the computation, all parameters are kept the same as in case 1 and 2 with the exception of  $\sigma$  and  $\kappa$ .

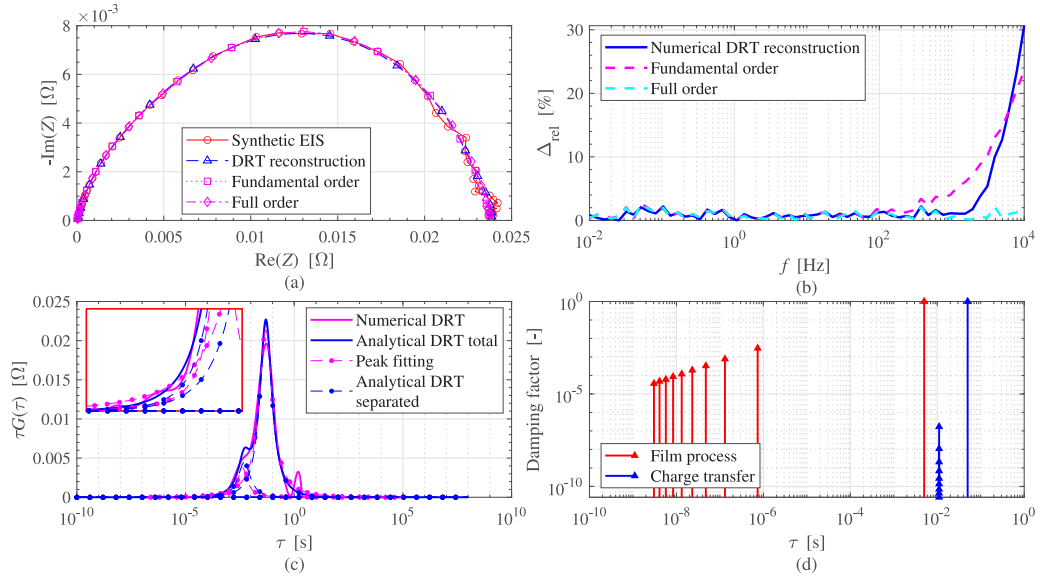


Fig. 2. Simulation and analysis results for case 2, (a): generated and reconstructed impedance, (b): relative impedance reconstruction error, (c): analytic DRT spectrum compared with the numerical calculated DRT spectrum, together with the separated peaks using APAM, (d): damping factors for charge transfer and SEI process.

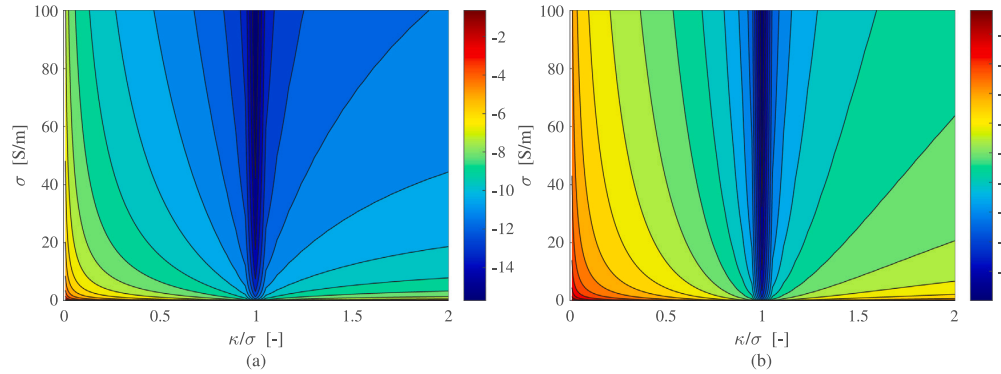


Fig. 3. Logarithmic damping factors for (a): charge transfer and (b): film process against  $\sigma$  and  $\kappa/\sigma$ .

Table 4  
Comparison of estimated parameters with reference parameters for case 2.

Parameter	$R_{ct}$ [Ω m <sup>2</sup> ]	$R_f$ [Ω m <sup>2</sup> ]	$\tau_{ct}$ [s]	$\tau_f$ [s]	$\phi_1$	$\phi_2$
Reference:	0.5	0.1	$5 \times 10^{-2}$	$5 \times 10^{-3}$	0.8	0.8
Estimated:	0.56	0.072	$4.92 \times 10^{-2}$	$4.2 \times 10^{-3}$	0.76	0.81

According to Fig. 3, when  $\kappa < \sigma$ ,  $\beta$  decreases with increasing  $\sigma$  and  $\kappa/\sigma$ ,  $\kappa/\sigma$  has a more prominent role than  $\sigma$ . Especially when  $\sigma \approx \kappa$ , the damping factor is approximately 0 irrespective of the values of  $\sigma$ , exactly as predicted by Eq. (41) and (42). When  $\kappa > \sigma$  (not normally valid for LIBs), the damping factor starts to increase with increasing  $\kappa/\sigma$ , but still decreases with increasing  $\sigma$ . From Fig. 3 we can also see that the dispersion phenomenon in the DRT spectrum is more likely to be caused by the film process than charge transfer.

### 3.2. Application to commercial LIB

In this section, the developed theory is applied to a commercial LIB, the DRT spectrum will be evaluated and a few fundamental physico-chemical parameters, including the area-specific SEI resistance and capacitance, the reaction rate constant and the corresponding activation energy will be estimated.

#### 3.2.1. Experimental

The commercial cell used in this work is a 3.35 Ah NMC-811/SiC LIB (INR18650-MJ1, LG Chem), which has been comprehensively parametrized and investigated by Sturm et al. [60]. The cell impedance was measured at 4 temperatures: 10 °C, 20 °C, 30 °C and 40 °C, at each temperature the impedance was measured at 11 SOC levels: 5%, 10%, 15%, 20%, 25%, 45%, 65%, 85%, 90%, 95% and 100%, and it was measured during cell discharging process.

To ensure a correct attribution of the peaks to the corresponding processes, another cell from the same production lot was fully discharged and then opened in an argon-filled glove-box, a piece of anode and a piece of cathode with a diameter of 14 mm were punched out of the anode and cathode respectively. Then each electrode sample

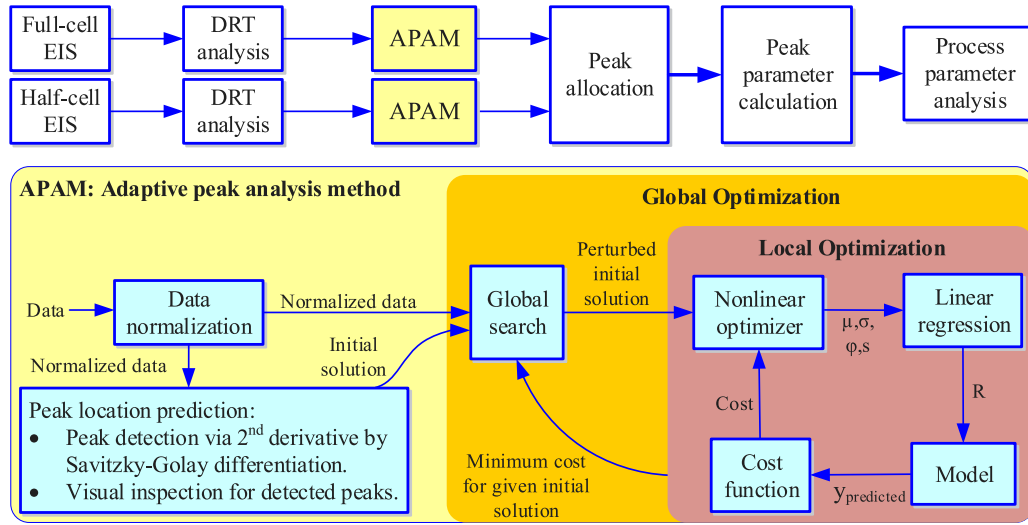


Fig. 4. Measurement data processing routines.

was assembled together with two pieces of glass fiber separator and a lithium-metal counter-electrode into a CR2032 type coin cell. The assembly also includes two aluminum spacers to achieve better electrical contact. Each half cell assembly was filled with 90  $\mu\text{L}$  of 1M LiPF<sub>6</sub> in 3:7 (wt:wt) ethylene carbonate (EC)/ethyl methyl carbonate (EMC) electrolyte (99.9% purity, Solvionic). The assembled coin cells were then rested for 24 h and subjected to two conditioning cycles. Subsequently the cell voltage of the coin cell with the anode was adjusted to ca. 0.294 V, the cell voltage of the half cell with the cathode was adjusted to ca. 3.60 V, the lithiation state in both half cells should correspond to 10% SOC of the full cell. The impedance of the half cells was measured at 20 °C. The 20 °C and 10% SOC were chosen because under this condition all peaks had similar height and could be well separated.

All impedance measurement was performed on an electrochemical workstation (VMP3, Biologic) and in a climate chamber (MKF, Binder). The frequency range was 10 mHz–10 kHz for full cell and 10 mHz–100 kHz for half cell.

### 3.2.2. Data processing

In this section the steps for measurement data processing will be introduced. After the impedance is measured, the impedance data is subjected to the following data processing routine: first the DRT analysis is conducted and the deconvolved DRT spectrum is acquired. Then the DRT spectrum is processed using the developed APAM in order to separate the contribution of respective processes. In the next step, the peak attribution is conducted using the coin cell impedance. Subsequently, the peak parameters are calculated and plotted against electrode stoichiometry/SOC and temperature, finally the results are analyzed. The detailed routines are summarized in Fig. 4.

### 3.2.3. Peak attribution

In this section, the peaks of the DRT spectrum will be attributed to different processes by comparing the results of the full cell with that of the half cells. The comparison of the normalized DRT spectra of the half and full cell are shown in Fig. 5a and b. The DRT spectra of the full cell at all SOCs and temperatures are shown in Fig. 5c–f. The relevant peaks in the DRT spectra of full cell are marked with P1–P4.

In Fig. 5b, all peaks of the anode DRT spectra are marked with A1–A4. By comparing the DRT spectra of the full cell with half cell of the anode, it can be concluded that all peaks with the time constant of  $\tau$

> 0.01 s should be correlated with the processes in the cathode. The peak A3 is much higher than the neighboring peaks, considering that the Lithium-metal counter electrode has a relatively smooth surface and no porous structure, the SEI layer formed on the Lithium-metal should have a much higher resistance because the interfacial area is much smaller than that of the porous SiC material. So we attribute peak A4 and P3 to the charge transfer in the anode, A3 and P2 to the SEI process. The peak A2 has a time constant of ca.  $3 \times 10^{-5}$  s and has nearly no SOC dependence (see Fig. 5c–f), therefore it is attributed to the contact resistance between the active material and the current collector, this phenomenon has also been reported by Nara et al. and Illig et al. [53,61]. It is worth noticing that the peaks A1 and C1 appear in the half cell spectra with similar time constants, we believe that this may be caused by the half cell assembling process, where possible new contact surface was formed. The peak attribution is summarized as follows:

- A1: new contact surface formed during cell assembly
- A2: contact surface between active material and current collector
- A3: SEI layer
- A4: anode charge transfer

In Fig. 5a, all peaks of the cathode DRT spectra are marked with C1–C7. The peak C3 has similar time constant to that of the peak A3 and P2 and is much higher than the neighboring peaks, therefore C3 is attributed to the SEI process of the Lithium-metal counter electrode. The peak C2 has a similar time constant to that of A2 and P1, so it is attributed to the contact resistance between the active material and the current collector. The peaks C5–C7 can be only observed in the spectra of the cathode, naturally they are attributed to the processes in the cathode. It can be seen that the peaks C6–C7 have a asymptotically decreasing magnitude (possibly a further smaller peak between C5 and C6, but overshadowed) and relatively higher time constants. This can be attributed to the diffusion process in the solid or liquid phase [36,62]. Between peak C3 and C5 a small peak C4 can be observed, we assume that this peak can be either caused by the cathode electrolyte interphase (CEI) formed during the half cell preparation process [45], or by the Lithium-metal counter electrode. Although the peak C4 has a similar time constant to that of the anode charge transfer, the possibility that this peak is caused by the anode charge transfer can be excluded because this peak has been observed in the spectra of the half cell with the anode. The peak attribution is summarized as follows:

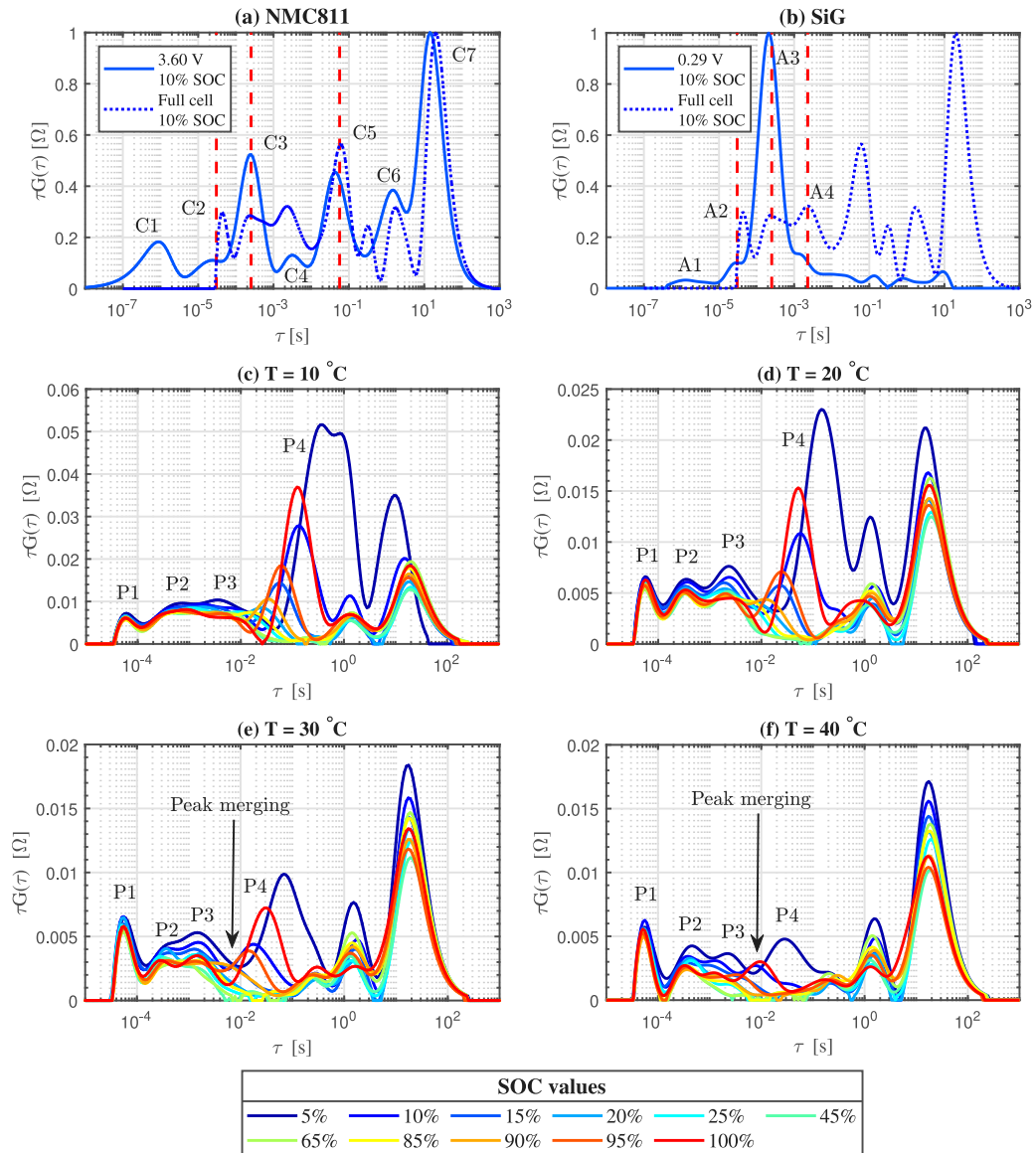


Fig. 5. Evaluation of half cell and full cell EIS measurement results and the comparison of half cell with full cell. (a): comparison of the DRT spectra of full cell with that of the half cell of cathode; (b): comparison of the DRT spectra of full cell with that of the half cell of anode; DRT spectra of full cell at (c): 10 °C, (d): 20 °C, (e): 30 °C and (f): 40 °C. The four investigated peaks in the mid-high frequency area are marked with P1, P2, P3 and P4.

- C1: new contact surface formed during cell assembly
- C2: contact surface between active material and current collector
- C3: SEI layer
- C4: CEI or contribution from the Lithium-metal counter electrode
- C5: cathode charge transfer
- C6–C7: solid or liquid phase diffusion in the cathode

Finally, the peak attribution for the full cell is summarized as follows:

- P1: contact surface between active material and current collector
- P2: SEI layer
- P3: anode charge transfer
- P4: cathode charge transfer

### 3.2.4. Evaluation of SEI process

In this section the evaluation results of the SEI process will be shown and interpreted. The calculated SEI resistance is shown in Fig. 6, here the area-specific resistance is used for analysis instead of the total resistance by scaling the total resistance with the total interfacial area (see Eq. (37)), which is taken from Strum et al. [60]. It can be observed that the SEI resistance shows a certain SOC dependence that it has a higher value when approaching the fully charged or discharged state and a lower value at the medium SOC values. Zhang et al. investigated the SEI resistance in dependence on the lithiation state and found out that the SEI resistance is correlated to the differential capacity, the SEI resistance has a higher value approaching the fully lithiated state and a lower value approaching the fully delithiated state [63]. Peled et al. investigated the structure of SEI layer using XPS and TOF-SIMS and also concluded that the SEI layer is thinner at delithiated state



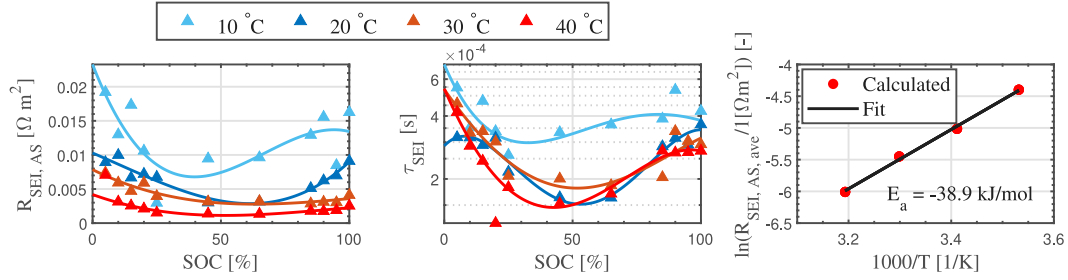


Fig. 6. Evaluation results for the SEI process. (a): The area-specific SEI resistance at different SOC and temperatures; (b): time constants of the SEI process at different SOC and temperatures; fitting of the SOC-averaged SEI resistance using the Arrhenius equation.

and thicker at lithiated state [64]. However in the present work we observe a higher SEI value at both the lithiated and the delithiated state, a similar behavior has also been reported by Ovejas et al. [65]. We assume that this phenomenon can be partly attributed to the silicon additive in the anode, because the “shortcut” of the Li-ions through the SEI layers (cracks) will be blocked due to the particle shrinking caused by the volume change at the fully delithiated state, as reported by Pan et al. [50]. On the other hand, some extra SEI materials will be pushed out to form a secondary SEI layer, which may lead to a decreased SEI porosity, thus hindering the diffusion of Li-ions through the SEI layer [66]. The SOC dependence of the SEI resistance is less pronounced at elevated temperatures, due to thermally activated transport and kinetic processes. The time constant of the SEI process is shown in Fig. 6b, a similar SOC dependence can be observed, at elevated temperatures (20–40 °C) only a minor temperature dependence can be seen. To evaluate the temperature dependence of the SEI resistance, the SEI resistance at each SOC is averaged over the SOC and the results are plotted in Fig. 6c. The Arrhenius equation is applied to the data and a clear linear relationship can be observed, the activation energy is calculated to be 38.9 kJ/mol, which is similar to the values derived by Yao et al. and Suresh et al. [67,68].

### 3.2.5. Evaluation of charge transfer process

In this section the evaluation results for the charge transfer process will be introduced and analyzed, the calculated exchange current density will be fitted to derive further physicochemical parameters. The results for the charge transfer process are shown in Fig. 7. To better investigate the charge transfer parameters, the exchange current density is used instead of the charge transfer resistance:

$$i_0 = \frac{RT}{A_{\text{cell}} a_v I R_{v,ct} F} \quad (46)$$

where  $A_{\text{cell}}$  is the total cross-sectional area of the electrode,  $R_{v,ct}$  is the volumetric charge transfer resistance calculated by the DRT and APAM,  $F$  is the Faraday constant,  $R$  is the gas constant. The SOC values are transformed into the electrode stoichiometry by using the cell balancing parameters derived in the work of Sturm et al. [60]. The exchange current density can be modeled using the following equation:

$$i_0 = Fk(c_{s,\text{max}} - c_s)^{\alpha_c} (c_s)^{\alpha_a} (c_l)^{\alpha_a} \quad (47)$$

where  $k$  is the reaction rate constant,  $c_{s,\text{max}}$  is the maximum solid phase concentration,  $c_s$  is the solid phase concentration,  $c_l$  is the liquid phase concentration, and  $\alpha$  is the charge transfer coefficient and is assumed to be 0.5 in this work. If we substitute  $\chi = c_s/c_{s,\text{max}}$  into the above equation, the following equation can be obtained:

$$i_0 = Fkc_{s,\text{max}}(1 - \chi)^{\alpha_c} (\chi)^{\alpha_a} (c_l)^{\alpha_a} \quad (48)$$

where  $\chi$  is the stoichiometry of the electrode,  $c_{s,\text{max}}$  is assumed to be 34684 mol/m<sup>3</sup> for the anode and 50060 mol/m<sup>3</sup> for the cathode; here the  $\chi$  value at any SOC can be calculated using the  $\chi$  value at 0% and

100% SOC [60]. We use the above-derived equation to fit the exchange current density and derive the reaction rate constant.

It is worth noticing that in the course of evaluating the charge transfer resistance from the DRT spectra, at elevated temperatures the peak P4 is gradually shifted to the lower time constant area at the medium SOC state and finally merge with the peak P3 (see Fig. 5e–f). At first an attempt is made to separate the peaks by reducing the regularization parameter; however, both peaks stay inseparable, a further reduced regularization parameter leads to invaluable DRT spectrum. This phenomenon also implies that simply applying the ECM to evaluate the DRT spectrum may cause parameter non-identifiability problem and lead to erroneous results. In this work we propose a method to estimate the parameters of the inseparable peaks by combining the DRT spectrum and the fitting equation for the exchange current density. The method assumes that the exchange current density for the anode and cathode is modeled using Eq. (48) and the sum of the volumetric charge transfer resistance for the anode and cathode should be equal to the value derived from the DRT spectrum, then the curve fitting problem can be transformed into the following optimization problem:

$$\theta(k_n, k_p, R_{v,ct,j}) = \underset{\theta > 0}{\text{argmin}} \left\{ \sum_{i=1, i \neq i_{ni}}^N \left[ i_{0,n,i} - \frac{RT}{A_{\text{cell}} a_{v,n} I_n R_{v,ct,n,j} F} \right]^2 + \sum_{i=1, i \neq i_{ni}}^N \left[ i_{0,p,i} - \frac{RT}{A_{\text{cell}} a_{v,p} I_p R_{v,ct,p,j} F} \right]^2 + \sum_{j=n_i} \left[ i_{0,n,j} - \frac{RT}{A_{\text{cell}} a_{v,n} I_n R_{v,ct,n,j} F} \right]^2 + \sum_{j=i_{ni}} \left[ i_{0,p,j} - \frac{RT}{A_{\text{cell}} a_{v,p} I_p R_{v,ct,p,j} F} \right]^2 \right\} \quad (49)$$

subjected to the constraint:

$$R_{v,ct,n,j} + R_{v,ct,p,j} = R_{v,ct,\text{total},j} \quad (50)$$

where  $i$  indicates the index for all identifiable separated peaks,  $N$  is the total number of identifiable cases,  $i_{ni}$  is the index for the non-identifiable cases. When peak P3 and P4 are inseparable, we assume that they have the same time constant. The fitting results are shown in Fig. 7. It can be seen that the overlapping peaks can be effectively separated and the peak parameters are close to the predicted values. Nevertheless, it is worth mentioning that all data points can be fitted with a good quality except the data points for cathode at the lower delithiated state and at each temperature, the measurement data tend to lie below the predicted value, namely, the cathode charge transfer resistance is for some reason overestimated. We believe that this overestimation is caused by the interaction of the cathode charge transfer with the diffusion process. Boukamp et al. investigated the DRT spectrum for solid diffusion and derived an analytical expression for the DRT spectrum [36]. The derived theory indicates that the DRT spectrum of the Warburg impedance shows a certain dispersion pattern, a series of peaks with decreasing time constant and magnitude are generated in the DRT spectra, which

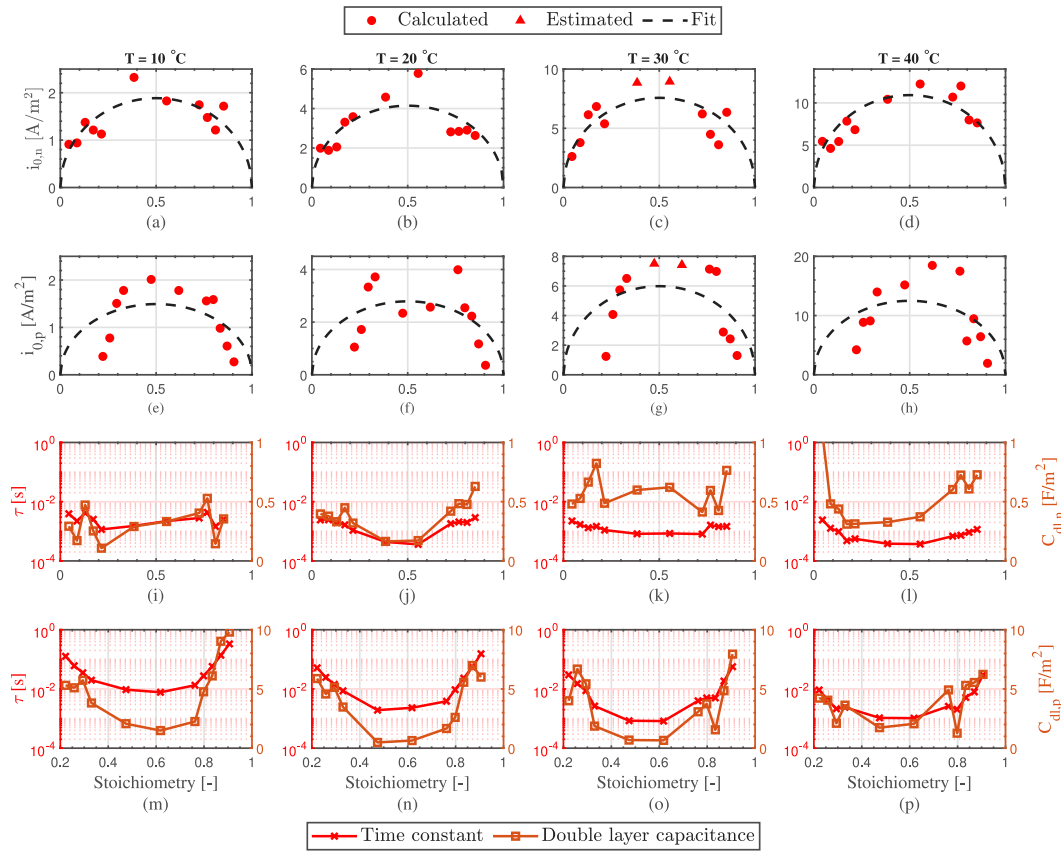


Fig. 7. Exchange current density of negative (first row) and positive (second row) electrode calculated with APAM at different lithiation state and temperature. Calculated area-specific double layer capacitance and the charge transfer time constant for the anode (third row) and cathode (fourth row).

can very likely overlap with the cathode charge transfer peak and lead to an overestimated charge transfer resistance. This interaction phenomenon can also be clearly observed in Fig. 5c–f, this behavior is more pronounced at lower temperatures because the charge transfer is more sluggish and has larger time constant. For the liquid phase diffusion a similar dispersion behavior is also expected [62].

The calculated double layer capacitances and charge transfer time constants for anode and cathode are plotted in Fig. 7i–p. It can be observed that the time constants of both electrodes have a higher value when approaching the fully lithiated/delithiated state and decrease gradually at elevated temperature, the time constant of the cathode charge transfer also shows a stronger SOC dependence than that of the anode, which can be readily seen in Fig. 5 as well. The double layer capacitance of the anode varies only slightly with both the SOC and the temperature and has an average value of approximately 0.5 F/m<sup>2</sup>. The double layer capacitance of the cathode shows a stronger SOC dependence but nearly no temperature dependence.

To investigate the temperature dependence of the charge transfer, the estimated reaction rate constant is fitted using the Arrhenius equation and the results are plotted in Fig. 8. The estimated reaction rate constants range from ca.  $2.9 \times 10^{-11}$  to  $2.8 \times 10^{-10}$  m/s. At room temperature (25 °C), the reaction rate constant for the NMC811 is approximately  $5.63 \times 10^{-11}$ , which agrees very well with the value measured by Chowdhury et al. [69]. The calculated activation energy for the anode and cathode is 43.5 kJ/mol and 52.5 kJ/mol respectively. For graphite anode similar values of 45–60 kJ/mol have been reported by

Smart et al. [70] depending on the electrolyte composition. For NMC811 no data for charge transfer activation energy has been found in the literature, a value of 57–69 kJ/mol is reported by Keefe et al. for an NMC532 electrode [71]. The measured activation energy depends strongly on the material used, the test procedure and even the electrolyte.

#### 4. Conclusions

In this work, a new theory is proposed to characterize the cell parameters and extract the useful information in a more effective way. The developed theory indicates that when considering the distributed nature of the electrode caused by transport phenomena in solid and liquid phases, the fundamental order peaks of the deconvolved DRT spectrum are only decided by the local particle impedance and electrode geometric parameters (thickness, cross-sectional area, particle size etc.). Therefore, the fundamental peaks can be applied to investigate the microscopic processes related to solid particles. Besides the fundamental order peaks, the dispersion peaks exist due to the distributed nature of the electrode. The dispersion occurs in the direction of decreasing time constants and magnitude. Especially when the conductivities in the solid and liquid phases have similar values or become high enough, no dispersion phenomenon can be observed in practice, which coincides with the single particle assumption, according to which the transport process in the liquid phase is simply neglected. Based on the developed theory, an adaptive peak analysis method is proposed to better interpret the deconvolved DRT spectrum. The proposed theory and model are

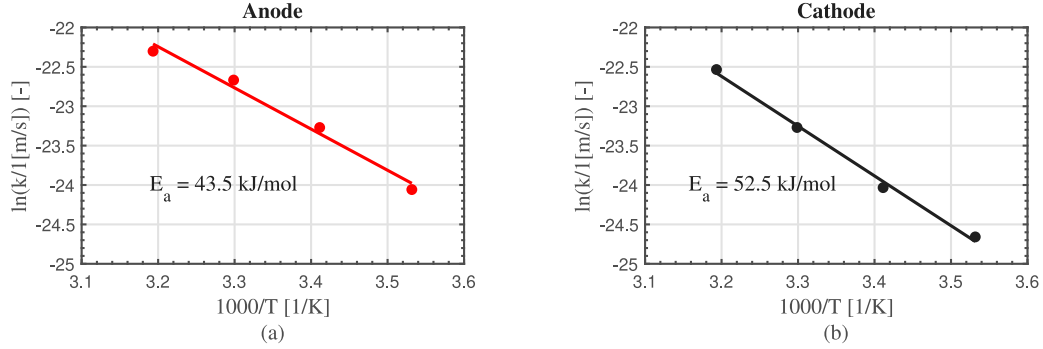


Fig. 8. Arrhenius plot for reaction rate constant of charge transfer reaction in the (a): anode and (b): cathode.

then applied to a commercial cell to demonstrate its advantage and effectiveness. The results indicate that the SEI resistance exhibits a more obvious SOC dependence at lower temperatures, while at higher temperatures only slight SOC dependence can be observed. The SEI resistance also shows an obvious temperature dependence and can be well fitted by Arrhenius equation. The kinetic reaction rate constant for both the anode and cathode at various temperatures can be well fitted using the Arrhenius equation, revealing that the charge transfer process can be assumed to generally obey the Arrhenius equation.

In our future work, we will further work on applying the DRT spectrum to the characterization of the diffusion phenomenon in the solid and liquid phase with a physics-based impedance model. Also the possibility of using mixed-integer programming approaches [72,73] to select candidate functions for peak fitting and verify the optimality of the selection will be investigated.

#### CRedit authorship contribution statement

**Yulong Zhao:** Conceptualization, Methodology, Software, Investigation, Validation, Data curation, Formal analysis, Writing – original draft, Project administration. **Volkan Kumtepe:** Software, Formal analysis, Writing – original draft, Writing – review & editing. **Sebastian Ludwig:** Investigation, Writing – review & editing. **Andreas Jossen:** Supervision, Writing – review & editing.

#### Declaration of competing interest

The authors declare that they have no known competing financial interests or personal relationships that could have appeared to influence the work reported in this paper.

#### Acknowledgment

This research is funded by the China Scholarship Council (CSC), the author gratefully thanks for the support and funding from CSC.

#### Appendix. Derivation of impedance model

The p2D model describes the transport processes in electrodes with a series of partial differential equations [37–39]. The model equations are transformed into the frequency domain using the Fourier transformation. All variables in the frequency domain are marked with a tilde sign. By further assuming that in mid-high frequency range liquid phase diffusion can be neglected and that the liquid phase current is driven only by ionic conduction, the model equations can be simplified and summarized as follows:

$$\tilde{i}_l = -\kappa \frac{d\tilde{\phi}_l}{dx} \quad (\text{A.1})$$

$$\frac{d\tilde{i}_l}{dx} = a_v \tilde{j}_{loc} \quad (\text{A.2})$$

$$\sigma \frac{d^2 \tilde{\phi}_s}{dx^2} = a_v \tilde{j}_{loc} \quad (\text{A.3})$$

where  $i_l$  is the liquid phase current density,  $\phi_l$  and  $\phi_s$  are potentials in the liquid and solid phase respectively,  $\tilde{j}_{loc}$  is the local reaction current density and  $x$  is the spatial coordinate along the electrode thickness. The potentials in liquid and solid phase are related through the following equation:

$$\tilde{\phi}_l - \tilde{\phi}_s = Z_{loc} \tilde{j}_{loc} \quad (\text{A.4})$$

Then Eq. (A.1) is substituted into Eq. (A.2) and (A.3),  $\tilde{j}_{loc}$  is eliminated by using Eq. (A.4), and the resulting equations can be converted into matrix form:

$$\frac{d^2}{dx^2} \begin{bmatrix} \tilde{\phi}_l \\ \tilde{\phi}_s \end{bmatrix} = \begin{bmatrix} -m_{11} & m_{11} \\ m_{21} & -m_{21} \end{bmatrix} \begin{bmatrix} \tilde{\phi}_l \\ \tilde{\phi}_s \end{bmatrix} \quad (\text{A.5})$$

where  $m_{11} = a_v / (\kappa Z_{loc})$ ,  $m_{21} = a_v / (\sigma Z_{loc})$ . The matrix form can be further written as  $\mathbf{u}'' = \mathbf{A}\mathbf{u}$  where  $\mathbf{A}$  is the system matrix and  $\mathbf{u}$  is the unknown variable to be solved for. In order to solve the 2nd order system, the following block matrix is built:

$$\mathbf{M} = \begin{pmatrix} \mathbf{0} & \mathbf{I} \\ \mathbf{A} & \mathbf{0} \end{pmatrix} \quad (\text{A.6})$$

and the 2nd order system can be transformed into the following 1st order system:

$$\mathbf{v}' = \mathbf{M}\mathbf{v} \quad (\text{A.7})$$

$$\mathbf{v} = [\mathbf{u}, \mathbf{u}']^T \quad (\text{A.8})$$

It can be shown that the general solution of Eq. (A.5) has the following form:

$$\mathbf{u} = C_1 \mathbf{V}_1 + C_2 \mathbf{V}_1 x + C_3 \mathbf{V}_2 e^{\lambda_3 x} + C_4 \mathbf{V}_3 e^{\lambda_4 x} \quad (\text{A.9})$$

where  $\lambda$  is the eigenvalue of block matrix  $\mathbf{M}$  and  $\lambda_1 = \lambda_2 = 0$ ,  $C$  is the unknown coefficient,  $\mathbf{V}$  is  $\text{diag}(\mathbf{I}, \mathbf{0})\mathbf{W}$  and  $\mathbf{W}$  is the eigenvector of  $\mathbf{M}$ . The boundary conditions for  $\phi_l$  and  $\phi_s$  are:

$$x = 0 : \quad -\kappa \frac{d\tilde{\phi}_l}{dx} = 0, \quad \tilde{\phi}_s = 0 \quad (\text{A.10})$$

$$x = l : \quad -\kappa \frac{d\tilde{\phi}_l}{dx} = i_{app}, \quad -\sigma \frac{d\tilde{\phi}_s}{dx} = 0 \quad (\text{A.11})$$

where  $i_{app}$  is the applied current density. If the boundary conditions are substituted into Eq. (A.9), a linear equation system of unknown coefficients can be obtained. Note that  $\lambda_4 = -\lambda_3$ , the system can be solved to obtain the following solution:

$$C_1 = -\frac{i_{app} m_{21} (m_{21} + 2 m_{11} e^{\lambda_3 l} + m_{21} e^{2\lambda_3 l})}{\kappa \lambda_3 m_{11} (m_{11} + m_{21}) (e^{2\lambda_3 l} - 1)} \quad (\text{A.12})$$

$$C_2 = -\frac{i_{app} m_{21}}{\kappa (m_{11} + m_{21})} \quad (A.13)$$

$$C_3 = -\frac{i_{app} m_{21} (m_{21} + m_{11} e^{l\lambda_3})}{\kappa \lambda_3 m_{11} \sqrt{-m_{11} - m_{21}} (e^{2l\lambda_3} - 1)} \quad (A.14)$$

$$C_4 = \frac{i_{app} m_{21} e^{l\lambda_3} (m_{11} + m_{21} e^{l\lambda_3})}{\kappa \lambda_3 m_{11} \sqrt{-m_{11} - m_{21}} (e^{2l\lambda_3} - 1)} \quad (A.15)$$

The electrode impedance is defined as:

$$Z_e = \frac{\tilde{\phi}_{l,x=i}}{i_{app}} \quad (A.16)$$

The solved coefficients are substituted into the equation above and the resulting expression can be simplified to obtain Eq. (3).

## References

- [1] N.W. Brady, C.A. Gould, A.C. West, Quantitative parameter estimation, model selection, and variable selection in battery science, *J. Electrochem. Soc.* 167 (1) (2019) 013501, <http://dx.doi.org/10.1149/2.0012001JES>.
- [2] L. Chen, R. Xu, W. Rao, H. Li, Y.-P. Wang, T.Y.H.-B. Jiang, Electrochemical model parameter identification of lithium-ion battery with temperature and current dependence, *Int. J. Electrochem. Sci.* (2019) <http://dx.doi.org/10.20964/2019.05.05>.
- [3] K. Gopalakrishnan, G.J. Offer, A composite single particle lithium-ion battery model through system identification, *IEEE Trans. Control Syst. Technol.* (2021) 1–13, <http://dx.doi.org/10.1109/TCST.2020.3047776>.
- [4] A. Pozzi, G. Ciaramella, S. Volkwein, D.M. Raimondo, Optimal design of experiments for a lithium-ion cell: Parameters identification of an isothermal single particle model with electrolyte dynamics, *Ind. Eng. Chem. Res.* 58 (3) (2019) 1286–1299, <http://dx.doi.org/10.1021/acs.iecr.8b04580>.
- [5] N. Jin, D.L. Danilov, P.M. van den Hof, M. Donkers, Parameter estimation of an electrochemistry-based lithium-ion battery model using a two-step procedure and a parameter sensitivity analysis, *Int. J. Energy Res.* 42 (7) (2018) 2417–2430, <http://dx.doi.org/10.1002/er.4022>.
- [6] J. Li, L. Wang, C. Lyu, E. Liu, Y. Xing, M. Pecht, A parameter estimation method for a simplified electrochemical model for Li-ion batteries, *Electrochim. Acta* 275 (2018) 50–58, <http://dx.doi.org/10.1016/j.electacta.2018.04.098>.
- [7] B. Rajabloo, A. Jokar, M. Désilets, M. Lacroix, An inverse method for estimating the electrochemical parameters of lithium-ion batteries, *J. Electrochem. Soc.* 164 (2) (2017) A99–A105, <http://dx.doi.org/10.1149/2.0221702jes>.
- [8] A. Jokar, B. Rajabloo, M. Désilets, M. Lacroix, An inverse method for estimating the electrochemical parameters of lithium-ion batteries, *J. Electrochem. Soc.* 163 (14) (2016) A2876–A2886, <http://dx.doi.org/10.1149/2.0191614jes>.
- [9] K. Uddin, S. Perera, W. Widanage, L. Somerville, J. Marco, Characterising lithium-ion battery degradation through the identification and tracking of electrochemical battery model parameters, *Batteries* 2 (2) (2016) 13, <http://dx.doi.org/10.3390/batteries2020013>.
- [10] T. Kalogiannis, M.S. Hosen, M.A. Sokkeh, S. Goutam, J. Jagemont, L. Jin, G. Qiao, M. Berecibar, J. Van Mierlo, Comparative study on parameter identification methods for dual-polarization lithium-ion equivalent circuit model, *Energies* 12 (21) (2019) 4031, <http://dx.doi.org/10.3390/en12214031>.
- [11] R. De Levie, On porous electrodes in electrolyte solutions: I. Capacitance effects, *Electrochim. Acta* 8 (10) (1963) 751–780, [http://dx.doi.org/10.1016/0013-4686\(63\)80042-0](http://dx.doi.org/10.1016/0013-4686(63)80042-0).
- [12] R. De Levie, On porous electrodes in electrolyte solutions—IV, *Electrochim. Acta* 9 (9) (1964) 1231–1245, [http://dx.doi.org/10.1016/0013-4686\(64\)85015-5](http://dx.doi.org/10.1016/0013-4686(64)85015-5).
- [13] P. Vyroubal, T. Kazda, Equivalent circuit model parameters extraction for lithium ion batteries using electrochemical impedance spectroscopy, *J. Energy Storage* 15 (2018) 23–31, <http://dx.doi.org/10.1016/j.est.2017.10.019>.
- [14] W. Choi, H.-C. Shin, J.M. Kim, J.-Y. Choi, W.-S. Yoon, Modeling and applications of electrochemical impedance spectroscopy (EIS) for lithium-ion batteries, *J. Electrochem. Sci. Technol.* 11 (1) (2020) 1–13, <http://dx.doi.org/10.33961/jecst.2019.00528>.
- [15] J. Illig, M. Ender, A. Weber, E. Ivers-Tiffée, Modeling graphite anodes with serial and transmission line models, *J. Power Sources* 282 (2015) 335–347, <http://dx.doi.org/10.1016/j.jpowsour.2015.02.038>.
- [16] J.P. Meyers, M. Doyle, R.M. Darling, J. Newman, The impedance response of a porous electrode composed of intercalation particles, *J. Electrochem. Soc.* 147 (8) (2000) 2930, <http://dx.doi.org/10.1149/1.1393627>.
- [17] M. Doyle, J.P. Meyers, J. Newman, Computer simulations of the impedance response of lithium rechargeable batteries, *J. Electrochem. Soc.* 147 (1) (2000) 99, <http://dx.doi.org/10.1149/1.1393162>.
- [18] G. Sikha, R.E. White, Analytical expression for the impedance response of an insertion electrode cell, *J. Electrochem. Soc.* 154 (1) (2006) A43, <http://dx.doi.org/10.1149/1.2372695>.
- [19] G. Sikha, R.E. White, Analytical expression for the impedance response for a lithium-ion cell, *J. Electrochem. Soc.* 155 (12) (2008) A893, <http://dx.doi.org/10.1149/1.2976359>.
- [20] J. Huang, J. Zhang, Theory of impedance response of porous electrodes: simplifications, inhomogeneities, non-stationarities and applications, *J. Electrochem. Soc.* 163 (9) (2016) A1983, <http://dx.doi.org/10.1149/2.0901609jes>.
- [21] C. Rabissi, A. Innocenti, G. Sordi, A. Casalegno, A comprehensive physical-based sensitivity analysis of the electrochemical impedance response of lithium-ion batteries, *Energy Technol.* 9 (3) (2021) 2000986, <http://dx.doi.org/10.1002/ente.202000986>.
- [22] B.A. Boukamp, Distribution (function) of relaxation times, successor to complex nonlinear least squares analysis of electrochemical impedance spectroscopy? *J. Electrochem. Soc.* 2 (4) (2020) 042001, <http://dx.doi.org/10.1088/2515-7655/aba9e0>.
- [23] A.L. Gavriluk, D.A. Osinkin, D.I. Bronin, On a variation of the tikhonov regularization method for calculating the distribution function of relaxation times in impedance spectroscopy, *Electrochim. Acta* 354 (2020) 136683, <http://dx.doi.org/10.1016/j.electacta.2020.136683>.
- [24] M.A. Danzer, Generalized distribution of relaxation times analysis for the characterization of impedance spectra, *Batteries* 5 (3) (2019) 53, <http://dx.doi.org/10.3390/batteries5030053>.
- [25] M. Hahn, S. Schindler, L.-C. Triebs, M.A. Danzer, Optimized process parameters for a reproducible distribution of relaxation times analysis of electrochemical systems, *Batteries* 5 (2) (2019) 43, <http://dx.doi.org/10.3390/batteries5020043>.
- [26] T.H. Wan, M. Saccoccio, C. Chen, F. Ciucci, Influence of the discretization methods on the distribution of relaxation times deconvolution: Implementing radial basis functions with DRTools, *Electrochim. Acta* 184 (2015) 483–499, <http://dx.doi.org/10.1016/j.electacta.2015.09.097>.
- [27] IVERS-TIFF&Eacute;Eacut, E. Ellen, A. Weber, Evaluation of electrochemical impedance spectra by the distribution of relaxation times, *J. Ceram. Soc. Japan* 125 (4) (2017) 193–201, <http://dx.doi.org/10.2109/jcersj2.16267>.
- [28] P. Shafiei Sabet, D.U. Sauer, Separation of predominant processes in electrochemical impedance spectra of lithium-ion batteries with nickel-manganese-cobalt cathodes, *J. Power Sources* 425 (2019) 121–129, <http://dx.doi.org/10.1016/j.jpowsour.2019.03.068>.
- [29] P. Shafiei Sabet, A.J. Warnecke, F. Meier, H. Witzhausen, E. Martinez-Laserna, D.U. Sauer, Non-invasive yet separate investigation of anode/cathode degradation of lithium-ion batteries (nickel–cobalt–manganese vs. graphite) due to accelerated aging, *J. Power Sources* 449 (2020) 227369, <http://dx.doi.org/10.1016/j.jpowsour.2019.227369>.
- [30] X. Li, M. Ahmadi, L. Collins, S.V. Kalinin, Deconvolving distribution of relaxation times, resistances and inductance from electrochemical impedance spectroscopy via statistical model selection: Exploiting structural-sparsity regularization and data-driven parameter tuning, *Electrochim. Acta* 313 (2) (2019) 570–583, <http://dx.doi.org/10.1016/j.electacta.2019.05.010>.
- [31] S. Schindler, M. Bauer, M. Petzl, M.A. Danzer, Voltage relaxation and impedance spectroscopy as in-operando methods for the detection of lithium plating on graphitic anodes in commercial lithium-ion cells, *J. Power Sources* 304 (2016) 170–180, <http://dx.doi.org/10.1016/j.jpowsour.2015.11.044>.
- [32] J. Illig, J.P. Schmidt, M. Weiss, A. Weber, E. Ivers-Tiffée, Understanding the impedance spectrum of 18650 LiFePO<sub>4</sub>-cells, *J. Power Sources* 239 (2013) 670–679, <http://dx.doi.org/10.1016/j.jpowsour.2012.12.020>.
- [33] J.R. Macdonald, M.K. Brachman, Linear-system integral transform relations, *Rev. Modern Phys.* 28 (4) (1956) 393–422, <http://dx.doi.org/10.1103/RevModPhys.28.393>.
- [34] F. Dion, A. Lasia, The use of regularization methods in the deconvolution of underlying distributions in electrochemical processes, *J. Electroanal. Soc.* 475 (1) (1999) 28–37, [http://dx.doi.org/10.1016/S0022-0728\(99\)00334-4](http://dx.doi.org/10.1016/S0022-0728(99)00334-4).
- [35] B.A. Boukamp, A. Rolle, Analysis and application of distribution of relaxation times in solid state ionics, *Solid State Ion.* 302 (2017) 12–18, <http://dx.doi.org/10.1016/j.ssi.2016.10.009>.
- [36] B.A. Boukamp, Derivation of a distribution function of relaxation times for the (fractal) finite length warburg, *Electrochim. Acta* 252 (2017) 154–163, <http://dx.doi.org/10.1016/j.electacta.2017.08.154>.
- [37] M. Doyle, T.F. Fuller, J. Newman, Modeling of galvanostatic charge and discharge of the lithium/polymer/insertion cell, *J. Electrochem. Soc.* 140 (6) (1993) 1526, <http://dx.doi.org/10.1149/1.2221597>.
- [38] M. Doyle, J. Newman, Modeling the performance of rechargeable lithium-based cells: design correlations for limiting cases, *J. Power Sources* 54 (1) (1995) 46–51, [http://dx.doi.org/10.1016/0378-7753\(94\)02038-5](http://dx.doi.org/10.1016/0378-7753(94)02038-5).
- [39] M. Doyle, J. Newman, A.S. Gozdz, C.N. Schmutz, J.-M. Tarascon, Comparison of modeling predictions with experimental data from plastic lithium ion cells, *J. Electrochem. Soc.* 143 (6) (1996) 1890–1903, <http://dx.doi.org/10.1149/1.1836921>.
- [40] J.R. Macdonald, M.K. Brachman, Linear-system integral transform relations, *Rev. Modern Phys.* 28 (4) (1956) 393.
- [41] F. Dion, A. Lasia, The use of regularization methods in the deconvolution of underlying distributions in electrochemical processes, *J. Electroanal. Soc.* 475 (1) (1999) 28–37, [http://dx.doi.org/10.1016/S0022-0728\(99\)00334-4](http://dx.doi.org/10.1016/S0022-0728(99)00334-4).

- [42] B.A. Boukamp, Distribution (function) of relaxation times, successor to complex nonlinear least squares analysis of electrochemical impedance spectroscopy? *J. Phys.: Energy* 2 (4) (2020) 042001, <http://dx.doi.org/10.1088/2515-7655/aba9e0>.
- [43] X. Chen, L. Li, M. Liu, T. Huang, A. Yu, Detection of lithium plating in lithium-ion batteries by distribution of relaxation times, *J. Power Sources* 496 (2021) 229867, <http://dx.doi.org/10.1016/j.jpowsour.2021.229867>.
- [44] P.S. Sabet, A.J. Warnecke, F. Meier, H. Witzhausen, E. Martinez-Laserna, D.U. Sauer, Non-invasive yet separate investigation of anode/cathode degradation of lithium-ion batteries (nickel-cobalt-manganese vs. graphite) due to accelerated aging, *J. Power Sources* 449 (2020) 227369, <http://dx.doi.org/10.1016/j.jpowsour.2019.227369>.
- [45] P.S. Sabet, D.U. Sauer, Separation of predominant processes in electrochemical impedance spectra of lithium-ion batteries with nickel-manganese-cobalt cathodes, *J. Power Sources* 425 (2019) 121–129, <http://dx.doi.org/10.1016/j.jpowsour.2019.03.068>.
- [46] M. Hahn, S. Schindler, L.-C. Triebes, M.A. Danzer, Optimized process parameters for a reproducible distribution of relaxation times analysis of electrochemical systems, *Batteries* 5 (2) (2019) 43, <http://dx.doi.org/10.3390/batteries5020043>.
- [47] M.A. Danzer, Generalized distribution of relaxation times analysis for the characterization of impedance spectra, *Batteries* 5 (3) (2019) 53, <http://dx.doi.org/10.3390/batteries5030053>.
- [48] A. Rolle, H.A.A. Mohamed, D. Huo, E. Capoen, O. Mentre, R.-N. Vannier, S. Daviero-Minaud, B.A. Boukamp, Ca<sub>3</sub>Co<sub>4</sub>O<sub>9</sub>+ $\delta$ , A growing potential SOFC cathode material: Impact of the layer composition and thickness on the electrochemical properties, *Solid State Ion.* 294 (2016) 21–30, <http://dx.doi.org/10.1016/j.ssi.2016.06.001>.
- [49] B.A. Boukamp, A. Rolle, Use of a distribution function of relaxation times (DFRT) in impedance analysis of SOFC electrodes, *Solid State Ion.* 314 (2018) 103–111, <http://dx.doi.org/10.1016/j.ssi.2017.11.021>.
- [50] K. Pan, F. Zou, M. Canova, Y. Zhu, J.-H. Kim, Comprehensive electrochemical impedance spectroscopy study of si-based anodes using distribution of relaxation times analysis, *J. Power Sources* 479 (2020) 229083, <http://dx.doi.org/10.1016/j.jpowsour.2020.229083>.
- [51] E. Ivers-Tiffée, A. Weber, Evaluation of electrochemical impedance spectra by the distribution of relaxation times, *J. Ceram. Soc. Japan* 125 (4) (2017) 193–201, <http://dx.doi.org/10.2109/jcersj2.16267>.
- [52] J. Illig, J.P. Schmidt, M. Weiss, A. Weber, E. Ivers-Tiffée, Understanding the impedance spectrum of 18650 LiFePO<sub>4</sub>-cells, *J. Power Sources* 239 (2013) 670–679, <http://dx.doi.org/10.1016/j.jpowsour.2012.12.020>.
- [53] J. Illig, M. Ender, T. Chrobak, J.P. Schmidt, D. Klotz, E. Ivers-Tiffée, Separation of charge transfer and contact resistance in LiFePO<sub>4</sub>-cathodes by impedance modeling, *J. Electrochem. Soc.* 159 (7) (2012) A952, <http://dx.doi.org/10.1149/2.030207jes>.
- [54] M.H. Martin, A. Lasia, Influence of experimental factors on the constant phase element behavior of Pt electrodes, *Electrochim. Acta* 56 (23) (2011) 8058–8068, <http://dx.doi.org/10.1016/j.electacta.2011.02.068>.
- [55] T. Pajkossy, Impedance of rough capacitive electrodes, *J. Electroanal. Soc.* 364 (1–2) (1994) 111–125, [http://dx.doi.org/10.1016/0022-0728\(93\)02949-1](http://dx.doi.org/10.1016/0022-0728(93)02949-1).
- [56] Z. Kerner, T. Pajkossy, Impedance of rough capacitive electrodes: the role of surface disorder, *J. Electroanal. Soc.* 448 (1) (1998) 139–142, [http://dx.doi.org/10.1016/S0022-0728\(98\)00025-4](http://dx.doi.org/10.1016/S0022-0728(98)00025-4).
- [57] E.C. Titchmarsh, *Introduction to the Theory of Fourier Integrals*, Clarendon Press, 1948.
- [58] G.B. Arfken, H.J. Weber, *Mathematical Methods for Physicists*, American Association of Physics Teachers, 1999.
- [59] X. Li, M. Ahmadi, L. Collins, S.V. Kalinin, Deconvolving distribution of relaxation times, resistances and inductance from electrochemical impedance spectroscopy via statistical model selection: Exploiting structural-sparsity regularization and data-driven parameter tuning, *Electrochim. Acta* 313 (2019) 570–583, <http://dx.doi.org/10.1016/j.electacta.2019.05.010>.
- [60] J. Sturm, A. Rheinfeld, I. Zilberman, F.B. Spingler, S. Kosch, F. Frie, A. Jossen, Modeling and simulation of inhomogeneities in a 18650 nickel-rich, silicon-graphite lithium-ion cell during fast charging, *J. Power Sources* 412 (2019) 204–223, <http://dx.doi.org/10.1016/j.jpowsour.2018.11.043>.
- [61] H. Nara, K. Morita, D. Mukoyama, T. Yokoshima, T. Momma, T. Osaka, Impedance analysis of LiNi<sub>1/3</sub>Mn<sub>1/3</sub>Co<sub>1/3</sub>O<sub>2</sub> cathodes with different secondary-particle size distribution in lithium-ion battery, *Electrochim. Acta* 241 (2017) 323–330, <http://dx.doi.org/10.1016/j.electacta.2017.04.153>.
- [62] M. Schönleber, C. Uhlmann, P. Braun, A. Weber, E. Ivers-Tiffée, A consistent derivation of the impedance of a lithium-ion battery electrode and its dependency on the state-of-charge, *Electrochim. Acta* 243 (2017) 250–259, <http://dx.doi.org/10.1016/j.electacta.2017.05.009>.
- [63] S. Zhang, K. Xu, T. Jow, EIS study on the formation of solid electrolyte interface in Li-ion battery, *Electrochim. Acta* 51 (8–9) (2006) 1636–1640, <http://dx.doi.org/10.1016/j.electacta.2005.02.137>.
- [64] J.O. Besenhard, *Handbook of Battery Materials*, John Wiley & Sons, 2008.
- [65] V.J. Ovejas, A. Cuadras, Impedance characterization of an LCO-NMC/graphite cell: Ohmic conduction, SEI transport and charge-transfer phenomenon, *Batteries* 4 (3) (2018) 43, <http://dx.doi.org/10.3390/batteries4030043>.
- [66] E. Peled, S. Menkin, SEI: past, present and future, *J. Electrochem. Soc.* 164 (7) (2017) A1703, <http://dx.doi.org/10.1149/2.1441707jes>.
- [67] Y.-X. Yao, X. Chen, C. Yan, X.-Q. Zhang, W.-L. Cai, J.-Q. Huang, Q. Zhang, Regulating interfacial chemistry in lithium-ion batteries by a weakly solvating electrolyte, *Angew. Chem.* 133 (8) (2021) 4136–4143, <http://dx.doi.org/10.1002/anie.202011482>.
- [68] P. Suresh, A. Shukla, N. Munichandraiah, Temperature dependence studies of ac impedance of lithium-ion cells, *J. Appl. Electrochem.* 32 (3) (2002) 267–273, <http://dx.doi.org/10.1023/A:1015565404343>.
- [69] R. Chowdhury, A. Banerjee, Y. Zhao, X. Liu, N. Brandon, Simulation of bi-layer cathode materials with experimentally validated parameters to improve ion diffusion and discharge capacity, *Sustain. Energy Fuels* 5 (4) (2021) 1103–1119, <http://dx.doi.org/10.1039/D0SE01611J>.
- [70] M. Smart, B. Ratnakumar, Effects of electrolyte composition on lithium plating in lithium-ion cells, *Journal of The Electrochemical Society* 158 (4) (2011) A379, <http://dx.doi.org/10.1149/1.3544439>.
- [71] A. Keefe, S. Buteau, I. Hill, J. Dahn, Temperature dependent EIS studies separating charge transfer impedance from contact impedance in lithium-ion symmetric cells, *J. Electrochem. Soc.* 166 (14) (2019) A3272, <http://dx.doi.org/10.1149/2.0541914jes>.
- [72] H.C. Hesse, V. Kumtepli, M. Schimpe, J. Reniers, D.A. Howey, A. Tripathi, Y. Wang, A. Jossen, Ageing and efficiency aware battery dispatch for arbitrage markets using mixed integer linear programming, *Energies* 12 (6) (2019) 999, <http://dx.doi.org/10.3390/en12060999>.
- [73] V. Kumtepli, H.C. Hesse, M. Schimpe, A. Tripathi, Y. Wang, A. Jossen, Energy arbitrage optimization with battery storage: 3D-MILP for electro-thermal performance and semi-empirical aging models, *IEEE Access* 8 (2020) 204325–204341, <http://dx.doi.org/10.1109/ACCESS.2020.3035504>.

## 5 Investigation of the Diffusion Phenomena in Lithium-ion Batteries with Distribution of Relaxation Times

While in chapter 4 a comprehensive theory has been developed to explain and interpret the DRT spectrum of a Lithium-ion battery with a physicochemical impedance model, the phenomena dominating in the mid-low frequency range have not been investigated. Such phenomena include the diffusion in the solid and liquid phase and the differential capacitive effect. One of the most important purposes of the investigation of the diffusion phenomenon is to estimate the diffusion coefficient, which usually requires a complicated measurement procedure and the accuracy is also problematic.

One of the most widely used methods for the diffusion coefficient estimation is the GITT. For the estimation of the solid diffusion coefficient, a current pulse of a defined time period will be applied to the battery and then the voltage relaxation is measured to calculate the diffusion coefficient. It can be shown that the GITT method has the following critical limitations:

- the GITT doesn't take the electrode structure and other processes into account
- the geometry of the solid particles is not considered, instead the diffusion is assumed to be semi-infinite and in a planar geometry
- under certain circumstances, the diffusion can be dominated by the liquid phase and the solid diffusion coefficient can be strongly underestimated

In this chapter, first a comprehensive theory has been developed to explain the DRT spectrum of a Lithium-ion battery in the mid-low frequency range and an analytical expression was derived to describe the DRT spectrum using the physicochemical parameters. The developed theory explained the DRT spectrum in the mid-low frequency range, which has also considered the porous structure of the electrode, the material transport in the electrolyte and the particle geometry. Furthermore, the developed theory was compared with the GITT regarding the estimation of the solid diffusion coefficient.

The developed theory was first explained and validated using a series of synthetic impedance data. Then the solid diffusion coefficients in the anode and cathode of a commercially available Lithium-ion battery cell have been estimated using both the DRT and the GITT method. The estimation results were in line with the theoretical prediction.

### **Author contribution**

Yulong Zhao was the principal author tasked with coordinating and writing the paper, developing the theory and model, conducting the lab experiment with the full cells and coin cells, and evaluating the data. Simon Kücher helped with the experimental material coordination and building the coin cells. Andreas Jossen contributed via fruitful scientific discussions and reviewed the manuscript.

## **Investigation of the diffusion phenomena in lithium-ion batteries with distribution of relaxation times**

Yulong Zhao, Simon Kücher and Andreas Jossen

Electrochimica Acta 432 (2022) 141174

Permanent weblink:

<https://doi.org/10.1016/j.electacta.2022.141174>

Reproduced by permission of Elsevier.



## Investigation of the diffusion phenomena in lithium-ion batteries with distribution of relaxation times

Yulong Zhao<sup>\*</sup>, Simon Kücher, Andreas Jossen

Chair for Electrical Energy Storage Technology, Department of Energy and Process Engineering, School of Engineering and Design, Technical University of Munich, Arcisstrasse 21, Munich, Bavaria 80333, Germany

### ARTICLE INFO

#### Keywords:

Lithium-ion battery  
Electrochemical impedance spectroscopy  
Physics-based model  
Distribution of relaxation times  
Diffusion

### ABSTRACT

The distribution of relaxation times method (DRT) has been widely used to quantify the numbers and characterize the properties of the physico-chemical processes inside the Li-ion battery (LIB). While most of the published works focused on the mid-high frequency range, the processes in the low frequency area, such as diffusion, have garnered less attention. The difficulties of applying the DRT to the diffusion processes include the more complicated mathematical treatment involved, the unknown influence of the porous electrode on the DRT spectra and the evaluation of the measured impedance with the developed theory. The galvanostatic intermittent titration technique (GITT) has been widely applied to determine the solid diffusion coefficient for the LIB. However, the GITT does not consider the geometry of the active material particles and cannot effectively separate the contribution of the solid diffusion from other processes, such as liquid diffusion. In the present work, a comprehensive theory is developed to investigate the DRT spectra of a LIB with a physics-based impedance model. Furthermore, an analytical expression is developed for the DRT spectra and analyzed in detail. The developed theory can help to determine the solid phase diffusion coefficient with a firm physico-chemical background. Based on the developed theory, the solid diffusion coefficients of the silicon graphite (SiC) and NMC811 are determined with a commercial cell. Besides, the galvanostatic intermittent titration technique (GITT) has been applied to the same cells and the measurement results are compared with that using the DRT method. The comparison indicates that GITT cannot exclude the influence of the liquid diffusion and the solid diffusion coefficients will be underestimated.

### 1. Introduction

With the increasing demand for electric vehicles and renewable energy resources, the pace of technology development and manufacturing of Li-ion batteries (LIBs) is speeding up. Currently, various diagnostic methods have been used for scientific research and in practical applications. Among them the electrochemical impedance spectroscopy (EIS), as a nondestructive diagnostic method, has been used to estimate the cell states and identify the internal cell parameters. Besides the EIS measurement technology itself, measurement data evaluation and interpretation is another knotty yet important engineering problem. For LIBs, currently the equivalent circuit model (ECM) is frequently selected to fit the measured impedance data and estimate the cell parameters [1, 2]. However, the structure and the circuit components selected to build the ECM strongly rely on the experience and knowledge of the operators. Researchers are sometimes faced with the situation in which the same

set of impedance data can be fitted with multiple ECMs of different structures [2]. In addition, the identifiability issue of the resulting nonlinear optimization problem may also lead to implausible results, which are simply caused by a missing comprehensive sensitivity analysis. This will sometimes result in confusing conclusions that different initial guesses lead to different solutions with the same or very close residual norm; even though a unique solution exists, it may not be easily found without using complicated optimization algorithms that are relatively computationally expensive.

#### 1.1. Determination of the solid diffusivity with DRT

To get rid of the ambiguity of ECM fitting and resolve the identifiability issue, instead of using nonlinear optimization, the distribution of relaxation times (DRT) method has been used to deconvolve the EIS data [3–5]. For a more comprehensive modeling, the original DRT model is extended with ohmic resistance, capacitance and inductance. Moreover,

<sup>\*</sup> Corresponding author.

E-mail address: [yulong.zhao@tum.de](mailto:yulong.zhao@tum.de) (Y. Zhao).

<https://doi.org/10.1016/j.electacta.2022.141174>

Received 31 May 2022; Received in revised form 30 August 2022; Accepted 8 September 2022

Available online 13 September 2022

0013-4686/© 2022 Elsevier Ltd. All rights reserved.



Nomenclature		ZARC	variables related to ZARC element
<i>Greek letters</i>		<i>Symbols</i>	
$\delta$	dirac delta function	F	Faraday constant
$\kappa$	liquid phase conductivity, $S\ m^{-1}$	$a$	pole for meromorphic function expansion
$\phi$	exponent for CPE element or fractal diffusion	$a_v$	specific volumetric area, $m^{-1}$
$\sigma$	solid phase conductivity, $S\ m^{-1}$	$b$	coefficient for meromorphic function expansion
$\tau$	time constant, s	$G$	DRT spectrum function of electrode
$\theta$	variable related to local particle impedance	$g$	DRT spectrum function of RC/ZARC element
$f$	frequency, Hz	$H$	magnitude of dispersion peak
<i>Subscripts</i>		$j$	imaginary unit
ct	variables related to charge transfer	$l$	electrode thickness, m
e	variables related to electrode or electrolyte	R	resistance (with subscript), $\Omega$ ; gas constant (without subscript), $J\ K^{-1}\ mol^{-1}$
f	variables related to film	$r$	particle radius, m
loc	variables related to active material particles	$s$	laplace variable, $j\omega$
p	variables related to solid particles	Y	admittance, S
RC	variables related to RC element	Z	impedance, $\Omega$
v	variables related to volume		

a comprehensive theory will be developed to explain the extended model and therefore interpret the results. The extended DRT model used in this work consists of an ohmic resistance, a series of parallel RL elements, parallel RC elements and a CPE element:

$$Z_e = R_{ohm} + \frac{1}{(j\omega C)^\phi} + j\omega L + \int_0^\infty \frac{j\omega\tau H(\tau)}{1 + j\omega\tau} d\tau + \int_0^\infty \frac{G(\tau)}{1 + j\omega\tau} d\tau \quad (1)$$

where  $Z_e$  is the measured impedance,  $R_{ohm}$  is the total ohmic resistance,  $H(\tau)$  is the distribution function for the RL elements,  $G(\tau)$  is the distribution function for the RC elements,  $C$  is the total capacitance and  $L$  is the total inductance. To solve the integral equation numerically, the equation above is discretized and transformed into a linear equation system. The resulting system is ill-posed by its nature and cannot be inverted directly. As a result, the regularization technique is applied to invert the equation. After discretization and transformation, the following linear optimization problem is obtained:

$$\{H(\tau), G(\tau), R_{ohm}, L, C\} = \underset{x>0}{\operatorname{argmin}} \left\{ \| \mathbf{Ax} - \mathbf{b} \|_2^2 + \lambda^2 \| \mathbf{Kx} \|_2^2 \right\} \quad (2)$$

where  $\lambda$  is the regularization parameter,  $\mathbf{A}$  is the system matrix after discretization,  $\mathbf{b}$  is the measurement data vector,  $\mathbf{x}$  is the solution vector,  $\mathbf{K}$  is a matrix defining which variables to regularize. In this work, the distribution functions  $H(\tau)$  and  $G(\tau)$  are regularized.

In our previous work [6], we developed a theory to explain the DRT spectrum for the fast kinetic processes (charge transfer, SEI etc.) using a physics-based impedance model. In this work, we will try to explain the DRT spectrum for the kinetic processes with higher time constants, such as diffusion in the solid and liquid phase. Boukamp et al. [3,4] derived an analytical expression for the DRT spectrum of the finite-length-Warburg (FLW) element and investigated the performance of the resulting model. Nevertheless, the derived theory is not related to the deconvolved DRT spectrum of a LIB and does not have a comprehensive physico-chemical model behind; in addition, the derived model only considered the FLW element with transmissive boundary conditions and the capacitive behavior and other possible particle geometries are not included. Besides, no particle size distribution (PSD) is considered for the diffusion impedance. The electrode of a LIB consists of a large number of solid particles and the pores are filled with electrolyte. A complicated physico-chemical model is thus needed to describe the processes in the electrode, including the electrochemical reaction, material transport and the charge balance. Obviously, a simple equivalent circuit model with a few circuit elements cannot account for the

mentioned processes satisfactorily and the estimation results are probably problematic. Furthermore, whether and how the impedance and the resulting DRT spectra will be influenced by the mentioned processes is still unknown. Therefore, a comprehensive theory for the DRT based on a physico-chemical model is necessary for the correct and effective estimation of the solid diffusion coefficients.

### 1.2. Determination of the solid diffusivity with GITT

Since proposed, the GITT has been widely applied to determine the solid diffusivity of Li-ion batteries. Due to its simple procedures, the original GITT has been used by various works to estimate the solid diffusion coefficient [7–12]. In the GITT measurement, the Li-ion battery is placed in an equilibrium state and a current pulse with a small amplitude and a duration of  $\Delta t$  is applied to the battery and then the battery will be fully relaxed [13]. Assuming that the overpotential caused by the dynamic processes without the ohmic conduction inside the battery is  $\Delta E_t$ , the change of the equilibrium potential is  $\Delta E_e$  and the diffusion length inside the solid phase is  $L$ , then the solid diffusion coefficient can be calculated as follows [13]:

$$D_{s,GITT} = \frac{4L^2}{\pi\Delta t} \left( \frac{\Delta E_e}{\Delta E_t} \right)^2 \quad (3)$$

The original GITT method applied to a Li-ion battery is based on the following assumptions: 1. the active material particles have a planar geometry; 2. all active material particles have the same size and no particle size distribution is considered; 3. the overpotential contribution caused by other dynamic processes, especially the liquid diffusion, is neglected; 4. the porous structure of the electrode and thus the transport processes inside the porous electrode are not considered. In reality, the measured overpotential in the case of a Li-ion battery is expressed by the following equation:

$$\Delta E_t = \Delta E_{t,ct} + \Delta E_{t,SEI} + \Delta E_{t,diff,l} + \Delta E_{t,diff,s} \quad (4)$$

where  $\Delta E_{t,ct}$ ,  $\Delta E_{t,SEI}$ ,  $\Delta E_{t,diff,l}$  and  $\Delta E_{t,diff,s}$  represent the overpotential attributed to the charge transfer, SEI process, liquid diffusion and solid diffusion respectively. In practical applications, the influence of the charge transfer and SEI process may be excluded if the sampling rate is high enough and an approximate time constant for the charge transfer and SEI process is assumed. However, the influence of the liquid diffusion usually cannot be effectively excluded because the diffusion time constants in the solid and liquid phases are similar. In such a case, the

**Table 1**  
Summary and comparison of the GITT and DRT methods used for determination of the solid diffusivity.

Method	GITT		DRT	
	[7–11]	[12]	[4]	Present work
Reference	[7–11]	[12]	[4]	Present work
Electrode model	no	no	no	physico-chemical
Particle geometry	planar	planar	planar	planar/cylindrical/spherical
Particle size distribution	no	no	no	yes
Liquid diffusion	–	excluded	–	considered
Special treatment of sample	no	yes	unknown	no

solid phase diffusivity may be underestimated if the overpotential caused by the liquid diffusion is non-negligible when compared to that caused by the solid diffusion.

To exclude the influence of the electrolytic diffusion, Kang et al. developed an improved GITT method by preparing a high-density bulk sample [12]. However, a specially prepared bulk sample with a high density was needed for the measurement so that the procedure could not be easily applied to commercial cells. Besides, the geometry and the size distribution of the particles are not considered.

### 1.3. Summary

From the analysis made above, it can be seen that although the DRT method can effectively separate the contribution of different processes with regard to the time constants, a comprehensive model for the interpretation of the calculated DRT spectra and thus a connection of the DRT spectra with the physico-chemical parameters are still missing. Similarly, the GITT is based on a strongly simplified case and many essential processes have been neglected.

In this work, we will try to develop a theory that can be used to interpret the DRT spectrum regarding the liquid and solid phase diffusion processes with a physics-based impedance model, a comparison of the method proposed in the present work with the existing methods is given in Table 1. Then an analytical expression for the DRT spectrum will be derived with the electrochemical parameters and the possible influence of the porous structure will be studied. With the developed DRT model based on a physico-chemical impedance model, the solid diffusion coefficient will be estimated using the DRT spectra. Meanwhile, a GITT measurement will be conducted to determine the solid diffusion coefficient, the results will be compared to that with the DRT and the advantage and effectiveness of the DRT based on a physico-chemical model will be demonstrated. The workflow of the present work is shown in Fig. 1.

The rest of the work is organized as follows: in Section 2, an analytical expression of the DRT for an electrode based on a physics-based impedance model is derived and analyzed; in Section 3, a simulation experiment will first be conducted to investigate the derived

theory, then the DRT spectra of a commercial LIB and two half cells will be evaluated and interpreted using the proposed model. Section 4 concludes the work.

## 2. Theory development

In this section, the DRT spectra for LIBs will be investigated and an analytical expression will be developed using a physics-based impedance model. While in our previous work we have focused on the fast kinetic processes such as charge transfer and SEI process, in this work we will concentrate on the diffusion in the liquid and solid phase. The impedance model used is derived using the pseudo-two-dimensional (p2D) model developed by Doyle and Newman [14–16]. Considering that the liquid phase diffusion coefficient is usually orders of magnitude greater than that in the solid phase and that for LIBs that are not strongly aged, the liquid phase diffusivity should still be high enough, we choose to first neglect the liquid phase diffusion when investigating the solid phase diffusion, later the model will be extended by the liquid phase diffusion. The derivation of the impedance model for an electrode without liquid phase diffusion has been shown in our previous work [6] and is thus omitted here. The impedance expression is given by:

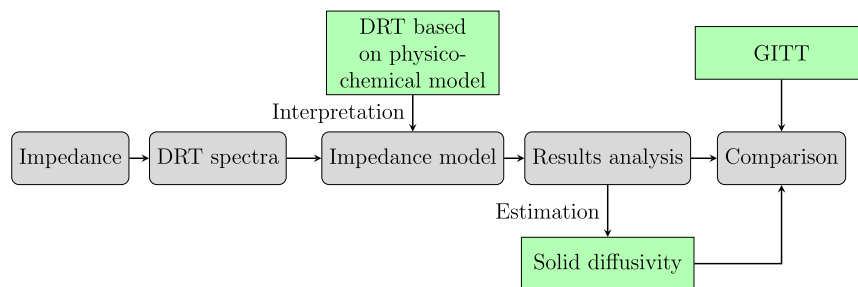
$$Z_e = \frac{l_e}{\kappa + \sigma} + \frac{(\kappa^2 + \sigma^2) \coth(\sqrt{\theta} l_e)}{\kappa \sigma (\kappa + \sigma) \sqrt{\theta}} + \frac{2}{(\kappa + \sigma) \sqrt{\theta} \sinh(\sqrt{\theta} l_e)} \quad (5)$$

$$\theta = \left( \frac{1}{\sigma} + \frac{1}{\kappa} \right) \frac{1}{Z_{v,loc}} = \left( \frac{1}{\sigma} + \frac{1}{\kappa} \right) Y_{v,loc} \quad (6)$$

where  $Z_e$  is the electrode impedance,  $l_e$  is the electrode thickness,  $\kappa$  and  $\sigma$  are conductivities in the liquid and solid phases respectively,  $\theta$  is a variable related to the local particle impedance and  $Z_{v,loc}$  and  $Y_{v,loc}$  are the volume-specific particle impedance and admittance respectively. The volume-specific impedance instead of the area-specific impedance is used to ease the derivation for the case where the PSD is considered.

### 2.1. Classification of dispersion phenomena in electrodes

According to our previous work [6], the porous structure and transport phenomena in the electrode will cause dispersion behavior with regard to the charge transfer and SEI processes when the diffusion is neglected in the mid-high frequency range. In the low frequency range where the diffusion cannot be neglected, it is still unclear whether the spectra will be influenced by the dispersion and how pronounced it will be. Hence, we start by analyzing the dispersion phenomenon in the low frequency range. We believe that according to the electrochemical processes occurring in an electrode, the spectrum dispersion has two origins: the first kind of dispersion is caused by the spatially distributed physical or electrochemical processes along the thickness of the electrode, such as the electronic/ionic conduction and the distributed electrochemical reactions, we refer to the first kind of dispersion as stage one dispersion. Another kind of dispersion arises from the local



**Fig. 1.** Workflow of determination of the solid diffusion coefficient using DRT and a physicochemical impedance model.

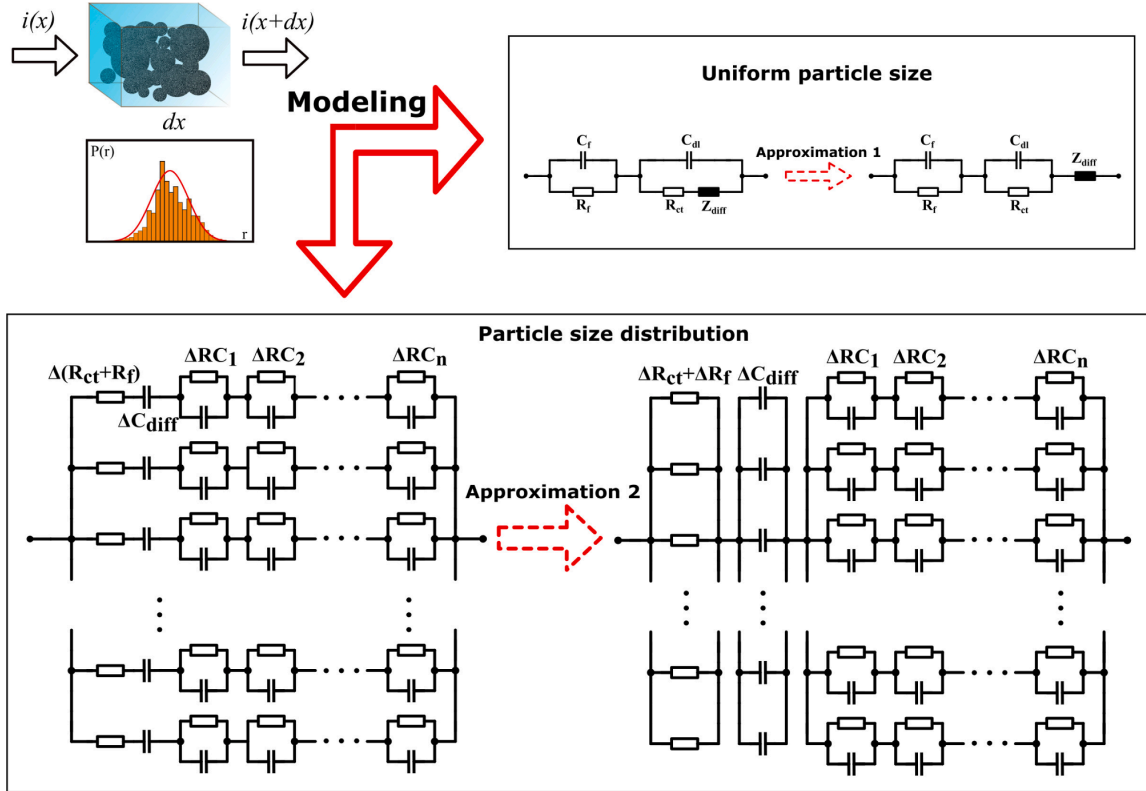


Fig. 2. Circuit approximation used for the model development, with approximation 1 in the upper part and approximation 2 in the lower part of the figure.

processes which will locally cause dispersion itself, such as charge transfer with a constant phase element (CPE) and the solid phase diffusion. We refer to the second kind of dispersion as stage two dispersion. Both dispersion behaviors are not simply superimposed but rather interacting with each other in a sophisticated way, a direct investigation of all dispersion phenomena at the same time will lead to an overly complicated mathematical problem which does not help to resolve the issue. Based on the cause and the scope of impact of the dispersion phenomena, we choose to develop the theory with a two-step procedure by investigating the dispersion of two stages separately. In the following sections, we will conduct the model derivation starting from stage one dispersion. Then, the stage two dispersion will be investigated based on the findings and conclusions from the stage one dispersion.

## 2.2. Stage one dispersion: electrode level dispersion

In this section the stage one dispersion phenomenon will be investigated. Upon substituting Eq. (6) into (5), a meromorphic function of the volume-specific admittance  $Y_{v,loc}$  is obtained, which can be reformulated as an infinite series using the Mittag-Leffler theorem [17]:

$$Z_e = Z_{e,Y_{v,loc,0}} + \sum_{n=0}^{\infty} \left( \frac{B_n}{Y_{v,loc} - A_n} + \frac{B_n}{A_n} \right) \quad (7)$$

where  $A_n$  and  $B_n$  are the corresponding poles and expansion coefficients respectively,  $Z_{e,Y_{v,loc,0}}$  is the electrode impedance when  $Y_{v,loc}$  approaches zero. If we let  $Y_{v,loc}$  approach infinity (equivalent to  $f \rightarrow \infty$ ) and evaluate the resulting equation, the following equation can be obtained:

$$Z_{e,Y_{v,loc,0}} + \sum_{n=0}^{\infty} \frac{B_n}{A_n} = \frac{l_e}{\kappa + \sigma} \quad (8)$$

The equation above is substituted into Eq. (7) and the following simplified equation is obtained:

$$Z_e = \frac{l_e}{\kappa + \sigma} + \sum_{n=0}^{\infty} \left( \frac{B_n}{Y_{v,loc} - A_n} \right) \quad (9)$$

In the equation derived above,  $l_e/(\kappa + \sigma)$  is the ohmic resistance of the electrode. The poles of the expansion are determined by solving the following equations:

$$\theta = 0 \quad (n = 0) \quad (10)$$

$$\sinh(\sqrt{\theta_n} l_e) = 0 \Rightarrow \sqrt{\theta_n} l_e = in\pi \quad (n = 1, 2, 3, \dots) \quad (11)$$

The solutions to the equations above are given as:

$$A_0 = 0 \quad (n = 0) \quad (12)$$

$$A_n = -\frac{n^2 \pi^2}{l_e^2 \left( \frac{1}{\kappa} + \frac{1}{\sigma} \right)} \quad (n = 1, 2, 3, \dots) \quad (13)$$

And the expansion coefficients  $B_n$  are solved for using the residue method:

$$B_n = \lim_{Y_{v,loc} \rightarrow A_n} (Y_{v,loc} - A_n) Z_e(Y_{v,loc}) \quad (14)$$

which gives the following solutions:

$$B_0 = \frac{1}{l_e} \quad (15)$$

**Table 2**  
 Solid diffusion impedance with different geometric shapes [18].

Particle geometry	Planar	Cylindrical	Spherical
$Z_d$	$\frac{\coth(\sqrt{s\tau_0})}{\sqrt{s\tau_0}}$	$\frac{I_0(\sqrt{s\tau_0})}{\sqrt{s\tau_0}I_1(\sqrt{s\tau_0})}$	$\frac{\tanh(\sqrt{s\tau_0})}{\sqrt{s\tau_0} - \tanh(\sqrt{s\tau_0})}$
$R_d$		$\left(-\frac{\partial U}{\partial c_s}\right) \frac{r_p}{FD_s}$	

$$B_n = \frac{2[\kappa^2 + 2\kappa\sigma(-1)^n + \sigma^2]}{l_e(\kappa + \sigma)^2} \quad (n = 1, 2, 3, \dots) \quad (16)$$

It can be seen from Eqs. (13) to (16) that the poles are a function of  $n$  and increase with the factor  $n^2$ , the expansion coefficients are swinging between two constant values and thus not decaying with increasing order. A qualitative inspection of Eqs. (9), (13) and (16) indicates that even the expansion coefficients are not decaying with increasing order, the denominator increases with increasing  $n$  because the poles are increasing. Through further model investigation, we can confirm that the dispersion magnitude decays quickly with the increasing time constants, so that for the solid diffusion process the stage one dispersion can be practically neglected. In order to show quantitatively that the magnitude of dispersion terms decreases with increasing time constants, the theorem on residue of composition function can be used to derive the coefficients corresponding to each process, the derivation is provided in Appendix A.4.

### 2.3. Stage two dispersion: particle dispersion

In the last section, we have analyzed the stage one dispersion in detail and concluded that the stage one dispersion can be practically neglected in the low frequency range. In this section, we will continue to investigate the local dispersion phenomena.

The area-specific local particle impedance of a LIB is usually expressed using the following equation [2]:

$$Z_{loc} = \frac{R_f}{1 + sR_fC_f} + \frac{1}{\frac{1}{R_{ct} + R_dZ_d} + sC_{dl}} \quad (17)$$

where  $R_f$  and  $R_{ct}$  are the film and charge transfer resistances respectively,  $C_f$  and  $C_{dl}$  are the film and double layer capacitances respectively,  $Z_d$  is the dimensionless diffusion impedance and  $R_d$  represents the diffusional resistance. For brevity, here we have only considered RC elements for charge transfer and SEI process, for ZARC elements a similar model can be derived, as shown in our previous work [6].

Due to the fact that the diffusion time constants are usually several orders of magnitude larger than those of the charge transfer and SEI processes, the particle impedance can be approximated with a series connection of two RC elements and one diffusion impedance (see Fig. 2):

$$Z_{loc} \approx \frac{R_f}{1 + sR_fC_f} + \frac{R_{ct}}{1 + sR_{ct}C_{dl}} + R_dZ_d \quad (18)$$

We refer to the approximation made above as approximation 1. Depending on the geometric shape of the particles, the dimensionless diffusion impedance  $Z_d$  has different forms which are listed in Table 2, where  $U$  is the open circuit voltage of the electrode,  $r_p$  is the particle size,  $c_s$  is the concentration of the Li-ions in the particles,  $\tau_0$  is the characteristic diffusion time constant with  $\tau_0 = r_p^2/D_s$ . An electrode with a uniform particle size (UPS) is only a strongly simplified case. In reality, the active material particles inside the electrode have a particular PSD, which will modify the diffusion impedance of a LIB in a specific way. In the following sections, the dispersion phenomenon as well as the DRT spectrum for the solid diffusion will be discussed in two cases: solid particles with UPS and PSD.

**Table 3**  
 Expansion parameters of diffusion impedance (see Appendices A.1–A.3).

Geometry	$\tau_n$	$R_n$	$C_d$	$\lambda_n$
Planar	$\frac{\tau_0}{\lambda_n^2}$	$\frac{2}{\lambda_n^2}$	$\tau_0$	$n\pi$
Cylindrical	$\frac{\tau_0}{\lambda_n^2}$	$\frac{2}{\lambda_n^2}$	$\frac{\tau_0}{2}$	$J_1(\lambda_n) = 0$
Spherical	$\frac{\tau_0}{\lambda_n^2}$	$\frac{2}{\lambda_n^2}$	$\frac{\tau_0}{3}$	$\tan(\lambda_n) = \lambda_n$

#### 2.3.1. Diffusion with uniform particle size

If the solid particles have a uniform size, the volume-specific particle impedance can be obtained by simply scaling the area-specific impedance using the volumetric interfacial area  $a_v$ :

$$Z_{v,loc} = \frac{Z_{loc}}{a_v} = \frac{1}{a_v} \left( \frac{R_f}{1 + sR_fC_f} + \frac{R_{ct}}{1 + sR_{ct}C_{dl}} \right) + \frac{1}{a_v} R_d Z_d \quad (19)$$

If we first neglect the higher order dispersion terms and only keep the 0th order terms, Eq. (9) can be rewritten as:

$$Z_{e,0} = \underbrace{\frac{l_e}{\kappa + \sigma}}_{\text{Ohmic resistance}} + \underbrace{\frac{1}{a_v l_e} \left( \frac{R_f}{1 + sR_fC_f} + \frac{R_{ct}}{1 + sR_{ct}C_{dl}} \right)}_{\text{Charge transfer and SEI process}} + \underbrace{\frac{1}{a_v l_e} R_d Z_d}_{\text{Solid diffusion}} \quad (20)$$

The resulting expression is equivalent to the well-known single particle model (SPM) assumption [19] and has a clear physical meaning: the first term represents the ohmic resistance of the electrode, the second term represents the charge transfer and SEI impedance, the last term is the diffusion impedance in the solid phase. The approximated electrode impedance represented by the equation above assumes that the higher order stage one dispersion is neglected, which is only true in the low frequency range. For processes with smaller time constants, a certain dispersion is expected and will cause discrepancy when compared to the original impedance. The dispersion phenomena in the mid-high frequency range has been studied in detail in our previous work. An alternative way to approximate the total electrode impedance is given as:

$$Z_{e,appr} = Z_{hf} + \frac{1}{a_v l_e} R_d Z_d \quad (21)$$

where  $Z_{hf}$  is the electrode impedance in the mid-high frequency range, in which the solid phase diffusion is neglected:

$$Z_{hf} = \frac{l_e}{\kappa + \sigma} + \frac{(\kappa^2 + \sigma^2) \coth(\sqrt{\theta_{hf}} l_e)}{\kappa \sigma (\kappa + \sigma) \sqrt{\theta_{hf}}} + \frac{2}{(\kappa + \sigma) \sqrt{\theta_{hf}} \sinh(\sqrt{\theta_{hf}} l_e)} \quad (22)$$

$$\theta_{hf} = \left( \frac{1}{\sigma} + \frac{1}{\kappa} \right) \left( \frac{R_f}{1 + sR_fC_f} + \frac{R_{ct}}{1 + sR_{ct}C_{dl}} \right)^{-1} \quad (23)$$

In order to show the discrepancy caused by the dispersion in the mid-high frequency range, we still choose Eq. (20) to reconstruct the impedance and compare the results. Next, to characterize the dispersion caused by the local solid diffusion in the particles, the dimensionless diffusion impedance  $Z_d$  is expanded as a sum of a capacitance and an infinite number of serially connected RC elements using the Mittag-Leffler theorem:

$$Z_d = \frac{1}{sC_d} + \sum_{n=1}^{\infty} \frac{R_n}{1 + s\tau_n} \quad (24)$$

The expansion coefficients and dispersion time constants for particles of different geometries are listed in Table 3 and the detailed derivation can be found in Appendices A.1–A.3. When conducting the DRT analysis, the ohmic resistance, inductive and capacitive components as well as the DRT spectrum will be calculated by an optimization algorithm. By combining Eqs. (20) and (24) and considering Table 3, the DRT spectrum can be expressed using the following equation:

$$G(\tau) = \frac{1}{a_v l_e} [R_{ct} \delta(\tau - \tau_{ct}) + R_f \delta(\tau - \tau_f)] + \sum_{n=1}^{\infty} \left( -\frac{\partial U}{\partial c_s} \right) \frac{r_p R_n}{a_v l_e F D_s} \delta(\tau - \tau_n) \quad (25)$$

We further notice that  $a_v = N c_s / r_p$  and  $C_d = \tau_0 / N$ , where  $N$  is the particle geometry index and  $N = 1, 2, 3$  stands for planar, cylindrical and spherical particles respectively. The total electrode capacitance is given by:

$$C_e = \frac{\epsilon_s l_e F}{\left( -\frac{\partial U}{\partial c_s} \right)} \quad (26)$$

Eq. (25) implies that the DRT spectrum corresponding to the solid phase diffusion consists of an infinite sum of Dirac delta functions with decreasing magnitude and time constants. We further notice that  $\lambda_n \approx n\pi$  regardless of the particle geometry. Therefore both the dispersion time constants and magnitudes also decay approximately with the factor  $1/n^2$ . By conducting DRT analysis, the diffusion time constants as well as the diffusion coefficients can be estimated using the relation listed in Table 3 if the particle geometry and size are known. Eq. (26) indicates that the capacitance of the electrode is decided by the electrode thickness  $l_e$ , volume fraction of active material  $\epsilon_s$  and the differential open circuit voltage (dOCV). The magnitude of the prominent peak (peak with the largest magnitude and time constants) can be calculated as:

$$H_1 = \left( -\frac{\partial U}{\partial c_s} \right) \frac{2\tau_1}{3\epsilon_s l_e F} \quad (27)$$

### 2.3.2. Diffusion with particle size distribution

In this section, the DRT spectrum for an electrode with a PSD will be derived and investigated. In practice, the particles in the electrode have a certain size distribution, which has a significant influence on the diffusion part of the impedance curve and cannot be neglected [20]. In this work, we will try to approximate the analytical DRT spectrum when the PSD is taken into account. Based on the theoretical investigation, an approximation method is proposed to interpret the DRT spectrum when considering the PSD. As in many practical applications of the p2D model the solid particles are assumed to be spherical [14–16], thus we choose to derive the model with spherical particle geometry. For particles with a planar or cylindrical geometry, the same development procedures can be performed and similar conclusions can be made.

In an infinitesimally small volume element, in which the potential in the liquid and solid phases can be regarded as spatially constant, the volume-specific particle impedance can be defined as:

$$Z_{v,loc} = \frac{\Phi_s - \Phi_l}{i_{v,loc}} \quad (28)$$

where  $\Phi_s$  and  $\Phi_l$  are potentials in the solid and liquid phases respectively,  $i_{v,loc}$  is the local volumetric reaction current density. Using the PSD, the volumetric current density can be expressed as:

$$i_{v,loc} = \int_0^{\infty} 4\pi r^2 N(r) i_{loc}(r) dr = \int_0^{\infty} 4\pi r^2 N(r) \frac{\Phi_s - \Phi_l}{Z_{loc}(r)} dr \quad (29)$$

where  $r$  is the particle radius,  $N(r)$  is the PSD function inside the unit volume and  $i_{loc}$  is the local area-specific reaction current density. Upon substituting Eq. (29) into (28), the volumetric particle impedance can be formulated as:

$$Z_{v,loc} = \frac{\Phi_s - \Phi_l}{i_{v,loc}} = \left[ \int_0^{\infty} \frac{4\pi r^2 N(r)}{Z_{loc}(r)} dr \right]^{-1} \quad (30)$$

To simplify the model derivation and enable an explicit expression, the following assumptions are made:

1. The ohmic resistance, capacitance and RC elements contribution to the local impedance can be approximately separated, to which we refer as as approximation 2, as depicted in Fig. 2.
2. Because the magnitude of the solid diffusion impedance dispersion decreases with  $1/n^2$  (see Table 3), the main component of the diffusion impedance can be approximated by the first three RC elements with the largest three time constants ( $\sum_{n=1}^3 1/\lambda_n^2 \approx 0.75 \sum_{n=1}^{\infty} 1/\lambda_n^2$ ), to which we refer as the 3RC approximation.

Due to the fact that the diffusion mainly occurs in the low frequency range ( $f \ll 1$  Hz), we neglect the terms  $s^n$  ( $n \geq 1$ ) in the nominator and  $s^n$  ( $n \geq 2$ ) in the denominator when summing the three RC elements up. Note that the resistances and time constants are related by  $\lambda_n$  (see Table 3), the following approximated expression is obtained:

$$Z_{3RC} = \sum_{n=1}^3 \frac{R_n}{1 + s\tau_n} \approx \frac{R_{3RC}}{1 + s\tau_{3RC}} \quad (31)$$

where the corresponding resistance and time constant are given as:

$$R_{3RC} = \left( 1 + \frac{\lambda_1^2 \lambda_2^2 + \lambda_1^2 \lambda_3^2}{\lambda_2^2 \lambda_3^2} \right) R_1 = \mu R_1 \quad (32)$$

$$\tau_{3RC} = \left( 1 + \frac{\lambda_1^2 \lambda_2^2 + \lambda_1^2 \lambda_3^2}{\lambda_2^2 \lambda_3^2} \right) \tau_1 = \mu \tau_1 \quad (33)$$

It can be seen that the approximated resistance and time constant are both scaled with the same factor  $\mu$  which is larger than one. With the assumptions and approximations made above, Eq. (30) can be reformulated as:

$$Z_{v,loc} = \left[ \int_0^{\infty} \frac{4\pi r^2 N(r)}{\frac{R_f}{1+sR_f C_f} + \frac{R_{ct}}{1+sR_{ct} C_{dl}}} dr \right]^{-1} + \left[ s \int_0^{\infty} 4\pi r^2 N(r) \frac{rF}{3 \left( -\frac{\partial U}{\partial c_s} \right)} dr \right]^{-1} + \left[ \frac{FD_s \lambda_1^2}{\mu \left( -\frac{\partial U}{\partial c_s} \right)} \int_0^{\infty} 2\pi r N(r) dr + \frac{sF}{\left( -\frac{\partial U}{\partial c_s} \right)} \int_0^{\infty} 2\pi r^3 N(r) dr \right]^{-1} \quad (34)$$

Note that the following relations hold for the PSD:

$$a_v = \int_0^{\infty} 4\pi r^2 N(r) dr \quad (35)$$

$$\epsilon_s = \int_0^{\infty} \frac{4}{3} \pi r^3 N(r) dr \quad (36)$$

$$\bar{r}_p = \frac{\int_0^{\infty} r N(r) dr}{N_p} = \int_0^{\infty} r P(r) dr \quad (37)$$

where  $a_v$  is the volumetric interfacial area defined by the PSD,  $\bar{r}_p$  is the average particle radius,  $N_p$  is the total number of the solid particles in unit volume,  $P(r)$  is the probability density function (PDF) of the particle radius.  $N_p$  and  $P(r)$  are defined as:

$$N_p = \int_0^{\infty} N(r) dr \quad (38)$$

$$P(r) = \frac{N(r)}{N_p} \quad (39)$$

If we substitute Eqs. (35)–(39) into Eq. (34), the following equation is obtained:

$$Z_{v,loc,3RC} = \frac{1}{a_v} \left( \frac{R_f}{1 + sR_f C_f} + \frac{R_{ct}}{1 + sR_{ct} C_{dl}} \right) + \frac{1}{s \left( \frac{Fl_e \epsilon_s}{\mu \left( -\frac{\partial U}{\partial c_s} \right)} \right)} + \left[ \frac{2\pi l_e F D_s \lambda_1^2 N_p \bar{r}_p}{\mu \left( -\frac{\partial U}{\partial c_s} \right)} + s \frac{3Fl_e \epsilon_s}{2 \left( -\frac{\partial U}{\partial c_s} \right)} \right]^{-1} \quad (40)$$

After the approximated local volume-specific particle impedance has been derived, the impedance must be scaled to obtain the electrode impedance. In Section 2.2, the electrode impedance expression has been expanded with regard to  $Y_{v,loc}$ . Similarly, the dispersion terms are neglected here due to the reasons explained before, the final expression for the approximated electrode impedance is given as:

$$Z_e = \frac{l_e}{\kappa + \sigma} + \frac{1}{a_v l_e} \left( \frac{R_f}{1 + sR_f C_f} + \frac{R_{ct}}{1 + sR_{ct} C_{dl}} \right) + \frac{1}{s \left( \frac{Fl_e \epsilon_s}{\mu \left( -\frac{\partial U}{\partial c_s} \right)} \right)} + \left[ \frac{2\pi l_e F D_s \lambda_1^2 N_p \bar{r}_p}{\mu \left( -\frac{\partial U}{\partial c_s} \right)} + s \frac{3l_e F \epsilon_s}{2 \left( -\frac{\partial U}{\partial c_s} \right)} \right]^{-1} \quad (41)$$

The equation above has a clear physical meaning and can be readily interpreted as follows:

1. The first term is the ohmic resistance of the electrode.
2. The second term represents the charge transfer and SEI impedance, which is simply the scaled local particle impedance and is equivalent to the SPM. As explained before, the first and second term can also be replaced by the electrode impedance without solid diffusion (see Eqs. (22) and (23)) to account for the dispersion terms in the mid-high frequency range:

$$Z_e = Z_{ef} + \frac{1}{s \left( \frac{Fl_e \epsilon_s}{\mu \left( -\frac{\partial U}{\partial c_s} \right)} \right)} + \left[ \frac{2\pi l_e F D_s \lambda_1^2 N_p \bar{r}_p}{\mu \left( -\frac{\partial U}{\partial c_s} \right)} + s \frac{3l_e F \epsilon_s}{2 \left( -\frac{\partial U}{\partial c_s} \right)} \right]^{-1} \quad (42)$$

3. The third term represents the approximated total electrode capacitance when the PSD is also taken into consideration. We can also observe that the total electrode capacitance has the same form as that of UPS and is thus not dependent on the PSD (see Eq. (26)).
4. The last term represents an RC element arising from the solid diffusion with the PSD and can be used to estimate the diffusion parameters.

The time constant of the RC element for the solid diffusion with the PSD defined above is given as:

$$\tau_{PSD} = \frac{3\mu \epsilon_s}{4\pi D_s N_p \lambda_1^2 \bar{r}_p} \quad (43)$$

Similarly, the magnitude of the prominent peak is given as:

$$H_{1,3RC} = \frac{\mu \left( -\frac{\partial U}{\partial c_s} \right)}{2\pi l_e F D_s \lambda_1^2 N_p \bar{r}_p} \quad (44)$$

The equations derived above indicate that although with the DRT spectrum the exact PSD cannot be determined in a straightforward way, still it can reflect particular average quantities of the electrode and can be used to estimate the diffusivity if specific electrode parameters are given. Furthermore, Eq. (43) also indicates that the time constant, when the PSD is considered, cannot be simply calculated using  $\bar{r}_p^2 / D_s \lambda_1^2$ , which will underestimate the diffusion time constant, especially when the PSD has a relatively high variance. Again the approximation and analysis made above assume that the higher order terms of the stage one dispersion are neglected. For the high frequency processes, the

dispersion generally cannot be neglected.

#### 2.4. Fractal diffusion

In practical applications, it is often found that in the low frequency area, instead of an ideal capacitive impedance ( $|\theta| = 90^\circ$ ), a CPE-type impedance ( $|\theta| < 90^\circ$ ) is observed. Correspondingly, in the Warburg region, slightly depressed circles are expected. The existence of such non-ideal diffusion behavior is usually attributed to the nonuniform diffusion or multiple paths in the system [1]. As a result, the  $(s\tau_0)$  term in Table 2 is replaced by  $(s\tau_0)^\phi$ , where  $\phi$  is the parameter describing the fractal diffusion and  $\phi \leq 1$ . When the fractal diffusion behavior is expected, the characterization method must be adapted to correctly estimate the parameters. Eq. (1) Then the time constants read from the DRT spectrum are related to the diffusion coefficients through the following equation:

$$\left( \frac{\tau_0}{\tau_n} \right)^\phi = \lambda_n^2 \quad (45)$$

As a prerequisite, the parameter  $\phi$  must first be estimated with the capacitive impedance of the EIS.

#### 2.5. Diffusion in the electrolyte

When the diffusivity in the electrolyte is large enough so that the electrolytic diffusion is no more a limiting factor, the impedance contribution of electrolytic diffusion can be practically neglected. In most published works related to DRT, the electrolytic diffusion is simply neglected, which may potentially cause errors when the assumption made above is not fulfilled [5,18,21,22]. Zhou et al. investigated a LIB using the DRT and emphasized the importance of considering the electrolytic diffusion [23]. However, an investigation of the qualitative and quantitative relation between the impedance and the DRT spectrum was not provided. Therefore, in this work we will propose an extended model to account for the electrolytic diffusion in a simplified way, based on which the DRT spectrum will be interpreted and explained.

To develop the model which can be used to derive the DRT expressions for the electrolytic diffusion, an analytical solution is a prerequisite. Sikha et al. developed an analytical solution for the impedance of a LIB and managed to simulate the cell impedance with physicochemical parameters [24,25]. Despite the closed-form solution, it cannot be directly used to derive the DRT expression due to its complicated form. Here we try to separate the contribution of electrolytic diffusion from the total impedance. We assume that the reaction current density is homogeneous along the electrode thickness, thus the equation for the Li-ion transport in the electrolyte is decoupled and can be rewritten as follows:

$$s\epsilon_c \tilde{c}_c = \frac{\partial}{\partial x} \left( D_{e,eff} \frac{\partial \tilde{c}_c}{\partial x} \right) + \frac{a\tilde{j}_{loc}(1-t_+)}{F} \quad (46)$$

where  $\tilde{c}_c$  is the liquid phase concentration,  $D_{e,eff}$  is the effective liquid phase diffusivity,  $s$  is the laplace variable and  $s = j\omega$ ,  $\tilde{j}_{loc}$  is the local reaction current density and is related to the total applied current density  $\tilde{i}_{app}$  by:

$$\tilde{j}_{loc} = \frac{\tilde{i}_{app}}{a_v l_e} \quad (47)$$

The equation derived above is subjected to the following boundary conditions:

$$D_{e,eff} \frac{\partial \tilde{c}_c}{\partial x} \Big|_{x=0} = 0 \quad (48)$$

$$\tilde{c}_c \Big|_{x=l_e} = 0 \quad (49)$$

**Table 4**  
 Summary of time constants for diffusion in the solid and liquid phases.

Physics	Solid diffusion		Liquid diffusion
Particle size	UPS	PSD	-
Time constant	$\frac{r_p^2}{D_s \lambda_1^2}$	$\frac{3\mu\epsilon_s}{4\pi D_s N_p \rho_1^2 \bar{r}_p}$	$\frac{4\epsilon_l l_e^2}{\pi^2 D_c \text{eff}}$
Approximation	1	1,2,3RC	SPM

Eq. (46) can be easily solved to obtain the following solution:

$$\tilde{c}_e(x=0) = \tilde{t}_{\text{app}} \frac{1-t_+}{F\epsilon_l l_e} \left( \frac{1}{s} - \frac{1}{s \cosh(\sqrt{s}\tau_{1,0})} \right) \quad (50)$$

where  $\tau_{1,0}$  is the characteristic diffusion time in the electrolyte and is defined as follows:

$$\tau_{1,0} = \epsilon_l \frac{l_e^2}{D_{1,\text{eff}}} \quad (51)$$

The overpotential caused by the electrolytic diffusion in the LIB is defined as:

$$\eta_{1,\text{diff}} = \frac{2RT(1-t_+)}{F c_{1,0}} \left( 1 + \frac{\partial \ln \gamma}{\partial \ln c} \right) \Delta c_1 \quad (52)$$

Note that the impedance caused by the electrolytic diffusion is:

$$Z_{1,\text{diff}} = \frac{\eta_{1,\text{diff}}}{\tilde{t}_{\text{app}}} \quad (53)$$

As a result, the electrolytic diffusion impedance can be expressed:

$$Z_{1,\text{diff}} = \frac{2RT(1-t_+)^2}{F^2 \epsilon_l l_e c_{1,0}} \left( 1 + \frac{\partial \ln \gamma}{\partial \ln c} \right) \left( \frac{1}{s} - \frac{1}{s \cosh(\sqrt{s}\tau_{1,0})} \right) \quad (54)$$

By applying the Mittag-Leffler theorem to the impedance expression, a series can be obtained:

$$Z_{1,\text{diff}} = \sum_{n=0}^{+\infty} \frac{b_n}{s - a_n} \quad (55)$$

where the expansion poles and coefficients are defined as follows:

$$a_n = -\frac{\pi^2 (n + \frac{1}{2})^2}{\tau_{1,0}} \quad (56)$$

$$b_n = \frac{4(-1)^n (1-t_+)^2 RT}{(2n+1)\pi F^2 \epsilon_l l_e c_{1,0}} \left( 1 + \frac{\partial \ln \gamma}{\partial \ln c} \right) \quad (57)$$

The equations derived above indicate that the contribution of the electrolytic diffusion corresponds to a series of peaks in the DRT spectrum with decreasing magnitude and time constants. But as the dispersion terms decay very fast, usually only one peak can be observed. The time constant  $\tau_{1,n}$  and magnitude  $h_n$  of each peak is calculated as:

$$\tau_{1,n} = \frac{1}{a_n} = \frac{\tau_{1,0}}{\pi^2 (n + \frac{1}{2})^2} \quad (58)$$

$$h_n = -\frac{b_n}{a_n} = \frac{32(-1)^n (1-t_+) RT \tau_{1,0}}{(2n+1)^3 \pi^3 F^2 \epsilon_l l_e c_{1,0}} \left( 1 + \frac{\partial \ln \gamma}{\partial \ln c} \right) \quad (59)$$

Because the fundamental order peak has the largest magnitude and can be better observed, the time constant of the fundamental order peak can be used to estimate the effective diffusivity in the electrolyte.

### 2.6. Summary of model and theory

In the previous sections, we have investigated the DRT spectrum of the LIB and the characterization of diffusion in the solid and liquid phases. For the case of UPS, given the particle radius, the solid phase

**Table 5**  
 Parameters used for simulation experiments.

Electrode	Anode	Separator	Cathode
Design and geometric parameters			
Electrode thickness $l_e$ [ $\mu\text{m}$ ]	86.7 <sup>c</sup>	12 <sup>c</sup>	66.2 <sup>c</sup>
Active material volume fraction $\epsilon_s$ [%]	69.4 <sup>c</sup>	-	74.5 <sup>c</sup>
Porosity $\epsilon_l$ [%]	21.6 <sup>c</sup>	45 <sup>c</sup>	17.1 <sup>c</sup>
Bruggeman coefficient $\alpha$ [-]	1.5 <sup>c</sup>	1.5 <sup>c</sup>	1.85 <sup>c</sup>
Transport parameters			
Ionic conductivity $\kappa$ [ $\text{m S}^{-1}$ ]	0.1199 <sup>bdg</sup>	0.3605 <sup>bdg</sup>	0.0455 <sup>bdg</sup>
Electronic conductivity $\sigma$ [ $\text{m S}^{-1}$ ]	57.81 <sup>bdg</sup>	-	0.0986 <sup>bdg</sup>
Solid diffusivity $D_s$ [ $\text{m}^2 \text{s}^{-1}$ ]	$1 \times 10^{-13\text{a}}$	-	$5 \times 10^{-15\text{a}}$
Liquid diffusivity $D_l$ [ $\text{m}^2 \text{s}^{-1}$ ]	$6.47 \times 10^{-11\text{a}}$	$1.94 \times 10^{-10\text{a}}$	$2.46 \times 10^{-11\text{a}}$
Thermodynamic parameters			
Differential OCV $\frac{\partial U}{\partial c_s}$ [ $\text{V m}^{-3} \text{mol}^{-1}$ ]	Calculated with the data from [26]		
Kinetic parameters			
Reaction rate constant $k$ [ $\text{ms}^{-1}$ ]	$3 \times 10^{-11\text{c}}$	-	$1 \times 10^{-11\text{c}}$
Film resistance $R_f$ [ $\Omega \text{m}^2$ ]	0.0035 <sup>c</sup>	-	0 <sup>c</sup>
Double layer capacitance $C_{dl}$ [ $\text{Fm}^{-2}$ ]	0.2 <sup>d</sup>	-	1 <sup>d</sup>
Film capacitance $C_f$ [ $\text{Fm}^{-2}$ ]	0.1 <sup>d</sup>	-	-
Simulation parameters			
Frequency $f$ [Hz]	$5 \times 10^{-3} \sim 10^4$		
Number of frequency points $N_f$	70 (logarithmic)		

<sup>a</sup> assumed.

<sup>b</sup> calculated.

<sup>c</sup> Ref. [26].

<sup>d</sup> Ref. [27].

<sup>g</sup> bulk value from literature and effective value calculated using Bruggeman relation.

**Table 6**  
 Summary of the particle size distribution parameters.

Electrode Model	Anode			Cathode		
	UPS	PSD		UPS	PSD	
Case	A	B	C	A	B	C
$r_{p,DSO}$ [ $\mu\text{m}$ ]	6.1	6.1	6.1	3.8	3.8	3.8
$\bar{r}_p$ [ $\mu\text{m}$ ]	6.1	6.03	6.5	3.8	3.76	4.0
$r_{min}$ [ $\mu\text{m}$ ]	-	0.1	0.1	-	0.1	0.1
$N_p$ [-]	$7.3 \times 10^{14}$	$6.6 \times 10^{14}$	$3.2 \times 10^{14}$	$3.2 \times 10^{15}$	$3.0 \times 10^{15}$	$1.4 \times 10^{15}$
$\alpha$ [-]	-	$6.5 \times 10^{-6}$	$7.2 \times 10^{-6}$	-	$4.0 \times 10^{-6}$	$4.4 \times 10^{-6}$
$b$ [-]	-	5	2	-	5	2

diffusivity can be simply estimated by reading the time constants from the DRT spectrum. When the particle size is nonuniform and has a certain PSD, more information about the PSD is needed to estimate the diffusivity more accurately. In addition, to account for the diffusion in the liquid phase, an extended model is proposed to estimate the effective diffusivity in the liquid phase, the diffusivity can be estimated with the DRT spectrum, if the electrode thickness and porosity are known. For brevity, the proposed models and conclusions are summarized in Table 4.

### 3. Results and discussion

In this section, the proposed theory is first investigated and validated using synthetic simulation experiments, where the developed model will be tested in various cases. Then the theory will be applied to a commercial cell, the impedance and DRT spectra will be analyzed and the

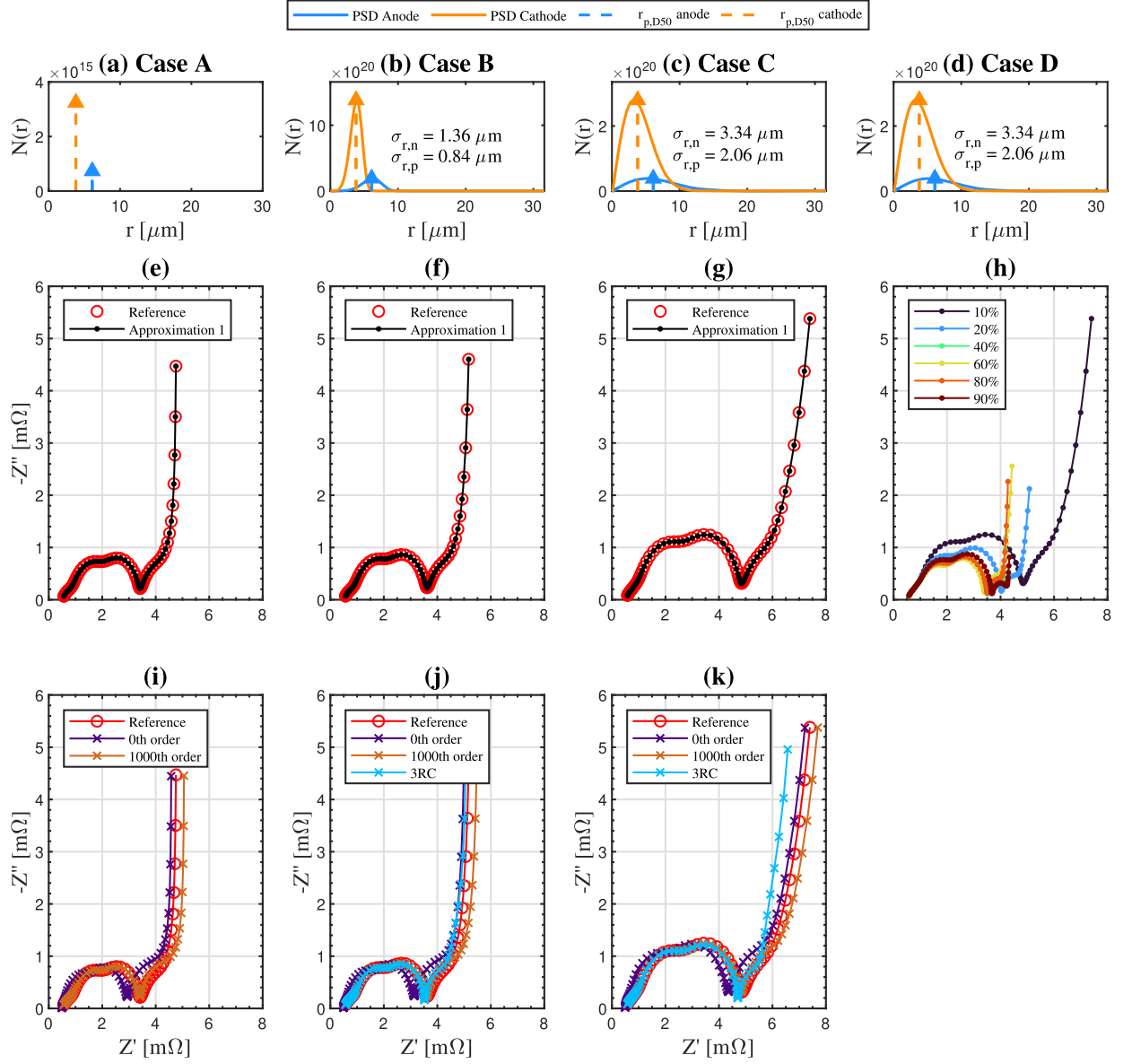


Fig. 3. Comparison of original model and the model with approximation 1. (a)–(d): the PSD used for the simulation; (e)–(g): comparison of the reference impedance with impedance generated using assumption one; (i)–(k): reconstructed impedance using different orders; (h): generated impedance at different SOC.

diffusion coefficients will be estimated (Table 6).

### 3.1. Synthetic simulation experiments

In this section, a synthetic simulation experiment will be conducted to validate the proposed theory and a detailed analysis of the results will be provided. To compare the results with regard to the PSD and show the effectiveness of the model when the PSD is considered, three cases are investigated. In case A, the UPS is assumed and simulated. In case B, a PSD with a moderate variance is assumed. In case C, the variance of the PSD is further increased. For both case B and C, the Weibull distribution is used, only the distribution parameters are varied. The thermodynamic parameters for case A, B and C correspond to 10% SOC. In addition, to investigate the SOC dependence of the liquid diffusion and ease the data

processing for the measurement data, the fourth case D will be investigated. In case D, the full order p2D impedance model is used to generate the impedance and all parameters are adopted from the case C except that the SOC is varied between 10% and 90% SOC. The common electrode parameters used for all cases are listed in Tables 5 and 6. The PSDs are generated using the following functions:

$$N(r) = \begin{cases} N_p \delta(r - r_{p,D50}) & (\text{UPS}) \\ N_p \frac{b}{a} \left(\frac{r}{a}\right)^{b-1} e^{-(r/a)^b} & (\text{PSD}) \end{cases} \quad (60)$$

where  $a$  and  $b$  are distribution parameters and  $r_{p,D50}$  is the median of the particle size. The distribution parameters are determined by the following relations:



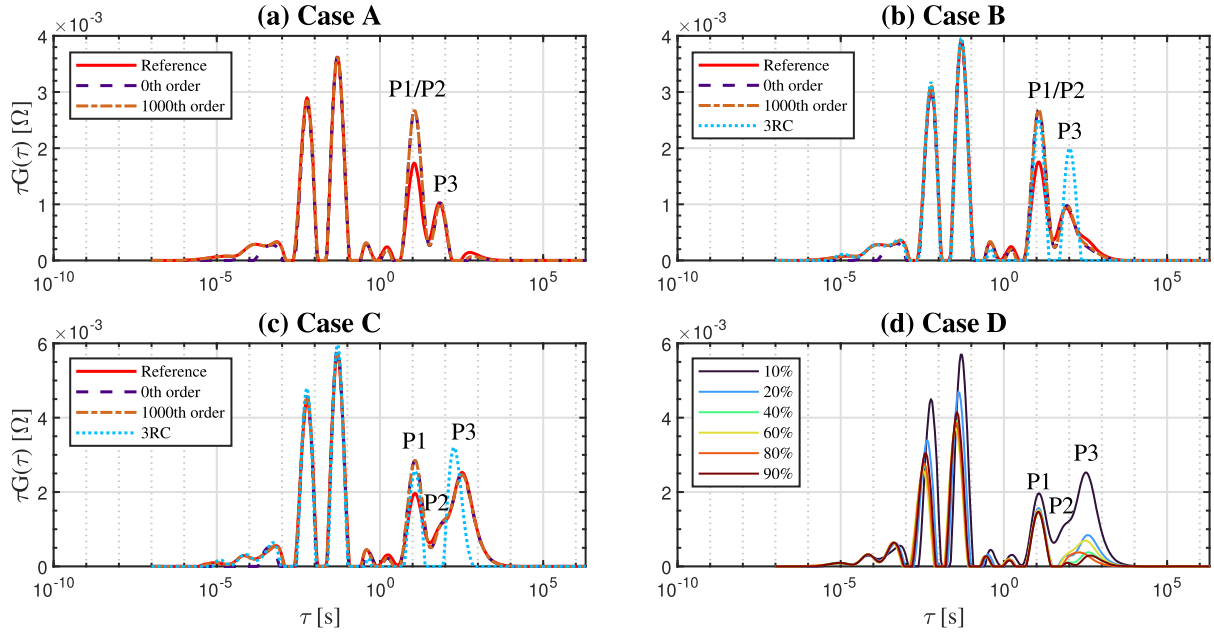


Fig. 4. Comparison of the the DRT spectra in various cases.

$$a = \frac{r_{p,D50} - r_{min}}{(\ln 2)^{\frac{1}{2}}} \quad (61)$$

$$N_p = \frac{\epsilon_s}{\int_0^{\infty} \frac{4}{3} \pi r^3 P(r) dr} \quad (62)$$

The generated UPS/PSDs for case A, B, C and D are shown in Fig. 3a–d. In both cases, the median of the particle radius is kept to the same value, which is namely the uniform particle size in case A.

The generated as well as the reconstructed impedances are shown in Fig. 3e–k. The comparison of the reference impedance with the impedance generated using the approximation 1 is plotted in Fig. 3e–g. No visible discrepancy can be observed, thus justifying the approximation 1 for the model development. Generally this approximation should be valid in most cases, as the time constants of the solid diffusion is usually orders of magnitude larger than that of the charge transfer and SEI. The simulation results for case D are shown in Fig. 3d and h.

To validate the theory on stage one dispersion, the impedance is reconstructed using Eq. (9) with the 0th order and 1000th order respectively. To test the performance of the 3RC approximation, the impedance is also reconstructed using the 3RC model. All reconstructed impedances together with the reference impedance is plotted in Fig. 3i–k. Besides, to better visualize the possible deviation between the various models, the corresponding DRT spectra are also calculated and shown in Fig. 4. In the low frequency area ( $\tau \geq 1$  s) in Fig. 4, two or three peaks can be recognized and are marked with P1, P2 and P3. By comparing the time constant of each peak with the simulation parameters, we can conclude that P1 represents the diffusion in the electrolyte, P2 is related to the solid phase diffusion in the cathode and P3 is attributable to the solid phase diffusion in the anode.

In case A (see Fig. 3i), we can see that there exists an obvious discrepancy between the reference impedance and the 0th order reconstruction, and only a minor discrepancy can be observed between the reference impedance and the 1000th order reconstruction. We assume that the discrepancy has two causes, namely the high frequency dispersion and the liquid phase diffusion. This can be confirmed by analyzing the DRT spectra in Fig. 4, where discrepancy between the reference and the 0th order reconstructed DRT can only be observed at

the peak P1/P2 representing the liquid diffusion and at the time constant  $10^{-4}$  s where the high frequency dispersion appears. It should be mentioned here that the peaks for the solid diffusion in the anode and diffusion in the electrolyte are overlapping because of similar time constants. In such case, it's not possible to separate the impedance contribution from the electrolyte and the anode. Although the magnitude of diffusion impedance cannot be precisely calculated, the time constant can be accurately reflected.

In case B (see Fig. 3j), instead of assuming a uniform particle size, the solid particles in the electrode are modeled using a size distribution. We can see from Fig. 3f that the impedance is quite similar to that in case A and a relatively clear transition from the Warburg region into the capacitive region can be observed, except that the impedance is slightly scaled because of the changed volumetric interfacial area. In the capacitive region, impact of the PSD is also observable. Instead of a nearly vertical line and an ideal capacitive behavior, the impedance shows a slow transition into the ideal capacitive region, which is believed to be caused by the larger particles with higher diffusion time constants. The DRT spectra for case B (see Fig. 4b) is similar to that of case A (see Fig. 4a), the time constants of all peaks are very similar. It is worth noting that the peak P3 in Fig. 4b is slightly wider than that of case A and extends further into the area of higher time constants. We believe that this is caused by the PSD and is in accordance with the observation in Fig. 4, where a slow transition into the capacitive region is observed.

In case C (see Fig. 3k), the transition is further blurred and there exists a nearly smooth transition from the Warburg region into the capacitive region. In Fig. 4c, the peak P2 is somehow shifted to the area of higher time constants and can be observed. We assume that this is again caused by the PSD, similar to the diffusion in the cathode. Similarly, we can see that the peak with the largest time constant is extended for about an order of magnitude compared to case A and the time constant defined by the peak is also shifted. The simulation results clearly indicate that although the median of the particle size and the diffusion coefficients are the same for all the three cases, the position of the peaks is changed due to the effect of the PSD. Therefore, estimating the diffusion coefficients with the UPS assumption will cause possible errors, the magnitude of the errors depend on the variance of the PSD. In

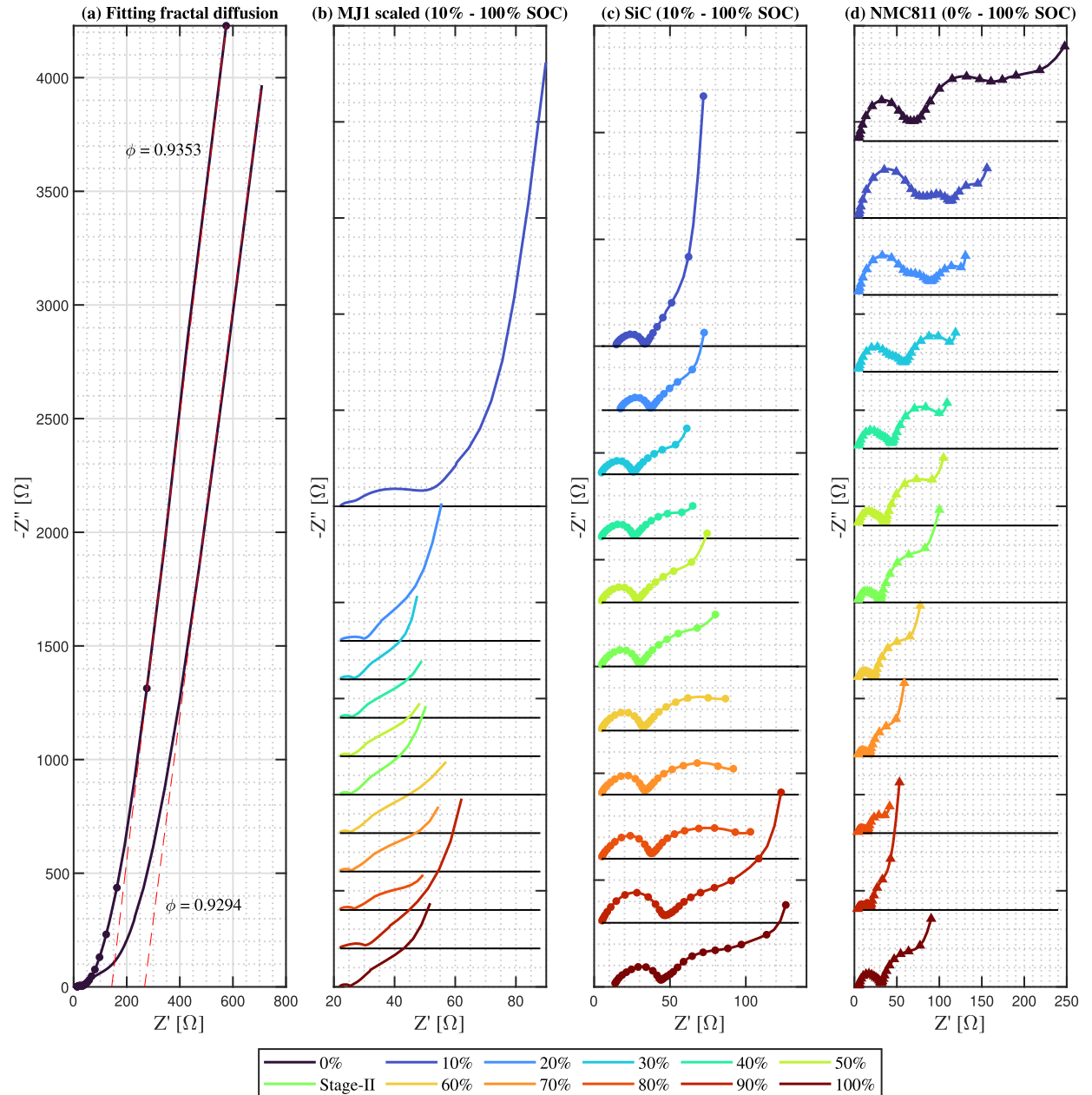
**Table 7**  
Description of the components in the coin cells.

Component	Description
Electrolyte	90 $\mu\text{L}$ of 1M LiPF <sub>6</sub> in 3:7 (wt:wt) ethylene carbonate (EC)/ethyl methyl carbonate (EMC) electrolyte (99.9% purity, Solvionic)
Separator	Celgard 2325
Counter-electrode	lithium-metal

case B and C, it can be seen that the 3RC model can well approximate the DRT spectra when the PSD is considered.

### 3.2. Application to commercial LIB

In this section, the developed theory will be applied to a commercial LIB, the diffusion coefficient of the Li-ion in the solid and liquid phase will be determined by evaluating the DRT spectra of the full cell and half cells.



**Fig. 5.** Scaled impedance of the full cell and impedance of the half cells. (a): Impedance of the full cell and half cell with SiC at 0% SOC used to determine the fractal exponent; (b): full cell impedance at 10% (uppermost)–100% (lowermost) SOC; (c): impedance of half cell with SiC at 10% (uppermost)–100% (lowermost) SOC; (d): impedance of half cell with NMC811 at 0% (uppermost)–100% (lowermost) SOC.

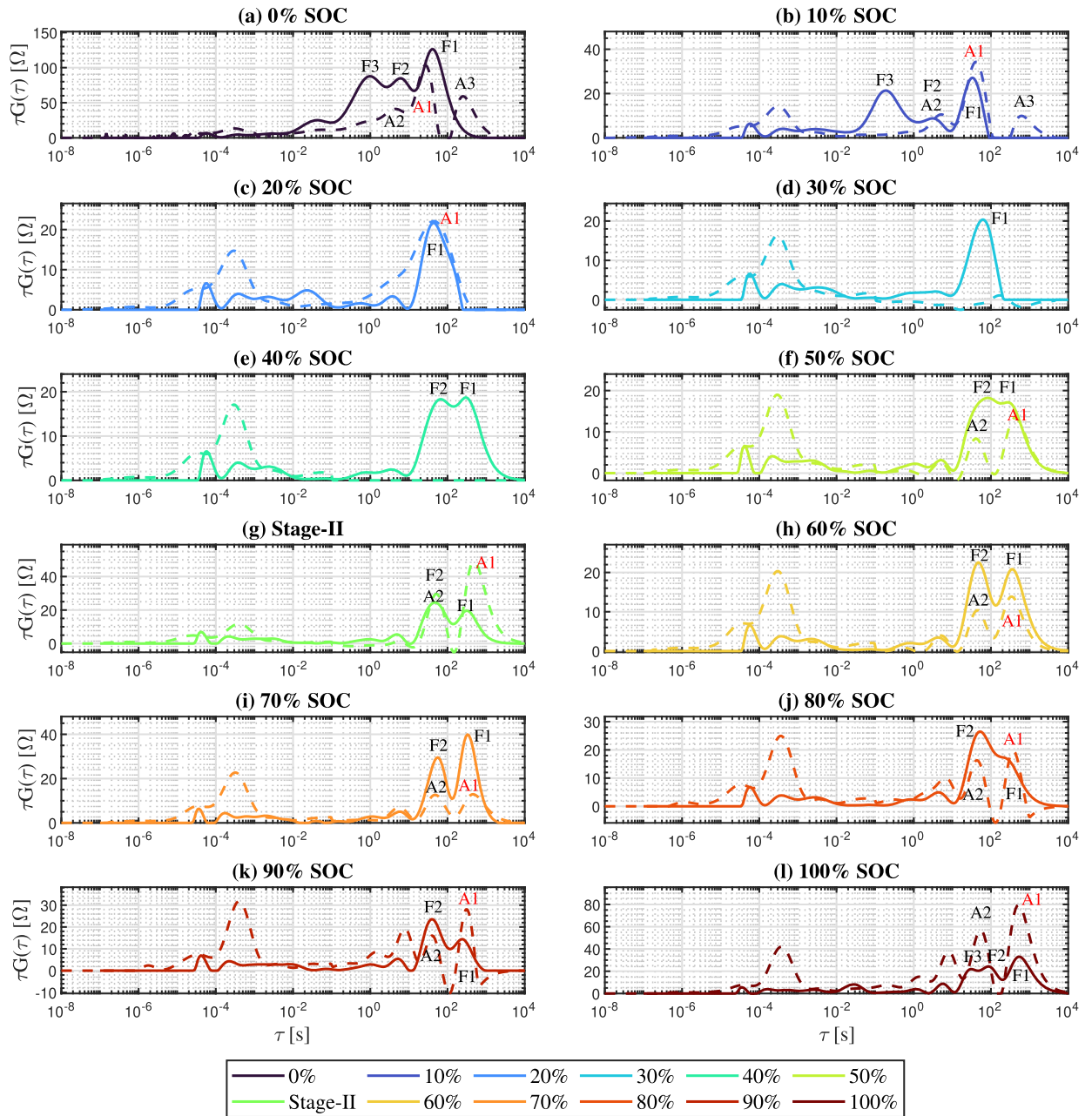


Fig. 6. DRT spectra of the full cell (solid line) and half cell (dashed line) with SiC at the lithiation state 2%–85.7%. The peaks that are attributed to the SiC are marked with red color. (For interpretation of the references to color in this figure legend, the reader is referred to the web version of this article.)

### 3.2.1. Experimental

The commercial cell investigated in this work is a 3.35 Ah NMC811/SiC LIB (INR18650-MJ1, LG Chem), which has been partly parametrized by Sturm et al. [26] and the fast kinetic processes have been investigated in our previous work as well [6]. First, the impedance of a full cell was measured at 0%–100% SOC with 10% increment under the temperature of 25 °C. Then another full cell from the same production lot was fully discharged and opened in an argon-filled glove-box, a piece of anode and cathode with a diameter of 10.95 mm were punched out of the electrode respectively. Because both sides of the electrodes were coated

with active material, so one side of each sample was scraped off to minimize the influence of the backside coating. Then all the components were assembled into a 2032-type coin cell and a detailed description of the components can be found in Table 7. The assembled coin cells were rested for 24 h to improve wetting of the electrode and separator. Next, the coin cells were charged/discharged with a current of 800  $\mu$ A to the lithiation state which corresponds to 100% SOC in the full cell. Then the impedance of the coin cells at the lithiation states which correspond to the 0–100% SOC in the full cell was measured under 25 °C. In addition, to characterize the diffusion of the Li-ions in graphite at the stage-II

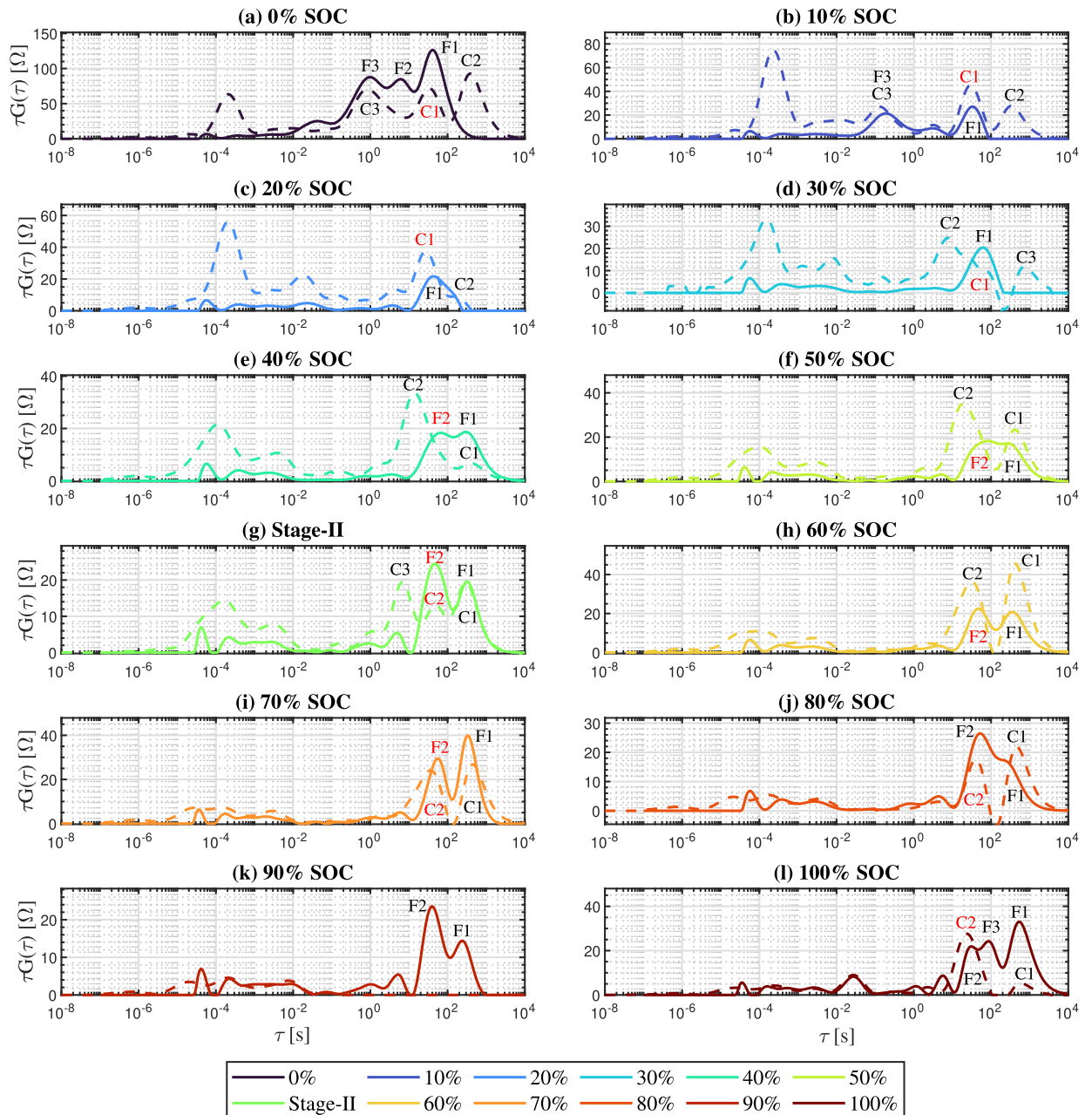


Fig. 7. DRT spectra of the full cell (solid line) and half cell (dashed line) with NMC811 at the lithiation state 22.2%-94.2%. The peaks that are attributed to the NMC811 are marked with red color. (For interpretation of the references to color in this figure legend, the reader is referred to the web version of this article.)

(LiC<sub>12</sub>), the impedance of the full cell at ca. 56% SOC and the coin cells at the lithiation state which corresponds to the same SOC in the full cell were measured at 25 °C. Between each two SOC adjustments, the cells were relaxed for 6h.

For the GITT experiment, the same coin cells were used and the test was conducted at the same SOC points as for the impedance measurement. At each SOC point, the coin cell was first subjected to a charging current pulse with a duration of 600 s and an amplitude of 200 μA. Subsequently, the coin cell was relaxed for 2 h and then subjected to a discharging current pulse with the same duration and amplitude. The

same procedure was repeated at each SOC point. At the upper voltage limit only discharging current pulse and at the lower voltage limit only charging current pulse was applied to protect the coin cell from overcharging and overdischarging.

The SOC adjustment, impedance measurement and GITT experiment were all performed on an electrochemical workstation (VMP3, Biologic), the frequency range of the impedance measurement was 10 kHz - 0.5 mHz for the full cell and 100 kHz - 0.5 mHz for the coin cells, the amplitude of the potential perturbation is 10 mV.

### 3.2.2. Results

In this section, the measured impedance data will be evaluated, the DRT spectra will be calculated and used to estimate the solid diffusion coefficients of Li-ions in the SiC and NMC811. In the rest of the work, for the purpose of brevity and consistency, we will refer to the lithiation state of the SiC and NMC811 in the half cells by using the corresponding SOC value in the full cell. The measured impedance data for half and full cells are shown in Fig. 5. The impedances at different SOCs are plotted against a shifted x-axis to achieve a better view and ease the comparison.

From Fig. 5, it can be clearly seen that while the full cell impedance is subjected to little influence from the liquid phase diffusion, the half cell impedance is strongly affected by the liquid phase diffusion, as in the low frequency range a big bump/half circle can be observed. For the SiC, except at the 0%–20% and 100% SOC, the rest of the impedance data is dominated by the liquid phase diffusion, which is superimposed on the solid diffusion impedance. For the NMC811, similar behavior can be observed, where at 0%–90% SOC the impedance is strongly influenced by the liquid diffusion.

Before the DRT spectra are calculated, a pre-processing step is carried out to characterize the fractal diffusion behavior in the solid phase and the fractal exponent is calculated. For the full cell, an obvious fractal diffusion can be recognized at the 0% SOC. In the capacitive region (see Fig. 5a), instead of an ideal capacitance with a 90° phase angle, a constant phase behavior with an angle smaller than 90° can be observed and the fractal exponent is calculated to be 0.9294. Similarly, the estimated fractal exponent is 0.9353 for the SiC electrode. Because the capacitive region of the NMC811 half cell impedance cannot guarantee a reliable estimation of the fractal exponent, no fractal diffusion is assumed for the NMC811. The calculated fractal exponents are further used for the DRT calculation. It is worth mentioning here that including the fractal exponents into the DRT calculation is crucial for the results, because without considering the fractal diffusion behavior the constant phase behavior will be misinterpreted as a part of the Warburg region and peaks with extremely high time constants and large magnitude will be obtained, which will lead to erroneous and unrealistic results.

Due to the fact that no precise information about the magnitude and time constants for the liquid phase diffusion is available, the influence of the liquid diffusion cannot be directly evaluated. Recalling the results of the synthetic simulation experiments, we can find that except for very high or low SOCs, the peak for the liquid diffusion only shows a tiny change, which can be approximately regarded as invariant in the mid SOC range. This feature can be used to remove the contribution of the liquid phase diffusion effectively even without precise information about the liquid phase diffusion. First, one specific SOC value is chosen for each half cell at which the impedance has the least solid phase diffusion impedance and the diffusion is dominated by the liquid diffusion. Then the DRT spectrum of the chosen SOC is subtracted from all DRT spectra in the mid SOC range to derive the approximated spectra without the influence of the liquid diffusion.

For the SiC, the impedance at 40% SOC is chosen as the reference and the DRT spectrum at 40% is subtracted from the spectra at the 30%–90% SOC. For the NMC811, the impedance at 90% SOC is chosen and the DRT spectrum at 90% SOC is subtracted from the spectra at 30%–90% SOC. The resulting DRT spectra are shown in Figs. 6 and 7 for the SiC and NMC811 respectively. In the following section, the resulting DRT spectra will be analyzed, the peak attribution will be performed and the solid diffusion coefficients will be estimated.

**0% SOC** For the SiC, a dominating solid diffusion impedance can be seen (see Fig. 5a) and in the DRT spectra a series of peaks with decreasing magnitude and time constants can be observed, which is a typical sign of solid diffusion. As a result, peak A1 is attributed to the solid diffusion in the SiC, the peaks F2 and A2 are caused by the frequency dispersion of the solid diffusion and will be excluded from further analysis. Peak F3 is missing in the SiC spectra but appears in the full cell, we will return to the attribution of the peak F3 later. Peak A3 only appears in the half cell, so it is attributed to the liquid diffusion in

the half cell. It is worth noticing that peak A1 doesn't fully coincide with the peak F1, we assume the deviation arises from the contribution of the NMC811, this conclusion will be confirmed later. For the NMC811, C3 coincides with the peak F3, considering that this peak is later shifted to the area of smaller time constants and the magnitude also decreases, we attributed F3 and C3 to the charge transfer in the NMC811, which has been investigated and confirmed in our previous work as well [6]. Peak C1 and F1 share the same time constant, so C1 is attributed to the solid diffusion in the NMC811, thus explaining the discrepancy between the peak A1 and F1. C2 has a similar time constant to that of A3, so it is attributed to the liquid diffusion in the half cell.

**10% SOC** Similar to 0% SOC, the SiC half cell shows a significant solid diffusion behavior (see Fig. 5c), as a result, the peaks F1 and A1 are attributed to the solid diffusion in the SiC. For the NMC811 (see Fig. 5d), the magnitude of the peak C1 decreases, which is in accordance with the impedance change of the NMC811 half cell. Hence, peak C1 is attributed to the NMC811. In both half cells, the magnitude of peak A1 and C1 is larger than that of the peak F1, hence, we believe that the liquid diffusion in the half cell has also contributed to the peak A1/C1.

**20% SOC** From the impedance plot in Fig. 5c it can be seen that solid diffusion impedance for the SiC further decreases (see the decreased Warburg impedance), which is most likely caused by the decreasing dOCV. In the DRT spectra, the peak A1 and F1 are almost overlapping (see Fig. 6c), so the peak A1/F1 is attributed to the solid diffusion in the SiC. For the NMC811 (see Fig. 7c), the peaks C1 and F1 share the same time constant, hence they are also attributed to the solid diffusion in the NMC811.

**30% SOC** Because the DRT spectrum at the 30% SOC has been chosen as the reference for the SiC, no information about solid diffusion in the SiC is available. For the NMC811 (see Fig. 7d), F1 and C1 have the same time constant, as a result, F1/C1 is attributed to the solid diffusion in the NMC811, while C2/C3 is attributed to the rest contribution from the liquid diffusion.

**40%–90% SOC** In this SOC range, all DRT spectra have a similar form and we choose to perform the peak attribution altogether for all these SOC values. In the DRT spectra of either material (see Figs. 6e–k and 7e–k), the peaks A1, A2, C1, C2, F1 and F2 are existent at the same time, making a direct peak attribution rather difficult. Therefore, we choose to conduct the peak attribution in an indirect way.

In the 40%–90% SOC range, we can notice that the peak F1 and F2 all have comparable magnitude, according to Eq. (27), for the magnitude of the prominent peak the following relation holds:

$$H_1 \propto \frac{\left(-\frac{\partial U}{\partial v_s}\right)}{D_s} \quad (63)$$

where  $H_1$  is the magnitude of the prominent peak. This relation indicates if two processes have comparable peak magnitude, then the process with higher diffusion coefficient should also have a higher dOCV value. In our case, the dOCV of SiC in the 40%–90% SOC range is much smaller than that of the NMC811, which means the SiC should also have a smaller solid diffusivity and a higher time constant. As a result, we attribute F2/C2 to the solid diffusion in the NMC811 and F1/A1 to the solid diffusion in the SiC. It is worth noticing that at the stage-II, the dOCV of the SiC is very close to that of the NMC811. Under such condition, if the diffusion coefficient (time constant) doesn't change, then the peak magnitude should increase significantly. At stage-II, it can be observed that peak A1 has increased significantly, thus it is also attributed to the SiC.

**100% SOC** By inspecting the DRT spectra of NMC811 (see Fig. 7l), we can easily attribute the peak C2/F2 to the solid diffusion in the NMC811. Then we can exclude the possibility that the peak F3 is attributed to the solid diffusion in the SiC, because the dOCV value and the time constant (no matter for F1/F3) both increase, as a result, the peak magnitude should increase as well. Hence, the peak A1/F1 is attributed to the solid diffusion in the SiC.

The results for the peak attribution and time constants for the SiC and

**Table 8**  
 Summary of the peak attribution.

SOC	SiC		NMC811	
	Peak attribution	Time constants [s]	Peak attribution	Time constants [s]
0%	A1	27	C1	39
10%	A1	39	C1	32
20%	A1	42	C1	27
30%	N.A.	N.A.	C1	62
40%	N.A.	N.A.	F2	62
50%	A1	359	F2	39
60%	A1	298	F2	32
70%	A1	393	F2/C2	35
80%	A1	393	C2	47
90%	A1	327	N.A.	N.A.
100%	A1	519	C2	27
stage-II	A1	431	F2/C2	38

NMC811 are summarized in the following Table 8.

After the peak attribution has been performed and the time constants for the peaks have been read, the solid diffusion coefficients can be estimated. Heenan et al. investigated the solid particle geometry and the particle size distribution of the same cell used in the present work [28]. According to the measurement of the particle size distribution, both the SiC and NMC811 have a wide particle size distribution and thus a large particle radius variance. As a result, we use the developed 3RC assumption to estimate the solid diffusion coefficients. Besides, the fractal diffusion behavior is also accounted for when estimating the diffusion coefficients. The estimated solid diffusion coefficients with DRT and GITT for the SiC and NMC811 are shown in Fig. 8.

For the SiC, it can be observed that the solid diffusion coefficients estimated at 0.2%, 8.7%, 47.8% (stage-II) and 85.2% lithiation state with both DRT and GITT are close to each other. The estimated values at the stage-II and 85.2% lithiation state are ca.  $1.8 \times 10^{-10} \text{ cm}^2 \text{ s}^{-1}$  and  $1 \times 10^{-10} \text{ cm}^2 \text{ s}^{-1}$  respectively, which are comparable to the values ( $1.8 \times 10^{-10} \text{ cm}^2 \text{ s}^{-1}$  and  $0.5 \times 10^{-10} \text{ cm}^2 \text{ s}^{-1}$ ) measured by Umegaki et al. [29] with the  $\mu^+$ SR method. Similar values have also been found for the same lithiation states in Cabañero et al. [7], Ecker et al. [30], Schmalstieg and Sauer [31]. Interestingly, the diffusion coefficients estimated at other lithiation states using GITT are much lower than that using the DRT. Furthermore, the estimated values with GITT using the charging and discharging current pulse generally follow a similar pattern. The shown pattern resembles the differential open circuit voltage (dOCV) of the anode, which has been observed by Cabañero et al. as well [7]. We believe that this phenomenon can be explained by analyzing the dOCV and the influence of the liquid phase diffusion. To ease the analysis, the

dOCV of the same material is plotted in the same figure in Fig. 8.

It can be seen in Fig. 8 that at each lithiation state where the estimated values using DRT and GITT coincide with each other, a peak can be observed on the dOCV curve. A peak on the dOCV curve indicates that when the electrode is perturbed at this lithiation state, the electrode will give a higher voltage response compared to other lithiation states. The higher voltage response will manifest itself as a higher solid diffusion impedance (see Fig. 5) and a higher diffusion-induced overpotential in the GITT experiment. On the other hand, during the GITT experiment, the overpotential will be inevitably influenced by the liquid diffusion, which is invisible in GITT experiment but can be well observed in impedance spectra (see Fig. 5). As a result, the total diffusion overpotential is consisted of the contribution of the solid and liquid diffusion:

$$\Delta E_{t,diff} = \Delta E_{t,diff,l} + \Delta E_{t,diff,s} \quad (64)$$

At the lithiation states with higher dOCV values, the  $\Delta E_{t,diff,s}$  is non-negligible or is even dominating, the estimated diffusion coefficients are close to the true values. On the contrary, at the lithiation states with low dOCV values,  $\Delta E_{t,diff,l} \gg \Delta E_{t,diff,s}$  so that the following relation is valid:

$$D_{s,GITT} \propto \left( \frac{\Delta E_s}{\Delta E_{t,diff,l} + E_{t,diff,s}} \right)^2 \ll \left( \frac{\Delta E_s}{\Delta E_{t,diff,s}} \right)^2 \quad (65)$$

This equation explains the phenomenon that the solid diffusion coefficients measured at lithiation states with higher dOCV values are much higher than that measured at lithiation states with low dOCV values. As a result, the measured diffusion coefficients with GITT follow the pattern of the dOCV curve, which has also been observed in Cabañero et al. [7].

For the NMC811, the similar phenomenon can be seen. At the 22.2%, 36.6% and 51% lithiation states with a higher dOCV value, the diffusion coefficients estimated with the DRT and GITT have similar values. At other lithiation states, the values estimated with GITT are much lower than that with the DRT as expected. The measured solid diffusion coefficients in the present work are comparable to the values found in Chen et al. [32], Noh et al. [33].

In summary, the DRT method can be applied to determine the solid diffusion coefficient even if the liquid diffusion exists, while the GITT is only able to estimate the diffusion coefficient when the diffusion is not or less affected by the liquid diffusion. At the lithiation states with low dOCV values, the diffusion coefficients will be strongly underestimated due to the influence of the liquid diffusion.

#### 4. Conclusions

In the present work, a theory is proposed to investigate the diffusion processes in a LIB using the DRT spectrum and with a physics-based

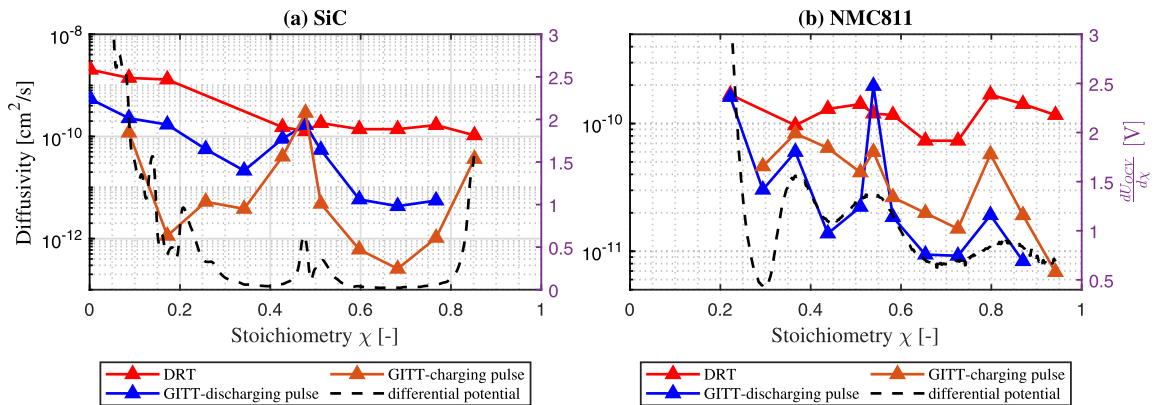


Fig. 8. Calculated solid diffusion coefficient of Li-ions in (a): SiC and (b): NMC811 at different lithiation states.

impedance model. Furthermore, an analytical expression for the DRT spectrum is proposed, which has related the electrochemical parameters to the DRT spectrum in an explicit way. Subsequently, simulation and lab experiments are conducted to validate the proposed model and the solid diffusivity of SiC and NMC811 is estimated using the developed model. Besides, GITT experiment has been conducted to estimate the solid diffusion coefficients for the SiC and NMC811. The results indicate that the GITT can significantly underestimate the solid diffusion coefficients when the electrode is subjected to the influence from the liquid diffusion and the dOCV value is low. Compared to the GITT which is based on the voltage measurement in time domain, DRT is based on the time constant and does not directly rely on the voltage measurement in time domain, even if the liquid diffusion exists, the solid diffusion coefficient can be reliably estimated.

#### CRediT authorship contribution statement

**Yulong Zhao:** Conceptualization, Methodology, Software,

Investigation, Validation, Data curation, Formal analysis, Writing – original draft, Project administration. **Simon Kücher:** Investigation, Resources, Writing – review & editing. **Andreas Jossen:** Supervision, Writing – review & editing.

#### Declaration of Competing Interest

The authors declare that they have no known competing financial interests or personal relationships that could have appeared to influence the work reported in this paper.

#### Acknowledgment

This research is funded by the China Scholarship Council (CSC), the author gratefully thanks for the support and funding from CSC.

### Appendix A. Derivation of series expansion for the diffusion impedance

#### A1. Planar solid particle

Obviously the impedance expression for planar solid particle has a pole of zero, the corresponding expansion coefficient is calculated as:

$$b_0 = \lim_{s \rightarrow 0} \frac{\coth(\sqrt{s\tau})}{\sqrt{s\tau}} = \frac{1}{\tau_0} \quad (\text{A.1})$$

The higher order poles are determined by solving the following equation:

$$\sinh\sqrt{a_n\tau_0} = 0 \Rightarrow a_n = -\frac{n^2\pi^2}{\tau_0} \quad (n = 1, 2, 3, \dots) \quad (\text{A.2})$$

The corresponding expansion coefficients are calculated with the same principle:

$$b_n = \lim_{s \rightarrow -a_n} (s - a_n) \frac{\coth(\sqrt{s\tau})}{\sqrt{s\tau}} = \frac{2}{\tau_0} \quad (\text{A.3})$$

As a result the expansion can be rewritten as:

$$\frac{\coth(\sqrt{s\tau})}{\sqrt{s\tau}} = \frac{b_0}{s} + \sum_{n=1}^{\infty} \frac{b_n}{s - a_n} = \frac{1}{s\tau_0} + \sum_{n=1}^{\infty} \left( -\frac{b_n}{a_n} \right) \frac{1}{1 + s\left(-\frac{1}{a_n}\right)} \quad (\text{A.4})$$

If the capacitance term is subtracted from the equation above and the DRT is conducted, the following equation can be obtained:

$$G(\tau) = \sum_{n=1}^{\infty} -\frac{b_n}{a_n} \delta\left(\tau + \frac{1}{a_n}\right) \quad (\text{A.5})$$

The dispersion time constants given as:

$$\tau_n = -\frac{1}{a_n} = \frac{\tau_0}{n^2\pi^2} \quad (\text{A.6})$$

The dispersion magnitude  $R_n$  is calculated as:

$$R_n = -\frac{b_n}{a_n} = \frac{2}{n^2\pi^2} \quad (\text{A.7})$$

#### A2. Cylindrical solid particle

Like the planar solid particle, for cylindrical particle there exists also a pole of zero, the corresponding coefficient is given as:

$$b_0 = \lim_{s \rightarrow 0} \frac{I_0(\sqrt{s\tau_0})}{\sqrt{s\tau_0} I_1(\sqrt{s\tau_0})} = \frac{2}{\tau_0} \quad (\text{A.8})$$

The higher order poles are calculated by solving the following equation:

$$I_1(\sqrt{s\tau_0}) = 0 \quad (\text{A.9})$$

Because the modified Bessel function above has an imaginary argument, it cannot be solved conveniently, therefore the following relation is applied to simplify the equation:

$$I_\alpha(ix) = i^{-\alpha} J_\alpha(-x) \quad (\text{A.10})$$

where  $J_\alpha$  is the Bessel function of the order  $\alpha$ . As a result Eq. (A.9) can be transformed into the following equation:

$$J_1\left(-\sqrt{|a_n|\tau_0}\right) = 0 \quad (\text{A.11})$$

The equation above can be readily solved using a look-up table for zeros of Bessel functions. If we assume the zeros of the Bessel function to be  $\lambda_n$ , then the poles can be expressed as:

$$a_n = -\frac{\lambda_n^2}{\tau_0} \quad (\text{A.12})$$

The expansion coefficients are calculated as:

$$b_n = \lim_{s \rightarrow a_n} (s - a_n) \frac{J_0(\sqrt{s\tau_0})}{\sqrt{s\tau_0} I_1(\sqrt{s\tau_0})} = \frac{2}{\tau_0} \quad (\text{A.13})$$

With the same procedures as shown for planar particles, the dispersion time constants and magnitude are given as:

$$\tau_n = -\frac{1}{a_n} = \frac{\tau_0}{\lambda_n^2} \quad (\text{A.14})$$

$$R_n = -\frac{b_n}{a_n} = \frac{2}{\lambda_n^2} \quad (\text{A.15})$$

### A3. Spherical solid particles

The impedance expression has a pole of zero, and the corresponding coefficient is calculated as:

$$b_0 = \lim_{s \rightarrow 0} s \frac{\tanh(\sqrt{s\tau_0})}{\sqrt{s\tau_0} - \tanh(\sqrt{s\tau_0})} = \frac{3}{\tau_0} \quad (\text{A.16})$$

The higher order poles are determined by solving the following equation:

$$\sqrt{a_n\tau_0} - \tanh(\sqrt{a_n\tau_0}) = 0 \quad (\text{A.17})$$

Note that  $\tanh(ix) = i\tan(x)$ , the equation above can be simplified to:

$$\sqrt{|a_n|\tau_0} - \tan\left(\sqrt{|a_n|\tau_0}\right) = 0 \quad (\text{A.18})$$

By using look-up tables or numerical algorithms the equation can be solved conveniently. If we assume the solutions of equation  $\tan(x) = x$  to be  $\lambda_n$ , then the poles are given as:

$$a_n = -\frac{\lambda_n^2}{\tau_0} \quad (\text{A.19})$$

The expansion coefficients are:

$$b_n = \lim_{s \rightarrow a_n} (s - a_n) \frac{\tanh(\sqrt{s\tau_0})}{\sqrt{s\tau_0} - \tanh(\sqrt{s\tau_0})} = \frac{2}{\tau_0} \quad (\text{A.20})$$

Similarly, the dispersion time constants and magnitude are calculated as:

$$\tau_n = -\frac{1}{a_n} = \frac{\tau_0}{\lambda_n^2} \quad (\text{A.21})$$

$$R_n = -\frac{b_n}{a_n} = \frac{2}{\lambda_n^2} \quad (\text{A.22})$$

### A4. Derivation of dispersion coefficients

According to the theorem on residue of composition function [34], the expansion coefficients can be calculated in the following way:

$$b_n = \text{Res}(Z_e(Y_{v,loc}), A_n) Y_{v,loc}(a_n)' \quad (\text{A.23})$$

where  $a_n$  and  $b_n$  are the corresponding expansion pole and coefficient of each process. When the frequency is not extremely low and the capacitive effect can be neglected, the particle impedance can be approximated as a sum of RC elements, the admittance is thus expressed as:

$$Y_{v,loc} = \left( \sum_{i=1}^{\infty} \frac{R_i}{1 + s\tau_i} \right)^{-1} \quad (\text{A.24})$$



If we consider the  $k$ -th RC element, the impedances of all the RC elements with smaller time constants can be approximated as an ohmic resistance  $R_{k-1}$  and the that of the RC elements with larger time constants can be approximated to be zero, therefore we have:

$$Y_{v,loc} = \left( R_{k-1} + \frac{R_k}{1 + s\tau_k} \right)^{-1} \quad (\text{A.25})$$

The pole corresponding to  $a_k$  is obtained by solving the following equation:

$$-\frac{k^2 \pi^2}{\Gamma_c^2 \left( \frac{1}{k} + \frac{1}{\sigma} \right)} = \left( \sum_{i=1}^{\infty} \frac{R_i}{1 + s\tau_i} \right)^{-1} \quad (\text{A.26})$$

Then the coefficient is calculated to be:

$$b_k = \frac{B_k R_k \tau_k}{(R_k + R_{k-1} - R_{k-1} a_k \tau_k)^2} \quad (\text{A.27})$$

The equation above shows that the dispersion coefficients decreases with the corresponding time constants. Noting that usually the diffusion time constants are orders of magnitude greater than that of charge transfer and SEI process, the dispersion for diffusion can be neglected in practice.

## References

- [1] A. Lasia, Electrochemical impedance spectroscopy and its applications. Modern Aspects of Electrochemistry, Springer, 2002, pp. 143–248.
- [2] J.R. Macdonald, E. Barsoukov, Impedance spectroscopy: theory, experiment, and applications, History 1 (8) (2005) 1–13.
- [3] B.A. Boukamp, Derivation of a distribution function of relaxation times for the (fractal) finite length warburg, Electrochim. Acta 252 (2017) 154–163.
- [4] B.A. Boukamp, A. Rolle, Use of a distribution function of relaxation times (DFRT) in impedance analysis of SOFC electrodes, Solid State Ionics 314 (2018) 103–111.
- [5] J. Illig, J.P. Schmidt, M. Weiss, A. Weber, E. Ivers-Tiffée, Understanding the impedance spectrum of 18650 lifePO4-cells, J. Power Sources 239 (2013) 670–679.
- [6] Y. Zhao, V. Kumtepe, S. Ludwig, A. Jossen, Investigation of the distribution of relaxation times of a porous electrode using a physics-based impedance model, J. Power Sources 530 (2022) 231250.
- [7] M.A. Cabañero, N. Boaretto, M. Röder, J. Müller, J. Kalló, A. Latz, Direct determination of diffusion coefficients in commercial li-ion batteries 165 (5) (2018) A847–A855, <https://doi.org/10.1149/2.0301805jes>.
- [8] D.W. Dees, S. Kawauchi, D.P. Abraham, J. Prakash, Analysis of the galvanostatic intermittent titration technique (GITT) as applied to a lithium-ion porous electrode 189 (1) (2009) 263–268, <https://doi.org/10.1016/j.jpowsour.2008.09.045>.
- [9] K.M. Shaju, G.V. Subba Rao, B.V.R. Chowdari, Li ion kinetic studies on spinel cathodes,  $\text{Li}(\text{M}_{1/6}\text{Mn}_{11/6})\text{O}_4$  ( $\text{M} = \text{Mn, Co, CoAl}$ ) by GITT and EIS 13 (1) (2003) 106–113, <https://doi.org/10.1039/B207407A>.
- [10] J.H. Park, H. Yoon, Y. Cho, C.-Y. Yoo, Investigation of lithium ion diffusion of graphite anode by the galvanostatic intermittent titration technique 14 (16) (2021), <https://doi.org/10.3390/ma14164683.34443205>
- [11] C.-H. Chen, F. Brosa Planella, K. O'Regan, D. Gastol, W.D. Widanage, E. Kendrick, Development of experimental techniques for parameterization of multi-scale lithium-ion battery models 167 (8) (2020) 080534, <https://doi.org/10.1149/1945-7111/ab9050>.
- [12] S.D. Kang, J.J. Kuo, N. Kapate, J. Hong, J. Park, W.C. Chueh, Galvanostatic intermittent titration technique reinvented: part II. Experiments 168 (12) (2021) 120503, <https://doi.org/10.1149/1945-7111/ac3939>.
- [13] C.-J. Wen, B.A. Boukamp, R.A. Huggins, W. Weppner, Thermodynamic and mass transport properties of "LiAl" 126 (12) (1979) 2258–2266, <https://doi.org/10.1149/1.2128939>.
- [14] M. Doyle, T.F. Fuller, J. Newman, Modeling of galvanostatic charge and discharge of the lithium/polymer/insertion cell, J. Electrochem. Soc. 140 (6) (1993) 1526.
- [15] M. Doyle, J. Newman, Modeling the performance of rechargeable lithium-based cells: design correlations for limiting cases, J. Power Sources 54 (1) (1995) 46–51.
- [16] M. Doyle, J. Newman, A.S. Gozdz, C.N. Schmutz, J.-M. Tarascon, Comparison of modeling predictions with experimental data from plastic lithium ion cells, J. Electrochem. Soc. 143 (6) (1996) 1890–1903.
- [17] G.B. Arfken, H.J. Weber, Mathematical methods for physicists, 1999.
- [18] J. Song, M.Z. Bazant, Electrochemical impedance imaging via the distribution of diffusion times, Phys. Rev. Lett. 120 (11) (2018) 116001.
- [19] J. Huang, J. Zhang, Theory of impedance response of porous electrodes: simplifications, inhomogeneities, non-stationarities and applications, J. Electrochem. Soc. 163 (9) (2016) A1983.
- [20] J. Song, M.Z. Bazant, Effects of nanoparticle geometry and size distribution on diffusion impedance of battery electrodes, J. Electrochem. Soc. 160 (1) (2012) A15.
- [21] E. Quattrocchi, T.H. Wan, A. Curcio, S. Pepe, M.B. Effat, F. Ciucci, A general model for the impedance of batteries and supercapacitors: the non-linear distribution of diffusion times, Electrochim. Acta 324 (2019) 134853.
- [22] T.H. Wan, M. Saccoccio, C. Chen, F. Ciucci, Influence of the discretization methods on the distribution of relaxation times deconvolution: implementing radial basis functions with DRTtools, Electrochim. Acta 184 (2015) 483–499.
- [23] X. Zhou, J. Huang, Z. Pan, M. Ouyang, Impedance characterization of lithium-ion batteries aging under high-temperature cycling: importance of electrolyte-phase diffusion, J. Power Sources 426 (2019) 216–222.
- [24] G. Sikha, R.E. White, Analytical expression for the impedance response of an insertion electrode cell, J. Electrochem. Soc. 154 (1) (2006) A43.
- [25] G. Sikha, R.E. White, Analytical expression for the impedance response for a lithium-ion cell, J. Electrochem. Soc. 155 (12) (2008) A893.
- [26] J. Sturm, A. Rheinfeld, I. Zilberman, F.B. Spingler, S. Kosch, F. Frie, A. Jossen, Modeling and simulation of inhomogeneities in a 18,650 nickel-rich, silicon-graphite lithium-ion cell during fast charging, J. Power Sources 412 (2019) 204–223.
- [27] L.O. Valoen, J.N. Reimers, Transport properties of LiPF6-based Li-ion battery electrolytes, J. Electrochem. Soc. 152 (5) (2005) A882.
- [28] T. Heenan, A. Jnawali, M. Kok, T.G. Tranter, C. Tan, A. Dimitrijevic, R. Jervis, D. Brett, P.R. Shearing, An advanced microstructural and electrochemical datasheet on 18,650 Li-ion batteries with nickel-rich NMC811 cathodes and graphite-silicon anodes, J. Electrochem. Soc. 167 (14) (2020) 140530.
- [29] I. Umegaki, S. Kawauchi, H. Sawada, H. Nozaki, Y. Higuchi, K. Miwa, Y. Kondo, M. Månsson, M. Telling, F.C. Coomer, et al., Li-ion diffusion in li intercalated graphite  $\text{C}_6$  Li and  $\text{C}_{12}$  Li probed by  $\mu$ -SR, Phys. Chem. Chem. Phys. 19 (29) (2017) 19058–19066.
- [30] M. Ecker, S. Käbitz, I. Laresgoiti, D.U. Sauer, Parameterization of a physico-chemical model of a lithium-ion battery: II. Model validation, J. Electrochem. Soc. 162 (9) (2015) A1849.
- [31] J. Schmalstieg, D.U. Sauer, Full cell parameterization of a high-power lithium-ion battery for a physico-chemical model: part II. Thermal parameters and validation, J. Electrochem. Soc. 165 (16) (2018) A3811.
- [32] C.-H. Chen, F.B. Planella, K. O'Regan, D. Gastol, W.D. Widanage, E. Kendrick, Development of experimental techniques for parameterization of multi-scale lithium-ion battery models, J. Electrochem. Soc. 167 (8) (2020) 080534.
- [33] H.-J. Noh, S. Youn, C.S. Yoon, Y.-K. Sun, Comparison of the structural and electrochemical properties of layered Li [nixcoymnz]  $\text{O}_2$  ( $X = 1/3, 0.5, 0.6, 0.7, 0.8$  and 0.85) cathode material for lithium-ion batteries, J. Power Sources 233 (2013) 121–130.
- [34] R. Remmert, Theory of Complex Functions vol. 122, Springer Science & Business Media, 1991.

## 6 Comparative Study of Parameter Identification with Frequency and Time Domain Fitting Using a Physics-Based Battery Model

In chapter 4 and 5, the DRT spectrum of a Lithium-ion battery has been comprehensively investigated and explained. Furthermore, a few important kinetic parameters including the reaction rate constant, the resistivity of the SEI and the solid diffusion coefficient have been estimated using a commercially available Lithium-ion battery cell. Although these kinetic parameters have been estimated, there still exist other parameters which cannot be estimated using the DRT method, such as the conductivity in the solid and liquid phases.

Naturally, an important research question can be raised: does the estimation method in time domain and frequency domain produce the same results? To reveal the identifiability of the various estimated parameters, a probability based method has been applied to sample the parameter space. Another important impact factor when estimating the parameters in time domain is the additional ohmic resistance caused by the current collector, cell connector and the contact surface between the current collector and the electrode. Finally, for the aforementioned reasons, four cases were defined to investigate the parameter identification:

1. All selected parameters were identified with the time domain fitting method; no additional ohmic resistance was considered in the identification.
2. All selected parameters were identified with the time domain fitting method; an additional ohmic resistance was considered in the identification.
3. the kinetic parameters identified using the frequency domain method in chapter 4 and 5 were directly substituted into the model and other selected parameters were still identified using the time domain fitting; no additional ohmic resistance was considered in the identification.
4. the kinetic parameters identified using the frequency domain method in chapter 4 and 5 were directly substituted into the model and other selected parameters were still identified using the time domain fitting; an additional ohmic resistance was considered in the identification.

The parameter identification results indicated: while the solid diffusion coefficients identified in time and frequency domain were comparable, the reaction rate constants and SEI parameters could not be identified at all by the time domain fitting method. Besides, the combined identification method produced more reliable results for a few parameters which were identified only in the time domain.

Finally, the parameter identification results were validated using two dynamic load profiles. The validation results indicated that the consideration of the additional ohmic resistance and the combined identification method would lead to significantly lower voltage error.

### Author contribution

Yulong Zhao was the principal author tasked with coordinating and writing the paper, developing the theory and model, conducting the lab experiment, and evaluating the measurement data. Andreas

Jossen contributed via fruitful scientific discussions and reviewed the manuscript.

# Comparative Study of Parameter Identification with Frequency and Time Domain Fitting Using a Physics-Based Battery Model

Yulong Zhao and Andreas Jossen

Batteries 2022, 8(11), 222

Permanent weblink:

<https://doi.org/10.3390/batteries8110222>

Reproduced under the terms of the Creative Commons Attribution 4.0 License (CC BY, <http://creativecommons.org/licenses/by/4.0/>), which permits unrestricted reuse of the work in any medium, provided the original work is properly cited.



Article

# Comparative Study of Parameter Identification with Frequency and Time Domain Fitting Using a Physics-Based Battery Model

Yulong Zhao \* and Andreas Jossen

Chair of Electrical Energy Storage Technology, TUM School of Engineering and Design,  
Technical University of Munich, Karlstraße 45, 80333 Munich, Germany

\* Correspondence: yulong.zhao@tum.de

**Abstract:** Parameter identification with the pseudo-two-dimensional (p2D) model has been an important research topic in battery engineering because some of the physicochemical parameters used in the model can be measured, while some can only be estimated or calculated based on the measurement data. Various methods, either in the time domain or frequency domain, have been proposed to identify the parameters of the p2D model. While the methods in each domain bring their advantages and disadvantages, a comprehensive comparison regarding parameter identifiability and accuracy is still missing. In this present work, some selected physicochemical parameters of the p2D model are identified in four different cases and with different methods, either only in the time domain or with a combined model. Which parameters are identified in the frequency domain is decided by a comprehensive analysis of the analytical expression for the DRT spectrum. Finally, the parameter identifiability results are analyzed and the validation results with two highly dynamic load profiles are shown and compared. The results indicate that the model with ohmic resistance and the combined method achieves the best performance and the average voltage error is at the level of 12 mV.

**Keywords:** electrochemical impedance spectroscopy; physics-based model; distribution of relaxation times; Markov chain Monte Carlo algorithm



**Citation:** Zhao, Y.; Jossen, A. Comparative Study of Parameter Identification with Frequency and Time Domain Fitting Using a Physics-Based Battery Model. *Batteries* **2022**, *8*, 222. <https://doi.org/10.3390/batteries8110222>

Academic Editor: Sylvain Franger

Received: 4 October 2022

Accepted: 31 October 2022

Published: 7 November 2022

**Publisher's Note:** MDPI stays neutral with regard to jurisdictional claims in published maps and institutional affiliations.



**Copyright:** © 2022 by the authors. Licensee MDPI, Basel, Switzerland. This article is an open access article distributed under the terms and conditions of the Creative Commons Attribution (CC BY) license (<https://creativecommons.org/licenses/by/4.0/>).

## 1. Introduction

To build a more robust power grid with growing renewable energy sources and to enable an electrified transportation system, lithium-ion batteries (LIBs) are being increasingly deployed in various sectors, such as stationary energy storage systems and electrical vehicles. While the demand for LIBs is increasing, a longer lifespan and safer operation should still be guaranteed. To realize a better design of BMS and ensure a safer operation, an accurate identification of the cell parameters is imperative [1]. In most cases, to estimate the cell parameters, a proper objective function will be chosen and an optimization problem will be established to identify the parameters of interest [2]. Generally, according to the input data for the optimization problem, the identification methods can be roughly classified into two groups: time domain and frequency domain methods [3]. Time domain methods use the measurement data gathered in the time domain, such as charging/discharging curves or pulse test data; frequency domain methods usually refer to electrochemical impedance spectroscopy (EIS), where the cell impedance is measured as a function of the frequency of the excitation signal. Due to the different measurement principles, parameters are identified with different identifiabilities and accuracies [3,4].

### 1.1. Parameter Identification in Time Domain

For the time domain methods, first, a preselected model is built to model the internal physicochemical processes of the LIBs. Depending on the desired model complexity and comprehensiveness, the equivalent circuit model (ECM), reduced-order model (ROM)

based on the physicochemical model, and full-order physicochemical model (PCM) are available as potential candidates. The ECM is able to model certain physicochemical processes using specific circuit elements such as resistance, capacitance, and inductance. On the one hand, the ECM models the LIBs only in a simplified way, many complicated electrochemical processes are modeled with a lumped circuit element or even simply neglected; therefore, some physicochemical parameters are not given in the ECM. On the other hand, due to its easy implementation and fast computational speed, the ECM is favored in real-time or on-board applications [5–7]. The PCM describes the physicochemical processes with the first principle equations and the model output (voltage, current, temperature, etc.) is directly related to the fundamental physicochemical parameters [8–13]. The PCM usually consists of a group of coupled partial differential equations (PDEs) and the required computational effort is much higher than that of the ECM. Normally, the PCM must be solved using numerical methods such as the finite-element-method, which prevents it from real-time applications and large-scale simulation studies. To resolve the computational burden issue and meanwhile keep the accuracy loss on an acceptable level, the ROM has been developed by neglecting the less important processes or conducting mathematical simplification [14–22]. Compared to the full-order PCM, the computational demand of the ROM can be largely reduced and the accuracy loss can be generally kept to an acceptable level.

As the next step for parameter identification, an objective function must be selected and an optimization program with an appropriate algorithm is established to solve the parameter identification program. Due to the strongly nonlinear nature of the LIB models, the resulting optimization problem is strongly nonlinear as well and a carefully chosen algorithm must be applied to solve the problem. Various nonlinear optimization algorithms have been applied to the parameter identification problem of LIBs, including gradient-based or Hessian-based methods [6,15,16], heuristic methods [5,9,12,17], and statistical methods [10,13]. ECM-based parameter identification has a low demand for computational capacity, while a direct connection with the fundamental physicochemical parameters is usually unclear or even missing, which is a considerable drawback for the identification of physicochemical parameters and cell design. The PCM is the most comprehensive model, and relates the physicochemical and geometric parameters directly to the model output.

While most parameter identification studies focus on model development and optimization algorithms, only a small part of the works considers the parameter identifiability and sensitivity issues. Forman et al. conducted a parameter identification test and identifiability analysis using the Fisher information [12], where the local parameter identifiability and variance were determined. Berliner et al. applied the Markov chain Monte Carlo (MCMC) method to explore the parameter space and identified the quantitative nonlinear correlation among three parameters [13]. The characterization of the quantitative correlation (especially nonlinear) among multiple (more than two) parameters is an essential step, because the emphasis has been mostly laid on the analysis of parameter sensitivity and correlation between only two parameters and an important fact has been neglected: a coordinated change of multiple parameters (more than two) may lead to the same model output and a unique global optimum may not exist. As a result, the parameter identifiability analysis suggests that simply minimizing the objective function and analyzing the local parameter sensitivity cannot guarantee a reliable and physically meaningful identification result.

### *1.2. Parameter Identification in Frequency Domain*

Parameter identification in the frequency domain is conducted in a similar manner, where the desired impedance model is selected and an optimization program is established to estimate the model parameters. Various models have been used to identify the cell parameters, including the ECM [23–28], ROM [29–31], and PCM [32–35]. The identification methods used in the aforementioned literature are all based on nonlinear optimization methods and naturally are faced with the same issues as in the time domain method. For example, the same impedance data can be fitted using different equivalent circuits with

different structures and numbers of circuit elements [36], thus the results could be quite confusing. Moreover, many local optima may exist and it needs more effort to find the global optimum. Recently, many researchers proposed to use the method distribution of relaxation times (DRT) to evaluate the impedance data, which is based on linear optimization and the identifiability issue is no more considerable [37–42]. However, an appropriate model is still necessary for the interpretation of the DRT results. Until now, most models that have been used to interpret the DRT results are based on the ECM and a direct relation to the physicochemical parameters is still missing [42–47].

### 1.3. Comparison and Unification of Time Domain and Frequency Domain Parameter Identification Methods

Both time domain methods and frequency domain methods characterize the cell parameters using a selected model. Due to the different properties of both methods, different parameters may be estimated with different identifiabilities. Laue et al. [4] investigated the sensitivity of the p2D model by considering the data both in the time domain and frequency domain. However, no universal analysis was made regarding the identifiability of the parameters with impedance data and the results were not validated. Wimmarshana et al. [3] investigated the parameter sensitivity by considering the measurement data in both the time and frequency domains. Again the parameters were not identified and the results were not validated and compared, which means that the effectiveness of the combined procedures is still unknown. After the parameters have been identified, the estimation results are usually simply validated by inserting the estimated parameters back into the model and the model will be simulated in a few limited application scenarios, mostly only with constant charging/discharging current. In most cases, the parametrized model gives a moderate to low error. As a result, three important questions are raised regarding the issues mentioned above: (1) How reliable are the parameters identified using the time domain fitting? (2) If a combined method with both time and frequency domain data is applied, which parameters will be better identified with impedance data and why? (3) Does a combined identification method with both the time domain and frequency domain data optimize the parameter identifiability and lead to better accuracy for the validation? In the present work, we will focus on the three questions raised above and try to find the answers.

The rest of the work is organized as follows: in Section 2, the used models and parameter identification procedures will be introduced; in Section 3, lab experiments are conducted to identify the model parameters and investigate the identifiability with each method; in Section 4, the results will be discussed; Section 5 concludes the work.

## 2. Theory and Model Development

In this section, the theoretical fundamentals, procedures, and algorithms used for different parameter identification methods will be introduced. Then the methodology for the parameter identifiability and correlation analysis will be explained.

### 2.1. Parameter Identification in the Time Domain

Since being proposed by Doyle and Newman [48–50], the p2D model has been widely applied to the design, simulation, and parameter identification of LIBs. The p2D model describes the internal physicochemical processes using a group of coupled PDEs, thus requiring a high computation capability. Therefore, a direct application of the p2D model to parameter identification is rather time-consuming and inefficient because the model must be iteratively computed a large number of times depending on the parameter identifiability and convergence rate. As an alternative, the reduced-order model (ROM) has been proposed by researchers to improve the computation speed, while the accuracy loss is nearly negligible when the model order is properly chosen. In one of our previous works, a ROM using the Chebyshev orthogonal collocation method has been developed and validated [20]. According to the conducted simulation experiment, it is found that the model with an (8, 5, 7) collocation point configuration in the anode, separator, and cathode,

respectively, can well approximate the relevant transport processes and the computation demand is much lower with a degree of freedom (DOF) of ca. 160. The simulation time of one charging/discharging process  $t_{CH/DCH}$  with Matlab/Simulink is about 0.2 s, the model setting is summarized in Table 1.

**Table 1.** Summary of the model setting for ROM used for parameter identification test.

Model Type	Polynomial Type	$(n_n, n_s, n_p)$	DOF	$t_{CH/DCH}$
ROM with p2D	Chebyshev	(8, 5, 7)	ca. 160	0.2 s

To assess the quality of the parameter estimation results, various methods have been proposed to quantify the identifiability of the estimated parameters. Commonly used methods include the once-at-a-time (OAT) method [3,51], Fisher information matrix (FIM) [12] and Sobol' indices [4,52]. In this present work, we choose to use Bayesian statistics combined with the MCMC sampling algorithm for the parameter estimation and identifiability characterization. The reasons for using the Bayesian MCMC method are as follows: (1) It quantifies the global identifiability of the parameters because the parameter values are randomly sampled in the whole defined parameter space. If the sample size is big enough, an empirical distribution close to the real posterior distribution can be obtained. (2) The posterior distribution of the parameters is able to characterize the unidentifiability when it arises either from non-sensitivity or parameter correlation, in both cases, a posterior distribution with a wide credible interval can be observed. (3) The credible interval and thus the identifiability of parameters can easily be visualized and computed with the resulting parameter distribution.

In practical applications, the measurement data is generally exposed to a normally distributed noise with a zero mean:

$$V_m = \hat{V}_m + \epsilon_e \quad (1)$$

where  $V_m$  is the measured cell voltage,  $\hat{V}_m$  is the cell voltage without noise,  $\epsilon_e$  is the measurement noise, and the following distribution is assumed:

$$\epsilon_e \sim \mathcal{N}(0, \sigma_e^2) \quad (2)$$

where  $\sigma_e$  is the standard deviation of the noise and is set to 10 mV in this work. As usually there is no information about the variance of the voltage noise, other proper values can be used as well and the results should not vary because this is equivalent to adding a constant to the logarithmic object function values. By using Bayes' theorem, the conditional probability of the model parameter  $\theta$ , given the measurement data, is defined as:

$$P(\theta|V_m) = \frac{P(V_m|\theta)P(\theta)}{P(V_m)} \quad (3)$$

where  $P(\theta)$  is the prior distribution for the parameters, which is based on the prior knowledge of the parameter. In certain situations, enough information can be collected to define an informative prior distribution for the parameter, for example the beta distribution. In this present work, the prior distribution  $P(\theta)$  is assumed to be uniformly distributed between its upper and lower bound because there is no information available to define an informative prior distribution. In our application, the measurement data  $V_m$  are given with a certain constant distribution, thus  $P(V_m)$  can be assumed to be a constant. As a result, the conditional probability can be reformulated as:

$$P(\theta|V_m) \propto P(V_m|\theta) \quad (4)$$

The probability of observing the measurement data  $V_m$  is equivalent to that of observing the measurement noise  $\epsilon_e$  given the model parameter  $\theta$  and can be defined as follows:



$$P(V_m|\theta) = \prod_{i=1}^{N_m} \frac{1}{\sigma_e \sqrt{2\pi}} \exp\left(-\frac{1}{2} \left(\frac{V_{m,i} - \hat{V}_{m,i}(\theta)}{\sigma_e}\right)^2\right) \quad (5)$$

where  $i$  represents the index of the measurement data points and  $N_m$  is the total number of the measured voltage data points. To sample the parameter space, the adaptive Metropolis–Hastings MCMC algorithm is used to generate the parameter samples [53], the sample size for each test is set to 50,000 and the desired acceptance rate is set to 0.23 [54].

While the OAT metrics only characterize the sensitivity and possible correlation of a parameter at a specific location, the Bayesian MCMC sampling results can well characterize both properties globally. Therefore, to quantify the general identifiability of a parameter, the following sensitivity index (SI)  $\mathcal{S}$  is defined:

$$\mathcal{S} = \frac{\theta_{\max} - \theta_{\min}}{\mathcal{L}} \quad (6)$$

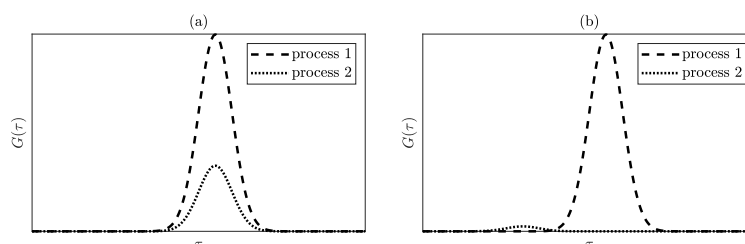
where  $\theta_{\max}$  and  $\theta_{\min}$  are the upper and lower bound of the parameter, respectively, and  $\mathcal{L}$  is the width of the 95% credible interval (CI) of the parameter. Unlike the equal-tailed-interval (ETI), in this work the CI of each parameter is calculated using the highest-density-probability (HDP) concept, where the interval with the highest probability density is chosen to calculate the CI, as some parameters, such as the diffusion coefficients, can range for multiple orders of magnitude, the logarithmic scale is used to calculate the SI. A high sensitivity index implies that the parameter is confined in a small credible interval compared to the bounds and thus can be reliably estimated, whereas a low SI indicates that the parameter is practically unidentifiable.

## 2.2. Parameter Identification in Frequency Domain

According to our previous works on the interpretation of a DRT spectrum using a physics-based impedance model, the diffusion coefficient in the solid and liquid phases and the interface parameters such as the kinetic reaction rate constant and the film resistance can be directly determined, if the related geometric parameters are known. For the Bruggeman coefficients and the conductivities in the solid and liquid phases, the corresponding contribution only appears in the ohmic resistance of the cell and possibly also in the high-frequency dispersion part of the impedance/DRT. The Bruggeman coefficients also contribute to the effective transportation in the liquid phase. However, the bulk value of the liquid diffusivity is usually unknown, thus it is still impossible to estimate the Bruggeman coefficients using the liquid phase diffusion. Considering that the dispersion of the DRT spectra in the high-frequency area is usually blurred by contributions of other processes in practical applications and it is impossible to separate the impedance contribution from the anode, separator, and cathode, the conductivity in the solid/liquid phase and the Bruggeman coefficient can be considered as unidentifiable with the DRT method.

Rabissi et al. [55] investigated the sensitivity and identifiability of the physicochemical parameters with a physicochemical impedance model. However, no general conclusions have been made with the impedance model regarding the parameter identifiability. To have a quantitative conclusion on the identifiability, a numerical analysis is still necessary. Based on the analysis made in our previous works, where the analytical expressions for the DRT have been derived and interpreted, a universal conclusion can be made regarding the identifiability of the physicochemical parameters used in the p2D model. Due to the fact that the DRT spectrum ( $\tau$  domain) is actually equivalent to the raw impedance data ( $f$  domain), the conclusions made with the DRT spectrum are also valid for the impedance. In the DRT spectrum, a process is characterized mainly by two key features: (1) the time constant of the peak (or the dominant peak) representing the process; (2) the area under the peak (or the dominant peak) which represents the polarization resistance of the process. As a result, a parameter is identifiable only when the following conditions are fulfilled: (1) the time constant of the process related to the parameter cannot be fully coinciding

with that of another peak at all SOCs; (2) the magnitude of the peak must be clearly visible and evaluable (at least significantly higher than noise). If any of the two aforementioned conditions is not fulfilled, the parameter will be unidentifiable, two examples where condition 1 or 2 are not fulfilled are shown in Figure 1. It is worth mentioning that here we assume that with each peak/process we aim to identify only one parameter, otherwise the analytical expression of the DRT spectrum must be analyzed to assess if the multiple parameters can be identified uniquely at the same time.



**Figure 1.** The two scenarios where the corresponding processes/parameters are unidentifiable with (a) overlapping peaks and (b) one peak of a negligible polarization resistance.

In summary, according to the analytical expressions of the DRT spectrum using a physico-chemical impedance model, a clear deterministic conclusion can be made on the identifiability of the kinetic and transport parameters. In ideal case that each process has a considerable polarization resistance and is not fully overlapping with any other process, the identifiability of the kinetic and transport parameters of interest are summarized in Table 2.

**Table 2.** Summary of parameter identifiability in the frequency domain.

Parameter	Symbol	Identifiability	Remark
Reaction rate constant	$k$	identifiable	EIS at multiple SOCs may be necessary
SEI film resistance	$R_f$	identifiable	-
Solid diffusivity	$D_s$	identifiable	particle geometric information needed
Liquid diffusivity	$D_l$	identifiable	usually only an average diffusivity can be estimated due to overlapping peaks of each electrode layer
Bruggeman coefficient	$\alpha$	unidentifiable	-
Solid phase conductivity	$\sigma$	unidentifiable	may be identifiable in extreme case
Liquid phase conductivity	$\kappa$	unidentifiable	may be identifiable in extreme case

### 2.3. Parameter Correlation Analysis

The reason for the structural non-identifiability is that the effect of the change of one parameter can be compensated by a coordinated change of some other parameters, thus leading to the same model output [56]. In such a situation, no unique global optimal solution exists. If the fitted model has a simple algebraic structure, the parameter correlation can be easily identified by directly inspecting the structure of the equations. However, the physicochemical model for a LIB consists of a few PDEs and has a complicated mathematical structure, thus making it impossible to directly identify the parameter correlation. To the author’s best knowledge, the parameter correlation analysis found in the literature has only been conducted on every two parameters, namely pairwise; moreover, the correlation analysis has merely been conducted by simply plotting the parameter values against each other and no theoretical model has been used or proposed. In this work, we try to identify the possible quantitative correlation among multiple parameters based on a theoretical model.

The essence of fitting a battery model to the measured voltage curve lies in the calculation of the overpotential under the given parameter set and input load profile, because the OCV-SOC relation can be relatively accurately measured using half cells and regarded as time-invariant within the measurement period and does not depend on the fitting parameters. Because the p2D model has no closed-form analytical solutions, we try to approximate

the cell overpotential using the concept of impedance and seek the possible correlation relationship among the parameters. According to the origin, the total cell overpotential can be divided into the liquid phase diffusion overpotential, the solid phase diffusion overpotential, the conduction overpotential in the liquid and solid phases, and the overpotential caused by the interfacial processes. Accordingly, we use the diffusional resistance, charge transfer resistance, and ohmic resistance to analyze the possible correlation:

$$\eta_{\text{cell}} = \eta_{l,\text{diff}} + \eta_{s,\text{diff}} + \eta_{s,R} + \eta_{l,R} + \eta_{\text{ct}} + \eta_{\text{f}} \quad (7)$$

where the subscripts l and s represent the processes related to the liquid and solid phases, respectively; diff, ct, R, and f represent the processes related to the diffusion, charge transfer, ohmic conduction, and film, respectively. Each component can be further separated into the contributions from the anode, separator, and cathode, if the corresponding components exist. The corresponding diffusion and activation impedance components are defined as [57,58]:

$$\eta_{l,\text{diff}} = \frac{RT(1-t^+)l_e}{2F^2c_{l,0}D_{l,\text{eff}}} \propto \frac{1}{D_{l,\text{eff}}} \quad (8)$$

$$\eta_{s,\text{diff}} = \left(-\frac{\partial U}{\partial c_s}\right) \frac{R_p}{FD_s} \propto \frac{1}{D_s} \quad (9)$$

$$\eta_{\text{ct}} = \frac{RT}{Fk(c_{s,\text{max}} - c_s)^{0.5}c_s^{0.5}c_{l,0}^{0.5}} \propto \frac{1}{k} \quad (10)$$

$$\eta_{\text{f}} \propto R_{\text{f}} \quad (11)$$

For the overpotential caused by the conduction process in the solid and liquid phases, we choose to model the corresponding components according to the definition of Nyman et al. [59] with the single particle assumption. As a result, the following definitions can be obtained:

$$\eta_{s,R} = \frac{l_e}{\epsilon_s^{1+\alpha}\sigma_s} \propto \frac{1}{\epsilon_s^{1+\alpha}\sigma_s} \quad (12)$$

$$\eta_{l,R} = \frac{l_e}{\epsilon_l^{1+\alpha}\kappa_l} \propto \frac{1}{\epsilon_l^{1+\alpha}\kappa_l} \quad (13)$$

where  $l_e$  is the thickness of the electrode or separator. We can easily see that all the overpotential components (left side of Equations (8)–(13)) have the unit of  $\Omega\text{m}^2$  and qualitatively reflect the impact of the parameters on the cell overpotential. The total cell overpotential is inversely correlated with the diffusivity, reaction rate constant, and conductivity and is proportional to the film resistivity. Intuitively, this is also easy to comprehend, since a higher kinetic or transport parameter will lead to a faster material transport and thus lower overpotential. Consequently, a possible linear correlation is sought among the following parameters (combinations) of each electrode:

$$\theta_{\text{corr}} = \left\{ \frac{1}{D_{l,n,\text{eff}}}, \frac{1}{D_{l,\text{sep},\text{eff}}}, \frac{1}{D_{l,p,\text{eff}}}, \frac{1}{D_{s,n}}, \frac{1}{D_{l,p}}, \frac{1}{\epsilon_{s,n}^{1+\alpha_n}\sigma_{s,n}}, \frac{1}{\epsilon_{l,n}^{1+\alpha_n}\kappa_n}, \frac{1}{\epsilon_{l,n}^{1+\alpha_n}\kappa_n}, \frac{1}{\epsilon_{l,p}^{1+\alpha_p}\kappa_p}, \frac{1}{\epsilon_{s,p}^{1+\alpha_p}\sigma_{s,p}}, \frac{1}{k_n}, \frac{1}{k_p}, R_{\text{f}} \right\} \quad (14)$$

To eliminate the possible influence of the parameter magnitude, each parameter (combination) sample vector is normalized by dividing it by the mean value of each sample vector, and the normalized vector is defined as  $\bar{\theta}_{\text{corr}}^i$ . To determine the correlation among the terms defined above, a linear optimization problem is defined. The linear correlation coefficients are determined by solving the following linear least square problem:

$$\rho(\vec{\theta}_{\text{corr}}^i) = \operatorname{argmin} \left\{ \left\| \sum_{j=1, j \neq i}^{N_\theta} a_j^i \vec{\theta}_{\text{corr}}^j + \beta_i - \vec{\theta}_{\text{corr}}^i \right\|_2 \right\} \quad (15)$$

where  $\rho$  represents the coefficient vector corresponding to each tested component sample vector and  $N_\theta$  is the total number of the tested components. To assess the fitting quality and further investigate if a correlation exists, the parameter samples are again reconstructed using the solved correlation coefficients:

$$\vec{\theta}_{\text{corr}}^* = \sum_{j=1, j \neq i}^{N_\theta} a_j^i \vec{\theta}_{\text{corr}}^j + \beta_i \quad (16)$$

where  $\vec{\theta}_{\text{corr}}^*$  is the reconstructed parameter sample vector. To visualize the fitting quality and the possible correlation, the original parameter samples are plotted against the reconstructed parameter samples  $\vec{\theta}_{\text{corr}}^*$  using the calculated coefficients in Equation (15). If a correlation is existent, then the data points  $(\vec{\theta}_{\text{corr}}, \vec{\theta}_{\text{corr}}^*)$  should lie close to the straight line  $\vec{\theta}_{\text{corr}}^* = \vec{\theta}_{\text{corr}}$ . If the reconstructed data points deviate far from the straight line  $\vec{\theta}_{\text{corr}}^* = \vec{\theta}_{\text{corr}}$ , then the tested component is not correlated with other components regarding the defined parameter combination. It is worth mentioning here that even if no correlation can be characterized using the defined relationship, the possibility that the tested component is correlated with other parameters still cannot be excluded, because they may be correlated by another unknown relationship. This phenomenon may especially appear in practical applications because the used model generally cannot describe the real physicochemical processes in an absolutely precise manner.

#### 2.4. Influence of the External Ohmic Resistance on the Parameter Estimation

In practical applications, besides the conduction process described by the p2D model, additional ohmic resistance may arise from the cell contact and current collector. While the p2D model does not take the external ohmic resistance of various origins, such as current collector and cell contact resistance, into consideration, it may have a considerable impact on the parameter estimation. When the external ohmic resistance is not considered in the model, then the ohmic resistance of the cell arises only from the conduction process in the solid and liquid phases inside the battery cell. However, when the external ohmic resistance is practically existent but not considered by the model, it can be suspected that the conductivity and Bruggeman coefficients will almost certainly be underestimated and overestimated, respectively, because the additional ohmic resistance must be compensated. Reimers et al. investigated the current distribution inside the current collector (CC) and proposed a model to account for the CC ohmic resistance for different tab arrangements [60]. Generally, the ohmic resistance of an 18,650 round cell measured by impedance spectroscopy ranges from a few milliohms to a few tens of milliohms. Through a simple qualitative calculation using the model given by Reimers et al., it can be seen that the CC ohmic resistance is generally non-negligible compared to the total ohmic resistance of a cylindrical cell. In this work, the impact of the external ohmic resistance on the parameter identifiability will be investigated.

#### 2.5. Influence of Parameter Identification Procedure on the Identifiability

While parameter estimation using only time domain or frequency domain methods can be frequently found in the literature, a comprehensive investigation and comparison of parameter identification using both time domain and frequency domain methods can seldomly be found. It has been widely acknowledged that the EIS can provide reliable parameter estimation results, especially for highly dynamic processes [36]. As a result, an important research question naturally arises: would a combined method using both time domain and frequency domain methods significantly optimize the identifiability and reduce the parameter uncertainty? In the present work, we will try to compare the

parameter estimation with only the time domain method and with the method combining the measurement data in both the time and frequency domains. For the time domain method, all parameters are estimated by fitting the p2D model. According to the conclusions made in Section 2.2 on the identifiability of the kinetic and transport parameters in the frequency domain, for the combined method, the selected kinetic parameters including the kinetic reaction rate constant, solid diffusivity, film resistance, and their SOC dependence are identified by the DRT method and the parameter values are taken from our previous work [61,62]. Then these parameters are directly substituted into the model as known parameters, other parameters are still estimated by fitting the p2D model, which results in a reduced number of fitted parameters. In this work, we refer to the former model as the full model and the latter as the combined model. In this work, we will not choose to identify the liquid phase diffusivity in the frequency domain due to the following reasons: (1) for fresh cells, the electrolyte degradation and thus the liquid diffusion overpotential can basically be neglected; (2) it is impossible to identify the bulk liquid diffusivity and the Bruggeman coefficients separately, as mentioned in Section 2.2.

Altogether, four cases for parameter identification will be investigated in this present work to characterize the impact of the external ohmic resistance and parameter characterization procedures on parameter identifiability and accuracy. The estimated parameters and corresponding models are summarized in Table 3, a summary of all estimated and substituted parameters can be found in Table 4.

Table 3. Summary of the investigated model cases and fitted parameters.

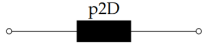

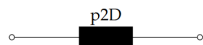

Case	Circuit Model	Fitted Parameters	Substituted Parameters
1		1–12	-
2		1–12	-
3		6–12	13–17
4		6–12	13–17

Table 4. Summary of all estimated and substituted parameters in the time and frequency domains.

Number	Parameter	Scale	Bound	Reference
<b>Fitted Parameters with p2D Model</b>				
1	Bruggeman coefficient $\alpha_n$ , (-)	linear	[0.5, 3.82]	[63,64]
2	Bruggeman coefficient $\alpha_s$ , (-)	linear	[0.5, 2.87]	[63–65]
3	Bruggeman coefficient $\alpha_p$ , (-)	linear	[0.5, 3.14]	[63,64,66,67]
4	Anode solid diffusivity $D_{s,n,lumped}$ , ( $m^2s^{-1}$ )	log	[-15, -12]	[63,64]
5	Cathode solid diffusivity $D_{s,p,lumped}$ , ( $m^2s^{-1}$ )	log	[-15, -12]	[63,64,66,67]
6	Liquid bulk diffusivity $D_{l,0}$ , ( $m^2s^{-1}$ )	log	[-11, -8.15]	[68–71]
7	Liquid bulk conductivity $\kappa_0$ , ( $Sm^{-1}$ )	log	[-0.82, 0.42]	[68,70–72]
8	Anode bulk solid phase conductivity $\sigma_n$ , ( $Sm^{-1}$ )	log	[0, 2]	[63]
9	Cathode bulk solid phase conductivity $\sigma_p$ , ( $Sm^{-1}$ )	log	[-3.1, -0.47]	[63,67]
10	Anode film resistance $R_{f,lumped}$ , ( $\Omega m^2$ )	log	[-5, -1]	assumed
11	Anodic reaction rate constant $k_n$ , ( $ms^{-1}$ )	log	[-12, -9]	[63]
12	Cathodic reaction rate constant $k_p$ , ( $ms^{-1}$ )	log	[-12, -9]	[63]
<b>Parameters Determined in Frequency Domain</b>				
13	Anode solid diffusivity $D_{s,n}(SOC)$ , ( $m^2s^{-1}$ )			[62]
14	Cathode solid diffusivity $D_{s,p}(SOC)$ , ( $m^2s^{-1}$ )			[62]
15	Film resistivity $R_f(SOC)$ ( $\Omega m^2$ )			[61]
16	Anodic reaction rate constant $k_n$ , ( $ms^{-1}$ )			[61]
17	Cathodic reaction rate constant $k_p$ , ( $ms^{-1}$ )			[61]

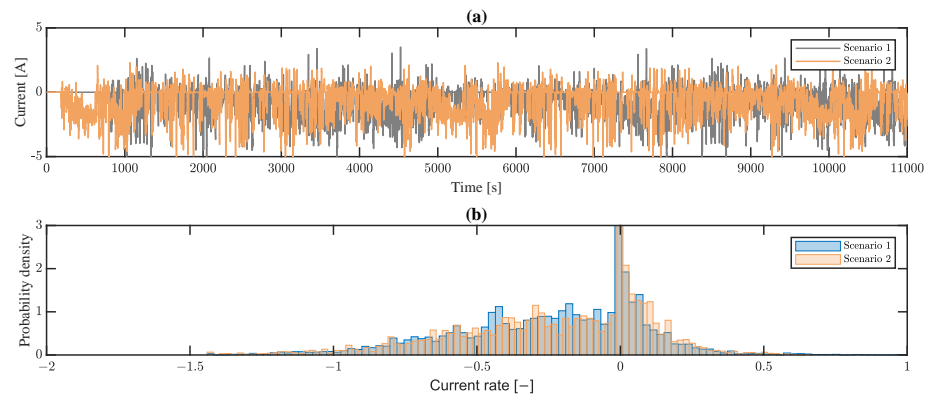
### 3. Experiment

The commercial cell used in this work is a 3.35 Ah NMC811/SiC LIB (INR18650-MJ1, LG Chem, Seoul, Korea), which has been investigated in our previous works as well. For parameter estimation in the time domain using the p2D model, the cell was first fully charged to 100% SOC using a CCCV charging protocol and then relaxed for about 6 h. Then the cell was discharged using a 1 C current rate until the lower voltage limit was reached. The test temperature is 25 °C. The 1 C discharging data was then used for the parameter estimation with the Bayesian statistics and MCMC sampling. The MJ1 cell has a single tab design [63] and the ohmic resistance caused by the ohmic conduction in the current collector can be calculated as follows [60]:

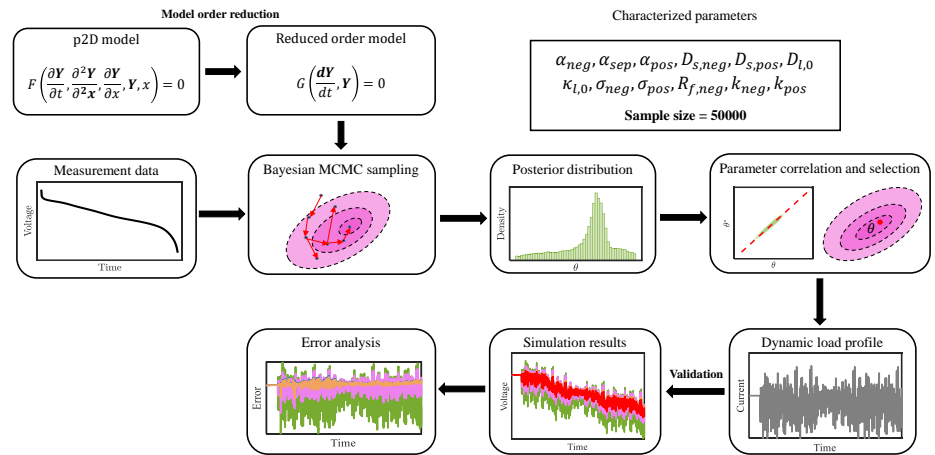
$$R_{CC} = \frac{1}{3}L_{CC} \left( \frac{\rho_a}{W_a t_a} + \frac{\rho_c}{W_c t_c} \right) \approx 11 \text{ m}\Omega \quad (17)$$

where  $\rho_a$  and  $\rho_c$  are resistivities of the anode and cathode CC, respectively,  $L_{CC}$  is the length of the current collector,  $W_a$  and  $W_c$  are the widths of the anode and cathode CC,  $t_a$  and  $t_c$  are the thicknesses of the anode and cathode CC. Another origin of ohmic resistance is the contact resistance between the current collector and the active material, which has been characterized to be about 1 m $\Omega$  in our previous work [61]. The ohmic resistance for the measurement cable and clamp is assumed to be 1 m $\Omega$ . As a result, the total external ohmic resistance used for the parameter estimation study is 13 m $\Omega$ . For each case of parameter identification, 50,000 samples were collected by the MCMC sampling algorithm, and the target acceptance rate is set to be 0.23 [54]. For the evaluation of the results, only the samples after the burn-in period will be used for the data evaluation. The lower and upper bounds for the parameter estimation are set by referring to the literature and are summarized in Table 4. Because some parameters can range for several orders of magnitude, the logarithmic scale is used for the representation and identifiability calculation of the parameters. To ensure completeness and avoid possible errors caused by the limited number of references, some values have been adapted moderately.

After the parameter estimation has been conducted and the parameters have been selected for validation, two application scenarios each with a time period of three hours are used to validate the parameter estimation results, then the accuracy and effectiveness of the four investigated cases in each scenario are compared. For each case, the parameter values used for validation will be selected according to their identifiability and based on a defined principle, which will be explained in detail later. The load profiles used for the validation and the distribution of the current rate are shown in Figure 2. All lab experiments were conducted in a thermal chamber (Vötsch Industrietechnik GmbH) combined with a battery cycler (CTS, Basytec) under a temperature of 25 °C. The overall workflow for the parameter identification and validation is shown in Figure 3.



**Figure 2.** Dynamic load profile used for the validation of parameter estimation. (a) current profile; (b) distribution of the current rate.



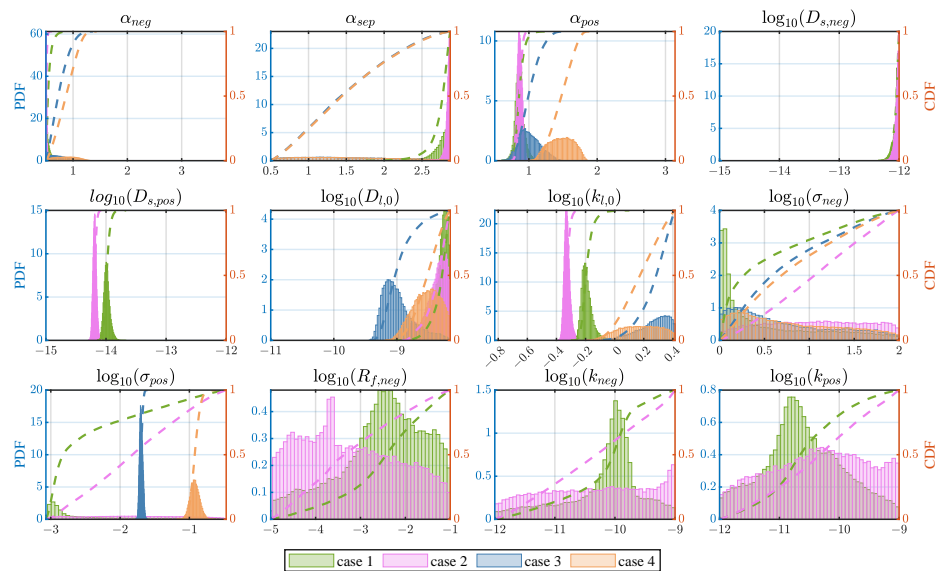
**Figure 3.** Workflow for the parameter identification and validation conducted in the present work. The different colors in the simulation results and error analysis sections represent the results of different test cases.

#### 4. Results and Discussion

In this section, the parameter sampling results will be shown and discussed, then the estimated parameters will be used to characterize the simulation performance in two application scenarios with highly dynamic load profiles.

##### 4.1. Parameter Distribution

The parameter sampling results are shown in Figure 4. In the following sections, the results for each parameter will be discussed.



**Figure 4.** Probability distribution of the sampled parameters in the four cases. The probability density distribution function (PDF) is shown with the histogram and the cumulative distribution function (CDF) for each PDF is shown with a dashed line using the same color as the PDF.

**Bruggeman coefficients.** The posterior distributions of the investigated parameters for the first two cases have a similar form and the parameters have a limited credible interval. As a result, the Bruggeman coefficients in the first two cases can be regarded as practically

identifiable. For the third and fourth cases, where the corresponding kinetic and transport parameters measured in the frequency domain with a SOC dependence are substituted, the form of the distribution has changed significantly. The Bruggeman coefficients for the negative electrode and separator show an extended distribution with a much wider credible interval compared to the first two cases. We can first exclude the possibility that the change is caused by the external ohmic resistance, as the parameter identifiability in the first two cases and in the last two cases is similar, respectively. We assume that this change can be attributed to the substituted transport parameters with SOC dependence, which has changed the form of the defined parameter space. It can be concluded here that the substitution of parameters with SOC dependence can have a significant impact on the parameter identifiability.

**Solid phase diffusivity.** The solid phase diffusivities are only estimated in the first two cases and are substituted as known parameters in the third and fourth cases. In both cases, the PDFs have similar forms. For the negative electrode, the PDFs have a clearly defined lower bound and are approaching the upper bound of the parameter, which is consistent with the fact that the diffusion process with a high diffusivity is no longer rate limiting. Therefore, the solid diffusivity in the anode is assumed to be unidentifiable, where only the lower bound can be determined. In contrast to the anode diffusivity, the cathode diffusivity shows a clearly defined peak for the PDF and a narrow credible interval. Moreover, the diffusivity in the first case is slightly higher than that in the second case. It is worth noticing that the solid phase diffusivity identified using time domain fitting has approximately the same order of magnitude as the value identified in the frequency domain [62], which implies that the diffusivity identified using time domain fitting may be used as an approximated value when a frequency domain based identification is not available.

**Liquid phase diffusivity.** The liquid phase diffusivity in the first two cases shows a distribution form similar to the solid diffusivity in the anode, where a clearly defined lower bound can be observed but the distribution approaches the upper bound, which leads to a non-rate-limiting behavior. In the third and fourth cases, though a peak can be seen, the credible interval is rather large compared to the parameter bound, thus the liquid diffusivity is practically unidentifiable in all cases. The unidentifiability is possibly attributed to the fact that in fresh cells with nondegraded electrolytes, the overpotential contribution caused by the liquid phase diffusion only amounts to a tiny part of the overall overpotential.

**Liquid phase conductivity.** The conductivity in the liquid phase can be well identified with a narrow credible interval in the first two cases, the identified values are slightly lower than those identified in the third and fourth cases. In the third and fourth cases, the credible interval becomes significantly wider and the parameter identifiability is lower than in the first two cases, this may imply that the liquid phase conduction is no longer a rate-limiting factor in the model. On the other hand, the distribution form has changed significantly as well, which can be only explained that the parameter space must have been changed by the SOC dependence of the substituted parameters. The phenomenon observed above is consistent with the fact that in fresh cells the liquid phase conduction is generally negligible and cannot be effectively identified.

**Solid phase conductivity.** The solid phase conductivity in the negative electrode has a wide credible interval and is practically unidentifiable in all cases, which is in line with our expectation that the solid phase conduction process in the anode is usually negligible due to the high conductivity of graphite [73]. The solid phase conductivity in the cathode in the first two cases has a wide credible interval and thus is unidentifiable, while in the third and fourth cases the parameter distribution has a well-defined credible interval and is thus identifiable. It is again worth noticing that the substitution of the SOC-dependent parameters in the model can significantly change the form of the posterior distribution and parameter identifiability irrespective of the external ohmic resistance. The parameter identified in the third case is lower than that in the fourth case by about an order of



magnitude, which is very likely caused by the inclusion of the external ohmic resistance in case 4. The estimated solid phase conductivity in the fourth case is close to the value measured using other methods [74], thus we tend to believe that the estimated value is plausible. Another phenomenon worth noticing is that the Bruggeman coefficient of the cathode in case 3 is lower than that in case 4, but the relation for the solid conductivity is reversed. Through a simple calculation, it is found that in both cases the effective solid conductivities in the cathode are nearly the same. By inspecting the equation for the current distribution in the liquid phase, only the effective solid phase conductivity appears and the bulk conductivity does not appear anywhere else. Theoretically, the posterior distribution of the bulk solid conductivity in cathode should give a wide credible interval as in the first two cases, but according to the results, the parameter turns out to be well identifiable. This phenomenon can only be ascribed to the SOC dependence of the substituted parameters. Due to the observed change of the posterior distribution in cases 3 and 4 compared to that in cases 1 and 2, we can basically draw the conclusion that the combined method can indeed change the identifiability of some parameters and obtain more reasonable results.

**Interfacial parameters.** The three interfacial parameters, namely the kinetic reaction rate constant in both electrodes and the film resistance in the SiC anode, are all unidentifiable in all cases. All PDFs show a credible interval almost comparable with the defined parameter range and a reliable estimation of each parameter is impossible. The results highlight the importance of choosing suitable characterization methods for different model parameters. In most cases, only constant charging/discharging data is selected to establish the identification problem; however, in such cases the current profile generally does not contain any considerable component with a frequency comparable to the characteristic frequency of the interfacial processes, which usually ranges from 100 Hz to 1000 Hz [41,61,75].

From the parameter estimation results and discussions made above, the following conclusions can be made: (1) while the inclusion of the external ohmic resistance may slightly change the probability distribution of the parameters, it basically does not change the identifiability of the parameters; (2) the substitution of identified parameters with SOC dependence may significantly change the posterior distribution of the parameters and identifiability of the parameters; (3) interfacial parameters may be hard or even impossible to identify using the time domain fitting method due to the lack of dynamic current component. The results for the calculated sensitivity indices and credible intervals of the parameters are summarized in Table 5.

Table 5. Summary of the calculated SI and CI of the parameters

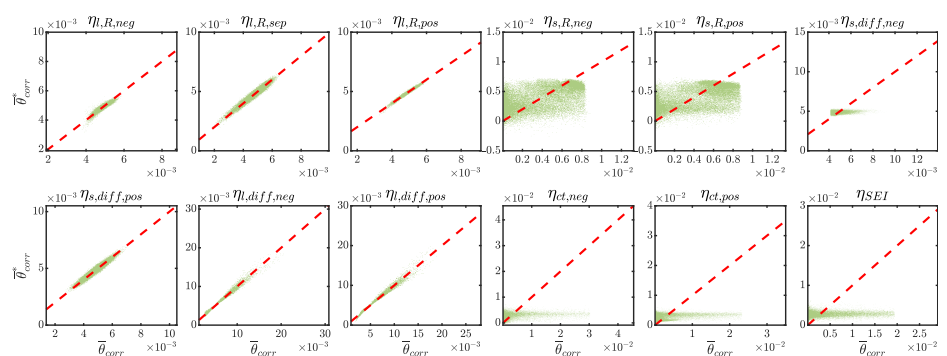
Parameter	Case 1		Case 2		Case 3		Case 4	
	S	CI	S	CI	S	CI	S	CI
$\alpha_{neg}$	18	[0.50, 0.69]	96	[0.50, 0.53]	5	[0.5, 1.11]	5	[0.50, 1.23]
$\alpha_{sep}$	5	[2.44, 2.87]	23	[2.77, 2.87]	1	[0.50, 2.68]	1	[0.50, 2.71]
$\alpha_{pos}$	8	[0.72, 1.03]	16	[0.78, 0.94]	4	[0.74, 1.34]	4	[1.15, 1.79]
$D_{s,neg}^*$	16	[-12.19, -12]	22	[-12.13, -12]	-	-	-	-
$D_{s,pos}^*$	14	[-14.08, -13.87]	25	[-14.24, -14.12]	-	-	-	-
$D_{l,0}^*$	6	[-8.63, -8.15]	4	[-8.81, -8.15]	3	[-9.36, -8.29]	4	[-8.92, -8.16]
$\kappa_{l,0}^*$	7	[-0.26, -0.08]	15	[-0.36, -0.28]	3	[0.03, 0.42]	2	[-0.09, 0.41]
$\sigma_{neg}^*$	1	[0, 1.97]	1	[0.05, 2.00]	1	[0, 1.93]	1	[0, 1.95]
$\sigma_{pos}^*$	1	[-3.07, -0.47]	1	[-3.04, -0.47]	29	[-1.74, -1.65]	9	[-1.06, -0.77]
$R_{f,neg}^*$	1	[-4.91, -1]	1	[-4.99, -1.14]	-	-	-	-
$k_{neg}^*$	1	[-11.97, -9]	1	[-11.94, -9]	-	-	-	-
$k_{pos}^*$	1	[-11.97, -9]	1	[-11.91, -9]	-	-	-	-

\* logarithmic scale; CI = 95% credible interval.

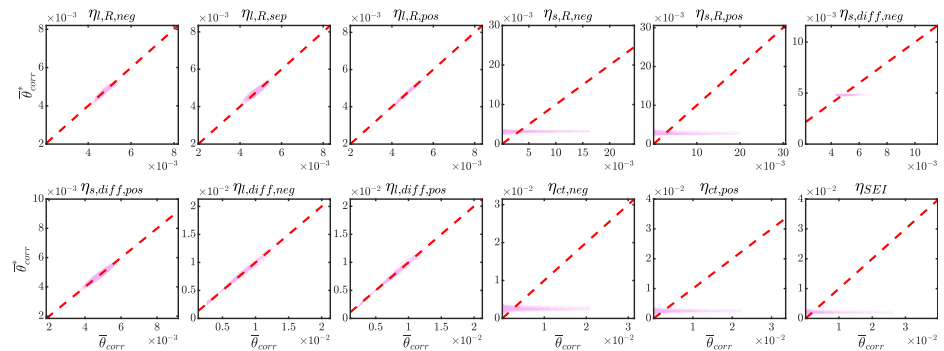
#### 4.2. Parameter Correlation Analysis

In the last section, the posterior parameter distributions have been characterized, where some parameters show a wide distribution and prove to be unidentifiable. Another important yet unsolved issue is: does any correlation relationship exist among the unidentifiable parameters? In Section 2.3, the principle for the parameter correlation test and the parameter combinations used for the test have been introduced. In this section, the parameter samples will be tested for possible correlation. The results for the sample evaluation are shown in Figures 5–9. To infer whether one parameter is possibly correlated with other parameters, the original samples, and the reconstructed sample vectors are plotted on the same axis. To visualize with which processes the tested process is correlated, a parameter correlation chart is generated and shown in Figure 10. In the correlation chart, the number in each column represents the correlation coefficient calculated using Equation (15). Each group of calculated coefficients is scaled by dividing the coefficients by the maximum absolute value of the coefficients in this group so that all values will be transformed into the interval  $[-1, 1]$  and are comparable.

The parameter correlations for cases 1 and 2 are shown in Figures 5 and 6. It can be observed that in both cases the liquid conduction and diffusion in all electrodes and the solid diffusion in the cathode show an obvious correlation behavior, which indicates that these processes are correlated with other processes. An unexpected result is that the solid conduction process in the cathode and the last three kinetic processes seem not to be correlated with any processes despite that the four parameters corresponding to the four processes have a wide posterior distribution. The solid conduction in the anode is excluded from the investigation here due to the fact that the solid conductivity in the graphite anode is orders of magnitude higher than that in the liquid phase and thus has only negligible contribution to the model output [73]. Berliner et al. [13] investigated the correlation relationship for the diffusion coefficients and reaction rate constant using a synthetic voltage curve and a correlation relationship between  $1/k_{neg}$  and  $1/k_{pos}$  was discovered. We assume that this correlation may arise from the low current rate used for the experiment. In such cases, the overpotential is less influenced by the diffusion and the fast kinetic processes at the particle–electrolyte interface are dominating. Another possible reason for this unexpected phenomenon is that the correlation relationship in Equation (10) may be distorted by the time-variant concentration in the solid particles and in the electrolyte. Since the correlation has been well observed in the work of Berliner et al. [13], we assume that this could be attributed to the nonuniform liquid phase concentration under 1 C discharging rate. Furthermore, the clearly defined correlation found in [13] may be attributed to the synthetic data generated using a well-defined model.

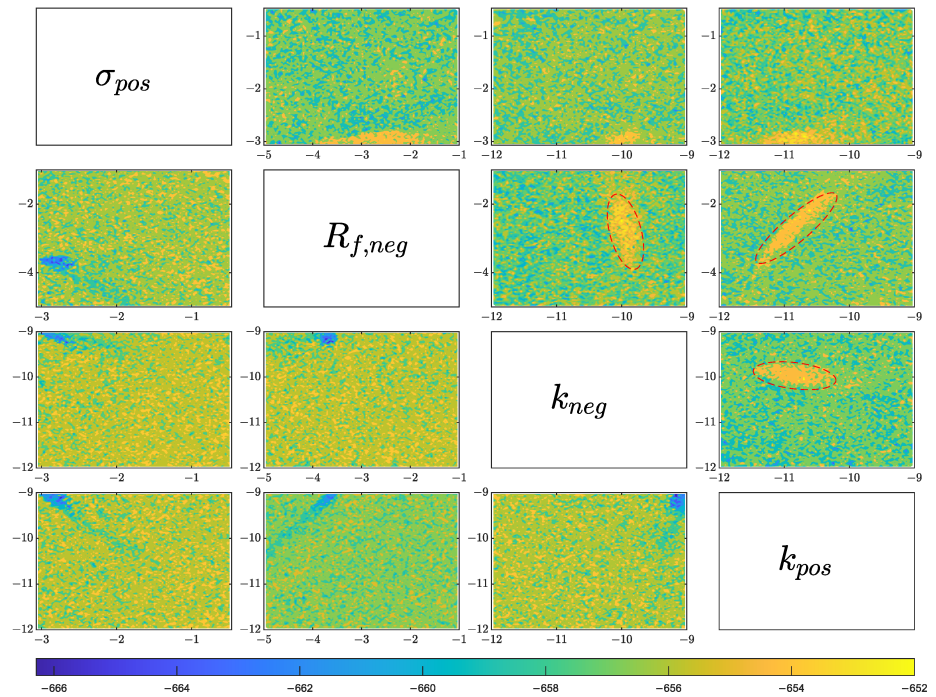


**Figure 5.** Results of parameter correlation for case 1. It can be observed that all processes except the conduction in the solid phase, the solid diffusion in the anode, and the interfacial processes are correlated with each other in different parameter ranges.



**Figure 6.** Results of parameter correlation for case 2. Similar to the results of case 1, it can be observed that all processes except the conduction in the solid phase, the solid diffusion in the anode, and the interfacial processes are correlated with each other in different parameter ranges.

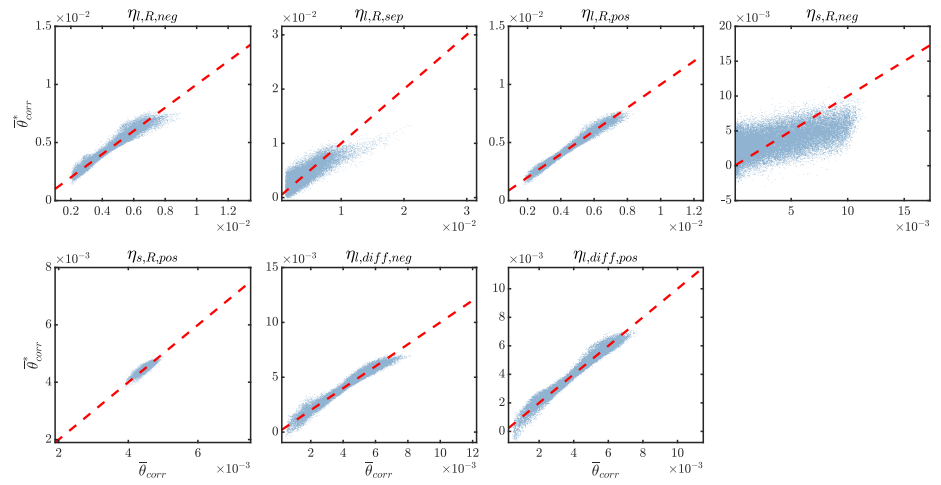
To find out whether the unidentifiability arises from the non-sensitivity or correlation relationship of the parameters, the objective function value inside the exponential function in Equation (5) is plotted for both case 1 and case 2 for each possible parameter combination (see Figure 7), the results for case 1 are shown in the upper triangular part of the figure and for case 2 in the lower triangular part. In Figure 7, it can be seen that for case 1 a clearly defined oval isosurface (marked with a red dashed line) can be seen for some parameter combinations, where all parameter combinations inside the ellipse have almost the same objective function value. For the solid conductivity in the cathode, no obvious correlation pattern can be observed, all data points with similar objective function values are concentrated in the region close to the lower bound, which coincides with the posterior distribution. The film resistance is slightly negatively correlated with the anode reaction rate constant. Similarly, a negative correlation is also seen between the anode and cathode reaction constant. Moreover, the found correlation relationship exists only in a limited area of each parameter, for the anode ca.  $6 \times 10^{-11} \sim 2 \times 10^{-10} \text{ ms}^{-1}$ , for the cathode ca.  $3 \times 10^{-11} \sim 1 \times 10^{-10} \text{ ms}^{-1}$ , which corresponds to the peak area in the posterior distribution for both parameters (see Figure 4). An obvious positive correlation can be observed between the cathode reaction constant and the film resistance. This may be caused by the coordinated change of the charge transfer overpotential between the anode and cathode. The phenomena shown above indicate that the investigations and conclusions made using synthetic data may not be valid in practical applications, which highlights the necessity of a comprehensive parameter identifiability analysis in practical applications.



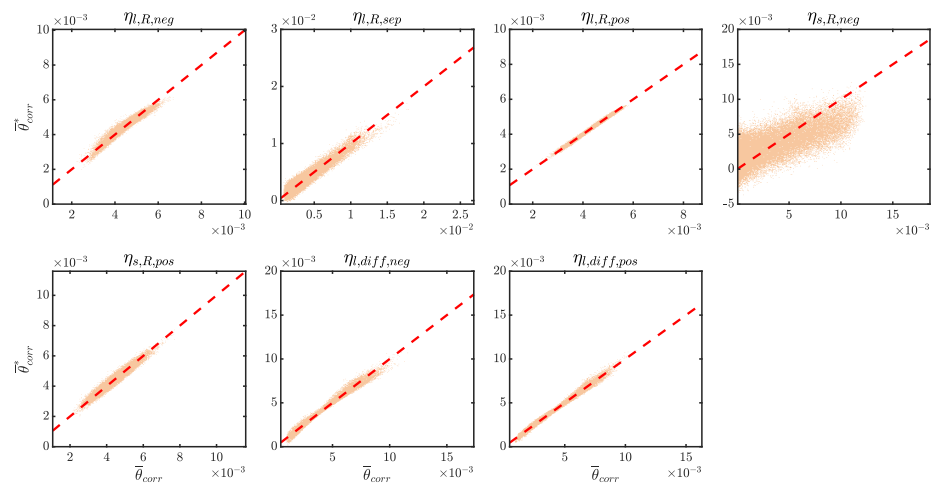
**Figure 7.** Two-dimensional plot of the objective function value for case 1 (upper triangular) and case 2 (lower triangular). For case 1, an obvious correlation can be observed between the film resistance and the anodic reaction rate constant, film resistance and the cathodic reaction rate constant, and anodic reaction rate constant and cathodic reaction rate constant. For case 2, no correlation pattern can be seen.

For case 2, it can be seen that no clearly defined isoline or isosurface is existent for any parameter combination, and all global optimum points are nearly evenly distributed. This phenomenon may have two origins: (1) the isoline or isosurface lies outside the defined parameter range and cannot be observed here; (2) these parameters have only negligible influence on the model output.

For cases 3 and 4, similar behavior can be observed in Figures 8 and 9. For all processes except for the solid conduction in the anode, a good correlation can be observed. The solid conduction in the anode is not well correlated with other processes, we assume that this is attributable to the higher conductivity and negligible overpotential caused by the graphite anode. According to Figure 10c,d, all processes investigated in the correlation chart are correlated and a unique optimal parameter combination does not exist. It is worth mentioning here that although the solid conduction in the cathode shows a correlation relationship with other processes, the solid conductivity in the cathode has a narrow credible interval (see Figure 4) and is thus regarded as identifiable.



**Figure 8.** Results of parameter correlation for case 3. A correlation relation can be observed for each process except for the solid conduction in the anode.



**Figure 9.** Results of parameter correlation for case 4. A correlation relation can be observed for each process except for the solid conduction in the anode.

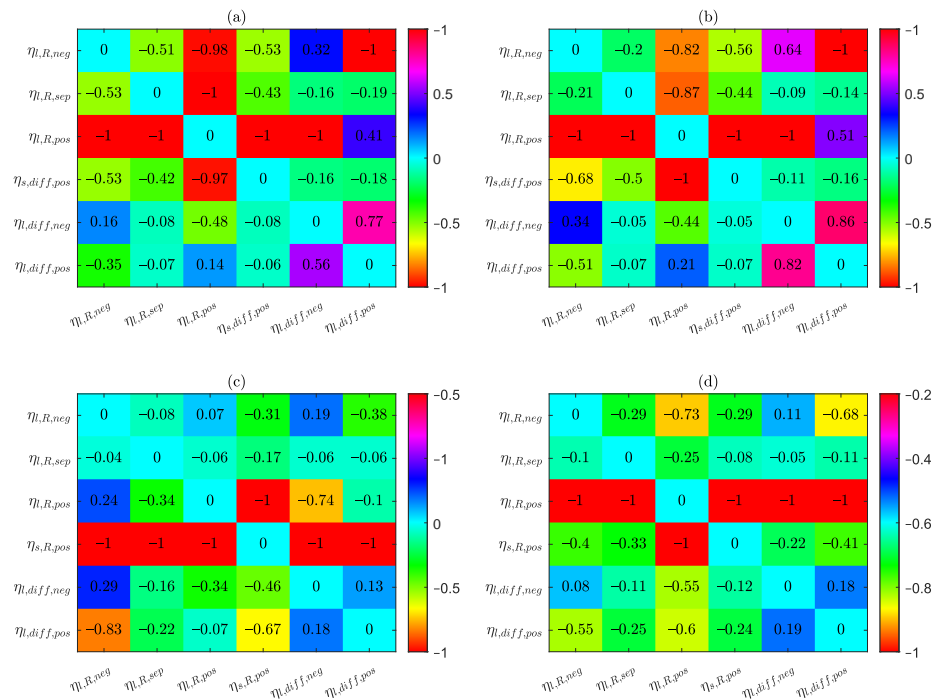


Figure 10. Correlation chart for cases 1–4, where each column in the matrix represents the correlation coefficients with the tested process.

#### 4.3. Selection of Parameters from Posterior Distributions

In previous sections, a comprehensive identifiability and correlation analysis has been conducted, the results have been shown and explained in detail. However, the resulting parameter distributions cannot be used as the input for the p2D model to validate the results; therefore, a point estimate must be selected from the posterior distributions. For the experimental validation, generally the expected value of each parameter is chosen and substituted into the model [10]. Nevertheless, the prerequisite for selecting the expected value as the point estimate is that either all parameters are not correlated or they are only simply linearly correlated so that for the expected values the linear correlation relationship is still valid. For example, if we assume that the parameters  $\theta_1$  and  $\theta_2$  are linearly correlated and the following relation holds:

$$\theta_1 = \alpha\theta_2 + \beta \quad (18)$$

where  $\alpha$  and  $\beta$  are correlation constants. If the expected value operator is applied to both sides of Equation (18), the following equation is obtained:

$$E[\theta_1] = \alpha E[\theta_2] + \beta \quad (19)$$

which implies that for both  $\theta_1$  and  $\theta_2$  the expected value can be selected as the point estimate. However, if  $\theta_1$  and  $\theta_2$  are not linearly but instead nonlinearly correlated, for example:

$$\theta_1 = \frac{\alpha}{\theta_2} + \beta \quad (20)$$

and then the expected value operator is again applied to both sides of the equation, the following equation can be obtained:

$$E[\theta_1] = \alpha E\left[\frac{1}{\theta_2}\right] + \beta \neq \alpha \frac{1}{E[\theta_2]} + \beta \quad (21)$$

This equation clearly indicates that if the parameters are not linearly correlated, the expected values of the parameters will not fulfill the correlation relationship. Simply selecting the expected value for each correlated parameter may lead to an unexpected error. In this work, the parameter combination used for the experimental validation will be selected according to the following principle:

1. For parameters with a small credible interval (irrespective of identifiability), the expected value is selected.
2. For parameters that are practically unidentifiable and there exists no correlation with other parameters, the expected value is selected.
3. For parameters that are correlated, the expected value of the parameter with the highest sensitivity index will be calculated and selected for validation, the values of other parameters will be determined accordingly so that the correlation among the chosen parameters is still valid. If multiple parameter combinations are possible, then the combination closest to the expected values is chosen.

According to the principles explained above, the determined parameter values are summarized in Table 6.

**Table 6.** Summary of the parameter values selected for the validation test.

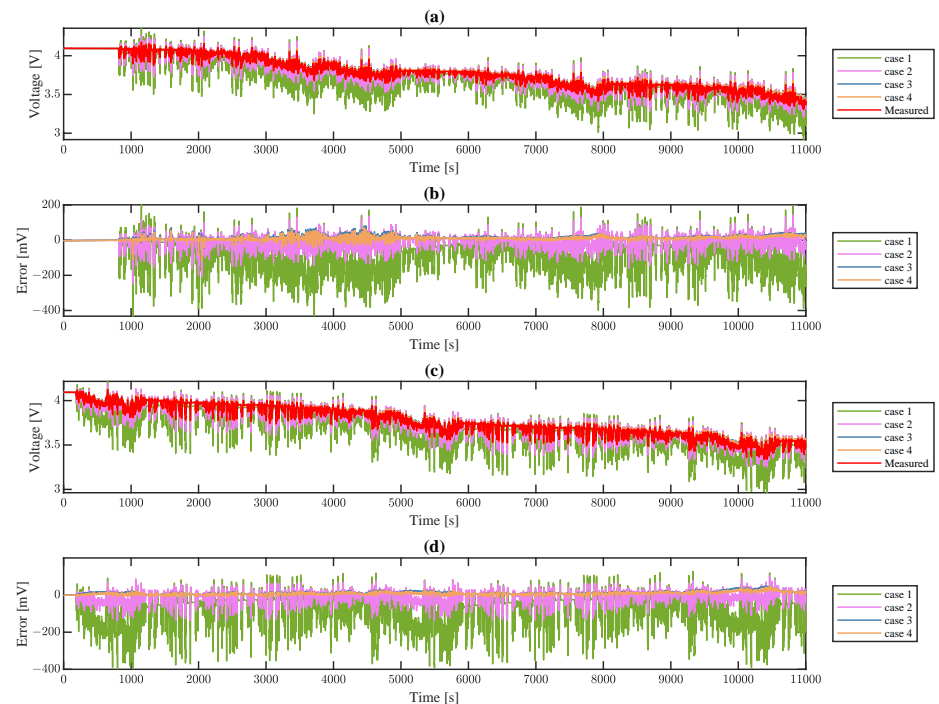
Parameter	Scale	Case 1	Case 2	Case 3	Case 4
$\alpha_{neg}$	linear	0.554	0.511	0.753	0.870
$\alpha_{sep}$	linear	2.736	2.843	1.256	2.756
$\alpha_{pos}$	linear	0.865	0.863	0.801	1.105
$D_{s,neg}$	log	-12.059	-12.042	-	-
$D_{s,pos}$	log	-13.986	-14.188	-	-
$D_{l,0}$	log	-8.323	-8.386	-8.964	-9.092
$\kappa_{l,0}$	log	-0.190	-0.327	0.068	0.064
$\sigma_{neg}$	log	0.531	1.967	0.729	0.793
$\sigma_{pos}$	log	-2.447	-1.809	-1.696	-0.920
$R_{f,neg}$	log	-2.533	-3.661	-	-
$k_{neg}$	log	-10.191	-10.352	-	-
$k_{pos}$	log	-10.595	-9.118	-	-

#### 4.4. Validation with Dynamic Load Profile

The results for the parameter validation with the two application scenarios are shown in Figure 11. In scenario 1, it can be observed that the full model without external ohmic resistance achieves the worst simulation performance, where the maximum error reaches about 400 mV and the root-mean-square error (RMSE) is calculated to be 124.7 mV. The voltage window of the investigated cell is between 2.5 V and 4.2 V, if the OCV curve is approximated with a straight line, then an RMSE of 124.7 mV corresponds to a 7.3% average SOC error, which is unacceptable for a state estimation application. Although in all cases the parameters are identified with the same discharging profile and the best objective function values are almost the same and show no qualitative difference, the most primitive model, namely where all parameters are fitted at the same time and without considering the external ohmic resistance, shows an unacceptable error and fails to model the dynamic operation. The results for the full model with the external ohmic resistance become much better with an RMSE of 35.8 mV, the error is below 100 mV at most times, but a maximum error of about 200 mV can still be seen. The combined model without the external ohmic resistance achieves a qualitative improvement, the RMSE is 17.4 mV and corresponds to a 1% average SOC error, assuming a linear relationship between the cell voltage (2.5~4.2 V) and the SOC (0~100%). The combined model with the external ohmic resistance achieves the best performance with an RMSE of only 12.6 mV, corresponding to a 0.7% average SOC error.

The results for scenario 2 are similar to that in scenario 1 and the error in all cases is slightly lower, again the combined model with external resistance achieves the lowest error,

thus justifying the application of the combined procedure for parameter identification. To have an overall comparison of the simulation performance for the four cases, the root-mean-square error (RMSE) has been calculated and listed in Table 7.



**Figure 11.** Validation results for for all cases with (a) the voltage profile in scenario 1, (b) voltage error in scenario 1, (c) voltage profile in scenario 2, and (d) voltage error in scenario 2.

**Table 7.** Calculated RMSE values for the validation of each case.

RMSE (mV)	Case 1	Case 2	Case 3	Case 4
scenario 1	124.7	35.8	17.4	12.6
scenario 2	117.8	31.7	16.1	11.8

### 5. Conclusions and Outlooks

In this present work, parameter identifiability with the p2D model in four cases is investigated and analyzed: models with or without external ohmic resistance, a model with all chosen parameters fitted, and a model where the kinetic parameters determined in the frequency domain are substituted (combined model). The results of the parameter space sampling indicate that the external ohmic resistance has a considerable impact on the parameter identifiability, especially on the bulk conductivity in the solid and liquid phases, while the results for the Bruggeman coefficients in each electrode layer only show small differences. In the first two cases, all interface parameters are practically unidentifiable. For the third and fourth cases, where the values for the kinetic parameters determined using the EIS are substituted, the parameter identifiability results have changed. Though the Bruggeman coefficients still cannot be uniquely identified, the bulk conductivities in the liquid phase and solid conductivity in the cathode are significantly better compared with the values determined using different methods from the literature.

The parameter correlation analysis indicates that the ohmic conduction and diffusion processes in the solid and liquid phases are generally correlated, given the constant discharging profile used for the parameter identifiability analysis. The only parameter that can be identified while considering the external ohmic resistance and the SOC dependence is



the solid conductivity in the cathode. Therefore, it is worth mentioning again that although the constant charging/discharging voltage profile can be easily fitted using a properly chosen nonlinear optimization algorithm to extract some physicochemical parameter values, the reliability and uniqueness of the results are usually problematic.

Then the estimated parameters are substituted into the p2D model and validated with two highly dynamic load profiles and the simulation results are compared with the experimentally measured voltage response. The results again confirm that the combined model with the external ohmic resistance performs the best and achieves an RMSE on the level of 12 mV. To sum up, the combined type model with both the time domain and frequency domain method clearly outperforms other model types investigated in this work and achieves the best RMSE even when the model is simulated with a highly dynamic profile.

Based on the analysis and conclusions made before, we suggest that the kinetic parameters such as the reaction rate constants and diffusion coefficients should be estimated using frequency domain methods. A carefully selected dynamic voltage and current profile should be used for the parameter identification in the time domain if only the time domain fitting is used for the parameter identification. The dynamic profiles should at least include the characteristic frequency components of the corresponding processes and parameters. Furthermore, we assume that with carefully designed current profiles some of the currently unidentifiable parameters may become identifiable.

**Author Contributions:** Y.Z.: Conceptualization, Methodology, Software, Investigation, Validation, Data Curation, Formal analysis, Writing—Original Draft, Project administration. A.J.: Supervision, Writing—Review and Editing. All authors have read and agreed to the published version of the manuscript.

**Funding:** This research received no external funding.

**Data Availability Statement:** Not applicable.

**Conflicts of Interest:** The authors declare no conflict of interest.

### Abbreviations

The following abbreviations are used in this manuscript:

LIB	lithium-ion battery
EIS	electrochemical impedance spectroscopy
MCMC	Markov Chain Monte Carlo
p2D	pseudo-two dimensional
ECM	equivalent circuit model
PCM	physicochemical model
ROM	reduced-order model
DRT	distribution of relaxation times
DOF	degree of freedom
OAT	once at a time
FIM	Fisher information matrix
HDP	highest density probability
ETI	equal-tailed interval
CI	confidence interval
SI	sensitivity index
SOC	state of charge
OCV	open-circuit voltage
CC	current collector
PDF	probability density function
CDF	cumulative density function
RMSE	root-mean-square error

## References

- Masouidi, R.; Uchida, T.; McPhee, J. Parameter estimation of an electrochemistry-based lithium-ion battery model. *J. Power Sources* **2015**, *291*, 215–224. [\[CrossRef\]](#)
- Miniguano, H.; Barrado, A.; Lázaro, A.; Zumel, P.; Fernández, C. General parameter identification procedure and comparative study of Li-Ion battery models. *IEEE Trans. Veh. Technol.* **2019**, *69*, 235–245. [\[CrossRef\]](#)
- Wimarshana, B.; Bin-Mat-Arishad, I.; Fly, A. Parameter sensitivity analysis of a physico-chemical lithium-ion battery model with combined discharge voltage and electrochemical impedance data. *J. Power Sources* **2022**, *527*, 231125. [\[CrossRef\]](#)
- Laue, V.; Röder, F.; Krewer, U. Practical identifiability of electrochemical P2D models for lithium-ion batteries. *J. Appl. Electrochem.* **2021**, *51*, 1253–1265. [\[CrossRef\]](#)
- Lai, X.; Gao, W.; Zheng, Y.; Ouyang, M.; Li, J.; Han, X.; Zhou, L. A comparative study of global optimization methods for parameter identification of different equivalent circuit models for Li-ion batteries. *Electrochim. Acta* **2019**, *295*, 1057–1066. [\[CrossRef\]](#)
- Tran, M.K.; DaCosta, A.; Mevawalla, A.; Panchal, S.; Fowler, M. Comparative study of equivalent circuit models performance in four common lithium-ion batteries: LFP, NMC, LMO, NCA. *Batteries* **2021**, *7*, 51. [\[CrossRef\]](#)
- Uddin, K.; Picarelli, A.; Lyness, C.; Taylor, N.; Marco, J. An acausal Li-ion battery pack model for automotive applications. *Energies* **2014**, *7*, 5675–5700. [\[CrossRef\]](#)
- Uddin, K.; Perera, S.; Widanage, W.D.; Marco, J. Characterising Li-ion battery degradation through the identification of perturbations in electrochemical battery models. *World Electr. Veh. J.* **2015**, *7*, 76–84. [\[CrossRef\]](#)
- Yang, X.; Chen, L.; Xu, X.; Wang, W.; Xu, Q.; Lin, Y.; Zhou, Z. Parameter identification of electrochemical model for vehicular lithium-ion battery based on particle swarm optimization. *Energies* **2017**, *10*, 1811. [\[CrossRef\]](#)
- Brady, N.W.; Gould, C.A.; West, A.C. Quantitative parameter estimation, model selection, and variable selection in battery science. *J. Electrochem. Soc.* **2019**, *167*, 013501. [\[CrossRef\]](#)
- Rahman, M.A.; Anwar, S.; Izadian, A. Electrochemical model parameter identification of a lithium-ion battery using particle swarm optimization method. *J. Power Sources* **2016**, *307*, 86–97. [\[CrossRef\]](#)
- Forman, J.C.; Moura, S.J.; Stein, J.L.; Fathy, H.K. Genetic identification and fisher identifiability analysis of the Doyle–Fuller–Newman model from experimental cycling of a LiFePO<sub>4</sub> cell. *J. Power Sources* **2012**, *210*, 263–275. [\[CrossRef\]](#)
- Berliner, M.D.; Zhao, H.; Das, S.; Forsuelo, M.; Jiang, B.; Chueh, W.H.; Bazant, M.Z.; Braatz, R.D. Nonlinear Identifiability Analysis of the Porous Electrode Theory Model of Lithium-Ion Batteries. *J. Electrochem. Soc.* **2021**, *168*, 090546. [\[CrossRef\]](#)
- Rajabloo, B.; Jokar, A.; Désilets, M.; Lacroix, M. An inverse method for estimating the electrochemical parameters of lithium-ion batteries. *J. Electrochem. Soc.* **2016**, *164*, A99. [\[CrossRef\]](#)
- Pozzi, A.; Ciarabella, G.; Volkwein, S.; Raimondo, D.M. Optimal design of experiments for a lithium-ion cell: Parameters identification of an isothermal single particle model with electrolyte dynamics. *Ind. Eng. Chem. Res.* **2018**, *58*, 1286–1299. [\[CrossRef\]](#)
- Jin, N.; Danilov, D.L.; Van den Hof, P.M.; Donkers, M. Parameter estimation of an electrochemistry-based lithium-ion battery model using a two-step procedure and a parameter sensitivity analysis. *Int. J. Energy Res.* **2018**, *42*, 2417–2430. [\[CrossRef\]](#)
- Li, J.; Wang, L.; Lyu, C.; Liu, E.; Xing, Y.; Pecht, M. A parameter estimation method for a simplified electrochemical model for Li-ion batteries. *Electrochim. Acta* **2018**, *275*, 50–58. [\[CrossRef\]](#)
- Gopalakrishnan, K.; Offer, G.J. A Composite Single Particle Lithium-ion Battery Model through System Identification. *IEEE Trans. Control Syst. Technol.* **2021**, *30*, 1–13. [\[CrossRef\]](#)
- Deng, Z.; Deng, H.; Yang, L.; Cai, Y.; Zhao, X. Implementation of reduced-order physics-based model and multi-parameters identification strategy for lithium-ion battery. *Energy* **2017**, *138*, 509–519. [\[CrossRef\]](#)
- Kosch, S.; Zhao, Y.; Sturm, J.; Schuster, J.; Mulder, G.; Ayerbe, E.; Jossen, A. A computationally efficient multi-scale model for lithium-ion cells. *J. Electrochem. Soc.* **2018**, *165*, A2374. [\[CrossRef\]](#)
- Wu, L.; Pang, H.; Geng, Y.; Liu, X.; Liu, J.; Liu, K. Low-complexity state of charge and anode potential prediction for lithium-ion batteries using a simplified electrochemical model-based observer under variable load condition. *Int. J. Energy Res.* **2022**, *46*, 11834–11848. [\[CrossRef\]](#)
- Ding, Q.; Wang, Y.; Chen, Z. Parameter identification of reduced-order electrochemical model simplified by spectral methods and state estimation based on square-root cubature Kalman filter. *J. Energy Storage* **2022**, *46*, 103828. [\[CrossRef\]](#)
- Kalogiannis, T.; Hosen, M.S.; Sokkeh, M.A.; Goutam, S.; Jaguemont, J.; Jin, L.; Qiao, G.; Berecibar, M.; Van Mierlo, J. Comparative Study on Parameter Identification Methods for Dual-Polarization Lithium-Ion Equivalent Circuit Model. *Energies* **2019**, *12*, 4031. [\[CrossRef\]](#)
- De Levie, R. On porous electrodes in electrolyte solutions: I. Capacitance effects. *Electrochim. Acta* **1963**, *8*, 751–780. [\[CrossRef\]](#)
- De Levie, R. On porous electrodes in electrolyte solutions—IV. *Electrochim. Acta* **1964**, *9*, 1231–1245. [\[CrossRef\]](#)
- Vyroubal, P.; Kazda, T. Equivalent circuit model parameters extraction for lithium ion batteries using electrochemical impedance spectroscopy. *J. Energy Storage* **2018**, *15*, 23–31. [\[CrossRef\]](#)
- Choi, W.; Shin, H.C.; Kim, J.M.; Choi, J.Y.; Yoon, W.S. Modeling and Applications of Electrochemical Impedance Spectroscopy (EIS) for Lithium-ion Batteries. *J. Electrochem. Sci. Technol.* **2020**, *11*, 1–13. [\[CrossRef\]](#)
- Illig, J.; Ender, M.; Weber, A.; Ivers-Tiffée, E. Modeling graphite anodes with serial and transmission line models. *J. Power Sources* **2015**, *282*, 335–347. [\[CrossRef\]](#)

29. Bizeray, A.M.; Kim, J.H.; Duncan, S.R.; Howey, D.A. Identifiability and parameter estimation of the single particle lithium-ion battery model. *IEEE Trans. Control Syst. Technol.* **2018**, *27*, 1862–1877. [[CrossRef](#)]
30. Dokko, K.; Mohamedi, M.; Fujita, Y.; Itoh, T.; Nishizawa, M.; Umeda, M.; Uchida, I. Kinetic characterization of single particles of LiCoO<sub>2</sub> by AC impedance and potential step methods. *J. Electrochem. Soc.* **2001**, *148*, A422. [[CrossRef](#)]
31. Prasad, G.K.; Rahn, C.D. Reduced order impedance models of lithium ion batteries. *J. Dyn. Syst. Meas. Control* **2014**, *136*, 041012. [[CrossRef](#)]
32. Sikha, G.; White, R.E. Analytical expression for the impedance response of an insertion electrode cell. *J. Electrochem. Soc.* **2006**, *154*, A43. [[CrossRef](#)]
33. Sikha, G.; White, R.E. Analytical expression for the impedance response for a lithium-ion cell. *J. Electrochem. Soc.* **2008**, *155*, A893. [[CrossRef](#)]
34. Murbach, M.D.; Schwartz, D.T. Extending Newman’s pseudo-two-dimensional lithium-ion battery impedance simulation approach to include the nonlinear harmonic response. *J. Electrochem. Soc.* **2017**, *164*, E3311. [[CrossRef](#)]
35. Zhou, X.; Huang, J. Impedance-Based diagnosis of lithium ion batteries: Identification of physical parameters using multi-output relevance vector regression. *J. Energy Storage* **2020**, *31*, 101629. [[CrossRef](#)]
36. Lasia, A. Electrochemical impedance spectroscopy and its applications. In *Modern Aspects of Electrochemistry*; Springer: Berlin/Heidelberg, Germany, 2002; pp. 143–248.
37. Boukamp, B.A. Distribution (function) of relaxation times, successor to complex nonlinear least squares analysis of electrochemical impedance spectroscopy? *J. Electrochem. Soc.* **2020**, *2*, 042001. [[CrossRef](#)]
38. Danzer, M.A. Generalized Distribution of Relaxation Times Analysis for the Characterization of Impedance Spectra. *Batteries* **2019**, *5*, 53. [[CrossRef](#)]
39. Hahn, M.; Schindler, S.; Triebs, L.C.; Danzer, M.A. Optimized Process Parameters for a Reproducible Distribution of Relaxation Times Analysis of Electrochemical Systems. *Batteries* **2019**, *5*, 43. [[CrossRef](#)]
40. Gavriljuk, A.L.; Osinkin, D.A.; Bronin, D.I. On a variation of the Tikhonov regularization method for calculating the distribution function of relaxation times in impedance spectroscopy. *Electrochim. Acta* **2020**, *354*, 136683. [[CrossRef](#)]
41. Shafiei Sabet, P.; Warnecke, A.J.; Meier, F.; Witzenhause, H.; Martinez-Laserna, E.; Sauer, D.U. Non-invasive yet separate investigation of anode/cathode degradation of lithium-ion batteries (nickel–cobalt–manganese vs. graphite) due to accelerated aging. *J. Power Sources* **2020**, *449*, 227369. [[CrossRef](#)]
42. Ivers-Tiffée, E.; Weber, A. Evaluation of electrochemical impedance spectra by the distribution of relaxation times. *J. Ceram. Soc. Jpn.* **2017**, *125*, 193–201. [[CrossRef](#)]
43. Boukamp, B.A.; Rolle, A. Analysis and application of distribution of relaxation times in solid state ionics. *Solid State Ionics* **2017**, *302*, 12–18. [[CrossRef](#)]
44. Boukamp, B.A.; Rolle, A. Use of a distribution function of relaxation times (DFRT) in impedance analysis of SOFC electrodes. *Solid State Ionics* **2018**, *314*, 103–111. [[CrossRef](#)]
45. Rolle, A.; Mohamed, H.A.A.; Huo, D.; Capoen, E.; Mentre, O.; Vannier, R.N.; Daviero-Minaud, S.; Boukamp, B.A. Ca<sub>3</sub>Co<sub>4</sub>O<sub>9+δ</sub>, a growing potential SOFC cathode material: Impact of the layer composition and thickness on the electrochemical properties. *Solid State Ionics* **2016**, *294*, 21–30. [[CrossRef](#)]
46. Illig, J.; Ender, M.; Chrobak, T.; Schmidt, J.P.; Klotz, D.; Ivers-Tiffée, E. Separation of charge transfer and contact resistance in LiFePO<sub>4</sub>-cathodes by impedance modeling. *J. Electrochem. Soc.* **2012**, *159*, A952. [[CrossRef](#)]
47. Illig, J.; Schmidt, J.P.; Weiss, M.; Weber, A.; Ivers-Tiffée, E. Understanding the impedance spectrum of 18650 LiFePO<sub>4</sub>-cells. *J. Power Sources* **2013**, *239*, 670–679. [[CrossRef](#)]
48. Doyle, M.; Fuller, T.F.; Newman, J. Modeling of galvanostatic charge and discharge of the lithium/polymer/insertion cell. *J. Electrochem. Soc.* **1993**, *140*, 1526. [[CrossRef](#)]
49. Doyle, M.; Newman, J. Modeling the performance of rechargeable lithium-based cells: Design correlations for limiting cases. *J. Power Sources* **1995**, *54*, 46–51. [[CrossRef](#)]
50. Doyle, M.; Newman, J.; Gozdz, A.S.; Schmutz, C.N.; Tarascon, J.M. Comparison of modeling predictions with experimental data from plastic lithium ion cells. *J. Electrochem. Soc.* **1996**, *143*, 1890–1903. [[CrossRef](#)]
51. Iooss, B.; Lemaître, P. A review on global sensitivity analysis methods. In *Uncertainty Management in Simulation-Optimization of Complex Systems*; Springer: Berlin/Heidelberg, Germany, 2015; pp. 101–122.
52. Sobol, I.M. Global sensitivity indices for nonlinear mathematical models and their Monte Carlo estimates. *Math. Comput. Simul.* **2001**, *55*, 271–280. [[CrossRef](#)]
53. Kumbhare, S.; Shahmoradi, A. MatDRAM: A pure-MATLAB Delayed-Rejection Adaptive Metropolis-Hastings Markov Chain Monte Carlo Sampler. *arXiv* **2020**, arXiv:2010.04190.
54. Gelman, A.; Gilks, W.R.; Roberts, G.O. Weak convergence and optimal scaling of random walk Metropolis algorithms. *Ann. Appl. Probab.* **1997**, *7*, 110–120. [[CrossRef](#)]
55. Rabissi, C.; Innocenti, A.; Sordi, G.; Casalegno, A. A Comprehensive Physical-Based Sensitivity Analysis of the Electrochemical Impedance Response of Lithium-Ion Batteries. *Energy Technol.* **2021**, *9*, 2000986. [[CrossRef](#)]
56. Astrom, K.; Bellman, R. On structural identifiability. *Math. Biosci.* **1970**, *7*, 329–339.
57. Meyers, J.P.; Doyle, M.; Darling, R.M.; Newman, J. The impedance response of a porous electrode composed of intercalation particles. *J. Electrochem. Soc.* **2000**, *147*, 2930. [[CrossRef](#)]

58. Schönleber, M.; Uhlmann, C.; Braun, P.; Weber, A.; Ivers-Tiffée, E. A consistent derivation of the impedance of a lithium-ion battery electrode and its dependency on the state-of-charge. *Electrochim. Acta* **2017**, *243*, 250–259. [[CrossRef](#)]
59. Nyman, A.; Zavalis, T.G.; Elger, R.; Behm, M.; Lindbergh, G. Analysis of the polarization in a Li-ion battery cell by numerical simulations. *J. Electrochem. Soc.* **2010**, *157*, A1236. [[CrossRef](#)]
60. Reimers, J.N. Accurate and efficient treatment of foil currents in a spiral wound Li-ion cell. *J. Electrochem. Soc.* **2013**, *161*, A118. [[CrossRef](#)]
61. Zhao, Y.; Kumtepli, V.; Ludwig, S.; Jossen, A. Investigation of the distribution of relaxation times of a porous electrode using a physics-based impedance model. *J. Power Sources* **2022**, *530*, 231250. [[CrossRef](#)]
62. Zhao, Y.; Kücher, S.; Jossen, A. Investigation of the Diffusion Phenomena in Lithium-ion Batteries with Distribution of Relaxation Times. *Electrochim. Acta* **2022**, *432*, 141174. [[CrossRef](#)]
63. Sturm, J.; Rheinfeld, A.; Zilberman, I.; Spingler, F.B.; Kosch, S.; Frie, F.; Jossen, A. Modeling and simulation of inhomogeneities in a 18650 nickel-rich, silicon-graphite lithium-ion cell during fast charging. *J. Power Sources* **2019**, *412*, 204–223. [[CrossRef](#)]
64. Chen, C.H.; Planella, F.B.; O'regan, K.; Gastol, D.; Widanage, W.D.; Kendrick, E. Development of experimental techniques for parameterization of multi-scale lithium-ion battery models. *J. Electrochem. Soc.* **2020**, *167*, 080534. [[CrossRef](#)]
65. Tang, S.; Wang, Z.; Guo, H.; Wang, J.; Li, X.; Yan, G. Systematic parameter acquisition method for electrochemical model of 4.35 V LiCoO<sub>2</sub> batteries. *Solid State Ionics* **2019**, *343*, 115083. [[CrossRef](#)]
66. Wei, Y.; Zheng, J.; Cui, S.; Song, X.; Su, Y.; Deng, W.; Wu, Z.; Wang, X.; Rao, M.; et al. Kinetics tuning of Li-ion diffusion in layered Li (Ni<sub>x</sub>Mn<sub>y</sub>Co<sub>z</sub>) O<sub>2</sub>. *J. Am. Chem. Soc.* **2015**, *137*, 8364–8367. [[CrossRef](#)] [[PubMed](#)]
67. Noh, H.J.; Youn, S.; Yoon, C.S.; Sun, Y.K. Comparison of the structural and electrochemical properties of layered Li [Ni<sub>x</sub>Co<sub>y</sub>Mn<sub>z</sub>] O<sub>2</sub> (x = 1/3, 0.5, 0.6, 0.7, 0.8 and 0.85) cathode material for lithium-ion batteries. *J. Power Sources* **2013**, *233*, 121–130. [[CrossRef](#)]
68. Landesfeind, J.; Gasteiger, H.A. Temperature and concentration dependence of the ionic transport properties of lithium-ion battery electrolytes. *J. Electrochem. Soc.* **2019**, *166*, A3079. [[CrossRef](#)]
69. Richardson, G.; Foster, J.M.; Sethurajan, A.K.; Krachkovskiy, S.A.; Halalay, I.C.; Goward, G.R.; Protas, B. The effect of ionic aggregates on the transport of charged species in lithium electrolyte solutions. *J. Electrochem. Soc.* **2018**, *165*, H561. [[CrossRef](#)]
70. Krachkovskiy, S.A.; Bazak, J.D.; Fraser, S.; Halalay, I.C.; Goward, G.R. Determination of mass transfer parameters and ionic association of LiPF<sub>6</sub>: Organic carbonates solutions. *J. Electrochem. Soc.* **2017**, *164*, A912. [[CrossRef](#)]
71. Farkhondeh, M.; Safari, M.; Pritzker, M.; Fowler, M.; Han, T.; Wang, J.; Delacourt, C. Full-range simulation of a commercial LiFePO<sub>4</sub> electrode accounting for bulk and surface effects: A comparative analysis. *J. Electrochem. Soc.* **2013**, *161*, A201. [[CrossRef](#)]
72. Prada, E.; Di Domenico, D.; Creff, Y.; Bernard, J.; Sauvante-Moynot, V.; Huet, F. Simplified electrochemical and thermal model of LiFePO<sub>4</sub>-graphite Li-ion batteries for fast charge applications. *J. Electrochem. Soc.* **2012**, *159*, A1508. [[CrossRef](#)]
73. Park, M.; Zhang, X.; Chung, M.; Less, G.B.; Sastry, A.M. A review of conduction phenomena in Li-ion batteries. *J. Power Sources* **2010**, *195*, 7904–7929. [[CrossRef](#)]
74. Wang, S.; Yan, M.; Li, Y.; Vinado, C.; Yang, J. Separating electronic and ionic conductivity in mix-conducting layered lithium transition-metal oxides. *J. Power Sources* **2018**, *393*, 75–82. [[CrossRef](#)]
75. Shafiei Sabet, P.; Sauer, D.U. Separation of predominant processes in electrochemical impedance spectra of lithium-ion batteries with nickel-manganese-cobalt cathodes. *J. Power Sources* **2019**, *425*, 121–129. [[CrossRef](#)]

## 7 Conclusions and Outlooks

In the present thesis, the application of the DRT technique to the parameter estimation and validation of the Lithium-ion battery combined with a physicochemical impedance model was investigated comprehensively. The analytical expressions of the DRT spectrum in the mid-high and mid-low frequency range were derived and analyzed. Besides, lab experiments using a commercially available Lithium-ion battery cell were conducted to estimate a few key kinetic parameters: electrochemical reaction rate constant, SEI resistivity and the solid phase diffusion coefficient. As a result, the following two key issues for the parameter estimation using the EIS technique and a physicochemical impedance model have been resolved:

1. The nonlinear fitting problem which arises when trying to fit the physicochemical impedance model can be transformed to a LLS problem, which is defined by the DRT and has a unique solution.
2. A quantitative interpretation of the calculated DRT spectrum based on a physicochemical impedance model has been proposed, with which the DRT spectrum can be described with the fundamental theory and the physicochemical parameters.

Furthermore, a comprehensive study was carried out which compared the parameter identifiability in various combined scenarios and the influence of the additional ohmic resistance was investigated. The identification results have shown that the identification method does have a significant impact on the parameter identifiability. Besides, the validation results indicate that the combined parameter identification method with the additional ohmic resistance achieves the best validation performance.

### 7.1 Conclusions

Due to the rapidly increasing market share of the Lithium-ion battery in various sectors, an increasingly number of research works have focused on the development and application of the Lithium-ion battery. Among the focused research topics, the estimation of the kinetic parameters of the Lithium-ion battery has gained much attention. On the one hand, an accurate characterization of the battery materials is crucial for the product development and optimization. On the other hand, numerous application scenarios of the Lithium-ion battery require an accurate calculation of the battery states such as the voltage, temperature, and SOC using a properly selected battery model. The selected battery model must be well parametrized and thus demand the model parameters be accurately estimated. Among the various characterization techniques, the EIS technique, as a fast and nondestructive technique, has been widely applied to characterize the Lithium-ion battery. The EIS technique can well separate the kinetic processes with different characteristic frequencies, which is generally hard to realize with time domain methods.

Although the EIS technique can provide the measurement data suitable for the estimation of the kinetic parameters, still an appropriate impedance model must be selected to evaluate the data. For a long time, the ECM has been selected as the candidate model for the data evaluation and parameter

estimation due to the following features: 1. the ECM has a simple structure and thus a low computation effort, which makes it especially suitable for the parameter estimation problem; 2. the simple structure of the ECM originates from the intuitive understanding of the physicochemical processes in the Lithium-ion battery, based on which the process attribution has been made. However, the merits of the ECM has also revealed its limitations: 1. for a certain application scenario, the structure of the ECM is usually not unique and strongly relies on the experience of the operators, generally the same impedance data can be fitted with multiple circuits of different structures; 2. the choice of the circuit elements along with the structure of the ECM is rather based on a phenomenological understanding of the physicochemical processes than any fundamental theory. Hence, the estimation results can be hardly correlated with the physicochemical parameters of the Lithium-ion battery. To fill the gap between the measurement results and the physicochemical parameters, instead of the ECM, the physicochemical impedance model must be used to fit the impedance data. Due to the strongly non-linear nature of the physicochemical impedance model and complicated mathematical structure, the model fitting is usually faced with the identifiability issue and the computation effort is significantly higher than that of the ECM as well.

To effectively distinguish between the processes with different characteristic frequencies and reduce the computation effort, the DRT method has been frequently applied to the evaluation and interpretation of the impedance data. By using DRT, the impedance data in frequency domain can be easily transformed into time constant domain ( $\tau$  domain) and represented by the DRT spectrum. The processes with different time constants and amplitude can be effectively separated and clearly visualized in the spectrum. Nevertheless, the DRT spectrum characterizes the distribution of the time constants of the RC elements and is thus model-free, the interpretation of the DRT spectrum still requires a properly selected battery model. As mentioned above, both the physicochemical impedance model and the DRT method have their respective advantages and limitations. Naturally, a combined use of the physicochemical impedance model and the DRT technique should be able to resolve the identifiability and interpretation issue and improved parameter estimation results can be expected.

In chapter 4, the present thesis has focused on the mid-high frequency range and a physicochemical impedance model based on the well-known p2D model was derived. In the frequency range of interest, the diffusion phenomena in the solid and liquid phases were neglected due to their sluggish dynamics and tiny contribution to the impedance. The developed impedance model was combined with the DRT technique and an analytical expression for the DRT spectrum was derived and analyzed. The developed theory indicates that the frequency dispersion phenomenon will possibly occur in the high frequency range and one process will cause more than one peak in the resulting DRT spectrum, the dispersion occurs in the direction of decreasing amplitude and time constant. This conclusion is especially crucial for the interpretation of the DRT spectrum and peak attribution, because each peak will not be necessarily attributed to different processes. Furthermore, the dispersion could also be erroneously interpreted as multiple different processes, if the spectrum has not been comprehensively analyzed using the developed theory. Another improvement brought by the developed theory is that a quantitative relationship has been established between the DRT spectrum and the physicochemical parameters of the Lithium-ion battery. On this basis, a commercially available Lithium-ion battery cell was used to estimate the electrochemical reaction rate constants and the SEI parameters under different temperatures. Besides, the developed theory shows that the CPE type behavior of the solid particle impedance will lead to another dispersion phenomenon, which can be observed in the DRT spectrum of the full cell, i.e., a proper fitting function must be selected to conduct the peak analysis. For this purpose, the adaptive peak analysis method (APAM) has been developed to improve the

quality of the peak analysis, where not only the peak fitting parameters, but also the functional form of the fitting functions is optimized. The estimated parameters are consistent and comparable with the values measured using different techniques. While the derived theory has well explained the DRT spectrum of a Lithium-ion battery in the mid-high frequency range, attributing each peak to the right process has been a key issue when evaluating the DRT spectrum. In the present thesis, the peak attribution was conducted by comparing the DRT spectrum of the coin cells made of the anode and cathode samples of the full cell. Although the peak attribution can be conducted indirectly and has proven to be effective in this thesis, the impedance and DRT spectra of the coin cells were disturbed by the Li-metal counter electrode and the separator inevitably. Therefore, further improvement on the experimental procedure is then suggested to avoid the disturbance caused by the coin cells.

While in chapter 4 the physicochemical processes in mid-high frequency range have been investigated and the corresponding parameters were estimated using the DRT spectrum, in chapter 5 the processes in mid-low frequency range was investigated, including the diffusion phenomena in the solid and liquid phases. With the liquid phase diffusion considered, the conduction and diffusion phenomena in the electrode cannot be decoupled, the mathematical structure of the model thus becomes much more sophisticated. To ease the model development, the diffusion in the liquid phase was neglected at first and the assumption 1 was applied. The developed theory indicates that the frequency dispersion will significantly decay with increasing time constant so that in the mid-low frequency range the dispersion can be practically neglected. Furthermore, the application scenario where the particle size distribution was considered has also been investigated and a model for the estimation of the solid diffusion coefficient has been developed. Besides, a brief mathematical analysis of the GITT was made and it was concluded that when the contribution of the liquid diffusion cannot be neglected, the solid diffusion coefficient will be vastly underestimated. The developed theory was then validated using a group of synthetic experimental data. To validate the developed theory, first a group of synthetic impedance data was generated and the DRT spectra were calculated using the developed theory and numerical algorithm respectively. The validation results display that the numerically calculated DRT spectra coincide well with the theoretical prediction except that the amplitude of the peak for the liquid diffusion is overestimated. The amplitude discrepancy is believed to be caused by the simplified model development procedure. However, the calculated time constant for the liquid diffusion agrees well with the theoretical prediction. Subsequently, the developed model was applied to a commercially available Lithium-ion battery to estimate the solid diffusion coefficient. The used full cell was opened and a piece of anode and cathode sample were taken to build the coin cells with a Li-metal counter electrode. The impedance of the full cell and coin cells were measured at different lithiation states and then the DRT spectra were calculated to estimate the solid diffusion coefficient of the anode and cathode material respectively. Meanwhile, the GITT technique has been conducted on the same coin cells to estimate the solid diffusion coefficient. The estimation results with the DRT technique were well comparable with the values measured using different methods from the literature. Furthermore, the results of the solid diffusion coefficient estimation fully meet the expectation that when the low frequency impedance is dominated by the liquid diffusion, the solid diffusion coefficient would be strongly underestimated by the GITT method. Specifically, at the lithiation states where the solid diffusion dominates, both estimation methods gave similar results. In summary, the developed method can be a promising alternative to the GITT technique, which only provides valid measurement results when the contribution of the liquid diffusion is practically negligible.

As the EIS technique is only one of the various methods for cell characterization and each method brings its advantages and disadvantages with regard to computation effort, identifiability, accuracy, etc..

Therefore a comparative study of the parameter characterization in time and frequency domain has been conducted in the present thesis. In this study, four cases were created to carry out the parameter identification and a reduced order physicochemical model was used to accelerate the identification process. The four cases describe the following application scenarios: time domain fitting without external ohmic resistance, time domain fitting with external ohmic resistance, combined model without ohmic resistance, and combined model with ohmic resistance. The parameter identification results indicate that the SOC dependence of certain parameters brought by the combined model does change the whole parameter space and some parameters which were unidentifiable in case 1 and 2 became identifiable in case 3 and 4. Besides, it is worth mentioning that parameters like the Bruggeman coefficients and anode electronic conductivity are poorly identifiable in all cases. To identify the possible correlation relationship among the identified parameters, a multidimensional parameter correlation analysis was conducted. The results indicate that the correlation generally exists among most of the identified parameters, including the parameters with a well defined credible interval. Furthermore, it has been shown that the key kinetic parameters can be perfectly estimated in frequency domain, while time domain fitting method does not bring any benefit. Then the identified parameters in each case were validated using two highly dynamic load profiles and the root-mean-square-error (RMSE) was calculated for each case. The validation results indicate, as expected, that time domain fitting without external ohmic resistance achieves the worst validation performance, the RMSE exceeds 100 V. The combined model with the external ohmic resistance has achieved the best validation performance with ca. 11 mV RMSE. It can be concluded that a combined model will change the parameter space and lead to improved calculation results in time domain. Furthermore, the investigation conducted in this chapter also suggests that a constant charging/discharging profile may not be suitable for the parameter identification application owing to the lack of dynamic current/voltage information.

## 7.2 Outlooks for Future Work

The present thesis has conducted a systematic investigation of the DRT spectrum of the Lithium-ion battery combined with a physicochemical impedance model in the mid-high and mid-low frequency range respectively. Based on the developed theory, the key kinetic parameters of the electrode have been estimated and validated using two highly dynamic load profiles.

While the research study conducted in this thesis has focused on the characterization of fresh cells, it might be worthwhile conducting an aging study to investigate the aging mechanisms with the help of the DRT spectrum. Because the developed theory has assigned a clear physical meaning to the corresponding peaks, therefore the evolution of the relevant processes can be precisely tracked and evaluated. Furthermore, a combined application of the DRT technique and other diagnostic methods like the differential voltage analysis (DVA) may lead to a more comprehensive characterization of the tested battery cell and provide more reliable conclusions.

In chapter 6 it has been concluded that a combined model will change the whole parameter space and thus improve the parameter identifiability. However, only a constant discharging profile has been used for the parameter identification and it turns out that most of the material transport parameters cannot be reliably estimated. It can be assumed that the poor identifiability of the parameters may arise from the current and voltage profile, which does not contain enough information about the kinetic processes necessary for the parameter characterization. As a result, the overpotential components that are crucial for kinetic processes may be missing. Hence, a properly designed current profile and characterization



procedure which specifically considers the kinetic processes may help to produce improved parameter estimation results.

## References

- [1] IEA: *Global EV Outlook 2021*. Technical report. IEA, 2021. URL: <https://www.iea.org/reports/global-ev-outlook-2021> (see p. 1).
- [2] König, A., Nicoletti, L., Schröder, D., Wolff, S., Waclaw, A., and Lienkamp, M.: *An overview of parameter and cost for battery electric vehicles*. In: *World Electric Vehicle Journal* 12.1 (2021), p. 21 (see p. 1).
- [3] Xiong, R., Li, L., and Tian, J.: *Towards a smarter battery management system: A critical review on battery state of health monitoring methods*. In: *Electrochemical and Solid-State Letters* 405 (2018), pp. 18–29. ISSN: 0378-7753. DOI: 10.1016/j.jpowsour.2018.10.019 (see p. 1).
- [4] Lasia, A.: *Electrochemical impedance spectroscopy and its applications*. In: *Modern aspects of electrochemistry*. Springer, 2002, pp. 143–248 (see pp. 1, 5, 25, 26, 30).
- [5] Kalogiannis, T., Hosen, M., Sokkeh, M., Goutam, S., Jaguemont, J., Jin, L., Qiao, G., Berecibar, M., and van Mierlo, J.: *Comparative Study on Parameter Identification Methods for Dual-Polarization Lithium-Ion Equivalent Circuit Model*. In: *Energies* 12.21 (2019), p. 4031. ISSN: 1996-1073. DOI: 10.3390/en12214031 (see p. 4).
- [6] Vyroubal, P. and Kazda, T.: *Equivalent circuit model parameters extraction for lithium ion batteries using electrochemical impedance spectroscopy*. In: *Journal of Energy Storage* 15 (2018), pp. 23–31. DOI: 10.1016/j.est.2017.10.019 (see p. 4).
- [7] Charbonneau, V., Lasia, A., and Brisard, G.: *Impedance studies of Li<sup>+</sup> diffusion in nickel manganese cobalt oxide (NMC) during charge/discharge cycles*. In: *Journal of Electroanalytical Chemistry* (2020), p. 113944. ISSN: 15726657. DOI: 10.1016/j.jelechem.2020.113944 (see p. 4).
- [8] Gabano, J.-D., Poinot, T., and Huard, B.: *Bounded diffusion impedance characterization of battery electrodes using fractional modeling*. In: *Communications in Nonlinear Science and Numerical Simulation* 47 (2017), pp. 164–177. ISSN: 10075704. DOI: 10.1016/j.cnsns.2016.11.016 (see p. 4).
- [9] Sikha, G. and White, R. E.: *Analytical Expression for the Impedance Response of an Insertion Electrode Cell*. In: *Journal of The Electrochemical Society* 154.1 (2007), A43. ISSN: 0013-4651. DOI: 10.1149/1.2372695 (see p. 4).
- [10] Sikha, G. and White, R. E.: *Analytical Expression for the Impedance Response for a Lithium-Ion Cell*. In: *Journal of The Electrochemical Society* 155.12 (2008), A893. ISSN: 0013-4651. DOI: 10.1149/1.2976359 (see p. 4).
- [11] Murbach, M. d. and Schwartz, D. T.: *Analysis of Li-Ion Battery Electrochemical Impedance Spectroscopy Data: An Easy-to-Implement Approach for Physics-Based Parameter Estimation Using an Open-Source Tool*. In: *Journal of The Electrochemical Society* 165.2 (2018), A297–A304. ISSN: 0013-4651. DOI: 10.1149/2.1021802jes (see p. 4).

- [12] Huang, J., Li, Z., Zhang, J., Song, S., Lou, Z., and Wu, N.: *An Analytical Three-Scale Impedance Model for Porous Electrode with Agglomerates in Lithium-Ion Batteries*. In: *Journal of The Electrochemical Society* 162.4 (2015), A585–A595. ISSN: 0013-4651. DOI: 10.1149/2.0241504jes (see p. 4).
- [13] Fuoss, R. M. and Kirkwood, J. G.: *Electrical Properties of Solids. VIII. Dipole Moments in Polyvinyl Chloride-Diphenyl Systems \**. In: *Journal of the American Chemical Society* 63.2 (1941), pp. 385–394. ISSN: 0002-7863. DOI: 10.1021/ja01847a013 (see p. 5).
- [14] Kleitz, M. and Dupuy, J.: *Electrode Processes in Solid State Ionics: Theory and Application to Energy Conversion and Storage Proceedings of the NATO Advanced Study Institute Held at Ajaccio (Corsica), 28 August-9 September 1975*. Vol. 25. Springer Science & Business Media, 2012 (see p. 5).
- [15] Franklin, A. and De Bruin, H.: *The fourier analysis of impedance spectra for electroded solid electrolytes*. In: *physica status solidi (a)* 75.2 (1983), pp. 647–656 (see p. 5).
- [16] Dion, F. and Lasia, A.: *The use of regularization methods in the deconvolution of underlying distributions in electrochemical processes*. In: *Journal of Electroanalytical Chemistry* 475.1 (1999), pp. 28–37. ISSN: 15726657. DOI: 10.1016/s0022-0728(99)00334-4 (see pp. 5, 35).
- [17] Macdonald, J. R. and Brachman, M. K.: *Linear-System Integral Transform Relations*. In: *Reviews of Modern Physics* 28.4 (1956), pp. 393–422. ISSN: 0034-6861. DOI: 10.1103/RevModPhys.28.393 (see p. 6).
- [18] Boukamp, B. A. and Rolle, A.: *Analysis and Application of Distribution of Relaxation Times in Solid State Ionics*. In: *Solid State Ionics* 302 (2017), pp. 12–18. ISSN: 01672738. DOI: 10.1016/j.ssi.2016.10.009 (see pp. 6, 7, 35).
- [19] Boukamp, B. A. and Rolle, A.: *Use of a distribution function of relaxation times (DFRT) in impedance analysis of SOFC electrodes*. In: *Solid State Ionics* 314 (2018), pp. 103–111. ISSN: 01672738. DOI: 10.1016/j.ssi.2017.11.021 (see pp. 6, 35).
- [20] Boukamp, B. A.: *Distribution (function) of relaxation times, successor to complex nonlinear least squares analysis of electrochemical impedance spectroscopy?* In: *Journal of The Electrochemical Society* 2.4 (2020), p. 042001. ISSN: 0013-4651. DOI: 10.1088/2515-7655/aba9e0 (see pp. 6, 35).
- [21] Illig, J., Schmidt, J. P., Weiss, M., Weber, A., and Ivers-Tiffée, E.: *Understanding the impedance spectrum of 18650 LiFePO<sub>4</sub>-cells*. In: *Journal of Power Sources* 239 (2013), pp. 670–679. ISSN: 03787753. DOI: 10.1016/j.jpowsour.2012.12.020 (see p. 6).
- [22] Tikhonov, A. N.: “On the solution of ill-posed problems and the method of regularization.” In: *Doklady Akademii Nauk*. Vol. 151. 3. Russian Academy of Sciences. 1963, pp. 501–504 (see p. 6).
- [23] Wan, T. H., Saccoccio, M., Chen, C., and Ciucci, F.: *Influence of the Discretization Methods on the Distribution of Relaxation Times Deconvolution: Implementing Radial Basis Functions with DRTtools*. In: *Electrochimica Acta* 184 (2015), pp. 483–499. ISSN: 00134686. DOI: 10.1016/j.electacta.2015.09.097 (see p. 7).
- [24] Liu, J. and Ciucci, F.: *The Gaussian process distribution of relaxation times: A machine learning tool for the analysis and prediction of electrochemical impedance spectroscopy data*. In: *Electrochimica Acta* 331 (2020), p. 135316. ISSN: 00134686. DOI: 10.1016/j.electacta.2019.135316 (see pp. 7, 35).

- [25] Danzer, M. A.: *Generalized Distribution of Relaxation Times Analysis for the Characterization of Impedance Spectra*. In: *Batteries* 5.3 (2019), p. 53. DOI: 10.3390/batteries5030053 (see pp. 7, 35).
- [26] Boukamp, B. A.: *Derivation of a Distribution Function of Relaxation Times for the (fractal) Finite Length Warburg*. In: *Electrochimica acta* 252 (2017), pp. 154–163 (see p. 7).
- [27] Bagotsky, V. S.: *Fundamentals of electrochemistry*. John Wiley & Sons, 2005 (see p. 10).
- [28] Kim, S. W. and Cho, K. Y.: *Current Collectors for Flexible Lithium Ion Batteries: A Review of Materials*. In: *Journal of Electrochemical Science and Technology* 6.1 (2015), pp. 1–6. ISSN: 2093-8551. DOI: 10.5229/JECST.2015.6.1.1 (see p. 11).
- [29] Winter, M., Besenhard, J. O., Spahr, M. E., and Novák, P.: *Insertion Electrode Materials for Rechargeable Lithium Batteries*. In: *Advanced Materials* 10.10 (1998), pp. 725–763. ISSN: 0935-9648. DOI: 10.1002/(SICI)1521-4095(199807)10:10<725::AID-ADMA725>3.0.CO;2-Z (see p. 11).
- [30] Lee, W., Muhammad, S., Sergey, C., Lee, H., Yoon, J., Kang, Y.-M., and Yoon, W.-S.: *Advances in the Cathode Materials for Lithium Rechargeable Batteries*. eng. In: *Angewandte Chemie (International ed. in English)* 59.7 (2020), pp. 2578–2605. DOI: 10.1002/anie.201902359. eprint: 31034134 (see p. 11).
- [31] Deimede, V. and Elmasides, C.: *Separators for Lithium-Ion Batteries: A Review on the Production Processes and Recent Developments*. In: *Energy Technology* 3.5 (2015), pp. 453–468. ISSN: 2194-4288. DOI: 10.1002/ente.201402215 (see p. 11).
- [32] Korthauer, R.: *Lithium-ion batteries: basics and applications*. Springer, 2018 (see p. 11).
- [33] Doyle, M., Fuller, T. F., and Newman, J.: *Modeling of galvanostatic charge and discharge of the lithium/polymer/insertion cell*. In: *Journal of the Electrochemical society* 140.6 (1993), p. 1526 (see pp. 11, 12).
- [34] Doyle, M. and Newman, J.: *Modeling the performance of rechargeable lithium-based cells: design correlations for limiting cases*. In: *Journal of Power Sources* 54.1 (1995), pp. 46–51 (see pp. 11, 12).
- [35] Doyle, M., Newman, J., Gozdz, A. S., Schmutz, C. N., and Tarascon, J.-M.: *Comparison of modeling predictions with experimental data from plastic lithium ion cells*. In: *Journal of the Electrochemical Society* 143.6 (1996), pp. 1890–1903 (see pp. 11, 12, 17).
- [36] Kosch, S., Zhao, Y., Sturm, J., Schuster, J., Mulder, G., Ayerbe, E., and Jossen, A.: *A computationally efficient multi-scale model for lithium-ion cells*. In: *Journal of The Electrochemical Society* 165.10 (2018), A2374 (see p. 11).
- [37] Sturm, J., Rheinfeld, A., Zilberman, I., Spingler, F. B., Kosch, S., Frie, F., and Jossen, A.: *Modeling and simulation of inhomogeneities in a 18650 nickel-rich, silicon-graphite lithium-ion cell during fast charging*. In: *Journal of Power Sources* 412 (2019), pp. 204–223 (see pp. 11, 20).
- [38] Srinivasan, V. and Newman, J.: *Design and Optimization of a Natural Graphite/Iron Phosphate Lithium-Ion Cell*. In: *Journal of The Electrochemical Society* 151.10 (2004), A1530. ISSN: 0013-4651. DOI: 10.1149/1.1785013 (see p. 11).
- [39] Appiah, W. A., Park, J., Song, S., Byun, S., Ryou, M.-H., and Lee, Y. M.: *Design optimization of  $\text{LiNi}_0.6\text{Co}_0.2\text{Mn}_0.2\text{O}_2/\text{graphite}$  lithium-ion cells based on simulation and experimental data*. In: *Electrochemical and Solid-State Letters* 319 (2016), pp. 147–158. ISSN: 0378-7753. DOI: 10.1016/j.jpowsour.2016.04.052 (see p. 11).

- [40] Berliner, M. D., Zhao, H., Das, S., Forsuelo, M., Jiang, B., Chueh, W. H., Bazant, M. Z., and Braatz, R. D.: *Nonlinear Identifiability Analysis of the Porous Electrode Theory Model of Lithium-Ion Batteries*. In: *Journal of The Electrochemical Society* 168.9 (2021), p. 090546. ISSN: 0013-4651. DOI: 10.1149/1945-7111/ac26b1 (see pp. 11, 20).
- [41] Yang, X., Chen, L., Xu, X., Wang, W., Xu, Q., Lin, Y., and Zhou, Z.: *Parameter Identification of Electrochemical Model for Vehicular Lithium-Ion Battery Based on Particle Swarm Optimization*. In: *Energies* 10.11 (2017), p. 1811. ISSN: 1996-1073. DOI: 10.3390/en10111811 (see pp. 11, 20).
- [42] Masoudi, R., Uchida, T., and McPhee, J.: *Parameter estimation of an electrochemistry-based lithium-ion battery model*. In: *Electrochemical and Solid-State Letters* 291 (2015), pp. 215–224. ISSN: 0378-7753. DOI: 10.1016/j.jpowsour.2015.04.154 (see p. 11).
- [43] Newman, J. and Thomas-Alyea, K. E.: *Electrochemical systems*. John Wiley & Sons, 2012 (see pp. 12, 14, 15).
- [44] Thorat, I. V., Stephenson, D. E., Zacharias, N. A., Zaghbi, K., Harb, J. N., and Wheeler, D. R.: *Quantifying tortuosity in porous Li-ion battery materials*. In: *Journal of Power Sources* 188.2 (2009), pp. 592–600 (see p. 17).
- [45] Landesfeind, J., Ebner, M., Eldiven, A., Wood, V., and Gasteiger, H. A.: *Tortuosity of Battery Electrodes: Validation of Impedance-Derived Values and Critical Comparison with 3D Tomography*. In: *Journal of The Electrochemical Society* 165.3 (2018), A469–A476. DOI: 10.1149/2.0231803jes (see p. 18).
- [46] Heenan, T. M. M., Jnawali, A., Kok, M. D. R., Tranter, T. G., Tan, C., Dimitrijevic, A., Jervis, R., Brett, D. J. L., and Shearing, P. R.: *An Advanced Microstructural and Electrochemical Datasheet on 18650 Li-Ion Batteries with Nickel-Rich NMC811 Cathodes and Graphite-Silicon Anodes*. In: *Journal of The Electrochemical Society* 167.14 (2020), p. 140530. ISSN: 0013-4651. DOI: 10.1149/1945-7111/abc4c1 (see p. 20).
- [47] Khalik, Z., Donkers, M., Sturm, J., and Bergveld, H. J.: *Parameter estimation of the Doyle–Fuller–Newman model for Lithium-ion batteries by parameter normalization, grouping, and sensitivity analysis*. In: *Electrochemical and Solid-State Letters* 499 (2021), p. 229901. ISSN: 0378-7753. DOI: 10.1016/j.jpowsour.2021.229901 (see p. 20).
- [48] Pozzi, A., Ciamarella, G., Volkwein, S., and Raimondo, D. M.: *Optimal Design of Experiments for a Lithium-Ion Cell: Parameters Identification of an Isothermal Single Particle Model with Electrolyte Dynamics*. In: *Industrial & Engineering Chemistry Research* 58.3 (2019), pp. 1286–1299. ISSN: 0888-5885. DOI: 10.1021/acs.iecr.8b04580 (see p. 20).
- [49] Jin, N., Danilov, D. L., van den Hof, P. M., and Donkers, M.: *Parameter estimation of an electrochemistry-based lithium-ion battery model using a two-step procedure and a parameter sensitivity analysis*. In: *International Journal of Energy Research* 42.7 (2018), pp. 2417–2430. DOI: 10.1002/er.4022 (see p. 20).
- [50] Lai, X., Gao, W., Zheng, Y., Ouyang, M., Li, J., Han, X., and Zhou, L.: *A comparative study of global optimization methods for parameter identification of different equivalent circuit models for Li-ion batteries*. In: *Electrochimica Acta* 295 (2019), pp. 1057–1066. ISSN: 00134686. DOI: 10.1016/j.electacta.2018.11.134 (see p. 20).

- [51] Forman, J. C., Moura, S. J., Stein, J. L., and Fathy, H. K.: “Genetic parameter identification of the Doyle-Fuller-Newman model from experimental cycling of a LiFePO<sub>4</sub> battery.” In: *American Control Conference (ACC), 2011 – June 29 - July 1 2011, San Francisco, CA, USA*. 2011 American Control Conference (San Francisco, CA). American Automatic Control Council, American Control Conference, and ACC. Piscataway, NJ: IEEE, 2011, pp. 362–369. ISBN: 978-1-4577-0081-1. DOI: 10.1109/ACC.2011.5991183 (see p. 20).
- [52] Brady, N. W., Gould, C. A., and West, A. C.: *Quantitative Parameter Estimation, Model Selection, and Variable Selection in Battery Science*. In: *Journal of The Electrochemical Society* 167.1 (2020), p. 013501. ISSN: 0013-4651. DOI: 10.1149/2.0012001JES (see p. 20).
- [53] Kosch, S., Zhao, Y., Sturm, J., Schuster, J., Mulder, G., Ayerbe, E., and Jossen, A.: *A Computationally Efficient Multi-Scale Model for Lithium-Ion Cells*. In: *Journal of The Electrochemical Society* 165.10 (2018), A2374–A2388. ISSN: 0013-4651. DOI: 10.1149/2.1241810jes (see p. 20).
- [54] Marshall, L., Nott, D., and Sharma, A.: *A comparative study of Markov chain Monte Carlo methods for conceptual rainfall-runoff modeling*. In: *Water Resources Research* 40.2 (2004). DOI: 10.1029/2003WR002378 (see p. 22).
- [55] Mira, A.: *MCMC Methods to Estimate Bayesian Parametric Models*. In: *Bayesian Thinking - Modeling and Computation*. Vol. 25. Handbook of Statistics. Elsevier, 2005, pp. 415–436. ISBN: 9780444515391. DOI: 10.1016/S0169-7161(05)25014-9 (see p. 22).
- [56] Kumbhare, S. and Shahmoradi, A.: *MatDRAM: A pure-MATLAB Delayed-Rejection Adaptive Metropolis-Hastings Markov Chain Monte Carlo Sampler*. 2020. DOI: 10.48550/arXiv.2010.04190 (see p. 22).
- [57] Barsoukov, E. and Macdonald, J. R.: *Impedance Spectroscopy Theory, Experiment, and Applications, 2nd ed.* (Hoboken, NJ: John Wiley & Sons, Inc., 2005) (2005) (see p. 24).
- [58] Urquidi-Macdonald, M., Real, S., and Macdonald, D. D.: *Application of Kramers–Kronig Transforms in the Analysis of Electrochemical Impedance Data: II . Transformations in the Complex Plane*. In: *Journal of The Electrochemical Society* 133.10 (1986), pp. 2018–2024. ISSN: 0013-4651. DOI: 10.1149/1.2108332 (see p. 26).
- [59] Urquidi-Macdonald, M., Real, S., and Macdonald, D. D.: *Applications of Kramers–Kronig transforms in the analysis of electrochemical impedance data—III. Stability and linearity*. In: *Electrochimica Acta* 35.10 (1990), pp. 1559–1566. ISSN: 00134686. DOI: 10.1016/0013-4686(90)80010-L (see p. 26).
- [60] Scully, J. R., Silverman, D. C., and Kendig, M. W.: *Electrochemical Impedance: Analysis and Interpretation*. 100 Barr Harbor Drive, PO Box C700, West Conshohocken, PA 19428-2959: ASTM International, 1993. ISBN: 978-0-8031-1861-4. DOI: 10.1520/STP1188-EB (see p. 26).
- [61] Agarwal, P., Crisalle, O. D., Orazem, M. E., and Garcia-Rubio, L. H.: *Application of Measurement Models to Impedance Spectroscopy: II . Determination of the Stochastic Contribution to the Error Structure*. In: *Journal of The Electrochemical Society* 142.12 (1995), pp. 4149–4158. ISSN: 0013-4651. DOI: 10.1149/1.2048478 (see p. 26).
- [62] Agarwal, P., Orazem, M. E., and Garcia-Rubio, L. H.: *Application of Measurement Models to Impedance Spectroscopy: III . Evaluation of Consistency with the Kramers–Kronig Relations*. In: *Journal of The Electrochemical Society* 142.12 (1995), pp. 4159–4168. ISSN: 0013-4651. DOI: 10.1149/1.2048479 (see p. 26).

- [63] BOUKAMP, B. and ROSSMACDONALD, J.: *Alternatives to Kronig-Kramers transformation and testing, and estimation of distributions*. In: *Solid State Ionics* 74.1-2 (1994), pp. 85–101. ISSN: 01672738. DOI: 10.1016/0167-2738(94)90440-5 (see p. 26).
- [64] Pajkossy, T.: *Impedance of rough capacitive electrodes*. In: *Journal of Electroanalytical Chemistry* 364.1-2 (1994), pp. 111–125. ISSN: 15726657. DOI: 10.1016/0022-0728(93)02949-I (see p. 27).
- [65] Martin, M. H. and Lasia, A.: *Influence of experimental factors on the constant phase element behavior of Pt electrodes*. In: *Electrochimica Acta* 56.23 (2011), pp. 8058–8068. ISSN: 00134686. DOI: 10.1016/j.electacta.2011.02.068 (see p. 27).
- [66] Kerner, Z. and Pajkossy, T.: *Impedance of rough capacitive electrodes: the role of surface disorder*. In: *Journal of Electroanalytical Chemistry* 448.1 (1998), pp. 139–142. ISSN: 15726657. DOI: 10.1016/S0022-0728(98)00025-4 (see p. 27).
- [67] Huang, J.: *Diffusion impedance of electroactive materials, electrolytic solutions and porous electrodes: Warburg impedance and beyond*. In: *Electrochimica Acta* 281 (2018), pp. 170–188. DOI: 10.1016/j.electacta.2018.05.136 (see pp. 29, 30).
- [68] Taylor, S. and Gileadi, E.: *Physical interpretation of the Warburg impedance*. In: *Corrosion* 51.09 (1995) (see p. 29).
- [69] Meyers, J. P., Doyle, M., Darling, R. M., and Newman, J.: *The Impedance Response of a Porous Electrode Composed of Intercalation Particles*. In: *Journal of The Electrochemical Society* 147.8 (2000), p. 2930. ISSN: 0013-4651. DOI: 10.1149/1.1393627 (see p. 29).
- [70] Jacobsen, T. and West, K.: *Diffusion impedance in planar, cylindrical and spherical symmetry*. In: *Electrochimica Acta* 40.2 (1995), pp. 255–262. ISSN: 00134686. DOI: 10.1016/0013-4686(94)E0192-3 (see p. 29).
- [71] Schönleber, M., Uhlmann, C., Braun, P., Weber, A., and Ivers-Tiffée, E.: *A consistent derivation of the impedance of a lithium-ion battery electrode and its dependency on the state-of-charge*. In: *Electrochimica Acta* 243 (2017), pp. 250–259 (see p. 30).
- [72] Song, J. and Bazant, M. Z.: *Electrochemical impedance imaging via the distribution of diffusion times*. In: *Physical review letters* 120.11 (2018), p. 116001 (see p. 30).
- [73] Zhou, X., Huang, J., Pan, Z., and Ouyang, M.: *Impedance characterization of lithium-ion batteries aging under high-temperature cycling: Importance of electrolyte-phase diffusion*. In: *Journal of Power Sources* 426 (2019), pp. 216–222 (see p. 30).
- [74] Davidson, D. W. and Cole, R. H.: *Dielectric Relaxation in Glycerol, Propylene Glycol, and n-Propanol*. In: *The Journal of Chemical Physics* 19.12 (1951), pp. 1484–1490. ISSN: 0021-9606. DOI: 10.1063/1.1748105 (see p. 35).
- [75] Li, X., Ahmadi, M., Collins, L., and Kalinin, S. V.: *Deconvolving distribution of relaxation times, resistances and inductance from electrochemical impedance spectroscopy via statistical model selection: Exploiting structural-sparsity regularization and data-driven parameter tuning*. In: *Electrochimica Acta* 313.2 (2019), pp. 570–583. ISSN: 00134686. DOI: 10.1016/j.electacta.2019.05.010 (see p. 35).
- [76] Hannan, M. A., Lipu, M., Hussain, A., and Mohamed, A.: *A review of lithium-ion battery state of charge estimation and management system in electric vehicle applications – Challenges and recommendations*. In: *Renewable and Sustainable Energy Reviews* 78 (2017), pp. 834–854. ISSN: 13640321. DOI: 10.1016/j.rser.2017.05.001.

- [77] Hahn, M., Schindler, S., Triebs, L.-C., and Danzer, M. A.: *Optimized Process Parameters for a Reproducible Distribution of Relaxation Times Analysis of Electrochemical Systems*. In: *Batteries* 5.2 (2019), p. 43. DOI: 10.3390/batteries5020043.
- [78] Brady, N. W., Gould, C. A., and West, A. C.: *Quantitative parameter estimation, model selection, and variable selection in battery science*. In: *Journal of The Electrochemical Society* 167.1 (2019), p. 013501.
- [79] Chen, L., Xu, R., Rao, W., Li, H., Wang, Y.-P., and Jiang, T. Y. H.-B.: *Electrochemical Model Parameter Identification of Lithium-Ion Battery with Temperature and Current Dependence*. In: *International journal of electrochemical science* (2019).
- [80] Gopalakrishnan, K. and Offer, G. J.: *A Composite Single Particle Lithium-Ion Battery Model Through System Identification*. In: *IEEE Transactions on Control Systems Technology* (2021), pp. 1–13. ISSN: 1063-6536.
- [81] Li, J., Wang, L., Lyu, C., Liu, E., Xing, Y., and Pecht, M.: *A parameter estimation method for a simplified electrochemical model for Li-ion batteries*. In: *Electrochimica Acta* 275 (2018), pp. 50–58. ISSN: 00134686. DOI: 10.1016/j.electacta.2018.04.098.
- [82] Rajabloo, B., Jokar, A., Désilets, M., and Lacroix, M.: *An Inverse Method for Estimating the Electrochemical Parameters of Lithium-Ion Batteries*. In: *Journal of The Electrochemical Society* 164.2 (2017), A99–A105. ISSN: 0013-4651. DOI: 10.1149/2.0221702jes.
- [83] Jokar, A., Rajabloo, B., Désilets, M., and Lacroix, M.: *An Inverse Method for Estimating the Electrochemical Parameters of Lithium-Ion Batteries*. In: *Journal of The Electrochemical Society* 163.14 (2016), A2876–A2886. ISSN: 0013-4651. DOI: 10.1149/2.0191614jes.
- [84] Uddin, K., Perera, S., Widanage, W., Somerville, L., and Marco, J.: *Characterising Lithium-Ion Battery Degradation through the Identification and Tracking of Electrochemical Battery Model Parameters*. In: *Batteries* 2.2 (2016), p. 13. DOI: 10.3390/batteries2020013.
- [85] Kalogiannis, T., Hosen, M. S., Sokkeh, M. A., Goutam, S., Jaguemont, J., Jin, L., Qiao, G., Berecibar, M., and Van Mierlo, J.: *Comparative Study on Parameter Identification Methods for Dual-Polarization Lithium-Ion Equivalent Circuit Model*. In: *Energies* 12.21 (2019), p. 4031.
- [86] Kumtepli, V., Wang, Y., and Tripathi, A.: “Multi-area model predictive load frequency control: A decentralized approach.” In: *2016 Asian Conference on Energy, Power and Transportation Electrification (ACEPT)*. IEEE. 2016, pp. 1–5.
- [87] Vadlamudi, S. D. V. R., Kumtepli, V., Ozcira, S., and Tripathi, A.: “Hybrid energy storage power allocation and motor control for electric forklifts.” In: *2016 Asian Conference on Energy, Power and Transportation Electrification (ACEPT)*. IEEE. 2016, pp. 1–5.
- [88] Naumann, M., Kumtepli, V., Hesse, H. C., Tripathi, A., and Jossen, A.: *Design and control of battery energy storage systems in island grids*. In: (2017).
- [89] Jiang, H., Kumtepli, V., Nguyen, D. D., Tripathi, A., and Wang, Y.: “Secondary reactive power balancing and voltage stability in microgrid using prioritized centralized controller.” In: *2018 IEEE Innovative Smart Grid Technologies-Asia (ISGT Asia)*. IEEE. 2018, pp. 1209–1214.
- [90] Kocer, B. B., Kumtepli, V., Tjahjowidodo, T., Pratama, M., Tripathi, A., Lee, G. S. G., and Wang, Y.: “Uav control in close proximities-ceiling effect on battery lifetime.” In: *2019 2nd International Conference on Intelligent Autonomous Systems (ICoIAS)*. IEEE. 2019, pp. 193–197.



- [91] Hesse, H. C., Kumtepelı, V., Schimpe, M., Reniers, J., Howey, D. A., Tripathi, A., Wang, Y., and Jossen, A.: *Ageing and Efficiency Aware Battery Dispatch for Arbitrage Markets Using Mixed Integer Linear Programming*. In: *Energies* 12.6 (2019), p. 999.
- [92] Kumtepelı, V., Zhao, Y., Naumann, M., Tripathi, A., Wang, Y., Jossen, A., and Hesse, H.: *Design and analysis of an aging-aware energy management system for islanded grids using mixed-integer quadratic programming*. In: *International Journal of Energy Research* 43.9 (2019), pp. 4127–4147.
- [93] Zhao, Y., Naumann, M., Kumtepelı, V., Hesse, H. C., and Jossen, A.: “Application of Energy Storage System to Microgrid.” In: *DESIGN&ELEKTRONIK 25 2018*. 2018.
- [94] Kanbur, B. B., Kumtepelı, V., and Duan, F.: *Thermal performance prediction of the battery surface via dynamic mode decomposition*. In: *Energy* 201 (2020), p. 117642.
- [95] Kumtepelı, V., Hesse, H. C., Schimpe, M., Tripathi, A., Wang, Y., and Jossen, A.: *Energy arbitrage optimization with battery storage: 3D-MILP for electro-thermal performance and semi-empirical aging models*. In: *IEEE Access* 8 (2020), pp. 204325–204341.
- [96] Tanis-Kanbur, M. B., Kumtepelı, V., Kanbur, B. B., Ren, J., and Duan, F.: *Transient prediction of nanoparticle-laden droplet drying patterns through dynamic mode decomposition*. In: *Langmuir* 37.8 (2021), pp. 2787–2799.
- [97] Kanbur, B. B., Shen, S., Kumtepelı, V., Zhou, Y., and Duan, F.: *Multiobjective Optimization of 3D-Printed Injection Molds via Hybrid Latin Hypercube Sampling-Delaunay Triangulation Approach*. In: *Recent Advances in Manufacturing Engineering and Processes*. Springer, Singapore, 2022, pp. 15–19.
- [98] De Levie, R.: *On porous electrodes in electrolyte solutions: I. Capacitance effects*. In: *Electrochimica acta* 8.10 (1963), pp. 751–780.
- [99] De Levie, R.: *On porous electrodes in electrolyte solutions—IV*. In: *Electrochimica Acta* 9.9 (1964), pp. 1231–1245.
- [100] Vyroubal, P. and Kazda, T.: *Equivalent circuit model parameters extraction for lithium ion batteries using electrochemical impedance spectroscopy*. In: *Journal of Energy Storage* 15 (2018), pp. 23–31.
- [101] Choi, W., Shin, H.-C., Kim, J. M., Choi, J.-Y., and Yoon, W.-S.: *Modeling and Applications of Electrochemical Impedance Spectroscopy (EIS) for Lithium-ion Batteries*. In: *Journal of Electrochemical Science and Technology* 11.1 (2020), pp. 1–13.
- [102] Illig, J., Ender, M., Weber, A., and Ivers-Tiffée, E.: *Modeling graphite anodes with serial and transmission line models*. In: *Journal of Power Sources* 282 (2015), pp. 335–347.
- [103] Meyers, J. P., Doyle, M., Darling, R. M., and Newman, J.: *The impedance response of a porous electrode composed of intercalation particles*. In: *Journal of The Electrochemical Society* 147.8 (2000), p. 2930.
- [104] Doyle, M., Meyers, J. P., and Newman, J.: *Computer simulations of the impedance response of lithium rechargeable batteries*. In: *Journal of the Electrochemical Society* 147.1 (2000), p. 99.
- [105] Sikha, G. and White, R. E.: *Analytical expression for the impedance response of an insertion electrode cell*. In: *Journal of The Electrochemical Society* 154.1 (2006), A43.
- [106] Sikha, G. and White, R. E.: *Analytical expression for the impedance response for a lithium-ion cell*. In: *Journal of the Electrochemical Society* 155.12 (2008), A893.

- [107] Huang, J. and Zhang, J.: *Theory of impedance response of porous electrodes: simplifications, inhomogeneities, non-stationarities and applications*. In: *Journal of the Electrochemical Society* 163.9 (2016), A1983.
- [108] IVERS-TIFFE, E. E., and WEBER, A.: *Evaluation of electrochemical impedance spectra by the distribution of relaxation times*. In: *Journal of the Ceramic Society of Japan* 125.4 (2017), pp. 193–201. ISSN: 1882-0743. DOI: 10.2109/jcersj2.16267.
- [109] Gavriluk, A. L., Osinkin, D. A., and Bronin, D. I.: *On a variation of the Tikhonov regularization method for calculating the distribution function of relaxation times in impedance spectroscopy*. In: *Electrochimica Acta* 354 (2020), p. 136683. ISSN: 00134686. DOI: 10.1016/j.electacta.2020.136683.
- [110] Shafiei Sabet, P., Warnecke, A. J., Meier, F., Witzenhause, H., Martinez-Laserna, E., and Sauer, D. U.: *Non-invasive yet separate investigation of anode/cathode degradation of lithium-ion batteries (nickel-cobalt-manganese vs. graphite) due to accelerated aging*. In: *Journal of Power Sources* 449 (2020), p. 227369. ISSN: 03787753. DOI: 10.1016/j.jpowsour.2019.227369.
- [111] Shafiei Sabet, P. and Sauer, D. U.: *Separation of predominant processes in electrochemical impedance spectra of lithium-ion batteries with nickel-manganese-cobalt cathodes*. In: *Journal of Power Sources* 425 (2019), pp. 121–129. ISSN: 03787753. DOI: 10.1016/j.jpowsour.2019.03.068.
- [112] Schindler, S., Bauer, M., Petzl, M., and Danzer, M. A.: *Voltage relaxation and impedance spectroscopy as in-operando methods for the detection of lithium plating on graphitic anodes in commercial lithium-ion cells*. In: *Journal of Power Sources* 304 (2016), pp. 170–180. ISSN: 03787753. DOI: 10.1016/j.jpowsour.2015.11.044.
- [113] Jorcin, J.-B., Orazem, M. E., Pébère, N., and Tribollet, B.: *CPE analysis by local electrochemical impedance spectroscopy*. In: *Electrochimica Acta* 51.8-9 (2006), pp. 1473–1479. ISSN: 00134686. DOI: 10.1016/j.electacta.2005.02.128.
- [114] Titchmarsh, E. C.: *Introduction to the theory of Fourier integrals*. In: (1948).
- [115] Arfken, G. B. and Weber, H. J.: *Mathematical methods for physicists*. 1999.
- [116] Li, X., Ahmadi, M., Collins, L., and Kalinin, S. V.: *Deconvolving distribution of relaxation times, resistances and inductance from electrochemical impedance spectroscopy via statistical model selection: Exploiting structural-sparsity regularization and data-driven parameter tuning*. In: *Electrochimica Acta* 313 (2019), pp. 570–583.
- [117] Boukamp, B. A. and Rolle, A.: *Analysis and application of distribution of relaxation times in solid state ionics*. In: *Solid state ionics* 302 (2017), pp. 12–18.
- [118] Ogihara, N., Kawauchi, S., Okuda, C., Itou, Y., Takeuchi, Y., and Ukyo, Y.: *Theoretical and experimental analysis of porous electrodes for lithium-ion batteries by electrochemical impedance spectroscopy using a symmetric cell*. In: *Journal of The Electrochemical Society* 159.7 (2012), A1034.
- [119] Suresh, P., Shukla, A., and Munichandraiah, N.: *Temperature dependence studies of ac impedance of lithium-ion cells*. In: *Journal of applied electrochemistry* 32.3 (2002), pp. 267–273.
- [120] Peled, E. and Menkin, S.: *SEI: past, present and future*. In: *Journal of The Electrochemical Society* 164.7 (2017), A1703.

- [121] Qiu, X.-Y., Zhuang, Q.-C., Zhang, Q.-Q., Cao, R., Ying, P.-Z., Qiang, Y.-H., and Sun, S.-G.: *Electrochemical and electronic properties of LiCoO<sub>2</sub> cathode investigated by galvanostatic cycling and EIS*. In: *Physical Chemistry Chemical Physics* 14.8 (2012), pp. 2617–2630.
- [122] Spingler, F. B., Kücher, S., Phillips, R., Moyassari, E., and Jossen, A.: *Electrochemically Stable In Situ Dilatometry of NMC, NCA and Graphite Electrodes for Lithium-Ion Cells Compared to XRD Measurements*. In: *Journal of The Electrochemical Society* 168.4 (2021), p. 040515.
- [123] Nara, H., Morita, K., Mukoyama, D., Yokoshima, T., Momma, T., and Osaka, T.: *Impedance analysis of LiNi<sub>1/3</sub>Mn<sub>1/3</sub>Co<sub>1/3</sub>O<sub>2</sub> cathodes with different secondary-particle size distribution in lithium-ion battery*. In: *Electrochimica Acta* 241 (2017), pp. 323–330.
- [124] Illig, J., Ender, M., Chrobak, T., Schmidt, J. P., Klotz, D., and Ivers-Tiffée, E.: *Separation of charge transfer and contact resistance in LiFePO<sub>4</sub>-cathodes by impedance modeling*. In: *Journal of the Electrochemical Society* 159.7 (2012), A952.
- [125] Zhang, S., Xu, K., and Jow, T.: *EIS study on the formation of solid electrolyte interface in Li-ion battery*. In: *Electrochimica acta* 51.8-9 (2006), pp. 1636–1640.
- [126] Wang, S., Yan, M., Li, Y., Vinado, C., and Yang, J.: *Separating electronic and ionic conductivity in mix-conducting layered lithium transition-metal oxides*. In: *Journal of Power Sources* 393 (2018), pp. 75–82.
- [127] Valøen, L. O. and Reimers, J. N.: *Transport properties of LiPF<sub>6</sub>-based Li-ion battery electrolytes*. In: *Journal of The Electrochemical Society* 152.5 (2005), A882.
- [128] Besenhard, J. O.: *Handbook of battery materials*. John Wiley & Sons, 2008.
- [129] Pan, K., Zou, F., Canova, M., Zhu, Y., and Kim, J.-H.: *Comprehensive electrochemical impedance spectroscopy study of Si-Based anodes using distribution of relaxation times analysis*. In: *Journal of Power Sources* 479 (2020), p. 229083.
- [130] Ovejas, V. J. and Cuadras, A.: *Impedance characterization of an LCO-NMC/graphite cell: Ohmic conduction, SEI transport and charge-transfer phenomenon*. In: *Batteries* 4.3 (2018), p. 43.
- [131] Yao, Y.-X., Chen, X., Yan, C., Zhang, X.-Q., Cai, W.-L., Huang, J.-Q., and Zhang, Q.: *Regulating Interfacial Chemistry in Lithium-Ion Batteries by a Weakly Solvating Electrolyte*. In: *Angewandte Chemie* 133.8 (2021), pp. 4136–4143.
- [132] Chowdhury, R., Banerjee, A., Zhao, Y., Liu, X., and Brandon, N.: *Simulation of bi-layer cathode materials with experimentally validated parameters to improve ion diffusion and discharge capacity*. In: *Sustainable Energy & Fuels* 5.4 (2021), pp. 1103–1119.
- [133] Smart, M. and Ratnakumar, B.: *Effects of electrolyte composition on lithium plating in lithium-ion cells*. In: *Journal of The Electrochemical Society* 158.4 (2011), A379.
- [134] Keefe, A., Buteau, S., Hill, I., and Dahn, J.: *Temperature dependent EIS studies separating charge transfer impedance from contact impedance in lithium-ion symmetric cells*. In: *Journal of the Electrochemical Society* 166.14 (2019), A3272.
- [135] Rabissi, C., Innocenti, A., Sordi, G., and Casalegno, A.: *A Comprehensive Physical-Based Sensitivity Analysis of the Electrochemical Impedance Response of Lithium-Ion Batteries*. In: *Energy Technology* 9.3 (2021), p. 2000986.
- [136] Macdonald, J. R. and Brachman, M. K.: *Linear-system integral transform relations*. In: *Reviews of modern physics* 28.4 (1956), p. 393.

- [137] Dion, F. and Lasia, A.: *The use of regularization methods in the deconvolution of underlying distributions in electrochemical processes*. In: *Journal of Electroanalytical Chemistry* 475.1 (1999), pp. 28–37.
- [138] Rolle, A., Mohamed, H. A. A., Huo, D., Capoen, E., Mentre, O., Vannier, R.-N., Daviero-Minaud, S., and Boukamp, B. A.: *Ca<sub>3</sub>Co<sub>4</sub>O<sub>9</sub>+ $\delta$ , a growing potential SOFC cathode material: Impact of the layer composition and thickness on the electrochemical properties*. In: *Solid state ionics* 294 (2016), pp. 21–30.
- [139] Boukamp, B. A. and Rolle, A.: *Use of a distribution function of relaxation times (DFRT) in impedance analysis of SOFC electrodes*. In: *Solid state ionics* 314 (2018), pp. 103–111.
- [140] Boukamp, B. A.: *Distribution (function) of relaxation times, successor to complex nonlinear least squares analysis of electrochemical impedance spectroscopy?* In: *Journal of Physics: Energy* 2.4 (2020), p. 042001.
- [141] Chen, X., Li, L., Liu, M., Huang, T., and Yu, A.: *Detection of lithium plating in lithium-ion batteries by distribution of relaxation times*. In: *Journal of Power Sources* 496 (2021), p. 229867.
- [142] Sabet, P. S., Warnecke, A. J., Meier, F., Witzhausen, H., Martinez-Laserna, E., and Sauer, D. U.: *Non-invasive yet separate investigation of anode/cathode degradation of lithium-ion batteries (nickel–cobalt–manganese vs. graphite) due to accelerated aging*. In: *Journal of Power Sources* 449 (2020), p. 227369.
- [143] Sabet, P. S. and Sauer, D. U.: *Separation of predominant processes in electrochemical impedance spectra of lithium-ion batteries with nickel-manganese-cobalt cathodes*. In: *Journal of Power Sources* 425 (2019), pp. 121–129.
- [144] Ivers-Tiffée, E. and Weber, A.: *Evaluation of electrochemical impedance spectra by the distribution of relaxation times*. In: *Journal of the Ceramic Society of Japan* 125.4 (2017), pp. 193–201.
- [145] Illig, J., Schmidt, J. P., Weiss, M., Weber, A., and Ivers-Tiffée, E.: *Understanding the impedance spectrum of 18650 LiFePO<sub>4</sub>-cells*. In: *Journal of Power Sources* 239 (2013), pp. 670–679.
- [146] Hahn, M., Schindler, S., Triebs, L.-C., and Danzer, M. A.: *Optimized process parameters for a reproducible distribution of relaxation times analysis of electrochemical systems*. In: *Batteries* 5.2 (2019), p. 43.
- [147] Danzer, M. A.: *Generalized distribution of relaxation times analysis for the characterization of impedance spectra*. In: *Batteries* 5.3 (2019), p. 53.
- [148] Ecker, M., Käbitz, S., Laresgoiti, I., and Sauer, D. U.: *Parameterization of a physico-chemical model of a lithium-ion battery: II. Model validation*. In: *Journal of The Electrochemical Society* 162.9 (2015), A1849.
- [149] Schmalstieg, J., Rahe, C., Ecker, M., and Sauer, D. U.: *Full cell parameterization of a high-power lithium-ion battery for a physico-chemical model: Part I. Physical and electrochemical parameters*. In: *Journal of The Electrochemical Society* 165.16 (2018), A3799.
- [150] Macdonald, J. R. and Barsoukov, E.: *Impedance spectroscopy: theory, experiment, and applications*. In: *History* 1.8 (2005), pp. 1–13.
- [151] Song, J. and Bazant, M. Z.: *Effects of nanoparticle geometry and size distribution on diffusion impedance of battery electrodes*. In: *Journal of The Electrochemical Society* 160.1 (2012), A15.

- [152] Park, M., Zhang, X., Chung, M., and Less, G.: *B, Sastry AM*. In: *J Power Sources* 195 (2010), pp. 7904–7929.
- [153] Thorat, I. V., Joshi, T., Zaghbi, K., Harb, J. N., and Wheeler, D. R.: *Understanding rate-limiting mechanisms in LiFePO<sub>4</sub> cathodes for Li-ion batteries*. In: *Journal of The Electrochemical Society* 158.11 (2011), A1185.
- [154] Remmert, R.: *Theory of complex functions*. Vol. 122. Springer Science & Business Media, 1991.
- [155] Quattrocchi, E., Wan, T. H., Curcio, A., Pepe, S., Effat, M. B., and Ciucci, F.: *A general model for the impedance of batteries and supercapacitors: The non-linear distribution of diffusion times*. In: *Electrochimica Acta* 324 (2019), p. 134853.
- [156] Wan, T. H., Saccoccio, M., Chen, C., and Ciucci, F.: *Influence of the discretization methods on the distribution of relaxation times deconvolution: implementing radial basis functions with DRTtools*. In: *Electrochimica Acta* 184 (2015), pp. 483–499.
- [157] Zhao, Y., Kumtepe, V., Ludwig, S., and Jossen, A.: *Investigation of the distribution of relaxation times of a porous electrode using a physics-based impedance model*. In: *Journal of Power Sources* 530 (2022), p. 231250.
- [158] Heenan, T., Jnawali, A., Kok, M., Tranter, T., Tan, C., Dimitrijevic, A., Jervis, R., Brett, D., and Shearing, P.: *An advanced microstructural and electrochemical datasheet on 18650 li-ion batteries with nickel-rich NMC811 cathodes and graphite-silicon anodes*. In: *Journal of The Electrochemical Society* 167.14 (2020), p. 140530.
- [159] Umegaki, I. et al.: *Li-ion diffusion in Li intercalated graphite C<sub>6</sub>Li and C<sub>12</sub>Li probed by  $\mu$ -SR*. In: *Physical Chemistry Chemical Physics* 19.29 (2017), pp. 19058–19066.
- [160] Cabanero, M. A., Boaretto, N., Roeder, M., Mueller, J., Kallo, J., and Latz, A.: *Direct determination of diffusion coefficients in commercial Li-ion batteries*. In: *Journal of The Electrochemical Society* 165.5 (2018), A847.
- [161] Noh, H.-J., Youn, S., Yoon, C. S., and Sun, Y.-K.: *Comparison of the structural and electrochemical properties of layered Li [Ni<sub>x</sub>Co<sub>y</sub>Mn<sub>z</sub>]O<sub>2</sub> (x = 1/3, 0.5, 0.6, 0.7, 0.8 and 0.85) cathode material for lithium-ion batteries*. In: *Journal of power sources* 233 (2013), pp. 121–130.
- [162] Chen, C.-H., Planella, F. B., O’regan, K., Gastol, D., Widanage, W. D., and Kendrick, E.: *Development of experimental techniques for parameterization of multi-scale lithium-ion battery models*. In: *Journal of The Electrochemical Society* 167.8 (2020), p. 080534.
- [163] Wen, C. J., Boukamp, B. A., Huggins, R. A., and Weppner, W.: *Thermodynamic and Mass Transport Properties of “LiAl”*. In: *Journal of The Electrochemical Society* 126.12 (1979), pp. 2258–2266. ISSN: 0013-4651. DOI: 10.1149/1.2128939.
- [164] Cabañero, M. A., Boaretto, N., Röder, M., Müller, J., Kallo, J., and Latz, A.: *Direct Determination of Diffusion Coefficients in Commercial Li-Ion Batteries*. In: *Journal of The Electrochemical Society* 165.5 (2018), A847–A855. ISSN: 0013-4651. DOI: 10.1149/2.0301805jes.
- [165] Dees, D. W., Kawauchi, S., Abraham, D. P., and Prakash, J.: *Analysis of the Galvanostatic Intermittent Titration Technique (GITT) as applied to a lithium-ion porous electrode*. In: *Journal of Power Sources* 189.1 (2009), pp. 263–268. ISSN: 03787753. DOI: 10.1016/j.jpowsour.2008.09.045.
- [166] Shaju, K. M., Subba Rao, G. V., and Chowdari, B. V. R.: *Li ion kinetic studies on spinel cathodes, Li(M<sub>1</sub>/6Mn<sub>11</sub>/6)O<sub>4</sub> (M = Mn, Co, CoAl) by GITT and EIS*. In: *Journal of Materials Chemistry* 13.1 (2003), pp. 106–113. ISSN: 09599428. DOI: 10.1039/B207407A.

- [167] Park, J. H., Yoon, H., Cho, Y., and Yoo, C.-Y.: *Investigation of Lithium Ion Diffusion of Graphite Anode by the Galvanostatic Intermittent Titration Technique*. eng. In: *Materials (Basel, Switzerland)* 14.16 (2021). ISSN: 1996-1944. DOI: 10.3390/ma14164683. eprint: 34443205.
- [168] Chen, C.-H., Brosa Planella, F., O'Regan, K., Gastol, D., Widanage, W. D., and Kendrick, E.: *Development of Experimental Techniques for Parameterization of Multi-scale Lithium-ion Battery Models*. In: *Journal of The Electrochemical Society* 167.8 (2020), p. 080534. ISSN: 0013-4651. DOI: 10.1149/1945-7111/ab9050.
- [169] Kang, S. D., Kuo, J. J., Kapate, N., Hong, J., Park, J., and Chueh, W. C.: *Galvanostatic Intermittent Titration Technique Reinvented: Part II. Experiments*. In: *Journal of The Electrochemical Society* 168.12 (2021), p. 120503. ISSN: 0013-4651. DOI: 10.1149/1945-7111/ac3939.
- [170] Lai, X., Gao, W., Zheng, Y., Ouyang, M., Li, J., Han, X., and Zhou, L.: *A comparative study of global optimization methods for parameter identification of different equivalent circuit models for Li-ion batteries*. In: *Electrochimica Acta* 295 (2019), pp. 1057–1066.
- [171] Tran, M.-K., DaCosta, A., Mevawalla, A., Panchal, S., and Fowler, M.: *Comparative study of equivalent circuit models performance in four common lithium-ion batteries: LFP, NMC, LMO, NCA*. In: *Batteries* 7.3 (2021), p. 51.
- [172] Uddin, K., Picarelli, A., Lyness, C., Taylor, N., and Marco, J.: *An acausal Li-ion battery pack model for automotive applications*. In: *Energies* 7.9 (2014), pp. 5675–5700.
- [173] Uddin, K., Perera, S., Widanage, W. D., and Marco, J.: *Characterising Li-ion battery degradation through the identification of perturbations in electrochemical battery models*. In: *World Electric Vehicle Journal* 7.1 (2015), pp. 76–84.
- [174] Yang, X., Chen, L., Xu, X., Wang, W., Xu, Q., Lin, Y., and Zhou, Z.: *Parameter identification of electrochemical model for vehicular lithium-ion battery based on particle swarm optimization*. In: *Energies* 10.11 (2017), p. 1811.
- [175] Rahman, M. A., Anwar, S., and Izadian, A.: *Electrochemical model parameter identification of a lithium-ion battery using particle swarm optimization method*. In: *Journal of Power Sources* 307 (2016), pp. 86–97.
- [176] Forman, J. C., Moura, S. J., Stein, J. L., and Fathy, H. K.: *Genetic identification and fisher identifiability analysis of the Doyle–Fuller–Newman model from experimental cycling of a LiFePO<sub>4</sub> cell*. In: *Journal of Power Sources* 210 (2012), pp. 263–275.
- [177] Berliner, M. D., Zhao, H., Das, S., Forsuelo, M., Jiang, B., Chueh, W. H., Bazant, M. Z., and Braatz, R. D.: *Nonlinear Identifiability Analysis of the Porous Electrode Theory Model of Lithium-Ion Batteries*. In: *Journal of The Electrochemical Society* 168.9 (2021), p. 090546.
- [178] Rajabloo, B., Jokar, A., Désilets, M., and Lacroix, M.: *An inverse method for estimating the electrochemical parameters of lithium-ion batteries*. In: *Journal of The Electrochemical Society* 164.2 (2016), A99.
- [179] Pozzi, A., Ciaramella, G., Volkwein, S., and Raimondo, D. M.: *Optimal design of experiments for a lithium-ion cell: parameters identification of an isothermal single particle model with electrolyte dynamics*. In: *Industrial & Engineering Chemistry Research* 58.3 (2018), pp. 1286–1299.
- [180] Jin, N., Danilov, D. L., Van den Hof, P. M., and Donkers, M.: *Parameter estimation of an electrochemistry-based lithium-ion battery model using a two-step procedure and a parameter sensitivity analysis*. In: *International Journal of Energy Research* 42.7 (2018), pp. 2417–2430.

- [181] Li, J., Wang, L., Lyu, C., Liu, E., Xing, Y., and Pecht, M.: *A parameter estimation method for a simplified electrochemical model for Li-ion batteries*. In: *Electrochimica Acta* 275 (2018), pp. 50–58.
- [182] Gopalakrishnan, K. and Offer, G. J.: *A Composite Single Particle Lithium-ion Battery Model through System Identification*. In: *IEEE Transactions on Control Systems Technology* (2021).
- [183] Deng, Z., Deng, H., Yang, L., Cai, Y., and Zhao, X.: *Implementation of reduced-order physics-based model and multi-parameters identification strategy for lithium-ion battery*. In: *Energy* 138 (2017), pp. 509–519.
- [184] Bizeray, A. M., Kim, J.-H., Duncan, S. R., and Howey, D. A.: *Identifiability and parameter estimation of the single particle lithium-ion battery model*. In: *IEEE Transactions on Control Systems Technology* 27.5 (2018), pp. 1862–1877.
- [185] Dokko, K., Mohamedi, M., Fujita, Y., Itoh, T., Nishizawa, M., Umeda, M., and Uchida, I.: *Kinetic characterization of single particles of LiCoO<sub>2</sub> by AC impedance and potential step methods*. In: *Journal of the Electrochemical Society* 148.5 (2001), A422.
- [186] Prasad, G. K. and Rahn, C. D.: *Reduced order impedance models of lithium ion batteries*. In: *Journal of Dynamic Systems, Measurement, and Control* 136.4 (2014), p. 041012.
- [187] Iooss, B. and Lemaître, P.: *A review on global sensitivity analysis methods*. In: *Uncertainty management in simulation-optimization of complex systems* (2015), pp. 101–122.
- [188] Sobol, I. M.: *Global sensitivity indices for nonlinear mathematical models and their Monte Carlo estimates*. In: *Mathematics and computers in simulation* 55.1-3 (2001), pp. 271–280.
- [189] Murbach, M. D. and Schwartz, D. T.: *Extending Newman’s pseudo-two-dimensional lithium-ion battery impedance simulation approach to include the nonlinear harmonic response*. In: *Journal of The Electrochemical Society* 164.11 (2017), E3311.
- [190] Zhou, X. and Huang, J.: *Impedance-Based diagnosis of lithium ion batteries: Identification of physical parameters using multi-output relevance vector regression*. In: *Journal of Energy Storage* 31 (2020), p. 101629.
- [191] Kumbhare, S. and Shahmoradi, A.: *MatDRAM: A pure-MATLAB Delayed-Rejection Adaptive Metropolis-Hastings Markov Chain Monte Carlo Sampler*. In: *arXiv preprint arXiv:2010.04190* (2020).
- [192] Astrom, K. and Bellman, R.: *On structural identifiability*. In: *Math. Biosci.* 7 (1970), pp. 329–339.
- [193] Correia, T. M., Gibson, A. P., Schweiger, M., and Hebden, J. C.: *Selection of regularization parameter for optical topography*. In: *Journal of biomedical optics* 14.3 (2009), p. 034044.
- [194] Reimers, J. N.: *Accurate and efficient treatment of foil currents in a spiral wound Li-ion cell*. In: *Journal of The Electrochemical Society* 161.1 (2013), A118.
- [195] Wei, Y. et al.: *Kinetics tuning of Li-ion diffusion in layered Li (Ni<sub>x</sub>Mn<sub>y</sub>Co<sub>z</sub>)O<sub>2</sub>*. In: *Journal of the American Chemical Society* 137.26 (2015), pp. 8364–8367.
- [196] Tang, S., Wang, Z., Guo, H., Wang, J., Li, X., and Yan, G.: *Systematic parameter acquisition method for electrochemical model of 4.35 V LiCoO<sub>2</sub> batteries*. In: *Solid State Ionics* 343 (2019), p. 115083.

- [197] Landesfeind, J. and Gasteiger, H. A.: *Temperature and concentration dependence of the ionic transport properties of lithium-ion battery electrolytes*. In: *Journal of The Electrochemical Society* 166.14 (2019), A3079.
- [198] Krachkovskiy, S. A., Bazak, J. D., Fraser, S., Halalay, I. C., and Goward, G. R.: *Determination of mass transfer parameters and ionic association of LiPF<sub>6</sub>: Organic carbonates solutions*. In: *Journal of The Electrochemical Society* 164.4 (2017), A912.
- [199] Farkhondeh, M., Safari, M., Pritzker, M., Fowler, M., Han, T., Wang, J., and Delacourt, C.: *Full-range simulation of a commercial LiFePO<sub>4</sub> electrode accounting for bulk and surface effects: A comparative analysis*. In: *Journal of The Electrochemical Society* 161.3 (2013), A201.
- [200] Prada, E., Di Domenico, D., Creff, Y., Bernard, J., Sauvant-Moynot, V., and Huet, F.: *Simplified electrochemical and thermal model of LiFePO<sub>4</sub>-graphite Li-ion batteries for fast charge applications*. In: *Journal of The Electrochemical Society* 159.9 (2012), A1508.
- [201] Richardson, G., Foster, J. M., Sethurajan, A. K., Krachkovskiy, S. A., Halalay, I. C., Goward, G. R., and Protas, B.: *The effect of ionic aggregates on the transport of charged species in lithium electrolyte solutions*. In: *Journal of The Electrochemical Society* 165.9 (2018), H561.
- [202] Gelman, A., Gilks, W. R., and Roberts, G. O.: *Weak convergence and optimal scaling of random walk Metropolis algorithms*. In: *The annals of applied probability* 7.1 (1997), pp. 110–120.
- [203] Nyman, A., Zavalis, T. G., Elger, R., Behm, M., and Lindbergh, G.: *Analysis of the polarization in a Li-ion battery cell by numerical simulations*. In: *Journal of The Electrochemical Society* 157.11 (2010), A1236.
- [204] Park, M., Zhang, X., Chung, M., Less, G. B., and Sastry, A. M.: *A review of conduction phenomena in Li-ion batteries*. In: *Journal of power sources* 195.24 (2010), pp. 7904–7929.
- [205] Wimarshana, B., Bin-Mat-Arishad, I., and Fly, A.: *Parameter sensitivity analysis of a physico-chemical lithium-ion battery model with combined discharge voltage and electrochemical impedance data*. In: *Journal of Power Sources* 527 (2022), p. 231125.
- [206] Laue, V., Röder, F., and Krewer, U.: *Practical identifiability of electrochemical P2D models for lithium-ion batteries*. In: *Journal of Applied Electrochemistry* 51.9 (2021), pp. 1253–1265.
- [207] Zhao, Y., Kücher, S., and Jossen, A.: *Investigation of the Diffusion Phenomena in Lithium-ion Batteries with Distribution of Relaxation Times*. In: *Electrochimica Acta* (2022), p. 141174. ISSN: 0013-4686. DOI: <https://doi.org/10.1016/j.electacta.2022.141174>. URL: <https://www.sciencedirect.com/science/article/pii/S0013468622013317>.
- [208] Masoudi, R., Uchida, T., and McPhee, J.: *Parameter estimation of an electrochemistry-based lithium-ion battery model*. In: *Journal of Power Sources* 291 (2015), pp. 215–224.
- [209] Miniguano, H., Barrado, A., Lázaro, A., Zumel, P., and Fernández, C.: *General parameter identification procedure and comparative study of Li-Ion battery models*. In: *IEEE Transactions on Vehicular Technology* 69.1 (2019), pp. 235–245.
- [210] Wu, L., Pang, H., Geng, Y., Liu, X., Liu, J., and Liu, K.: *Low-complexity state of charge and anode potential prediction for lithium-ion batteries using a simplified electrochemical model-based observer under variable load condition*. In: *International Journal of Energy Research* (2022).
- [211] Ding, Q., Wang, Y., and Chen, Z.: *Parameter identification of reduced-order electrochemical model simplified by spectral methods and state estimation based on square-root cubature Kalman filter*. In: *Journal of Energy Storage* 46 (2022), p. 103828.



# List of Figures

1.1	A schematic representation of (a): the structure of an electrode and (b): the corresponding impedance part in each frequency range and (c): the DRT spectrum corresponding to the shown impedance . . . . .	3
1.2	Typical equivalent circuit impedance model of a Lithium-ion battery . . . . .	3
1.3	Outline of the thesis . . . . .	8
2.1	Schematic structure of a Lithium-ion battery. The battery is discharged and the lithium ions move from the anode toward the cathode . . . . .	10
2.2	Different packaging types and the p2D modeling concept for the Lithium-ion battery . .	12
3.1	The working principle of the EIS (left) and a typical EIS of a Lithium-ion battery (right). The shown impedance is separated into three parts which are marked with I, II, and III.	24
3.2	Nyquist plot for (a): ohmic resistance and (b): inductance . . . . .	27
3.3	Nyquist plot for (a): capacitance and (b): CPE element . . . . .	27
3.4	Nyquist plot for (a): RC-element and (b): RQ-element . . . . .	28
3.5	The Nyquist plot of the Warburg impedance element in the frequency range 1 mHz ~ 1 kHz with (a): planar geometry, (b): cylindrical geometry, (c): spherical geometry, and (d) with transmissive boundary conditions and planar geometry . . . . .	29
3.6	The surface structure of an active material particle in a Lithium-ion battery and its equivalent circuit model. The active material particles are assumed to have a spherical geometry and the same size . . . . .	33
3.7	Schematic illustration of an impedance, where the capacitive region is represented by a CPE element . . . . .	36
3.8	Flow chart of the toolbox DRT-Analyzer. The toolbox consists of three principal sections: data validation and DRT calculation, peak analysis and results and data export. .	39
3.9	Calculation of the CPE exponent by curve fitting in different cases. In case b the capacitive part is much larger and a linear relationship can be clearly observed in the capacitive region. As a result, case b is more suitable for calculating the CPE exponent	40
3.10	Peak view of the calculated DRT spectrum with the defined peak locations and boundaries.	40
3.11	Results for the peak analysis with (a): the separated peaks showing the contribution of each process and (b): the calculated parameters of each separated peak, where the time constant $\tau$ is in s and the resistance is in $\Omega$ . . . . .	41